Cosmological signatures of the Epoch of Reionisation

Adélie Gorce

université
PARIS-SACLAY

Cosmological signatures of the Epoch of Reionisation

Thèse de doctorat de l'Université Paris-Saclay

École doctorale n° 127, Astronomie & Astrophysique d'Ile-de-France (AAIF)
Spécialité de doctorat : Astronomie et Astrophysique
Unité de recherche : Université Paris-Saclay, CNRS, Institut d'astrophysique spatiale, 91405, Orsay, France
Référent : Faculté des sciences d'Orsay

Thèse présentée et soutenue à Orsay, le 23 septembre 2020, par

Adélie GORCE

Composition du jury:

Cathryn Trott Associate Professor, Curtin Institute of Radio Astronomy, Curtin University, Perth (AU)	Rapporteure
Saleem Zaroubi Professor, Kapteyn Astronomical Institute, University of Groningen (NL)	Rapporteur
Hervé Dole Professeur des Universités, Institut d'Astrophysique Spatiale (UMR8617), Université Paris-Saclay (FR)	Président
Anastasia Fialkov Research Fellow, Institute of Astronomy, Cambridge University (UK)	Examinatrice
Garrelt Mellema Professeur, Oskar Klein Centre, Stockholm University (SW)	Examinateur
Matthieu Tristram Chargé de recherche, Laboratoire de l'Accélérateur Linéaire (UMR 8607), Université Paris-Saclay (FR)	Examinateur
Marian Douspis Astronome, Institut d'Astrophysique Spatiale (UMR8617), Université Paris-Saclay (FR)	Directeur
Jonathan Pritchard Reader in Astrostatistics, Imperial College London (UK)	Co-directeur
Benoît Semelin Professeur des Universités, LERMA (UMR8112), Observatoire de Paris (FR)	Invité

Thèse de doctorat

NNT: 2020UPASP026

A mes deux grands-pères, qui n'ont pas eu la chance de faire des études,
mais qui, je l'espère, me regardent de là-haut avec fierté.

« If tortured sufficiently, data will confess to almost anything. »

Fred Menger

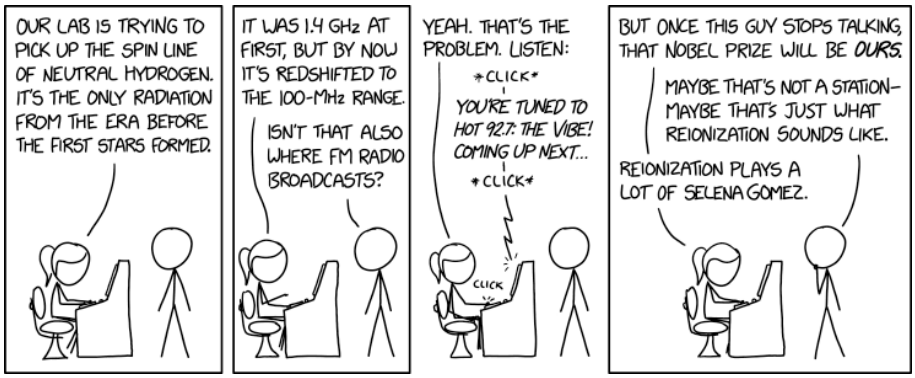

Selena Gomez vs. reionisation (source: xkcd).

Acknowledgements

These three years have been a wonderful, but also difficult, journey, and I have so many people to acknowledge for supporting me and helping me get to the final stages of this PhD.

First, of course, I warmly thank my two supervisors. Jonathan, for always taking the time to explain astrophysics and cosmology to me – even if it included grilling me once on Friedmann equations. Marian, bien sûr, pour avoir toujours été disponible quand j'avais besoin d'aide, que ce soit pour parler de science ou manger des dim sum aux quatre coins du monde. Both of you for supporting my ideas, encouraging me to always go further, and allowing me to finish this PhD with stars in my eyes and a deep love for cosmology in general and reionisation in particular.

Je remercie évidemment ma famille, pour avoir supporté mes maintes explications de ce qu'est la réionisation, pour avoir fait semblant d'être passionné par ce que je disais, et pour avoir supporté mes petits craquages, surtout ces dernières semaines. Maman pour toujours savoir ce qui ne va pas ; Papa pour toujours chercher un moyen de m'aider, quelque soit le problème ; Lulu pour me comprendre si bien puisqu'on est tellement similaires ; Lilou pour être toujours là quand j'ai besoin d'elle, que ce soit pour partir de l'autre côté de la planète ou juste de la Manche ; et enfin Basile et Léon pour être des sources infinies de bonheur. Je n'aurais jamais terminé cette thèse sans vous !

Ce sera dur de n'oublier personne mais je remercie ma bande de toujours, que l'on a parfois nommée l'AdC, qui est à mes côtés depuis plus de dix ans et j'en suis tellement heureuse. Lucie, Rémi, Tom, Alex, Vio, merci pour me faire penser à autre chose qu'aux sciences. Merci à Edouard et Edith pour nos week-ends d'aventure, véritables bols d'air et de joie. Merci à Léa pour être toujours si positive. Et merci à Lorène, si loin et pourtant si proche, sans laquelle je n'aurais jamais survécu à toutes les aventures (émotionnelles) de ces trois dernières années.

Merci à Alex, Sophie et Wacim pour avoir pris la peine de venir me voir à Londres et être venus évacuer le stress avec moi au club de fromage !

Thank you Joanna. I am so grateful that we met and bonded over our shared love of cheese. Without you these four years with you in London would not have been the same.

Merci à mes copains de l'IAS. A Dany, pour avoir enflammé le 3ème étage avec Beyoncé et Lady Gaga (qui a besoin d'être au même étage que tout le monde quand on a un bureau pareil ?!). A Victor et Louis, les stagiaires/thésards/postdocs du dimanche avec qui cette aventure a commencé. On s'est serré les coudes pendant quatre ans et j'espère bien que ça va continuer ! Merci à Mathieu, toujours très occupé mais aussi toujours disponible pour partager sa passion pour la cosmologie (et la gym suédoise); à Nabila, qui a toujours été là non seulement pour me pousser à faire mieux mais aussi me soutenir. Merci à tout le laboratoire, une vraie petite famille, avec qui j'aurais aimé passer encore plus de temps et avec qui j'espère passer plus de temps dans le futur !

I thank the Imperial astrophysics group, who welcomed me so warmly despite being in London just half of the year and not being able to graduate with them. Thank you to my office buddies: Wahid, Lena, Joe, James, Dan and Ian, for the laughs inside and outside of the office. We'll come back for this raspberry pie! And of course, a special thank you to one of you, a sunshine who has beamed over the second part of my PhD and given me incredible memories to bring back to Paris and over to Montreal.

Finally, I would like to thank the members of my thesis committee for taking the time to read my thesis and attend my viva, despite technical difficulties very specific to 2020; as well as for their comments which will help me become a better researcher.

Résumé

Depuis le Big Bang jusqu'à nos jours, l'Univers subit deux grandes transitions de phase. La première est la recombinaison : les ions et électrons du plasma primordial s'associent pour former les premiers atomes neutres. Les photons, auparavant retenus dans ce même plasma par leurs interactions avec les particules chargées, sont alors libérés, formant ainsi le fond diffus cosmologique (CMB). La seconde grande étape de l'histoire de l'Univers est la réionisation cosmique. Pendant les quelques milliards d'années que dure ce processus, le rayonnement des premières étoiles ionise les atomes du milieu intergalactique (IGM). Malgré son évidente importance, cette période est méconnue. Notamment, sa chronologie et la nature de ses sources sont encore discutées. De nombreux projets observationnels sont en cours pour répondre à ces questions, comme le SKA, le plus grand radio télescope du monde, ou la prochaine génération d'observatoires du CMB. Les premiers résultats de ces expériences devraient nous parvenir dans les années à venir, pourtant la communauté scientifique n'est pas encore prête, à la fois à cause de limitations observationnelles, et car le processus de réionisation en lui-même est mal modélisé.

Au cours de mes trois années de doctorat, j'ai développé des outils permettant d'améliorer l'analyse et l'interprétation des observations dont on dispose.

M'intéressant dans un premier chapitre au processus dans sa globalité, c'est-à-dire l'évolution de la fraction ionisée de l'IGM avec le temps, je donne un scénario de référence pour la réionisation, mené par les galaxies, fondé sur quelques hypothèses simples à propos de l'Univers jeune, et qui pour la première fois est en accord avec toutes les données disponibles. Il s'agit de spectres de quasars, des fonctions de luminosité des galaxies, ainsi que de l'épaisseur optique de Thomson, obtenue en observant le CMB. Dans ce scénario, la réionisation est un processus asymétrique qui commence lentement, autour d'un redshift $z \sim 15$, puis accélère une fois que 20% de l'IGM est ionisé, et finit avant $z = 5$.

Cependant, la réionisation intervient également à de plus petites échelles, et la façon dont les galaxies ionisent leur environnement immédiat nous renseigne sur leurs propriétés physiques. C'est pourquoi dans un second chapitre, j'introduis des outils statistiques innovants, de complexité croissante et fondés sur une meilleure modélisation du processus, qui pourront être appliqués à des cartes d'intensité du signal à 21cm, ou aux plus grand multipoles observés dans le CMB. Pour ce dernier, je propose une nouvelle description du spectre de puissance de l'effet Sunyaev-Zel'dovich cinétique, dont les paramètres sont reliés

à la réionisation et aux propriétés ionisantes des sources. Cette méthode permettra, pour la première fois, de mesurer non seulement l'amplitude mais aussi la forme de ce spectre à partir de données CMB à petite échelle de qualité. En ce qui concerne le signal à 21cm, j'introduis premièrement une fonction de corrélation à un point, qui utilise la variance d'échantillon à notre avantage, puis une fonction de corrélation à trois points, conçue spécialement pour caractériser la forme sphérique des bulles d'ionisation. Ces deux outils sont construits dans l'objectif d'être robustes aux contraintes liées à l'observation du signal à 21cm.

Enfin, dans le dernier chapitre, je discute les limitations de ces outils, liées à la fois aux méthodes d'observation elles-mêmes, ainsi qu'à des erreurs de modélisation. Je m'intéresse par exemple à l'impact que peut avoir la valeur de certains paramètres mal connus, comme la fraction de photons qui parviennent à s'échapper de leur galaxie hôte pour atteindre l'IGM, sur nos contraintes actuelles.

Le résultat de ces trois années de doctorat est un modèle cohérent de la réionisation, fondé sur toutes les observations disponibles, et dont les limitations sont comprises et quantifiées. J'ai cherché à mieux comprendre et décrire ce processus en développant des outils dédiés, robustes aux limitations spécifiques à l'étude de la réionisation et disponibles publiquement. Avec ce travail, j'ouvre la voie à une analyse cosmologique cohérente des données qui permettra d'obtenir, une fois que la nouvelle génération de télescopes aura donné ses premiers résultats, une compréhension à la fois globale et locale de la réionisation, c'est-à-dire nous renseignant sur l'Univers dans son intégralité, mais également sur la nature de ses premières sources de lumière.

Ce travail a donné lieu à la publication de trois articles dans des journaux scientifiques : Gorce et al. (2018), publié dans Astronomy & Astrophysics en août 2018; Gorce & Pritchard (2019), publié dans MNRAS en août 2019; ainsi que Gorce et al. (2020), publié dans Astronomy & Astrophysics en août 2020. Un quatrième article est en cours de rédaction. La plupart des programmes informatiques développés pendant mon doctorat sont disponibles sur ma page GitHub[1].

[1] Voir `https://github.com/adeliegorce/tools4reionisation`.

Abstract

From the Big Bang to this day, the Universe goes through two main phase transitions. The first is recombination, when Cosmic Microwave Background (CMB) photons are released as the ions and electrons of the primordial plasma recombine to form neutral atoms. The second, which starts a few hundred million years later, is the Epoch of Reionisation (EoR), when the first galaxies slowly ionise the atoms of their surrounding intergalactic medium (IGM). Despite its importance regarding our knowledge of the young Universe, little is known about this period, notably its timeline and the nature of its sources. Many ambitious observational projects are ongoing to answer these questions, such as the SKA, the largest radio telescope in the world, and next generation CMB observatories on small and large scales. These experiments should give their first results in the coming years, yet the scientific community is not ready, both because the observational limitations are poorly known and because the reionisation process in itself is poorly modelled. During my PhD, I have developed statistical tools to improve the analysis and interpretation of this data.

In the first chapter of this work, I consider a large-scale approach. In order to overcome individual sources of bias, I combine for the first time all the observational data currently available, from quasar spectra and galaxy luminosity functions to the CMB optical depth, in order to infer a comprehensive global history of reionisation. The resulting scenario, based on a few reasonable assumptions about the high-redshift Universe, brings the data back together in a simple history where reionisation is an asymmetric process driven by galaxies, starting slowly around $z = 15$, before accelerating when 20% of the IGM is ionised, and ending before $z = 5$.

However, reionisation is not only a large-scale process, and we can learn about the properties of the first stars and galaxies when looking at how they ionise their immediate surroundings, on scales of a few hundreds of megaparsecs. In this perspective, in a second chapter, I introduce new statistical tools to be applied to small-scale data, from intensity mapping of the 21cm signal of neutral hydrogen to high-multipole CMB observations. For the latter, I formulate a new parameterisation of the patchy kinetic Sunyaev Zel'dovich (kSZ) angular power spectrum in terms of reionisation. The complicated physics involved in kSZ signal is summarised in this quick and easy-to-forward-model formalism, based on two parameters, related to the underlying physics of the IGM and early galaxies. With this

parameterisation, it will be possible to extract for the first time the accurate amplitude and shape of the reionisation kSZ power spectrum from CMB data. Regarding 21cm intensity mapping, I first introduce a one-point statistic which makes use of sample variance to our benefit, and, secondly, an improved 3-point correlation function, optimised for the study of the bubbly structure of the ionisation field during the EoR. These tools are designed to be robust to some of the difficulties encountered when looking for the 21cm signal from reionisation, such as thermal noise and instrument resolution.

In the last chapter, I discuss the observations- and model-related limitations of current results, by looking at the way poorly known parameters impact our scenarios of reionisation and by proposing unbiased and efficient observational strategies.

In these three years of work, I have developed new tools, designed for the study of the EoR, namely to overcome specific model- and observations-related limitations, and made them available for the community. Doing so, I have paved the way for a clean cosmological analysis of reionisation data. Once next-generation data is available, these methods will give reliable constraints on the global and local history of cosmic reionisation, telling us about the Universe as a whole and about the nature of its early light sources. Using the data available today, I have provided a reference history of reionisation – confirming that astrophysical and cosmological observations give a coherent picture, as well as a better understanding of what limits current results.

These results were published in three journal articles: Gorce et al. (2018), published by Astronomy & Astrophysics in August 2018; Gorce & Pritchard (2019), published by MNRAS in August 2019; and Gorce et al. (2020), published by Astronomy & Astrophysics in August 2020. A final article is currently being written. Most of the computing programmes developed during my PhD are available on my GitHub page[2].

[2]See `https://github.com/adeliegorce/tools4reionisation`.

Synthèse

Le fond diffus cosmologique, cliché de l'Univers alors vieux de seulement 380 000 ans, est une source précieuse d'informations sur l'Univers jeune. A cette époque, il est suffisamment froid pour que les ions et les électrons du plasma primordial se recombinent et donnent les premiers atomes neutres. Les photons, auparavant retenus par leurs interactions avec les particules chargées, s'échappent, formant ainsi la première lumière visible dans l'histoire de l'Univers. Les quelques milliards d'années qui suivent voient la naissance des premières étoiles, trous noirs et galaxies, durant ce que l'on appelle le printemps cosmique et l'époque de la réionisation. A cette époque, les premières galaxies réchauffent et ionisent les atomes d'hydrogène et d'hélium du milieu intergalactique (IGM) environnant, tant et si bien qu'aujourd'hui, l'intégralité de l'IGM est ionisé. Améliorer notre connaissance de l'époque de la réionisation est essentiel, non seulement car elle représente une période centrale de l'histoire de l'Univers, mais également car elle peut nous apprendre de nombreuses choses sur la formation et l'évolution des premières galaxies, ainsi que leurs propriétés physiques. Par exemple, suivre l'évolution des bulles d'ionisation formées par ces galaxies nous renseignera sur la luminosité, l'âge et même la métallicité de ces dernières. D'autre part, s'il s'avère que les galaxies ne sont pas suffisantes pour réioniser l'IGM seules, cela sera un indice sur la densité de trous noirs à haut redshift. La chronologie de la réionisation cosmique et la nature de ses sources sont discutées car à ce jour, peu d'observations sont disponibles pour contraindre cette période si éloignée. Elles sont cependant suffisantes pour en donner une image globale, où les premières galaxies apparaissent à un redshift $z \sim 15$, commencent à doucement ioniser l'IGM, avant d'accélérer pour ioniser les 80% restants sur un intervalle $6 < z < 8$, comme illustré sur la figure 1.

Le CMB et le signal 21cm sont deux observables cosmologiques essentielles dans l'étude de la réionisation, et ont été au centre de mon travail de doctorat. En effet, l'interaction des photons du CMB avec les électrons libérés par la réionisation laisse des traces dans le spectre de puissance du CMB qui nous renseignent sur l'évolution et la distribution de ces électrons. D'autre part, le signal de la raie à 21 centimètres correspond à la transition atomique entre les deux sous-niveaux de la structure hyperfine du niveau fondamental de l'atome d'hydrogène neutre. Ce signal est donc sensible aux variations de température, de densité et d'ionisation du gaz intergalactique et nous renseigne directement sur la nature de l'IGM à une fréquence – et donc redshift, donnés. Les bases nécessaires à l'analyse de ces deux signaux, ainsi qu'une introduction générale à la cosmologie, sont données dans le

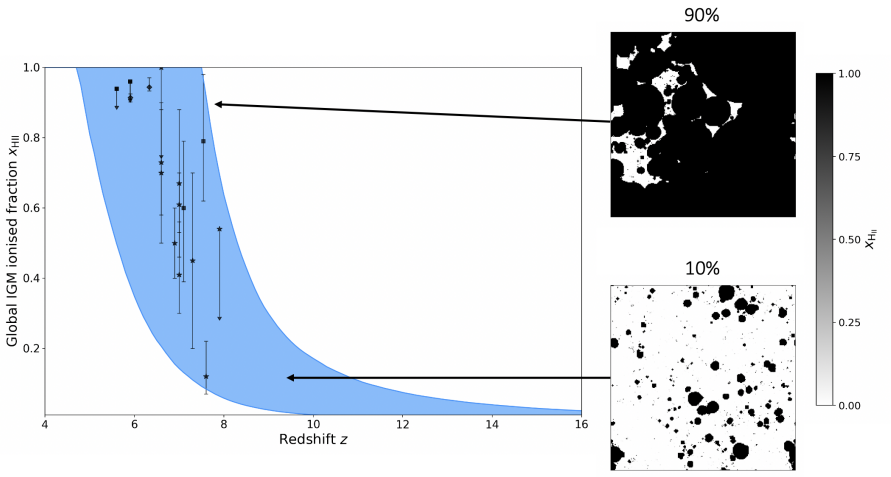

Figure 1: L'image de gauche présente l'idée que l'on a aujourd'hui de l'histoire globale de la réionisation, grâce à des observations astrophysiques (points de données) et du CMB (zone bleue). Les deux images de droite présentes les champs d'ionisation de la simulation `rsage SFR` à 10% et 90% d'ionisation (Seiler et al. 2019).

premier chapitre.

D'ambitieux projets sont en cours pour répondre aux questions posées par la réionisation, comme le Square Kilometre Array (SKA), le plus grand radiotélescope du monde, et les expériences CMB de nouvelle génération, appelées CMB-Stage 4 ou CMB-S4. Elles devraient donner leurs premiers résultats dans les années à venir et pourtant la communauté scientifique n'est pas encore prête, non seulement car les limitations observationnelles sont mal connues, mais également car le processus en lui-même est mal modélisé. Pendant mon doctorat, je me suis attachée à améliorer ces deux aspects, afin de pouvoir donner une image exhaustive de la réionisation quand les premières observations seront faites. Cette image inclut la description du processus d'ionisation du milieu galactique dans sa globalité, à des échelles cosmologiques, comme présenté sur la figure 1; mais également d'un point de vue local. En effet, selon la nature et densité des premières sources de lumière, l'ionisation de l'IGM se fera de façon plus ou moins homogène. Ces deux approches ont structuré mon travail de doctorat et sont présentées dans les chapitres 2 et 3, respectivement. Le dernier chapitre s'attache à étudier les limites des différentes méthodes développées au cours des trois dernières années, ainsi qu'à proposer des outils permettant de les surmonter.

Dans le chapitre 2, je décris les différents types d'observations disponibles pour contraindre l'histoire globale de la réionisation. Il s'agit des dernières mesures du taux de formation stellaire cosmique, qui donne une estimation du nombre de photons disponibles à différents redshifts pour ioniser l'IGM; ainsi que du taux d'ionisation du milieu intergalactique, mesuré dans les spectres de quasars et galaxies à haut redshift. En combinant pour la première fois ces observations astrophysiques à la valeur de l'épaisseur optique de Thomson mesurée par Planck, j'obtiens un scénario cohérent où la réionisation commence

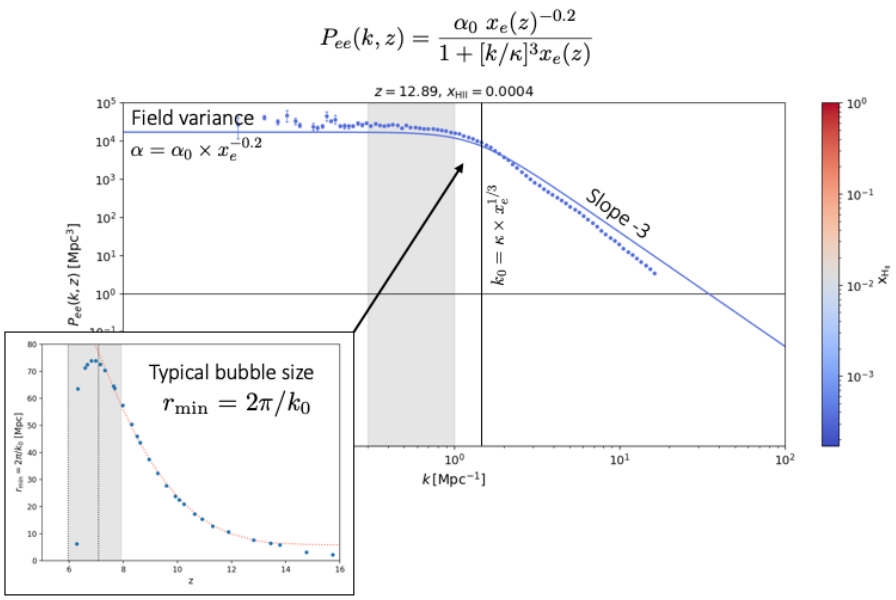

Figure 2: Paramétrisation du spectre de puissance des fluctuations de densité des électrons libres de l'IGM (ligne bleue), calibrée sur la simulation EMMA (points), et illustration de l'interprétation physique des paramètres: la fréquence de coupure κ peut être reliée à la taille caractéristique des bulles d'ionisation, tandis que α_0 est la variance maximale du champ d'électrons libres, au début du processus d'ionisation.

autour de $z = 15$ et finit avant $z = 5$, confirmant que malgré des origines très différentes, toutes ces observations sont compatibles (Gorce et al. 2018).

Dans le troisième chapitre, je m'intéresse à la réionisation à une échelle locale, afin de contraindre les propriétés physiques des premières galaxies. Les deux champs d'ionisation présentés dans la figure 1 montrent que ces derniers ont une morphologie très spécifique, avec des zones d'ionisation que l'on peut associer à des sphères, autour de chaque galaxie. La forme et la densité de ces zones peut être reliée à la masse, composition et luminosité des galaxies. Par conséquent, je propose un nouvel outil statistique simple, qui permet de décrire ces différences morphologiques, appelé la variance locale. Fondé sur l'analyse de tranches de champs d'ionisation obtenus à partir d'une simulation ou d'observations à redshift donné, cet outil, qui s'assimile à une fonction de corrélation à un point, est très rapide à calculer. Il est introduit dans Gorce et al. (in prep), en cours de rédaction.

Je m'intéresse ensuite aux fonctions de corrélation à deux points, et, plus particulièrement, au spectre de puissance de l'effet kSZ. Cet effet correspond à la diffusion Compton inverse de photons du CMB, peu énergétiques, sur des électrons qui ont une vitesse propre par rapport au CMB. Lors de cette interaction, les électrons transfèrent une partie de leur énergie aux photons, ce qui se traduit par un excès d'amplitude du spectre de température du CMB aux petites échelles. Durant la réionisation, ces électrons sont concentrés autour des galaxies, et cet effet est donc sensible à la morphologie du champ d'ionisation, en plus de son évolution globale. Dans ce chapitre, je propose une façon simple de paramétriser

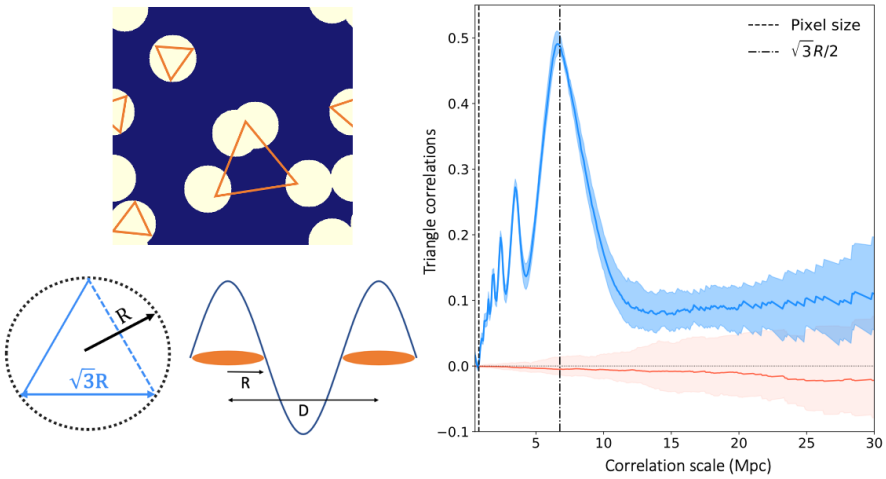

Figure 3: Illustration de la fonction de corrélation triangulaire appliquée à un modèle simplifié. La corrélation est maximale pour les modes correspondant aux triangles équilatéraux inscrits dans les bulles d'ionisation (en bleu) et nulle pour un champ gaussien aléatoire (en rouge).

cette double dépendance, et la calibre sur différents types de simulations (Gorce et al. 2020). Cette paramétrisation concerne le spectre de puissance des fluctuations de densité des électrons libres de l'IGM, et est illustrée en figure 2. Appliquée aux futures données CMB, elle permettra pour la première fois d'obtenir l'amplitude *et* la forme du spectre kSZ.

Enfin, la dernière partie de ce chapitre se concentre sur le bispectre, transformée de Fourier inverse de la fonction de corrélation à trois points. Le bispectre permet d'étudier la non-Gaussianité du signal à 21cm issu de la réionisation, là où le spectre de puissance l'ignore. Je propose une approche qui permet de s'affranchir d'étapes de transformation du signal qui ralentissent le traitement des données, tout en isolant la partie même du signal qui nous donne des informations sur la structure du champ d'ionisation, les phases. Cet outil, appelé la fonction de corrélation triangulaire des phases (TCF), est conçu de manière à ce que les modes correspondant aux triangles équilatéraux inscrits dans les bulles d'ionisation donnent le signal maximal, comme illustré sur la figure 3. On peut ainsi suivre l'évolution du taux d'ionisation de l'IGM et l'augmentation de la taille des bulles ionisées autour des premières galaxies à différents redshifts (Gorce & Pritchard 2019).

Enfin, dans le quatrième et dernier chapitre de cette thèse de doctorat, je présente les différentes limitations dont souffre encore l'analyse de données sur la réionisation. Certaines de ces limitations sont dues aux observations elles-mêmes, comme c'est le cas de la variance cosmique et de la variance liée à la taille limitée des observations. Par ailleurs, dans le cas du CMB comme du signal à 21cm, la modélisation et soustraction des avant-plans des observations, afin d'accéder au signal cosmologique, est un problème central. Une fois les avant-plans supprimés, une bonne connaissance de l'instrument est nécessaire pour s'affranchir des systématiques comme le bruit thermique ou la résolution angulaire. Les

outils présentés ici se trouvent être robustes à ces biais : je montre que la variance locale et la TCF parviennent toutes deux à extraire des informations d'une carte bruitée ou lissée avec la résolution angulaire de SKA1-*Low*.

D'autres limitations proviennent de la façon dont le processus de réionisation est modélisé : la paramétrisation choisie pour analyser les données CMB va par exemple avoir un fort impact sur la mesure de l'épaisseur optique τ et l'amplitude du signal kSZ. Par ailleurs, nombre de paramètres utilisés pour convertir des données astrophysiques en observables de la réionisation sont mal connus et corrélés. Dans ce chapitre, j'évalue le biais lié à la modélisation de ces paramètres et prouve, par exemple, que la valeur exacte du taux d'agrégation de l'hydrogène ionisé dans l'IGM n'a pas autant d'impact que ce à quoi l'on pourrait s'attendre. La fraction de photons ionisants qui parviennent à s'échapper de leur galaxie hôte pour atteindre l'IGM, en revanche, joue un rôle essentiel dans l'estimation du taux d'ionisation : pour ioniser l'IGM en accord avec les données, une valeur moyenne de 20% au cours de la réionisation est nécessaire. Cette valeur est cependant largement dépendante de la façon dont les fonctions de luminosité des galaxies sont modélisées.

Le résultat de ces trois années de travail est un modèle cohérent de la réionisation, fondé sur toutes les observations disponibles, et dont les limitations sont comprises et quantifiées. De nouveaux outils, conçus pour étudier la réionisation, et notamment pour surmonter des limitations spécifiques à celle-ci, sont disponibles et pourront être appliqués aux futures observations du CMB et du signal à 21cm, afin de donner des contraintes fiables sur l'histoire globale et locale de la réionisation.

Contents

List of Figures

Chapter 1

Introduction

As a snapshot of the sky about 380 000 years after the Big Bang, the Cosmic Microwave Background (CMB) is a precious source of information about the very young Universe. At this time, primordial ions and electrons recombined to form neutral atoms, freeing the photons previously stuck in the primordial plasma by Thomson scattering. However, the first billion years that follow, which are expected to see the birth of the first stars, black holes and galaxies, are still widely unknown. During the Epoch of Reionisation (EoR), these first galaxies heated and ionised the neutral atoms of hydrogen and helium in their surrounding intergalactic medium (IGM), and eventually, all atoms. Despite its importance regarding our knowledge of the young Universe, both on small and large scales, little is known about this period, notably its timeline and the nature of its sources. From the modest amount of data available today, we know that the bulk of reionisation must have occurred at redshifts $z \sim 7 - 8$, and that the process in general was driven by galaxies too faint and too distant to be observed directly. For example, looking at H I absorption in the spectra of distant sources gives an idea of the reionisation timeline, weakened by substantial error bars. However, improving our knowledge of reionisation is essential, not only to learn more about the history of the Universe as a whole, but also to understand galaxy formation and evolution, as the first galaxies are thought to have led the process. Estimates of the speed of the ionisation front on 21cm images (the shape and growth of the 'ionised bubbles') can help place constraints on the properties of early galaxies, such as their metallicity, brightness, or simply age. Additionally, if early galaxies are not sufficient to fully ionise the IGM, the existence of early black holes might be required. Reionisation studies are, therefore, essential to a wide range of cosmological and astrophysical subjects, but substantial efforts are required to be able to interpret the data coming in the next few years correctly and efficiently.

Many ambitious observational projects are ongoing to build on the 21cm signal and

CMB data, two essential cosmological sources of information about reionisation, and answer the questions of the timeline and origin of reionisation.

The interaction of CMB photons with electrons freed during the EoR leaves imprints in the primordial power spectrum which can tell us about the evolution of the distribution of electrons in the IGM with time. These include measurements of the Thomson optical depth and of the amplitude of the kinetic Sunyaev-Zel'dovich (kSZ) effect in CMB observations, which give coarse constraints on reionisation as a whole, namely on parameters such as its duration and endpoint. During my PhD, I have developed methods which, with sufficiently precise observations, will take reionisation constraints from CMB data to the next level by not only improving our current knowledge of the general reionisation timeline, but also providing information about the nature of the first galaxies, such as their efficiency to ionise neighbouring atoms. Such observations are expected in the coming years, first from current experiments, such as the South Pole telescope (SPT, Ruhl et al. 2004) and the Atacama Cosmology Telescope (ACT, Kosowsky 2003), and later from the CMB Stage-4 observatories (CMB-S4, Abazajian et al. 2016).

The 21cm signal corresponds to the spin-flip transition of neutral hydrogen, and is sensitive to temperature and ionisation variations of the cosmic gas. As a line transition, it is easy to relate observed frequency to emitted frequency, and we can map out the Universe at any time. Radio interferometry is, therefore, another pillar of reionisation study. The Square Kilometre Array (SKA, Koopmans et al. 2015), the largest radio telescope in the world, will produce such images by 2029. Many methods have been proposed to extract information about reionisation from these maps. However, due to the huge amount of data these telescopes will produce (160TB, the world internet traffic in 2015, in one second for SKA), data extraction must be efficient. During my PhD, I have designed time-saving techniques, allowing to efficiently analyse this data, while being robust to instrumental effects, that I will present in this work.

Reionising the IGM involves many different physical processes, from atomic to cosmological scales. This is both a curse, as it makes reionisation very difficult to simulate, and a blessing, as many different types of observations can help constraining it. As part of my doctoral work, I have shown that astrophysical observations, such as local measurements of the ionisation of the IGM, or the star formation rate, were compatible with large-scale CMB results, but also necessary to obtain robust constraints. Combining all the data available, from astrophysics to cosmology, will be essential to the analysis of future EoR observations, in the context of the James Webb Space Telescope (JWST, Gardner et al. 2006)[1] launching within the next few years, of CMB-S4 observatories (Abazajian et al. 2016) coming online, and of radio interferometers such as the Hydrogen Reionization Array (HERA, DeBoer et al. 2017) and the Murchison Widefield Array (MWA, Tingay et al. 2013) getting clean 21cm signal during reionisation in the coming months. In this perspective, I have looked during my PhD at improving the quality of the information we can

[1] See `https://www.jwst.nasa.gov`.

recover from current and future observations, in a bid to make the most of them, and give a comprehensive image of reionisation in the coming years. This doctoral thesis describes this work, looking at reionisation as a global, cosmological process, before moving on to the inhomogeneities of the IGM ionisation on more local scales. These methods are confronted to their limitations, both observations- and model-related, in order to only pick the most robust methods and develop efficient observational strategies. In this first chapter, we pave the way for later results, introducing basic concepts of general cosmology, as well as the physics underlying the study of the aforementioned CMB and 21cm signal. We also give a description of the current status of what is known about reionisation, and of the different questions still pending.

1.1 Context

In this section, we give context for the rest of this work. We introduce basic principles of cosmology, to place the Epoch of Reionisation in the general timeline of the Universe's history. We then give an overview of what is currently known of cosmic reionisation, and of the possible answers to unsolved questions about this epoch, namely about its sources.

1.1.1 Cosmology 101

Cosmology is the study of the Universe as a whole. Satellites such as the Planck satellite have investigated its first instants – here, meaning its first few hundreds of thousands years, through the study of its first light, the CMB. The CMB tells us that the Universe is extremely close to being isotropic and homogeneous, an image which has been confirmed by large-scale galaxy surveys of the local Universe. This Cosmological principle suggests that the Universe is the same everywhere, with no specific direction favoured, on scales larger than about 300 Mpc. Such results are concordant with the formalism developed to describe the dynamics of our Universe, general relativity, and in particular with the Friedmann-Lemaître-Robertson-Walker (FLRW) space-time metric, given in spherical coordinates by

$$\mathrm{d}s^2 = c^2\mathrm{d}t^2 - a(t)^2\left(\frac{\mathrm{d}r^2}{1-kr^2} + r^2\mathrm{d}\Omega^2\right), \tag{1.1}$$

where $\mathrm{d}s$, $\mathrm{d}t$, and $\mathrm{d}\Omega$ are intervals of space-time, time, and angle respectively and c is the speed of light in vacuum. The parameter $a(t)$ sets the scale of space at time t and k describes the geometry of the Universe. An example of a negatively curved surface ($k = -1$) would be the shape of a saddle; for $k = 1$, the Universe is spherical and closed; for $k = 0$, it is flat. By convention, today, $a(t_0) = 1$. a is related to the well-known cosmological redshift via $a = 1/(1+z)$.

A solution to the Einstein's equations involving the FLRW metric is the Friedmann equation. It writes

$$\left(\frac{\dot{a}}{a}\right)^2 = H^2(t) = \frac{8\pi G}{3}\rho - \frac{kc^2}{a^2}, \tag{1.2}$$

where we have defined the Hubble parameter $H(t) \equiv \dot{a}/a$, which describes the expansion rate of the Universe. A positive value of $H(t)$, as measured today, means the Universe is expanding. Matter conservation is additionally ensured by

$$\dot{\rho} + 3H(t)(\rho + P) = 0, \tag{1.3}$$

where ρ and P are the total energy density and pressure, respectively. If we consider that the Universe is made of a few different components, each an individual perfect fluid with equation of state $P_i = w_i\rho_i$, then they each verify this equation independently: $\dot{\rho}_i + (1 + w_i)\rho_i = 0$, solved by $\rho_i = \rho_{i,0}(a_0/a)^{3(1+w_i)}$. In this formalism, each of the Universe's components has its own equation of state: non-relativistic matter ρ_m ($w = 0$), radiation

ρ_r ($w = 1/3$), and dark energy ρ_Λ ($w = -1$). These parameters are often constrained as their ratio $\Omega_m = \rho_m/\rho_c$ to the critical density of the Universe, that is the density obtained when k is set to zero in Eq. (1.2) $\rho_c = 3H^2(t_0)/8\pi G$. We can then rewrite the Friedmann equation as

$$\left(\frac{H(t)}{H_0}\right)^2 = \Omega_\Lambda + \Omega_k \left(\frac{a_0}{a}\right)^2 + \Omega_m \left(\frac{a_0}{a}\right)^3 + \Omega_r \left(\frac{a_0}{a}\right)^4, \tag{1.4}$$

which shows the evolution of each Universe component with expansion. For example, cold matter is only geometrically diluted ($\rho_m \propto a^{-3}$) while dark energy is pervasive and uniform throughout the Universe ($\rho_\Lambda \propto a_0$). Here, a_0 and H_0 are the values of each parameter taken today, at $t = t_0$, and $\Omega_k \equiv -k/a_0^2 H_0^2$. Note that $\Omega_k + \Omega_r + \Omega_m + \Omega_\Lambda = 1$. Observations of the CMB have given constraints on these cosmological parameters: the latest release of Planck's data gives $\Omega_b h^2 = 0.0224 \pm 0.0001$, $\Omega_m = 0.315 \pm 0.007$, $\Omega_c h^2 = 0.120 \pm 0.001$, $\Omega_k = 0.001 \pm 0.002$, the dark energy equation of state $w_0 = -1.03 \pm 0.03$ and $H_0 = 67.4 \pm 0.5$ km s^{-1} Mpc^{-1} (Planck Collaboration et al. 2018), i.e. the Universe is close to flat and expanding.

Resulting from the Friedmann equation, we have the ΛCDM model, which is today the standard model of cosmology. In this model, the Universe goes through a period of hot big bang and then cools down by adiabatically expanding, at exponential speed for the first few 10^{-32} seconds, during inflation. According to Eq. (1.4), at different times, the evolution of the Universe is dominated by different components. At early times, radiation dominates, then we go through a matter-dominated, and then dark energy dominated era[2]. If we assume the Universe is filled by a perfect fluid, initially very hot and dense after the Big Bang, the fact that the Universe expands with time means that it progressively cools down until reaching $T_{\rm CMB} = 2.72548 \pm 0.00057$ K today, as measured by the FIRAS experiment on the Cosmic Background Explorer (COBE, Fixsen 2009). Additionally, all large-scale structures observed today, such as galaxies, are seeded by initial quantum fluctuations that exponentially grow during cosmic inflation. In this perspective, σ_8 is another important parameter of the ΛCDM model. By definition, σ_8 measures the amplitude of the (linear) matter power spectrum on the scale of 8 h^{-1}Mpc, but intuitively it describes the growth of fluctuations in the early Universe, and, in turn, the distribution of matter in the sky today.

According to ΛCDM, the Universe is initially hot enough ($k_B T \gg 13.6$ eV) to stay ionised, and therefore for the thermal bath of photons to remain tightly coupled to the ions through Thomson scattering. Around redshift $z = 1\,090$, when the Universe is sufficiently cool, protons pair with free electrons and neutrons to form neutral atoms, mostly of hydrogen, in the so-called recombination era. This process also frees the photons from their interactions with matter, and we see these photons today as the Cosmic Microwave Background (CMB). Through these recombinations, the Universe ionisation level falls to 0.0001% and remains low for about a billion years (Peebles 1968; Zel'dovich et al. 1969; Seager et al. 2000). Yet, observations of the Gunn-Peterson effect (Gunn & Peterson 1965)

[2]As experiments find $\Omega_k \sim 0$, there will no be curvature-dominated epoch.

in quasar spectra tell us that at $z = 5.9$, $96 \pm 5\,\%$ of the IGM hydrogen atoms are ionised (McGreer et al. 2015). What happened in the meantime, i.e. during the Epoch of Reionisation, is an essential source of information about the evolution of the young Universe, the formation of large cosmic structures and the properties of early galaxies, to cite only a few.

1.1.2 Sources of reionisation

The most commonly admitted scenario of reionisation is that, between $z \sim 20$ and $z \sim 6$, star-forming galaxies ionised their surrounding neutral medium – mostly hydrogen and helium, and the newly ionised regions then progressively overlapped (e.g. Aghanim et al. 1996; Becker et al. 2015), leading to a decrease in the neutral fraction of the Intergalactic Medium (IGM). Finally, quasars took over to perform the second ionisation of helium atoms around $z \simeq 4$ (Mesinger 2016). Yet, some doubts remain about the sources of hydrogen reionisation: some consider that quasars could have led the process (Madau & Haardt 2015; Grazian et al. 2018), although star-forming galaxies are often preferred: Robertson et al. (2015) find the latter are sufficient to maintain the IGM ionised until $z \sim 7$ and no proof of the existence of a sufficient number of quasars at redshifts $z \leq 10$ has been given yet. Ever lower values of the integrated Thomson optical depth given by CMB observations reduce the need for a significant contribution of not-yet observed very high-redshift galaxies (Planck Collaboration et al. 2016d).

Conversely, learning about reionisation tells us about the nature of its sources and the evolution of galaxies. For example, the stellar mass and so ionising efficiency of a newly born galaxy will depend on the mass of its host dark matter halo: a rule of thumbs gives the galaxy mass to be about ten times lower that the mass of its host dark matter halo (Zackrisson 2020). H_2 cooling in low-mass halos ($10^4\ M_\odot < M < 10^6\ M_\odot$) leads to the first generation of stars being born in about 150 Myr, but these masses are not sufficient to host a galaxy. Heavier halos, of mass $10^7\ M_\odot < M < 10^9\ M_\odot$, are expected to have formed around $z \sim 15$. In these, H I cooling allows efficient and prolonged star formation and so the formation of the first galaxies. These will however not be long-lived because of the gas potentially being blown out of the shallow gravitational potential of the halo (Wise 2019). Most galaxies live in halos with mass $M > 10^9\ M_\odot$, and are likely neighbours to a massive central black hole. Such galaxy masses allow for strong star formation rates by avoiding major gas losses. It is these star-forming halos that we expect to drive reionisation. The formation of dark matter halos is illustrated in Fig. 1.1. The most distant high-redshift galaxy known today has a stellar mass of about $10^9\ M_\odot$ and was observed at $z = 11.1$ (Oesch et al. 2016). High-redshift quasars could, if in sufficient number, be a main contributor of reionisation. These quasars are expected to be extremely rare, so that, despite their very high luminosity compared to same-redshift galaxies, only a couple have been detected at $z \geq 7$. The most distant quasar currently known was observed at $z = 7.5$ and has a mass of $8 \times 10^8\ M_\odot$ (Bañados et al. 2018). Other than

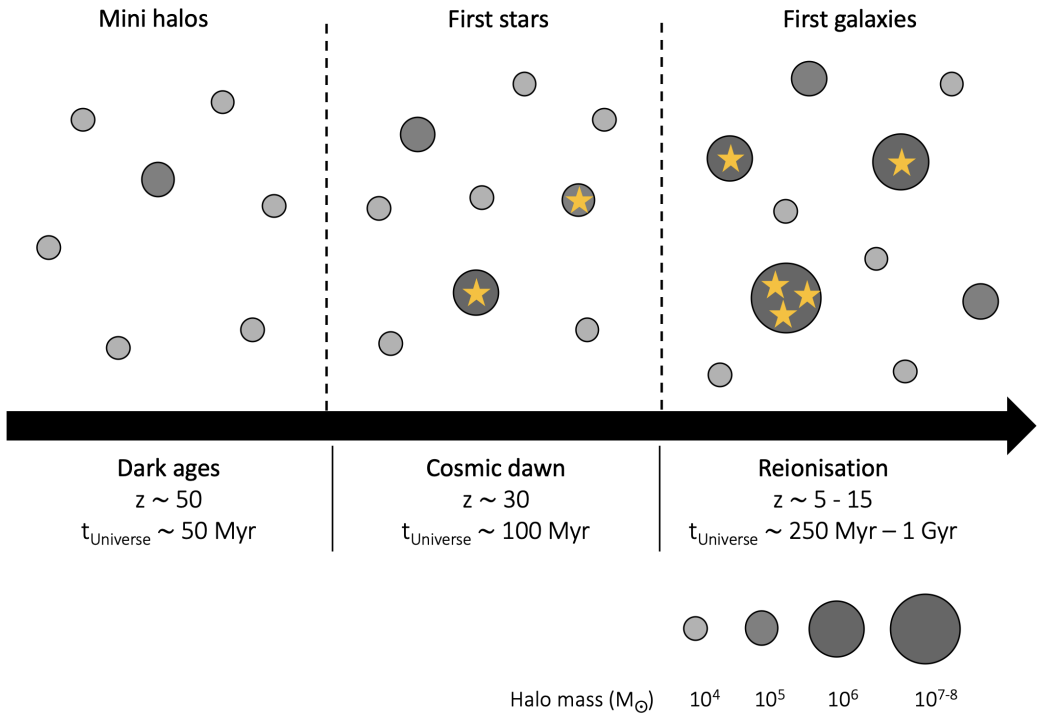

Figure 1.1: The formation of dark matter halos.

being sources, studying these quasars is interesting for reionisation as their spectrum can give us information about the ionisation level of the IGM between them and the observer. This will be investigated in Sec.2.2. Finally, long-duration high-redshift gamma-ray bursts (GRB), with a gamma-ray emission lasting over two seconds, leave afterglows which can be as bright as same-redshift quasars in infrared or radio wavelengths for about a day. These are not expected to contribute to reionisation, but because they are likely caused by the death of massive stars, they are a good tracer of active star formation at high redshift (Zackrisson 2020). Additionally, their spectrum can give information about the nature of the IGM at the time of the burst. The most distant GRB known today was observed at $z = 8.2$ (Tanvir et al. 2009), but the statistics are still very low. It is also worth mentioning fast radio bursts (FRB), whose dispersion measure can tell us about the density of free electrons at the time of emission (Cordes & Chatterjee 2019). In particular, they are expected, once a statistical sample of events have been observed (thousands of FRBs occur every day over the entire sky), to give constraints on the second reionisation of helium in the IGM (Linder 2020).

The existence of other sources, at higher redshifts, has been postulated but these objects are too distant and faint to be observed today. This category includes mini-quasars and Population III stars and supernovae. Star populations are counted backwards in time, so that Population III stars actually were the first stars, formed in mini-halos from primordial elements only (hydrogen, helium and traces of lithium). Because of the cooling properties of stars with a zero metallicity ($Z = 0$), these stars are expected to be very massive, hot

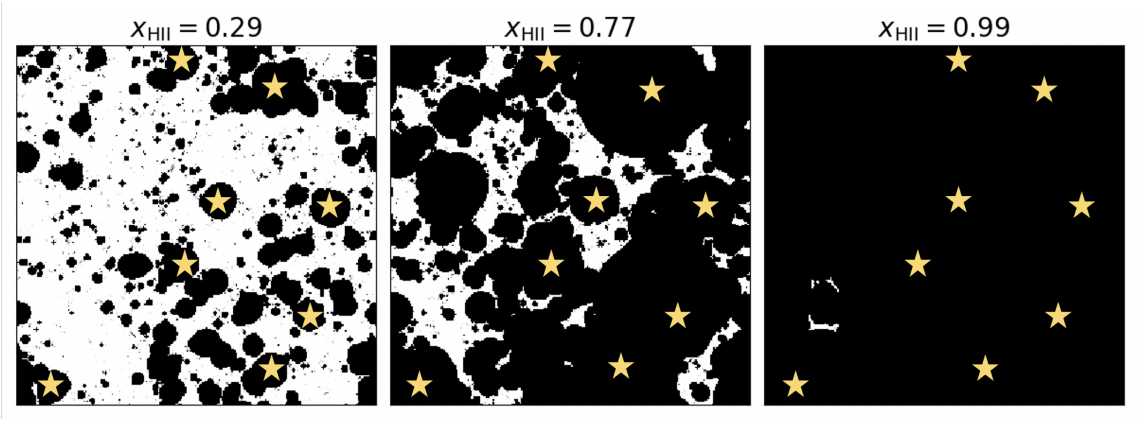

Figure 1.2: Snapshots of the ionisation field in the `rsage const` simulation (see App. B.2) at different phases in the reionisation process. *Left panel:* Pre-overlap: H_{II} regions grow around each isolated ionising source. *Middle panel:* Overlap: Galaxies form and remote ionised bubbles overlap. *Right panel:* Postoverlap: IGM is fully ionised.

and short-lived: stars formed today have a characteristic mass of 0.5 $M_\odot$ whereas Pop III stars likely had a characteristic mass of $10^1 - 10^3$ $M_\odot$ (Zackrisson 2020). Because of these physical properties, they are also expected to have a very bright UV emission, and so to have contributed to, if not the reionisation, the heating of the IGM. Simulations suggest that these stars could form Pop III galaxies, not heavier that $\sim 10^6$ $M_\odot$, if the host halo reaches the H I cooling mass (10^7 $M_\odot$) without the help of any prior star formation or metal pollution (Wise et al. 2012; Xu et al. 2016). Such galaxies would be brighter than individual Pop III stars and so easier to observe, but still very faint: Most are expected to have UV magnitudes in the range of $M_{UV} \sim -5$ to -12 (Xu et al. 2016), below the observational limit of even the next-generation infrared instruments, such as JWST and so would likely be more easily spotted in the 21cm power spectrum (Qin et al. 2020a). Finally, high-redshift mini-quasars are the potential low-mass seeds for $z > 7$ supermassive black holes. They could be the result of the direct collapse of Pop III stars, of primordial black holes, or be Pop III remnants (Zackrisson 2020). Because of their potential hard X-ray emission, they could also have contributed to IGM heating, and they are observable with far-future X-ray telescopes such as NASA's Lynx (Gaskin et al. 2019)[3], up to $z = 10$. One can also imagine contribution from Population III gamma-ray bursts or galaxies.

Reionisation of the IGM will happen once the first luminous objects appear in the sky, emit photons with sufficient energy to ionise an hydrogen atom ($E > 13.6$ eV) and once this radiation escapes from the halo hosting the source. If we consider that galaxies led the reionisation process, in an *inside-out* scenario, we assume that ionised bubbles form around each source and these bubbles grow in volume, eventually overlapping until they cover the entire IGM. This is illustrated in Fig. 1.2 in the case of the `rsage` simulation (Seiler et al. 2019). In this scenario, the densest regions of the IGM are the first ones to

[3]See `https://www.lynxobservatory.com`.

get ionised because they host the sources of reionisation. However, the high density of these regions also means that recombinations are most likely to happen at a higher rate in them. This can lead to newly formed ionised regions to recombine very quickly, and the least dense regions of the IGM to be the first definitively ionised regions of the sky, in a so-called *outside-in* scenario. Indeed, consider a source ionising its surrounding neutral medium[4]. As mentioned above, recombinations compete with ionisations until reaching an equilibrium in what we call a Strömgren sphere (Strömgren 1939). Cosmic expansion and the non-steadiness of sources also play a part in this equilibrium so that the resulting balance equation writes (Shapiro & Giroux 1987):

$$\frac{\mathrm{d}N_\gamma}{\mathrm{d}t} - \alpha_B \langle n_{\mathrm{H_{II}}}^2 \rangle V a^{-3} = a^3 \bar{n}_{\mathrm{H_{II}}} \frac{\mathrm{d}V}{\mathrm{d}t}, \tag{1.5}$$

where N_γ is the total number of ionising photons produced by the source, $\bar{n}_H$ is the comoving mean number density of hydrogen atoms and V is the comoving volume of the bubble considered. $\alpha_{\mathrm{B}}(T) = 1.3 \times 10^{-13}$ cm^{3}s^{-1} (Osterbrock 1989) is the case B recombination coefficient at a fiducial IGM temperature of $T = 20\,000$ K, often considered as the mean temperature around a newly ionised atom (Loeb & Furlanetto 2013; Wise 2019). Solving this equation for the radius of the Strömgren sphere, we find that a larger radius will either correspond to a more luminous source or to a smaller density of the surrounding medium. We see that reionisation is not expected to be a homogeneous process, happening at the same time and progressing at the same rate in the entire sky. This will be investigated in Chapter 3. In particular, it shows that recombinations depend on the square of the hydrogen density and so happen preferably in a strongly heterogeneous IGM. To account for this, a volume-averaged clumping factor $C_{\mathrm{H_{II}}}$ is often introduced via $C_{\mathrm{H_{II}}} = \langle n_{\mathrm{H_{II}}}^2 \rangle / \bar{n}_{\mathrm{H_{II}}}^2$. From Eq. (1.5), we can define the recombination time t_{rec}:

$$\frac{1}{t_{\mathrm{rec}}} = C_{\mathrm{H_{II}}}\, \alpha_{\mathrm{B}}(T) \left(1 + \frac{Y_{\mathrm{p}}}{4X_{\mathrm{p}}}\right) \langle n_{\mathrm{H}} \rangle\, (1+z)^3, \tag{1.6}$$

where X_{p} and Y_{p} are the primordial mass fraction of hydrogen and helium respectively. Generalising Eq. (1.5) to the entire IGM, we get the evolution of the ionised fraction of the IGM x_e with time:

$$\dot{x}_e = \frac{\dot{n}_{\mathrm{ion}}}{\langle n_{\mathrm{H}} \rangle} - \frac{x_e}{t_{\mathrm{rec}}}. \tag{1.7}$$

x_e is defined at the ratio of ionised hydrogen and helium atoms to the total number of baryons in the IGM and will be a central parameter used in this work. $\dot{n}_{\mathrm{ion}}$ is the cosmic reionisation rate, in units of photons per unit time per unit volume, which depends on the star formation rate density ρ_{SFR}, the escape fraction of ionising photons f_{esc} and the number of photons with sufficient energy to ionise hydrogen atoms. These results will be detailed and discussed in details in Chapter 2, but one can already see that it is easy to give a global description of the reionisation process. However, these simple equations also

[4]This formalism, originally derived in the case of a single star, is here generalised to a whole galaxy, more relevant for cosmic reionisation.

show that much smaller scales are involved in the process, from the clumpiness of baryons throughout the IGM to the properties of early galaxies and the photons they produces. Looking at reionisation on these two scales is, therefore, necessary to understand the process, and is at the centre of this work.

Despite making up for a few billion years in the history of the Universe, the Epoch of Reionisation is poorly known. As mentioned before, question marks remain on the nature of the sources of reionisation (Was it star-forming galaxies alone or with the help of early quasars?), and on its topology (Were the densest regions ionised first or last?). Even the global picture is unclear, as it is yet not known when reionisation began and ended. Answering these questions will give us information about the formation of the first structures and light sources in the Universe, as well as on the nature of these first sources – their mass, their radiation. Conversely, it is interesting to know how did reionisation affect galaxy formation, and, in general, galaxy properties.

According to the processes described above, signatures of cosmic reionisation can be found in many different types of observations, and can be the focus of many different types of simulations. Potential sources can be observed directly through spectroscopy or photometry. Measuring the spectrum of a source is the most complete way to learn about it but is very expensive; therefore photometry, that is measuring the flux received from a source per (wide) frequency bin, is often favoured. This can be sufficient for example when looking for Lyman-break galaxies, that is galaxies whose radiation is absorbed by the surrounding neutral IGM, creating a sudden drop in their flux. Spectroscopic techniques will be investigated in Sec. 2.2. JWST is expected to do photometry and imaging at magnitudes[5] $m_{AB} < 31$ and spectroscopy of sources $m_{AB} < 28$ (Gardner et al. 2006), hence picking up $z \sim 7$ quasars, which are expected to have magnitudes $m_{AB} \sim 20$. For now, most results on high-redshift galaxies were obtained with the Hubble Extreme Deep Field, which saw sources of magnitudes up to $m_{AB} = 30$ after 23 days of exposure time, both directly and through gravitational lensing. Results detailed in Sec. 2.2 are based on these observations.

Because of the difficulty of such observations, simulations are used to complement observations and get information about the nature and physics of the sources. Reionisation simulations require a good understanding of the formation of dark matter halos, of the photon production within these halos and of radiative transfer in the IGM. They need to cover huge dynamic ranges in length and in mass, from radiative transfer to cosmological scales. Indeed, to compute star formation, the inner structure of galaxies, on scales of a few parsecs, must be resolved, while the ionisation front propagates on scales of a few Gpc. For computational reasons, it is not currently possible to resolve all these scales with good accuracy, hence different types of simulations, of different levels of precision, exist. Fully

[5]The apparent AB magnitude at frequency ν is a log-measure of the flux f_ν compared to a reference value: $m_{AB}(\nu) \simeq -2.5 \log f_\nu + 8.90$.

numerical simulations consist of simulating a matter field, either through N-body or hydrodynamical methods, and adding radiative transfer to account for the radiation responsible for the heating and reionisation of the IGM. They are limited to scales of $1 - 10$ Mpc but can give information about radiative feedback, star formation or recombination clumps (Xu et al. 2016); they can extend to scales of 100 Mpc but at the price of approximating the physics, that is not resolving the ISM of galaxies or removing hydrodynamics and assigning galaxy properties as input (Ciardi et al. 2001; Finlator et al. 2012; Aubert et al. 2015). Post-processing cosmological hydrodynamical or dark matter only simulations with radiative transfer is a cheaper alternative, as the required resolution can be coarser, and allows to explore much larger box sizes $L < 500$ Mpc (Mellema et al. 2006; Trac & Cen 2007; Ciardi et al. 2012; Hutter et al. 2014; Iliev et al. 2014). Even larger box sizes, of a few Gpc in size, can be reached with semi-numerical simulations. These rely on approximations allowing to directly estimate the ionisation field from the matter distribution, using the so-called excursion-set formalism (Furlanetto et al. 2004a) and, therefore, bypassing entirely the expensive simulation of radiative transfer. The algorithm estimates the number of ionising photons available in each grid cell and then distributes them by comparing the number of ionisations and recombinations in decreasing sizes of spherical shells (Mesinger & Furlanetto 2007; Zahn et al. 2007; Mesinger et al. 2011; Fialkov & Barkana 2014; Hutter 2018b; Park et al. 2019). Alternatively, Thomas et al. (2009) or Ghara et al. (2015) map previously computed one-dimensional ionisation profiles of sources to a grid. Other works use simulations to derive a relation between the matter field and the corresponding ionisation field (Battaglia et al. 2013), but such methods still need accuracy. We refer the reader to Trac & Gnedin (2011) for a detailed review of reionisation simulations.

In this work, we have chosen to focus on two types of observations which can give us information of reionisation: the power spectrum of the Cosmic Microwave Background (CMB) and 21cm observations. We give the basics required to understand these two observables in the following two sections.

1.2 A quick review of CMB cosmology

As mentioned before, shortly after the Big Bang, the Universe was composed of a hot and dense plasma of hydrogen, helium and a bit of lithium nuclei, mixed with electrons and photons, at temperatures higher than $T \sim 1\,000$ K. Mostly because of Thomson scattering, this plasma is opaque, that is the mean path of a photon is much smaller than the Hubble radius at that time. Later, the Universe expands and cools down, allowing neutral atoms to form and photons to travel on larger scales, forming the Cosmic Microwave background (CMB), an image of the Last Scattering Surface (LSS). If recombinations happened at the

same time and in the same way everywhere on the LSS, the CMB should be uniform over the sky. However, early experiments such as the *Cosmic Background Explorer* (COBE) spacecraft, launched in 1989, noticed that the cosmic microwave radiation is a highly isotropic black-body radiation at $T_{\rm CMB} = 2.725$ K, but not perfectly so. COBE operated between 1989 and 1993. Its results include the first map of temperature anisotropies in the CMB with a resolution of about 10 deg, and were rewarded with the 2006 Nobel Prize. Later came the Wilkinson Microwave Anisotropy Probe (WMAP), and the Planck satellite, reaching ever smaller scales.

The CMB temperature fluctuations ΔT are often represented in terms of a angular temperature power spectrum. Because the LSS is considered a spherical surface, the power spectrum is angular, and we use spherical harmonics $Y_{\ell m}$ such that

$$\frac{\Delta T}{T_{\rm CMB}} = \sum_{\ell=1}^{\infty} \sum_{m=-\ell}^{\ell} a_{\ell m}\, Y_{\ell m}(\theta, \phi), \tag{1.8}$$

where ℓ is the angular multipole, proportional to the inverse of the angular scale θ. According to the cosmological principle, there should be no dependence on m in the equations, and the power spectrum amplitude at multipole ℓ writes

$$C_\ell = \frac{1}{2\ell + 1} \sum_m |a_{\ell m}|^2. \tag{1.9}$$

The contribution at $\ell = 1$ is the dipole anisotropy, which was first measured in the seventies to be $(\Delta T/T_{\rm CMB})_{\ell=1} \sim 10^{-3}$ (Henry 1971; Smoot et al. 1977). We had to wait for the launch of COBE in 1989 to observe for the first time anisotropies at the quadrupole level ($\ell = 2$) and higher, as they are two orders of magnitude smaller than dipole anisotropies. Today, the most recent observations come from the Planck satellite (Planck Collaboration et al. 2018). Planck was a space mission launched in 2009 which operated until 2013. It looked for anisotropies at microwave and infrared frequencies with high sensitivity and small angular resolution, three times better than the one of WMAP, largely improving constraints on cosmological parameters. For all these observations, it is important to note that there is an irreducible source of error biasing results, the cosmic variance. Indeed, there is a $1/\sqrt{N}$ uncertainty on each C_ℓ, where N is the number of independent wave modes probed at this scale. Because we can only observe one Universe, this number decreases, and so the associated error increases, as scales increase. The relative uncertainty is given by $\Delta C_\ell / C_\ell = 1/\sqrt{2\ell + 1}$ and dominates all others for $\ell < 1500$ for Planck.

1.2.1 Temperature anisotropies

Primary temperature anisotropies, which are due to effects that occur at the surface of last scattering and before, have three origins. The first stems from the inhomogeneities in the distribution of matter in the Universe and is called the Sachs-Wolfe effect: a photon coming from a denser than average region of the sky will be redshifted (Sachs & Wolfe

1967). Anisotropies due to this process are dominant on large angular scales. Secondly, because of gravity, baryons tend to collapse into overdense regions. Yet, photons, which the baryons are strongly coupled to, resist the collapse and hence push baryons outwards. The balance of these two forces creates oscillatory modes of compression and rarefaction of matter called acoustic oscillations. These density fluctuations translate into temperature fluctuations (Sakharov 1966), observed as peaks in the CMB temperature power spectrum (Peebles & Yu 1970). Finally, because the surface of last scattering is not infinitely thin, temperature fluctuations on scales smaller than its width, about 3 Mpc ($\ell > 800$), will be dampened, in a process called Silk damping (Silk 1968).

Secondary anisotropies stem from CMB photons losing or gaining energy on their way to us (Aghanim et al. 2008). For example, they can be gravitationally deflected by the large-scale distribution of matter in the Universe. If CMB photons propagate through a large overdense clump of matter on the line of sight, structures in the CMB at this point get magnified and appear bigger on the sky. One can also mention the integrated Sachs-Wolfe effect, describing the fact that photons exit potential wells with a higher energy than they entered it. Indeed, the energy they gain by falling into the void will be larger than the energy they lose exiting it: by this time, the Universe will have expanded and the well will be more shallow because of the presence of dark energy. Secondary anisotropies can also have an electromagnetic origin, and because reionisation releases charged particles, such anisotropies will be our main focus. Indeed, Thomson scattering between the free electrons from reionisation and the local CMB quadrupole will produce linear polarisation, hence increasing the amplitude of the polarisation anisotropies on the scales corresponding to the horizon then ($\ell < 10$). This will be seen as a 'reionisation bump' on the EE power spectrum, the amplitude of which scales as τ^2, where τ is the Thomson optical depth. Scatterings will also dampen temperature fluctuations on small scales as $\mathrm{e}^{-2\tau}$ ($\ell > 200$). Conversely, CMB photons can get a kick of energy scattering off high energy electrons. These electrons can be either hotter than the CMB, or have a proper velocity with respect to the CMB rest-frame. The resulting effects are called, respectively, thermal and kinetic Sunyaev Zel'dovich, and are most significant on small scales ($\ell > 1000$, Zeldovich & Sunyaev 1969; Sunyaev & Zeldovich 1970). These three imprints of reionisation on the CMB anisotropies were used simultaneously to constrain reionisation for the first time in Planck Collaboration et al. (2016d) and will be described in details in Sec. 2.1.

A final element one needs to understand to be able to analyse CMB data is the foregrounds. These are dominated by galactic emissions such as bremsstrahlung, synchrotron, and dust that emit in the microwave band. Point sources are also an important contaminant, so that they, along with a mask of the Milky Way, are removed from CMB maps to avoid any bias.

1.2.2 Polarisation anisotropies

If temperature anisotropies are the most significant, the CMB also exhibits polarisation anistropies, which, again, can have a primary or secondary origin. Polarised CMB radiation has two components: a curl-free component, called E-modes, and a divergence-free component, called B-modes, by analogy with electrostatics. The corresponding auto- and cross-spectra, also with temperature, are considered (TE, EE, BB,...)[6]. E-modes stem from the Thomson scattering of CMB photons off free electrons in an heterogeneous plasma. Polarised radiation was produced once the primordial plasma was sufficiently optically thin, while some free electrons were left, hence only during a very short period of time. Therefore, only a small fraction of the CMB photons observed today are E-polarised. B-modes can be produced by two different processes, either gravitational lensing of E-modes along the line-of-sight, or primordial gravitational waves during cosmic inflation. If the first type of B-modes has been observed since 2013 with SPT, the latter is still to be observed, and highly anticipated as it could confirm cosmic inflation. The difficulty of observing this signal comes from strong foregrounds and weak amplitude: if temperature anisotropies at the quadrupole have an amplitude of about 10^{-5}, E-modes and B-modes anisotropies are respectively about 10^{-6} and $10^{-7/8}$ (Planck Collaboration et al. 2016c).

1.3 A quick review of 21cm cosmology

21cm cosmology is based on the observation of the redshifted 21cm line of neutral hydrogen, corresponding to the spin-flip transition of an electron between the two hyperfine levels of the atom's ground state. The astrophysical signal was first observed by Ewen & Purcell (1951), who noticed a peak in the galactic spectrum at a frequency of 1420.405 MHz or 21.106 cm, a result corroborated by Dutch astronomers Muller & Oort (1951). Today, the emission frequency is measured in laboratories using the maser (Microwave Amplification by the Stimulated Emission of Radiation) technique, as less uncertainty on the non-redshifted transition will allow a better determination of the redshift of an observed astrophysical source. The 21cm transition is a forbidden transition with Einstein coefficient $A = 2.85 \times 10^{-15}$ s^{-1}, corresponding to a mean lifetime of the excited state of about ~ 10 Gy for spontaneous emission. However, because hydrogen atoms represent about 75% of the intergalactic gas, the signal is strong enough on cosmological scales to be observed and used as an astrophysical probe. As a tracer of neutral hydrogen, the 21cm signal is naturally a very interesting observable for the Epoch of Reionisation and, for the last decades, many radio astronomy experiments have been designed to detect this signal, with no confirmed detection to this day. Bowman et al. (2018) observed a flattened absorption profile in the sky-averaged radio spectrum, centred at a frequency of 78 MHz and with an

[6] B-modes do not correlate with E-modes or temperature because of their handedness.

amplitude of 0.5 K which they claim to be the first detection of the 21cm signal from the first stars. However, this result needs confirmation. Because of redshift, a photon emitted with a wavelength of 21cm about 100 million years after the Big Bang will reach us today with a frequency of 30 to 200 MHz. This frequency range is targeted by the new generation of radio interferometers, such as the Murchison Widefield Array (MWA, (Tingay et al. 2013)) and the Precision Array to Probe the Epoch of Reionization (PAPER) in Australia (Parsons et al. 2010), the low frequency array (LOFAR) in the Netherlands (van Haarlem et al. 2013b), the Square Kilometer Array (SKA) in South Africa and Australia (Koopmans et al. 2015) and the Hydrogen Epoch of Reionization Array (HERA) in South Africa (DeBoer et al. 2017).

1.3.1 The physics of the 21cm signal

The 21cm line of the neutral hydrogen atom corresponds to a transition from an excited state 1 where the spins of the electron and the proton are parallel to a lower energy state 0 where the spins are antiparallel. The spin temperature T_S is defined via the ratio of the populations n of the two energy levels considered:

$$\frac{n_1}{n_0} = \frac{g_1}{g_0} \exp\left[-\frac{T_{21}}{T_\mathrm{S}}\right], \tag{1.10}$$

where g_1 and g_0 are the statistical weights of both energy levels – respectively about 3 and 1. The 21cm emission temperature $T_{21} = h\nu_{10}/k_\mathrm{B} = 0.0681$ K (with k_B is the Boltzmann constant, h the Planck constant and ν_{21} the 21cm rest-frame frequency) is very small compared to the CMB temperature and the spin temperature. We will then write $n_1/n_0 \simeq 3\,(1 - T_{21}/T_\mathrm{S})$. This equation combined with the radiative transfer equation will give the intensity I_ν of the 21cm signal emerging from a clump of neutral hydrogen. In radio astronomy, the signal intensity is often expressed in terms of a brightness temperature T_b such that, in the Rayleigh-Jeans approximation for low frequencies $h\nu \ll k_\mathrm{B}T$ (Rybicki & Lightman 1986):

$$T_b(\nu) \simeq \frac{I_\nu c^2}{2k_\mathrm{B}\nu^2}. \tag{1.11}$$

Take the radiative transfer equation for a neutral cloud, considering both absorption and emission:

$$\frac{\mathrm{d}I_\nu}{\mathrm{d}\tau_\nu} = S_\nu - I_\nu, \tag{1.12}$$

where τ_ν is the optical depth and S_ν the source function. We have emission at the brightness temperature and absorption of the background radiation, taken to be the CMB[7], so that, in the Rayleigh-Jeans approximation, combining Eqs. 1.11 and 1.12 gives (Rybicki & Lightman 1986):

$$\frac{\mathrm{d}T_b}{\mathrm{d}\tau_\nu} = -T_b + T_\mathrm{CMB}. \tag{1.13}$$

[7]Because its temperature fluctuates with a relative amplitude of 10^{-5}, the CMB can be considered as a background radiation.

This can be solved easily to find the brightness temperature as measured by a telescope on Earth[8]:

$$T_b(\nu)\,(1+z) = T_{\rm S}\left(1-{\rm e}^{-\tau_\nu}\right) + T_{\rm CMB}{\rm e}^{-\tau_\nu} \simeq (T_{\rm S}-T_{\rm CMB})\,\tau_\nu, \tag{1.14}$$

where the spin temperature is actually the brightness temperature in the cloud itself: $T_{\rm S} = T_{\rm b}(\tau_\nu = 0)$ (Zaroubi 2013). We now need an expression of the optical depth τ_ν. It is defined as

$$\tau_\nu = \int \frac{h\nu}{4\pi}\,\phi(\nu)\;(n_1 B_{10} - n_0 B_{01})\;\,{\rm d}l, \tag{1.15}$$

for $\phi(\nu)$ the line profile (or broadening function) and B_{01} and B_{10} the stimulated Einstein coefficients for the 21cm transition. From this definition, it is possible to derive a simpler expression for the brightness temperature as measured today:

$$\delta T_{\rm b} = 27 x_{\rm H_I}\,(1+\delta_{\rm b})\,\frac{\Omega_{\rm b}h^2}{0.023}\sqrt{\frac{0.15}{\Omega_{\rm m}h^2}}\sqrt{\frac{1+z}{10}}\left(1-\frac{T_{\rm CMB}}{T_{\rm S}}\right)\frac{H(z)}{\partial_r v_r + H(z)}\;{\rm mK}, \tag{1.16}$$

where $x_{\rm H_I}$ is the neutral fraction of hydrogen, $\delta_{\rm b}$ the overdensity of baryons, $\partial_r v_r$ the comoving gradient of the line of sight component of the comoving velocity. This result was first derived by Field (1958), but here it is updated to more recent values of cosmological parameters (Pritchard & Loeb 2012; Zaroubi 2013). We often make the approximation $\partial_r v_r \ll H(z)$, so we can write:

$$\delta T_{\rm b} = 27 x_{\rm H_I}\,(1+\delta_{\rm b})\,\frac{\Omega_{\rm b}h^2}{0.023}\sqrt{\frac{0.15}{\Omega_{\rm m}h^2}}\sqrt{\frac{1+z}{10}}\left(1-\frac{T_{\rm CMB}}{T_{\rm S}}\right)\;{\rm mK}. \tag{1.17}$$

If we consider only the global signal, i.e. if we neglect local baryon fluctuations, we can take $\delta_{\rm b} \sim 0$ and $x_{\rm H_I}$ and $T_{\rm S}$ drive the evolution of the signal. If the background temperature is equal to the spin temperature, there is no signal. If $\delta T_b < 0$, that is if $T_{\rm S} < T_{\rm CMB}$, the signal will be seen in absorption. On the contrary, if $\delta T_b > 0$, or $T_{\rm S} > T_{\rm CMB}$, the signal is seen in emission. Looking at redshifts when X-rays have heated the gas sufficiently for the spin temperature to be much larger than the CMB temperature, the equation further simplifies to

$$\delta T_{\rm b} = 27 x_{\rm HI}\,(1+\delta_{\rm b})\,\frac{\Omega_{\rm b}h^2}{0.023}\sqrt{\frac{0.15}{\Omega_{\rm m}h^2}}\sqrt{\frac{1+z}{10}}\;{\rm mK}, \tag{1.18}$$

which will be used throughout this work, as we are mostly interested in the redshift range $5 < z < 15$. The evolution of the different temperatures involved in the $T_{\rm b}$ derivation will determine the evolution of the signal with time.

Apart from the Epoch of Reionisation, 21cm observations can give us insights about many other aspects of astrophysics and cosmology, like improving our measurements of cosmological parameters, testing models of inflation or learning about the properties of

[8]The $(1+z)$ term is added to the basic solution of the differential equation to account for the effect of redshift.

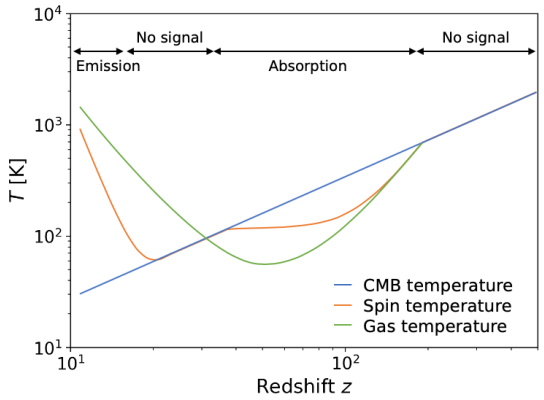

Figure 1.3: Evolution of the different temperature scales relevant to the 21cm brightness temperature with redshift.

the first galaxies (See Pritchard & Loeb 2012, for a complete review of the cosmological implications of measurements of the global 21cm signal). For about 20 years now, radio telescopes, from simple dipoles to hundreds of thousands of dipoles combined into a wide interferometer, have been designed in the hope to detect this signal, extremely faint and, therefore, difficult to isolate from foregrounds. Low frequency radio-telescopes such as LOFAR, MWA, HERA and the SKA target observations of the 21cm brightness temperature fluctuations to learn about the Epoch of Reionisation, through two different approaches: using the sky-averaged signal to construct the 21cm power spectrum, or looking at spatial fluctuations to map the ionisation level of the IGM at different times.

1.3.2 Different types of observations

Global 21cm signal and power spectrum

In order to obtain the sky-averaged 21cm signal, an interferometer such as a simple dipole is used to probe a sufficiently large portion of the sky for spatial fluctuations to average away. The output is the evolution of the differential brightness temperature with frequency (or redshift) $\delta T_b(z)$, which depends on the spin temperature and the CMB temperature. Their evolution is illustrated in Fig. 1.3. Theoretical predictions find than on average, the intensity of this signal varies between ~ -100 mK at minimum and ~ 30 mK at maximum (Pritchard & Loeb 2012; Koopmans et al. 2015), following the global evolution of the Universe: First, from recombination to $z \sim 200$, Compton scattering of CMB photons on the residual free electrons and a collisional coupling due to the high density of the gas keeps atoms and photons in thermal equilibrium, so that no 21cm can be detected. During the Dark Ages, i.e. until about $z \simeq 200$, the gas cools down adiabatically, as a function of $(1+z)^2$, eventually becoming cooler that the CMB. Collisions keep the spin temperature coupled to the gas until $z \sim 100$, and we see a signal in absorption. As the Universe expands, collisions become rare and radiative coupling to the CMB sets $T_S = T_{CMB}$. The signal vanishes. During Cosmic Dawn, the first sources start emitting Lyα and X-ray

photons and heat up the gas. The spin temperature is expected to be coupled to the cold gas so that, at first, $T_S \sim T_{gas} < T_{CMB}$. The gas keeps heating up until exceeding the CMB temperature and we see signal in emission. As heating continues, the CMB temperature becomes negligible compared to the spin temperature, and the last term of equation 1.17 can be dropped. The subsequent 21cm analysis is then greatly simplified. At this time, we expect ionised regions to be significant so that ionisation fluctuations start to dominate the 21cm signal (Furlanetto et al. 2004b). At the end of reionisation ($z \leq 6$), any remaining signal comes from leftover neutral islands.

There is a lot of uncertainties in the exact chronology of these sequences, and they most probably largely overlapped. Therefore observations, such as the 2018 claimed detection by EDGES (Bowman et al. 2018), which has an absorption amplitude two times larger than expected (Pritchard & Loeb 2012), need to be compared to theoretical predictions with caution. This large amplitude could indeed mean either that the background temperature is hotter than expected at that time, or that the IGM is cooler than expected, that is that first stars formed much earlier than previously thought.

21cm intensity mapping

Another interesting object is the spatial fluctuations of the 21cm brightness temperature. They can stem from dark matter or ionisation inhomogeneities and are extremely interesting for the study of the early Universe in general, and the Epoch of Reionisation in particular. One of the methods considered to analyse potential observations is called intensity mapping, i.e. mapping the large-scale fluctuations of the 21cm signal using the integrated radio emission from unresolved gas clouds rather than individual sources. From this we can draw maps of the ionised IGM at different times: a cell with zero signal will correspond to an ionised region, while non-zero signal stems from a combination of density fluctuations and the presence of neutral hydrogen. Interferometers are often easier to calibrate and detect weaker galactic foreground emissions than global signal experiments (Koopmans et al. 2015). However, fluctuations have a much smaller amplitude than the global signal, and observing them requires long integrating times ($\sim$ 1000 h). They additionally require to be deployed on very large areas to reach sufficient signal-to-noise ratio and resolution: in order to get a signal-to-noise ratio lower than 1, collecting areas of the order of 10 times the collecting area of LOFAR are required. This is what motivated the SKA project, whose antennas will cover 419 000 m^2 in Australia and 33 000 m^2 in South Africa, whereas LOFAR covers 52 000 m^2.

1.3.3 Interferometry basics

We now cover the basics of how to observe the 21cm signal with an interferometer. The signal is measured for pairs of antennae separated by a baseline D. The measurement is made in terms of a complex visibility $V(u, v)$, where u and v are the projection of the baseline in wavelength units on the plane perpendicular to the vector $\boldsymbol{s}_0$ pointing to the

phase reference position, the centre of the field to be imaged. In Eq. (1.18), the brightness temperature depends on the position in the sky $\boldsymbol{r}$ where the signal is observed and on the redshift z through $x_{\mathrm{H\,I}}(\boldsymbol{r}, z)$ and $\delta_b(\boldsymbol{r}, z)$. We assume the instrument to have narrow band-pass filters allowing to probe the intensity of the 21cm signal at exactly ν rather than a frequency band centred on ν. If the interferometer probes a sufficiently small region of the sky compared to the beam width of the antennae, we can approximate this region by a flat plane. Then the source intensity distribution is a function of two real spatial variables (l, m) and the van-Cittert theorem tells us that the complex visibility is the 2D inverse Fourier transform of the intensity I_ν, corrected by the normalised average effective collecting area $A(l, m)$ of the two antennae (Thompson et al. 2017):

$$A(l,m)\, I_\nu(l,m) = \sqrt{1-l^2-m^2} \iint V(u,v)\, \mathrm{e}^{2i\pi\,(ul+vm)}\, \mathrm{d}u\, \mathrm{d}v, \tag{1.19}$$

that we can re-write as

$$V(u,v) = \hat{A}^\star(u,v) * \hat{I}_\nu(u,v) \tag{1.20}$$

where $*$ denotes a convolution, $\hat{A}$ and $\hat{I}_\nu$ are respectively the 2D Fourier transforms of A and I_ν and we define $A^\star = A/\sqrt{1-l^2-m^2}$. Because $A(l, m)$ is a measurable instrumental characteristic, if we know our instrument sufficiently well, we can deconvolve the measured complex visibilities by $\hat{A}^\star$ and obtain, after correcting for the different pre-factors, the $\hat{x}(\boldsymbol{k})$ terms.

The 21cm signal from reionisation suffer from many observational obstacles one needs to overcome to make the first observations. For example, the limited number of modes accessible in practice (see Fig. 4.3) will make reconstructing real-space images from (u,v) observations challenging. Low instrument resolution and the increase of thermal noise with frequency also pose the risk of washing out the cosmological signal from observations, and so do the aforementioned foregrounds. One must then develop data analysis tools which are robust to these different effects, and such a robustness will be investigated in Chapter 4.

***

In this chapter, we have introduced basic concepts of cosmology in general, and CMB and 21cm cosmology in particular, as foundations for the methods described in the next chapters. We have also introduced the Epoch of Reionisation, and the questions associated with it, such as the nature of its sources. In this work, we will mostly focus on CMB and 21cm data. However, one must keep in mind that other types of observations are currently available to constrain reionisation, and that simulations are also a useful tool to learn about the physics of scales not reachable today. Ideally, all these sources of information will be

used together to give a global and comprehensive history of reionisation.

Chapter 2

Large-scale reionisation and global history

The Epoch of Reionisation is a global process, part of the history of the Universe as a whole, as it describes the evolution of the total ionisation level of the intergalactic medium (IGM) through times. In this perspective, currently available observations give global constraints, either on the duration of the process, its rough endpoint z_{end} or its midpoint z_{re}, that is when 50% of the IGM is ionised. These can be deduced from various sources, including looking at the interaction of CMB photons with free electrons stemming from reionisation; at the star formation history of the Universe, if galaxies are assumed to be the primary source of IGM ionisation; or at the absorption of Lyman-α galaxies or quasars radiation by surrounding neutral hydrogen. In Gorce et al. (2018), I showed that although these constraints come from very different sources and do not give consistent constraints when considered individually, when used simultaneously, they lead to a coherent storyline. In this asymmetric scenario, ionisation starts with the first sources of light forming around redshift $z \sim 15$, i.e. 300 Myr after the Big Bang, and lasts for about 1 Gyr to end before $z = 5$.

In this chapter, I first describe the different observational methods currently used to improve our knowledge of reionisation history in this work: the CMB will help set the value of the duration and midpoint of reionisation; observations of Lyman-α forests and Gunn-Peterson troughs in quasar spectra will tell use about the population of H I regions towards the end of the process; and galaxy densities about the available photon budget throughout the reionisation epoch. Secondly, I perform an analysis similar to the one of Gorce et al. (2018), but updated with new measurements.

2.1 Integrated constraints from the CMB

From the launch of the Cosmic Background Explorer (COBE) in 1989 to the publication of the latest results of the Planck satellite in 2018 (Planck Collaboration et al. 2018), the study of the Cosmic Microwave Background (CMB) has triggered a tremendous amount of research. Along the line-of-sight, the primordial CMB signal is largely modified by the interaction of CMB photons with structures formed at later times. Notably, their interaction with free electrons in the IGM modifies the shape and amplitude of the measured CMB temperature and polarisation power spectra. In Sec. 1.2, we have briefly described how temperature and polarisation anisotropies can be measured in the CMB. In this section, we will focus on how these anisotropies can tell us about the EoR, firstly on large scales, through measurements of the Thomson optical depth, and secondly on smalle scales, via the kinetic Sunyaev-Zel'dovich effect.

2.1.1 The Thomson optical depth

The analysis of CMB observations include the estimate of the asymptotic value of the Thomson optical depth τ, representing the fraction of photons scattered along the line-of-sight by free electrons. By construction, it is a direct tracer of the global ionisation rate of the IGM $x_e(z)$:

$$\tau(z) = c\ \langle n_{\rm H} \rangle\ \sigma_{\rm T} \int_0^z \frac{x_e(z')}{H(z')}\ (1+z')^2\ {\rm d}z', \tag{2.1}$$

where c the speed of light in vacuum, $\sigma_{\rm T}$ the cross-section of Thomson scattering, $\langle n_{\rm H} \rangle$ the mean hydrogen number density and $H(z)$ the Hubble parameter. In practice, the value of τ will be sensitive to baryon overdensities in the sky, and one should consider $x_e(1+\delta_b)$ with δ_b the local baryon overdensity in Eq. (2.1) rather than x_e alone. However, Planck Collaboration et al. (2016d) find this term to have only a weak influence on integrated results, so that we choose to keep the approximation of Eq. (2.1).

Figure 2.1 shows how the CMB TT temperature and EE polarisation power spectra, as well as the TE cross-spectrum, vary with the value of the Thomson optical depth. The temperature power spectrum is not very sensitive to the exact value of τ, whereas both the amplitude and shape of the EE and TE power spectra on large scales (low ℓ) are strongly impacted. In practice, the EE power spectrum alone is sufficient to discriminate different values of the optical depth from CMB polarisation measurements: its excess power around $\ell = 4-5$ is referred to as the reionisation bump. This bump occurs on large scales because CMB photons stream freely after decoupling on the LSS until they are scattered off newly formed free electrons (Kaplan et al. 2003). To improve constraints on τ, Planck large-scale observations can be combined with high-ℓ data from SPT and ACT. When using Planck EE low-ℓ (hereafter called `lollipop` for low-ℓ Planck polarised likelihood) and TT 2015 power spectra (Planck Collaboration et al. 2016b) and considering an instantaneous

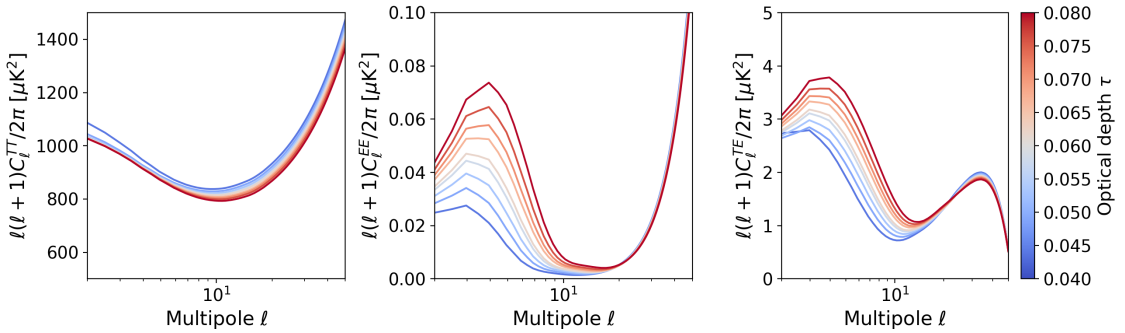

Figure 2.1: Theoretical temperature and polarisation CMB power spectra (respectively, TT, EE and TE) for different values of the Thomson optical depth τ computed from a redshift-symmetric parametrisation of the evolution of the IGM ionised fraction.

reionisation, Planck Collaboration et al. (2016d) find

$$\tau = 0.058^{+0.012}_{-0.012} \quad (\text{PlanckTT} + \texttt{lollipop}), \tag{2.2}$$

which was the value used in Gorce et al. (2018). Adding constraints from SPT (George et al. 2015) and ACT (Das et al. 2014), i.e. very high-ℓ TT spectrum (hereafter called VHL), reduces the value to

$$\tau = 0.054^{+0.012}_{-0.013} \quad (\text{PlanckTT} + \texttt{lollipop} + \text{VHL}). \tag{2.3}$$

This result is close to the latest Planck results which find $\tau = 0.054 \pm 0.007$ (Planck Collaboration et al. 2018). The left panel of Fig. 2.2 shows the evolution of measured τ values, from the first results of WMAP to the final results of Planck.

In CMB data analysis, the Thomson optical depth is one of the many parameters sampled via a Monte-Carlo Markov Chain (MCMC) algorithm, such as `CosmoMC`[1] (Lewis & Bridle 2002), to fit a theoretical expression of the temperature and polarisation power spectra to data. Theoretical predictions are computed with a Boltzmann integrator such as `CAMB`[2] (Lewis et al. 2000; Howlett et al. 2012). Among the many parameters considered, some are related to cosmology – such as Ω_Λ and h, and some to observations, such as instrument systematics or foreground amplitudes (see next Section). Eq. (2.1) shows that the derivation of τ requires a model for the evolution of the IGM ionised fraction with redshift $x_e(z)$. The model commonly used, notably in `CAMB`, is a step-like transition, illustrated on the right panel of Fig. 2.2 as the dash-dotted line and given by:

$$x_e(z) = \frac{f_\text{H}}{2}\left[1 + \tanh\left(\frac{y_\text{re} - y(z)}{\delta y(z)}\right)\right]. \tag{2.4}$$

Here, $y(z) = (1+z)^{\frac{3}{2}}$ and, at the midpoint z_re, $y_\text{re} = y\,(z = z_\text{re})$. The parameter $\delta y = \frac{3}{2}(1+z)^{\frac{1}{2}}\,\delta z$ is derived from δz, which characterises the duration of reionisation and is

[1] CosmoMC is available at `https://cosmologist.info/cosmomc/`.
[2] CAMB is available at `https://camb.info`.

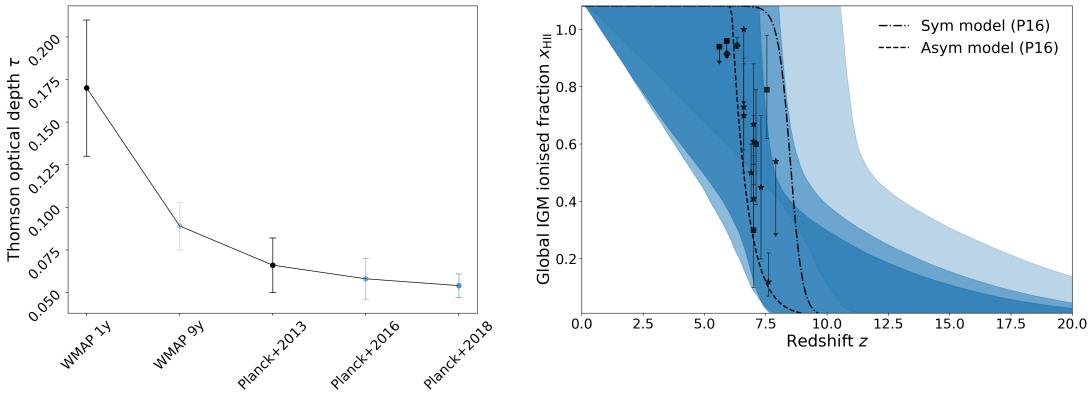

Figure 2.2: *Left panel:* Evolution of the τ measurements given by successive all-sky CMB experiments. *Right panel:* Corresponding ionisation histories allowed by CMB constraints, compared to direct x_e measurements, detailed in Sec. 2.2.2. P16 corresponds to Planck Collaboration et al. (2016d).

often set to $\delta z = 0.5$. f_H is the number of free electrons per hydrogen nucleus. If one assumes that helium is doubly ionised at $z \leq 4$, then $f_\mathrm{H} = 1 + \eta Y_\mathrm{p}/4X_\mathrm{p}$ with $\eta = 2$ for $z \leq 4$ and $\eta = 1$ for $z > 4$. Following results from simulations and observations, Douspis et al. (2015) recently suggested the more physical, redshift-asymmetric parameterisation

$$x_e(z) = \begin{cases} f_\mathrm{H} & \text{for } z < z_\mathrm{end}, \\ f_\mathrm{H} \left(\frac{z_\mathrm{early} - z}{z_\mathrm{early} - z_\mathrm{end}} \right)^\alpha & \text{for } z > z_\mathrm{end}, \end{cases} \tag{2.5}$$

shown as the dashed line on the right panel of Fig. 2.2. Here, z_early corresponds to the redshift around which the first emitting sources form, and at which $x_e(z)$ is matched to the ionised fraction left from recombination $\sim 10^{-4}$. In Planck Collaboration et al. (2016d), it is taken to be $z_\mathrm{early} = 20$, as the authors find that varying the value between 20 and 30 does not change the results significantly.

Although the EE spectrum allows to distinguish between different values of the Thomson optical depth, it cannot discriminate between different reionisation scenarios yielding the same value of τ, for example, the two parameterisations mentioned above. Additionally, as an integrated measurement of $x_e(z)$, it gives very weak constraints on the reionisation history, as illustrated on the right panel of Fig. 2.2. On the figure, we show the 95% confidence intervals resulting from fitting an asymmetric reionisation history (Eq. 2.5) to the value of τ derived from WMAP (Hinshaw et al. 2013), Planck 2016 (Planck Collaboration et al. 2016d) and Planck 2018 (Planck Collaboration et al. 2018) results. If z_re is well constrained, only an upper limit can be obtained without prior on the endpoint of the EoR, hence the slightly distorted shape of $x_e(z)$ on the figure. For $\tau = 0.054 \pm 0.07$ (Planck Collaboration et al. 2018), we find $z_\mathrm{re} = 6.4 \pm 0.8$ and $z_\mathrm{end} < 6.9$ at the 95% confidence level. We see that the direct effect of successively lower τ values, from WMAP to Planck, is to push reionisation to earlier times and speed up the overall process. We will therefore need to supplement τ measurements with other types of observations, such

as the amplitude of the kSZ effect, to improve these constraints.

2.1.2 The kinetic Sunyaev-Zel'dovich effect

The Sunyaev-Zel'dovich effect (SZ effect) is a distortion of the CMB spectral energy distribution due to inverse Compton scattering of CMB photons off high energy electrons. Rather than losing energy after the collision as they do in Thomson scattering, the photons gain energy from the encounter (Sunyaev & Zeldovich 1970; Zeldovich & Sunyaev 1969). When the energy of the scattered electrons comes from a high temperature, the process is called thermal SZ (tSZ) effect. Such electrons can be found in large clouds of hot ionised gas in galaxy clusters. Depending on the frequency of the incoming photon, the energy transfer will differ and the CMB temperature power spectrum will be distorted. When the energy of the scattered electrons comes from a proper velocity, the process is called kinetic SZ (kSZ) effect, illustrated in Fig. 2.3. Such electrons include the ones contained in intra-cluster plasma, which have the same proper motion relative to the CMB than their host cluster. The photons will get blue- or redshifted depending on the direction of this proper motion. Contrary to the tSZ effect, the kSZ effect will add power to the CMB electromagnetic spectrum, mostly on small scales ($\ell > 1000$, a few arcminutes), but not impact its shape. One must then remove the thermal distortion due to tSZ from the spectrum before hoping to measure the amplitude of the kSZ effect.

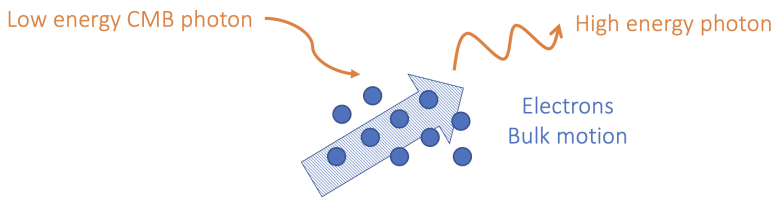

Figure 2.3: Illustration of CMB photons scattering off high-energy electrons, leading to kSZ effect.

The kSZ effect is often split between a homogeneous component, coming from the Doppler shift of photons on free electrons homogeneously distributed throughout the IGM once reionisation is over; and a patchy one, when CMB photons scatter off isolated ionised bubbles with a proper motion around their source along the otherwise neutral line-of-sight (Aghanim et al. 1996). The kSZ effect is thus a natural tracer of reionisation history and morphology. The power spectra of the two components have a distinctive shape, illustrated on Fig. 2.4. When extracting the kSZ signal from CMB observations, most authors consider templates for both power spectra and fit their respective amplitudes at $\ell = 3000$, $A_{\rm kSZ}^{h/p}$, to the measured temperature power spectrum, along with various other foregrounds (Dunkley et al. 2011; Reichardt et al. 2012; Planck Collaboration et al. 2018; Reichardt et al. 2020). Shaw et al. (2012) and Battaglia et al. (2013) calibrate direct relations between cosmological and reionisation parameters and $A_{\rm kSZ}^{h/p}$ on simulations, which can then be used to constrain the EoR (George et al. 2015; Planck Collaboration et al. 2016d; Reichardt et al. 2020).

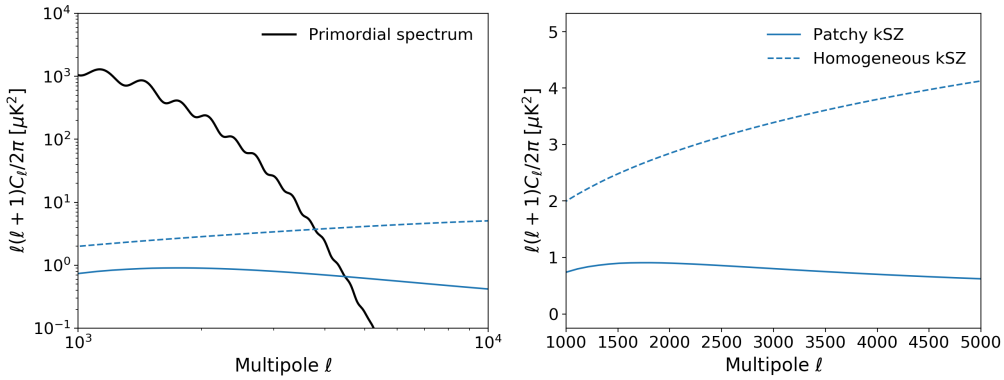

Figure 2.4: Theoretical kSZ angular power spectrum (following results in Gorce et al. 2020) compared to the theoretical CMB temperature power spectrum derived with `CAMB` (Lewis & Bridle 2002).

With the best-fit cosmology obtained with Planck 2015 data (Planck Collaboration et al. 2016b), the relations write:

$$\begin{aligned} A^{\mathrm{h}}_{\mathrm{kSZ}} &= \left(2.02\ \mu\mathrm{K}^2\right) \times \left(\frac{\tau}{0.076}\right)^{0.44}, \\ A^{\mathrm{p}}_{\mathrm{kSZ}} &= \left(2.03\ \mu\mathrm{K}^2\right) \times \left[\frac{1+z_{\mathrm{re}}}{11} - 0.12\right] \left(\frac{z_{0.25} - z_{0.75}}{1.05}\right)^{0.51}, \end{aligned} \tag{2.6}$$

where $z_{0.25}$ and $z_{0.75}$ are the redshifts at which $x_e = 0.25$ and $x_e = 0.75$, respectively. For the patchy amplitude, Battaglia et al. (2013) use large dark matter simulations ($L \gtrsim 2$ Gpc/h), post-processed to include reionisation, to construct light-cones of the kSZ signal and estimate its patchy power spectrum. Very large box sizes are necessary to capture the large-scale velocity flows contributing to the kSZ power spectrum at high-ℓ and results based on insufficiently large simulations will significantly underestimate the power at these scales. Shaw et al. (2012) find that a simulation box of side length 100 Mpc/h would miss 60% of the kSZ power at $\ell = 3000$. For their own work, Shaw et al. (2012) therefore choose a completely different approach: they use hydrodynamical simulations to map the gas density to the dark matter power spectrum and later include this bias in a purely analytical derivation of the kSZ angular power spectrum. Because the non-linear dark matter power spectrum can be computed using the `HALOFIT` procedure (Smith et al. 2003) and because the velocity modes can be estimated fully from linear theory under a few assumptions, they avoid the limitations caused by simulation resolution and size mentioned above. With this method, the authors find the above power-law, giving $A^{\mathrm{h}}_{\mathrm{kSZ}}$ as a function of z_{re} and τ. For $\tau = 0.058$ (Planck Collaboration et al. 2016d) and a step-like reionisation, the scalings give $A^{\mathrm{h}}_{\mathrm{kSZ}} = 1.79\ \mu\mathrm{K}^2$ and $A^{\mathrm{p}}_{\mathrm{kSZ}} = 1.01\ \mu\mathrm{K}^2$.

However, Park et al. (2013) and Gorce et al. (2020) show that these scalings are largely dependent on the simulations they were calibrated on, and therefore cannot be used as a universal formula to constrain reionisation. Notably, an asymmetric reionisation history $x_e(z)$ naturally deviates from this relation. As will be demonstrated in Sec. 3.2, global parameters such as Δz and z_{re} are not sufficient to accurately describe the patchy kSZ

signal, and one needs to take the physics of reionisation into account to get an accurate estimation of not only the shape, but also the amplitude of the power spectrum. A method is proposed to answer these problems in Sec. 3.2.

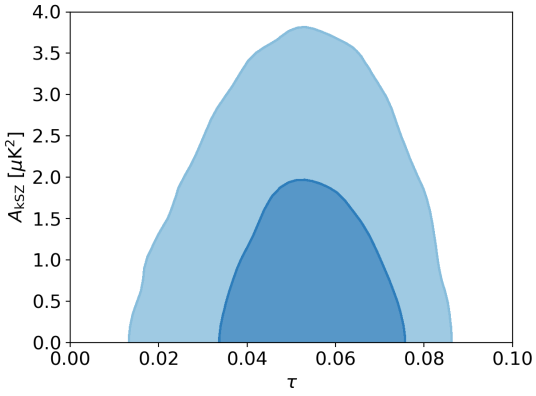

Figure 2.5: 2D probability distribution of parameters τ and $A_{\rm kSZ}$ using Planck 2015 and SPT 2015 data. Contours correspond to the 1- and 2σ confidence intervals.

Fig. 2.4 shows that the primordial power largely dominates kSZ at the scales probed by Planck. On the contrary, foregrounds, including kSZ, dominate on small scales ($\ell > 2000$), where the efforts of ground-based telescopes such as the South Pole Telescope (SPT) and the Atacama Cosmology Telescope (ACT) are focused. Using ACT observations at 148 GHz, Dunkley et al. (2011) find $\mathcal{D}^{\rm SZ}_{3000} \equiv \ell\,(\ell+1)\,C^{\rm SZ}_{\ell=3000}/2\pi = 6.8 \pm 2.9\ \mu{\rm K}^2$ at 68% confidence level (C.L.) for the sum of thermal and kinetic SZ. In a first analysis, Reichardt et al. (2012) derive from the three frequency bands used by SPT $\mathcal{D}^{\rm kSZ}_{3000} < 2.8\ \mu{\rm K}^2$ (95% C.L.). This limit is however significantly loosened when anti-correlations between the thermal SZ effect (tSZ) and the Cosmic Infrared Background (CIB) are considered. By combining SPT results with large-scale CMB polarisation measurements, Zahn et al. (2012) are subsequently able to constrain the amplitude of the patchy kSZ by setting an upper limit $\mathcal{D}^{\rm patchy}_{3000} \leq 2.1\ \mu{\rm K}^2$ (95% C.L.) translated into an upper limit on the duration of reionisation $\Delta z \equiv z\,(x_e = 0.20) - z\,(x_e = 0.99) \leq 4.4$ (95% C.L.), again largely loosened when CIB$\times t$SZ correlations are considered. More recently, adding new data from SPTpol[3] to their previous results (George et al. 2015), Reichardt et al. (2020) claim the first 3σ detection of the kSZ power spectrum with an amplitude $\mathcal{D}^{kSZ}_{3000} = 3.0 \pm 1.0\ \mu{\rm K}^2$, translated into a confidence interval on the patchy amplitude $\mathcal{D}^{{\rm p}kSZ}_{3000} = 1.1^{+1.0}_{-0.7}\ \mu{\rm K}^2$ using the models of homogeneous signal given in Shaw et al. (2012). These results are further pushed using the scaling relations derived by Battaglia et al. (2013) to obtain an upper limit on the duration of reionisation $\Delta z < 4.1$. Finally, adding SPT 2015 and ACT very high-ℓ (VHL) data to Planck EE low-ℓ and TT power spectra and considering an instantaneous reionisation of duration $\delta z = 0.5$, (Planck Collaboration et al. 2016d) find $A_{\rm kSZ} < 2.9\ \mu{\rm K}^2$ (95% CL) and $\tau = 0.054 \pm 0.012$. Their results are reproduced using `CosmoMC` and the publicly available

[3]The second camera deployed on SPT, polarisation sensitive.

data to derive the joint probability distribution of τ and $A_{\rm kSZ}$ presented on the left panel Fig. 2.5 for lollipop + PlanckTT + VHL.

Observations of CMB anisotropies can therefore constrain two parameters directly related to the Epoch of Reionisation, the Thomson optical depth and the amplitude of the kinetic Sunyaev-Zel'dovich effect. However, because these two parameters can at the moment only give general information about the reionisation process, such as its duration or midpoint redshift. Additionally, because the constraints obtained from CMB data are very coarse (see the error bars on Fig. 2.2), it will be useful to combine them with astrophysical data from galaxy observations.

2.2 Astrophysical data for reionisation

Reionisation is not only a cosmological process: astrophysical information such as the number of light sources and their ionising properties tells us about the radiation available to reionise the IGM at a given time. Additionally, the presence of neutral bubbles around bright sources such as quasi-stellar objects (QSO) or gamma-ray bursts (GRB) can leave imprints on their spectrum, allowing us to estimate the amount of neutral hydrogen left around them, and to generalise to the whole IGM at this time. To see how this unfolds, let us look at the equations behind the reionisation process as a whole.

Under the assumption that star-forming galaxies led the reionisation process, their density measured at a given redshift can give a direct estimate of the photon budget for reionisation then. The comoving ionisation rate $\dot{n}_{\rm ion}(z)$ is derived from the number of photons produced by star-forming galaxies per unit time and unit volume, keeping only the ones with sufficient energy to ionise a neutral atom of hydrogen – those below the Lyman-α limit and able to escape their host galaxy to reach the IGM. This writes

$$\dot{n}_{\rm ion}(z) = \int_{-\infty}^{M_{\rm lim}} \phi(M,z)\, f_{\rm esc}(M,z)\, \xi_{\rm ion}(M,z)\, {\rm d}M, \tag{2.7}$$

where M is the magnitude of the source and $\phi(M,z)$ the luminosity function or the number of galaxies of magnitude M at a given redshift. The quantity of Lyman continuum photons produced per second by a galaxy of magnitude M is given by $\xi_{\rm ion}$. Often, the value used is averaged per unit star formation rate density. Here, we use a value derived from rest-frame UV spectral energy distribution of $z \sim 7-8$ galaxies, so that $\xi_{\rm ion} = 10^{53.14}$ s$^{-1}M_\odot^{-1}$yr (Robertson et al. 2015). $f_{\rm esc}$ is the fraction of photons escaping their host galaxy. An effective value of 20%, averaged over stochasticity, halo-mass dependence, redshift and sources is often used as it is compatible with fiducial reionisation scenarios and data (Robertson et al. 2015; Gorce et al. 2018, and see Sec. 2.3). This averaged value is however difficult

to compare with observations of single galaxies or haloes, which give much lower values: Steidel et al. (2001) and Iwata et al. (2009) estimate the escape fraction of some $z \sim 3$ galaxies to be $\gtrsim 1\%$. Similarly, Gnedin et al. (2008) and Ma et al. (2015) find $f_{\rm esc} \leq 0.05$. Looking at the spectral energy distributions of high-redshift galaxies, Dunlop et al. (2013) find $f_{\rm esc} \approx 0.1 - 0.2$. Averaged values can be derived from simulations but are still highly uncertain: According to Finkelstein et al. (2015) and to agree with Lyman-α forests measurements (Bolton & Haehnelt 2007), $f_{\rm esc}$ should not be higher than 0.13. A simulation from Yajima et al. (2014), on which assumptions of Robertson et al. (2015) are based, shows that, amidst all types of photons produced in star-forming galaxies, the escape fraction of ionising photons is the only one which seems to depend neither on the redshift nor on the galaxy properties; it keeps a constant value of 0.2 with time. In the EAGLE simulation, Schaye et al. (2014) and Crain et al. (2015) find $f_{\rm esc} \leq 0.05 - 0.20$ at $z > 6$. Similarly, Wise & Cen (2009) obtain $f_{\rm esc} \sim 0.5$ for galaxies with halo masses lower than $10^8\ M_\odot$. For now, we choose to fix $f_{\rm esc} = 0.20$. In Sec. 4.2, we will discuss how this choice can impact our results.

From the ionising emissivity, we can deduce the redshift-evolution of the IGM ionisation level $x_e(z)$ given in Eq. (1.7), where the evolution of x_e depends on two contributions: a source term, proportional to $\dot{n}_{ion}$, and a sink term related to competing recombinations. The mean hydrogen number density is defined by $\langle n_{\rm H} \rangle \equiv X_{\rm p} \Omega_{\rm b} \rho_{\rm c} / m_{\rm H}$, with $t_{\rm rec}$ the IGM recombination defined in Eq. (1.6). Here, $X_{\rm p}$ and $Y_{\rm p}$ are the primordial mass fractions of Hydrogen and Helium respectively; $\alpha_{\rm B}(T)$ is the case B recombination coefficient at a fiducial IGM temperature of $T = 20\,000$ K, taken as the mean temperature around a newly ionised atom. This value is consistent with measurements at $z \sim 2 - 4$ (Lidz et al. 2010) but has been estimated to $T \lesssim 10^4$ K at $z \sim 5 - 6$ (Becker et al. 2011; Bolton et al. 2012). It fluctuates by a factor between 1 and 2, depending on the spectrum of the sources and on the time passed since reionisation (Hui & Haiman 2003). Yet, $\alpha_{\rm B}(T) \approx 2.6 \times 10^{-13}\ T_4^{-0.76}\ {\rm cm^3\ s^{-1}}$ with $T_4 = T/10^4$ K is a weak function of T so that variations of a factor of a few in T will not have a significant impact on $t_{\rm rec}$ (Osterbrock 1989). Rather than case A, we consider case B recombinations in order to exclude recombinations to the ground state: we assume that ionisations and recombinations are distributed uniformly throughout the IGM, so that each regenerated photon soon encounters another atom to ionise (Loeb & Furlanetto 2013). The clumping factor $C_{\rm H\,II}$ describes how ions are distributed throughout the IGM. $C_{\rm H\,II}$ and $t_{\rm rec}$ are inversely proportional as the more the matter is aggregated in clumps, the easier it is for ionised atoms to recombine in these very same clumps. We will discuss how we can assess its value, and the impact it has on reionisation scenarios, in Sec. 4.2. For now, we choose the fiducial value $C_{\rm H\,II} = 3$ (Robertson et al. 2015; Gorce et al. 2018).

If we can measure the values of some of the parameters defined in the previous equations, we can therefore constrain the reionisation process as a whole, looking at the evolution of $x_e(z)$ with time.

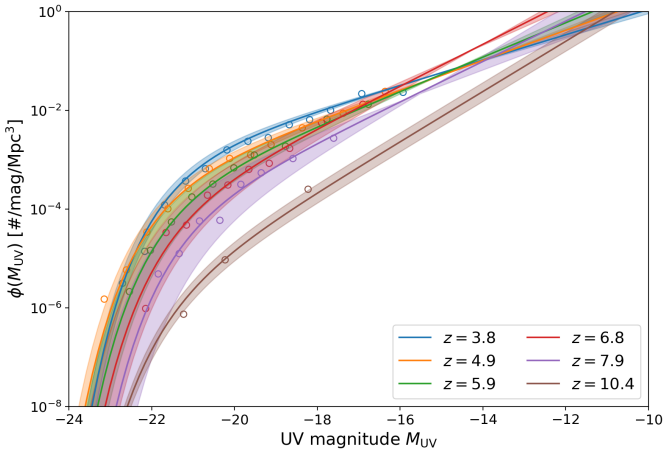

Figure 2.6: UV luminosity functions derived from the results of Bouwens et al. (2015b).

2.2.1 Star formation history

First, we can use star formation history to learn about the photon budget of reionisation $\dot{n}_{\rm ion}$ mentioned earlier, if we assume that star-forming galaxies are the main contributors to hydrogen reionisation.

Galaxy luminosity functions

The luminosity function of star-forming galaxies is inferred from large and deep galaxy surveys such as the various Hubble fields (Bouwens et al. 2015b; Ishigaki et al. 2015, 2018). On Fig. 2.6, we show the UV luminosity functions measured by Bouwens et al. (2015b). These data points are often fitted by the Schechter parameters $\phi^\star$, $L_\star$ (or $M_\star$) and α such that

$$\phi(L)\,\mathrm{d}L = \phi^\star \left(\frac{L}{L_\star}\right)^\alpha \mathrm{e}^{-L/L_\star}\,\frac{\mathrm{d}L}{L_\star}, \tag{2.8}$$

where L is the luminosity. This can be translated in terms of magnitude using $M = M_\odot - 2.5\log(L/L_\odot)$ to give

$$\phi(M)\,\mathrm{d}M = 0.4\phi^\star \ln 10 \left[10^{-0.4(M-M_\star)}\right]^{\alpha+1} \exp\left[-10^{-0.4(M-M_\star)}\right]. \tag{2.9}$$

Because dim objects are more common than very bright galaxies, Schechter functions decrease as a power-law of slope α with decreasing magnitude (and so increasing luminosities) until reaching a cut-off at $L = L_\star$. Some works suggest more elaborate parameterisations such as double power-laws (Bowler et al. 2020), but because we care about the integrated value of this function for reionisation, the precise shape of the function will not impact results by more than 0.1%. Fitting Eq. (2.8) to data points obtained with the Hubble telescope Legacy Fields, Bouwens et al. (2015b) find the functions represented as the solid lines on Fig. 2.6, with associated error bars shown as a shaded area.

From luminosity to mass

Integrating the UV luminosity function on a range of magnitudes at a given redshift, one can derive the UV luminosity density at this time $\rho_{UV}(z)$, expressed in $\mathrm{ergs\,s^{-1}Hz^{-1}Mpc^{-3}}$ i.e. unit energy per unit volume:

$$\rho_{UV} = \int_{-\infty}^{M_{\mathrm{lim}}} \phi(M_{UV})\,\mathrm{d}M_{UV}. \tag{2.10}$$

However, as seen on Fig. 2.6, current observations hardly reach galaxies fainter than $M = -15$. It is therefore necessary to extrapolate $\phi(M)$ to fainter magnitudes and choose a reasonable upper limit M_{lim} to the integral in Eq. (2.10). This problem will be investigated in more details in Sec. 4.2; for now, we choose the conservative value of $M_{\mathrm{lim}} = -13$ as Robertson et al. (2013) showed that it was required to reionise the IGM by $z = 6$. We will discuss this choice in Sec. 4.2.

From ρ_{UV}, one can derive the star formation rate density ρ_{SFR}, i.e. the stellar mass produced per unit time and volume at a given redshift. In general, when integrating over stellar population to find the overall stellar mass, low-mass stars, young and with a broad spectrum, dominate. However, at high redshift, the luminosity is dominated by the UV emission from massive stars (Madau & Dickinson 2014). Because these stars have short lifetimes, the UV emission fades quickly and it gives a good estimate of the stellar mass. Madau et al. (1997) give the conversion:

$$\rho_{UV}(z) = \kappa\ \rho_{\mathrm{SFR}}(z), \tag{2.11}$$

with $\kappa = 8.0\times10^{27}$ $\mathrm{ergs\,s^{-1}\ Hz^{-1}}$ and ρ_{SFR} expressed in solar masses per year. The emission properties of galaxies evolve with redshift, namely because of their metallicity, and it is unclear if κ should be redshift-independent, but the slow evolution of κ with redshift and metallicity observed by Madau & Dickinson (2014) gives grounds to this choice. The value of κ given above is the one used by Bouwens et al. (2015a), and a trade-off between the results of Kennicutt (1998) and of Madau & Dickinson (2014), which differ by about 20%. An implementation of the procedure of using fits on galaxy luminosity functions to derive the star formation rate density is available on my GitHub page (link).

A simplified version of Eq. (2.7), where f_{esc} and ξ_{ion} are averaged over galaxy properties and redshift, relates the ionising emissivity to the UV luminosity density:

$$\dot{n}_{\mathrm{ion}} \simeq f_{\mathrm{esc}}\,\xi_{\mathrm{ion}} \int_{-\infty}^{M_{\mathrm{lim}}} \phi(M_{\mathrm{UV}})\,\mathrm{d}M_{\mathrm{UV}} = f_{\mathrm{esc}}\,\xi_{\mathrm{ion}}\rho_{UV}. \tag{2.12}$$

Therefore measurements of the galaxy luminosity functions can directly constrain the global history of reionisation, by constraining its photon budget. Additionally, at low redshift ($z \leq 6$), $\dot{n}_{\mathrm{ion}}(z)$ can be estimated using the Lyman-α forest (Kuhlen & Faucher-Giguère 2012; Bolton & Haehnelt 2007), as will be detailed in the next paragraph.

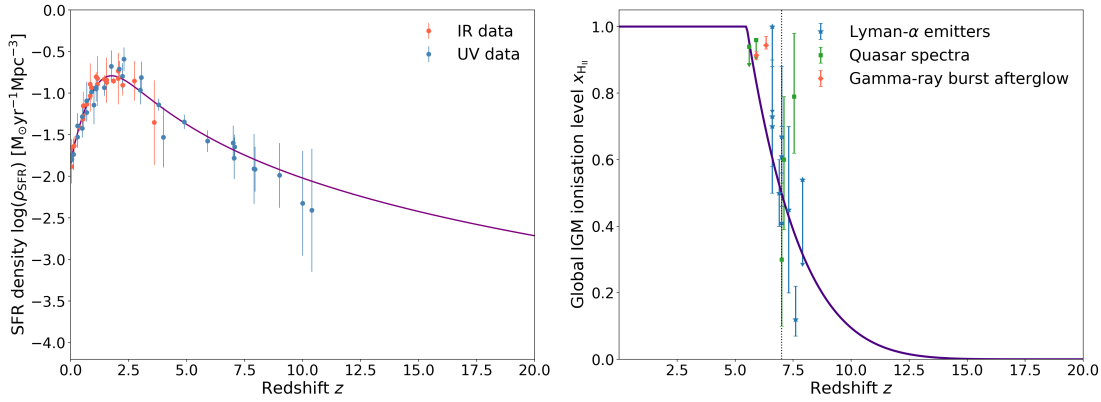

Figure 2.7: Current constraints on the IGM global ionised fraction coming from different types of observations (right panel) and on the star formation history (left panel), compared to the comprehensive scenario obtained by Gorce et al. (2018) by combining all available data (details in text).

The left-hand panel of Fig. 2.7 shows the star formation data points inferred from the UV and infrared galaxy luminosity functions by Robertson et al. (2015). There is a clear trend, visible in the global history proposed by Gorce et al. (2018) when combining these observations with measurements of the IGM ionised fraction and with the Thomson optical depth from Planck (Planck Collaboration et al. 2016d), and shown as the solid line. The error bars on redshifts $z > 6$, which correspond to the Epoch of Reionisation, are wide, mainly because of small sample sizes, and will largely limit the precision of reionisation constraints we can obtain from star formation history alone.

2.2.2 HI absorption troughs

A useful complement to star formation history is the imprint of neutral regions, absorbing ionising radiation, in the spectra of various astrophysical sources.

Quasar spectra

In the 1960s, interest in quasi-stellar objects (QSO) was triggered when astrophysicists such as Minkowski (Minkowski 1960) and Schmidt (Schmidt 1963) related lines in their spectra to redshifted hydrogen Balmer series lines. Indeed, most spectra exhibit absorption lines blueward of the quasar emission line, corresponding to the Lyman-α (Lyα) transitions of neutral hydrogen present between the quasar and us, called the Lyα forest. The idea is the following: consider a photon emitted at the QSO redshift, with wavelength λ smaller than the Lyα wavelength $\lambda_\alpha = 1216$ Å. As the Universe expands, the wavelength is stretched to eventually reach λ_α at a given redshift z. If there is neutral hydrogen at that position, there will be an absorption feature in the intrinsic quasar spectrum at $\lambda_\alpha(1+z)$ as illustrated on Fig. 2.8.

In 1965, Gunn and Peterson predicted that even with as few as a fraction of 10^{-4} of the

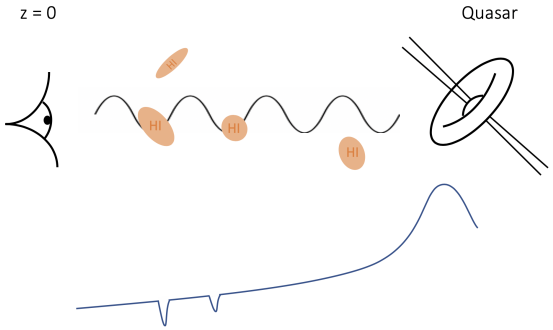

Figure 2.8: Illustration of the origin of absorption features in the spectrum of a quasar.

IGM being neutral around a quasar, its spectrum would show not a forest of absorption lines but a complete trough, now carrying their name (Gunn & Peterson 1965). Indeed, the high optical depth of Lyα photons (about $10^5\, x_{\mathrm{H\,I}}$ around $z = 3$) makes the IGM optically thick to ionising radiation for neutral fractions as low as $x_{\mathrm{H\,I}} = 10^{-4}$ (Wise 2019; Zaroubi 2013). Because of this low saturation limit, this method is limited to probing the very end of the reionisation process. A Gunn-Peterson (GP) trough was observed for the first time by Fan et al. (2001), about 40 years after its prediction, in the spectrum of a $z = 6.28$ quasar (J1030+0534) observed by the Sloan Digital Sky Survey (SDSS). On Fig. 2.9, we present its spectrum, showing a clear GP trough (Becker et al. 2001; White et al. 2003). Since then, the spectra of many high-redshift quasars, increasingly opaque with redshift, have given constraints on the ionisation level of the IGM. SDSS has discovered about 19 quasars around $z \sim 6$ (Fan et al. 2006b). From these spectra, the authors infer that reionisation is over by $z = 6$, a result which was originally widely accepted, but is now questioned. Indeed, the strong radiation surrounding the quasar means that nearby hydrogen atoms are more likely to be ionised than other IGM atoms. This over-ionised zone, called the proximity zone and illustrated on Fig. 2.9, can lead to overestimates of the global ionised level of the IGM if one extrapolates ionisation level around the quasar to ionisation level in the whole IGM carelessly (Wise 2019). Another risk of overestimate comes from the fact that reionisation is expected to be a highly inhomogeneous process. Therefore, when looking at a single quasar, we are likely to pick one whose spectrum goes through only ionised IGM, encountering none of the scarce remote islands contributing to a global ionisation level lower than 100%. The small sample of quasars available today limits constraints on $x_{\mathrm{H\,I}}$ to a 10% precision at $z \sim 6$ (Mesinger 2010) but the improved precision of instruments, as well as the improved efficiency of detection methods will lead to an increase in the pool size. To this day, the furthest quasar observed sits at $z = 7.5$ and has a mass of about $8 \times 10^8 M_\odot$ (Bañados et al. 2018); The most conservative constraint that can be derive from its spectrum is $x_{\mathrm{H\,I}} > 0.33$ at the 68% confidence level.

GP troughs are not the only imprint neutral regions have on quasar spectra. Less dense and more scarce H I regions at lower redshifts can lead to a forest of absorption lines, called the Lyα forest. It is possible to see such a feature in a QSO spectrum for column

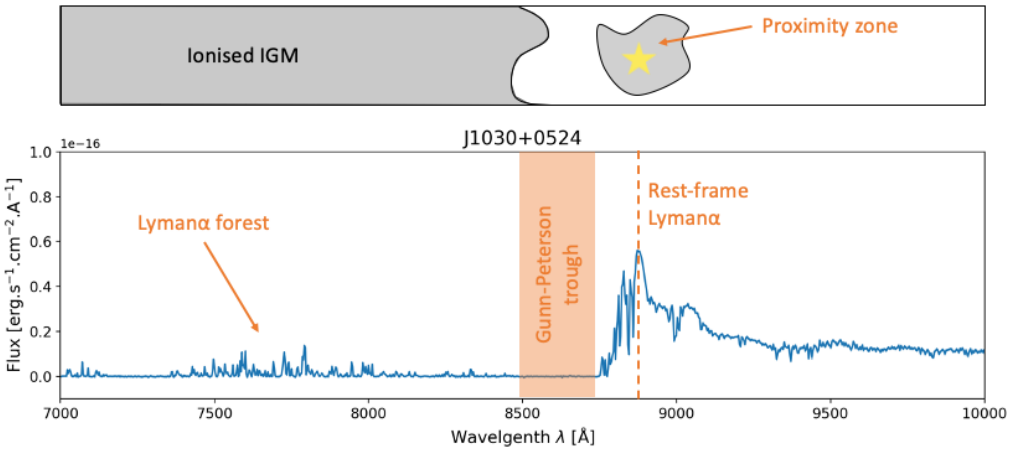

Figure 2.9: Illustration of the impact of H I regions on the spectrum of the quasar J1030+0524 first observed by (Fan et al. 2001). Spectrum from (White et al. 2003), courtesy of D. Mortlock.

densities as low as $N_{\mathrm{H\,I}} = 10^{12-16}$ cm^{-2} (Wise 2019). These low densities make the Lyα clouds likely to get ionised or heated up by the ultraviolet background (UVB) following the hydrogen ionisation rate

$$\Gamma(z) = 4\pi \int_{\nu_\infty}^{\infty} J_\nu(z)\, \sigma_{\mathrm{H\,I}}(\nu)\, \frac{\mathrm{d}\nu}{h\nu}. \tag{2.13}$$

In this equation, $\sigma_{\mathrm{H\,I}}$ is the photoionisation cross-section, J_ν the specific intensity and ν_∞ is the rest-frame frequency of the Lyα limit ($\lambda_\infty = 91.2$ nm). The photoionisation rate $\Gamma(z)$ can be estimated from the width of the Lyα forest lines (Rauch 1998). If we consider the emissivity $\dot{n}_{\mathrm{ion}}$ as the ratio of the intensity of the ionising background to the mean free path of ionising photons, one can use the Lyα forest to estimate the reionisation photon budget (Bolton & Haehnelt 2007). This method avoids two major caveats of $\dot{n}_{\mathrm{ion}}$ estimation through star formation as it includes contributions from all ionising sources, including very faint ones, and does not depend on the values of the escape fraction (Kuhlen & Faucher-Giguère 2012). Using SDSS data, Becker & Bolton (2013) found that if the ionisation rate is first constant on $2 < z < 3$, the production of ionising photons by galaxies is increased by a factor of ~ 3 between redshift 3 and 5. However, the ionising emissivity derived from these measured values of the photoionisation rate are too low to be compatible with other observables, in particular galaxy luminosity functions. As shown on Fig. 2.10, we find[4] that because there are not enough ionising photons at low redshift, reionisation needs to start overall much earlier than fiducial models (around $z = 20$) for the IGM to be fully ionised by $z = 5.5$ and the resulting τ to be compatible with Planck results (Planck Collaboration et al. 2018). This result holds even when the escape fraction is allowed to vary with redshift to compensate for the lack of ionising sources. Then, f_{esc} saturates at 100% for $z \geq 15$. This discrepancy can be linked to the poor modelling of the physics of the Lyman-α forest and of its redshift evolution.

[4]Details on the procedure can be found in the next Section.

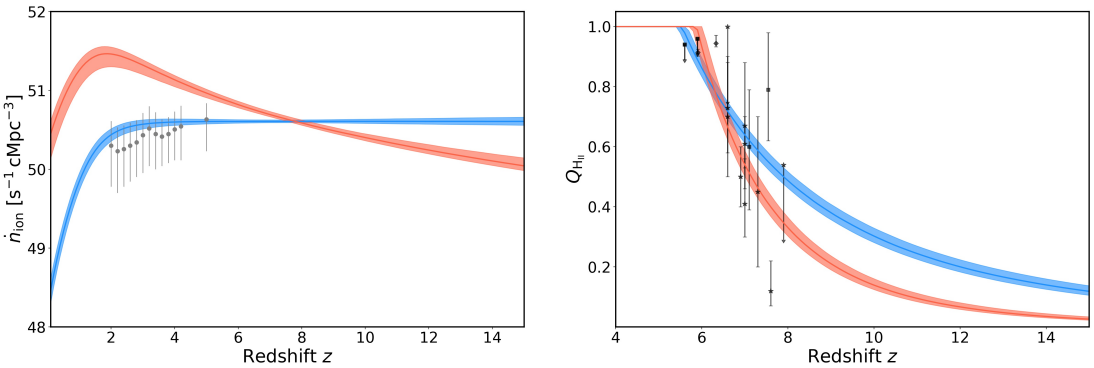

Figure 2.10: Results on global ionisation history when including constraints on ionising emissivity from the Lyman-α forest (blue regions) or ignoring them (red regions). *Left panel:* Ionising emissivity. *Middle panel:* Global ionisation history. *Right panel:* Redshift-evolution of the escape fraction. In each panel, the blue model includes $\dot{n}_{\rm ion}$ constraints from Kuhlen & Faucher-Giguère (2012), whereas the orange one ignores them. Shaded areas correspond to 68% confidence levels.

Gamma-ray bursts

Gamma-ray bursts (GRB) are the most energetic explosions observed in the Universe. They consist of an initial burst of gamma rays followed by a long afterglow at longer wavelengths. Because they are so bright and because time dilatation means that the afterglow of high-z GRB will survive for longer than low-redshift ones, very distant ($z > 10$) GRB can potentially be observed (Ciardi & Loeb 2000). When the Universe is still mostly neutral, the optical afterglow spectrum of the GRB will present a damping wing redward of the Lyα rest-frame emission of the host galaxy, related to H I absorption (Fan et al. 2006a). Proximity effects are not a problem for GRB spectra, however absorption from the neighbouring dense and neutral ISM complicates the interpretation of the damping wing. Fitting absorption models taking into account these two phenomena, one can place limits on the neutral fraction of the IGM at the time of the explosion. For example, looking at the spectrum of GRB080913, Patel et al. (2010) find $x_{\rm H\,I} < 0.73$ at $z = 6.7$ (90% confidence level). Because of the small number of detected GRBs, the statistics are however still poor: the furthest GRB observed to this day is a $z = 8.2$ event (Tanvir et al. 2009; Salvaterra et al. 2009).

Lyman-α emitters

Lyman-α emitters (LAE) are young star forming galaxies in the distant Universe emitting Lyα radiation, most likely because of recombinations taking place in the interstellar medium (Partridge & Peebles 1967). The morphology and global history of reionisation can be probed by LAE through the shape of the Lyα line luminosity function (LF) at high redshift. Indeed, because increasingly numerous neutral hydrogen clouds will absorb the ionising photons from LAE, the LF is expected to decline with increasing redshift. This has been confirmed between redshifts $z = 5.7$ and $z = 6.6$ by the Subaru Deep Field project (Kashikawa et al. 2006). From these measurements, the authors constrained the IGM neu-

tral fraction at $z = 6.6$ to $0 \leq x_{\mathrm{H\,I}} \leq 0.45$. Additionally, the morphology of ionised regions will impact the distribution of LAE by enhancing their clustering (Furlanetto et al. 2004b).

Results from these different types of observations lead to a profusion of constraints on the IGM ionised fraction at different redshifts. The right-hand panel of Fig. 2.7 shows some of these results, chosen for their reliability. The error bars on each measurement are wide and the different measurements do not seem compatible at first. However, on the figure, they are compared to the global history of reionisation obtained by Gorce et al. (2018) when combining this data with star formation history and the Thomson optical depth from Planck (Planck Collaboration et al. 2016d), in a procedure detailed in the following section.

2.3 A comprehensive reionisation history

From CMB measurements to observations of early astrophysical objects such as galaxies and quasars, many different options are available to constrain reionisation. Now that each of those measurements are statistically significant, the right question to ask is if they are coherent and can give a comprehensive picture of the reionisation history. Additionally, combining data can tell us about poorly-known parameters: as we will see in Sec. 4.2, in order to reionise the IGM according to x_e measurements, constraints can be placed on parameters such as f_{esc} and M_{lim}, related to the properties of early galaxies. In order to find a comprehensive model of reionisation, in agreement with all the data available today, we choose an analytical expression for the redshift-evolution of the star formation rate density $\rho_{\mathrm{SFR}}(z)$ and fit it to three sets of data: measurements of the IGM ionised fraction from QSOs, Lyα emitters and GRB; star formation history from UV and IR luminosity functions and the Thomson optical depth measured by Planck. The results presented here are similar to those of Gorce et al. (2018), reproduced in Appendix A.1, but with the value of τ used as constraint updated from $\tau = 0.058 \pm 0.012$ (Planck Collaboration et al. 2016d) to $\tau = 0.054 \pm 0.008$ (Planck Collaboration et al. 2018), and some data points on x_e have been added.

Aiming to reproduce observations on the star formation history from $z \sim 30$ to $z \sim 1$, we choose the 4-parameter model suggested by Robertson et al. (2015), updated from Madau & Dickinson (2014), and given below:

$$\rho_{\mathrm{SFR}}(z) = \frac{a(1+z)^b}{1 + [(1+z)/c]^d}. \tag{2.14}$$

This choice is motivated by the trend seen on Fig. 2.7: $\rho_{\mathrm{SFR}}(z)$ first follows a rising phase,

over $3 \lesssim z \lesssim 15$ ($\rho_{\rm SFR}(z) \propto (1+z)^{b-d}$), up to a peaking point around $z \sim 1.8$ i.e. when the Universe was around 3.6 Gyr old, called cosmic noon. It then declines as $\rho_{\rm SFR}(z) \propto (1+z)^b$ until $z = 0$. This evolution requires the priors $b > 0$ and $b - d < 0$ on our parameters. Other authors have proposed different parameterisations, such as Ishigaki et al. (2015) who focus on the redshift range $z > 4$: their analytical model

$$\rho_{\rm UV}(z) = \frac{2\,\rho_{\rm UV}(z=8)}{10^{a(z-8)} + 10^{b(z-8)}} \tag{2.15}$$

reproduces the rapid decrease of $\rho_{\rm UV}(z)$ from $z \sim 4$ towards higher redshifts but does not consider the cosmic noon. This redshift range naturally corresponds to the core of the reionisation process and should be sufficient to our analyses. However, Ishigaki et al. (2018) show that data slightly favours the 4-parameter model of Eq. (2.14). Additionally, as our aim is to obtain a comprehensive picture of reionisation and of the evolution of light sources in the Universe, we prefer including low redshifts in our analysis.

We adopt this analytical expression of $\rho_{\rm SFR}(z)$ into a Monte Carlo Markov chain (MCMC) approach, with convergence assessed using the Gelman-Rubin test (Gelman & Rubin 1992). We perform a maximum likelihood (ML) determination of the parameter values assuming Gaussian errors on a redshift range of $[0, 30]$. We fit to the star formation data described in Sec. 2.2.1 and then compute the range of credible reionisation histories for every value of the $\rho_{\rm SFR}$ model parameters by solving the differential equation of Eq. (1.7). The resulting history is confronted to IGM ionised fraction data. Finally, we evaluate the Thomson optical depth as a function of z via Eq. (2.1) and compare its asymptotic value (taken at $z = 30$) to the reference value of Planck (Planck Collaboration et al. 2018). These three data sets give three χ^2 values which are added together to obtain the likelihood of the corresponding parameters. We want to know what observable constrains reionisation history the most, so we compare results from

- the **all** run, which uses all three data sets as constraints;
- the **noq** run, which skips x_e data;
- the **notau** run, which skips τ constraints; and
- the **orho** run, which uses only star formation history.

We adopt the fiducial, constant with redshift values $f_{\rm esc} = 0.2$, $\log \xi_{\rm ion} = 53.14$ Lyc photons $\mathrm{s^{-1}M_\odot^{-1}yr}$ and $C_{\rm H\,II} = 3$ (Robertson et al. 2013, 2015), although this choice will be later discussed in Sec. 4.2. The algorithm used to perform this analysis is available on my GitHub page.

Results are summarised in Fig. 2.11, which shows the posterior distributions of our four parameters and of the Thomson optical depth τ, for the **all**, **noq** and **norho** runs. The maximum likelihood parameters for the **all** run are given in Table 2.1. Results obtained when using the star formation history as only constraints (**orho** run) and using the three

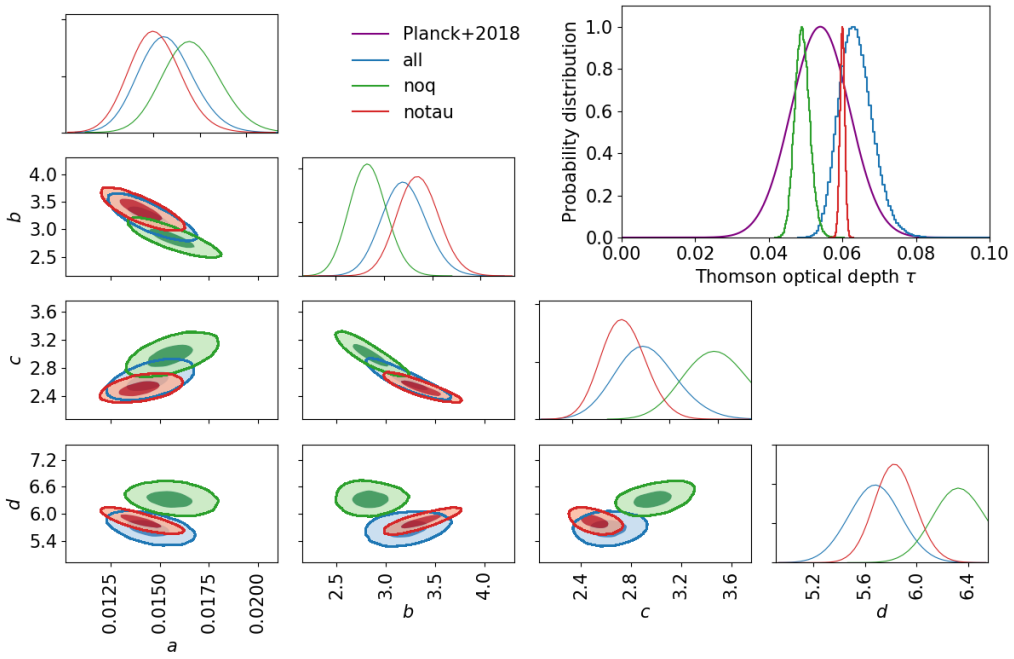

Figure 2.11: Results of the MCMC analysis for the **all** (blue), **noq** (green) and **notau** (red) runs. The contours show the 1, 2, 3σ confidence levels for a, b, c, d. The insert shows the Thomson optical depth probability distribution for the three runs.

Table 2.1: ML model parameters when using all three sets of constraints and resulting reionisation history. Errors correspond to 1σ.

a	b	c	d	τ	$z_{\rm re}$	$z_{\rm end}$	Δz
0.0145	3.20	2.68	5.68	0.064	7.14	5.93	2.06
$\pm$0.001	$\pm$0.22	$\pm$0.15	$\pm$0.19	$\pm$0.005	$\pm$0.32	$\pm$0.23	$\pm$0.17

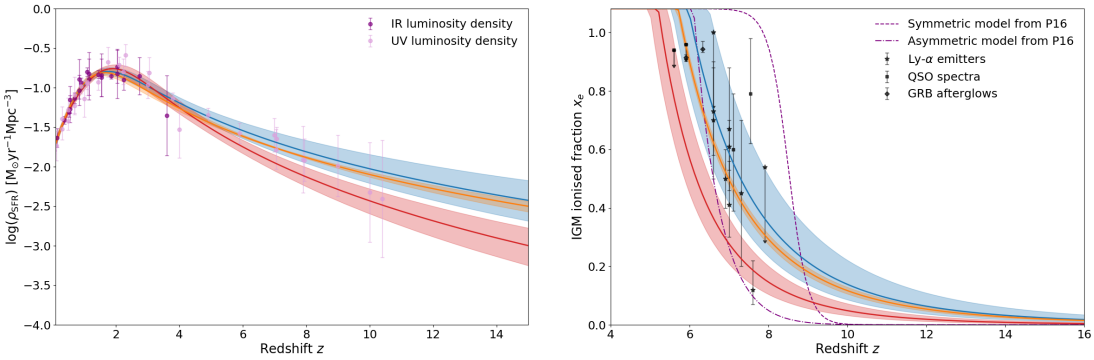

Figure 2.12: Results of fitting Eq. (2.14) to data. ML model and 95% confidence intervals are shown for the **all** (blue), **noq** (red) and **notau** (orange) runs. *Left panel:* Star formation history $\rho_{\rm SFR}(z)$ with redshift. *Right panel:* IGM ionised fraction $x_e(z)$ with redshift. Inferences are compared with results of Planck Collaboration et al. (2016d). The origin of data points is detailed in Secs. 2.2.1 and 2.2.2.

sets (**all** run) are almost identical, therefore we choose not to present results for **orho**. Overall, the **all** and **notau** runs give similar results, whereas **noq** yields largely different parameters, and in particular lower optical depths: $\tau_{\rm noq} = 0.049 \pm 0.002$ vs. $\tau_{\rm all} = 0.064 \pm 0.005$. Fig. 2.12 shows resulting star formation history and reionisation history for the three runs. For what we take to be the fiducial model, i.e. the best-fit model of the **all** run, reionisation finishes at $z = 5.93 \pm 0.23$ (1σ) and lasts on average $\Delta z = z(x_e = 0.25) - z(x_e = 0.75) = 2.06 \pm 0.17$ for a midpoint at $z_{\rm re} = 7.14 \pm 0.32$.

Overall, it seems that the Planck 2018 value of τ is in tension with the two other data sets: adding x_e data to the fit leads to reionisation happening earlier than for **notau**, and so to a larger τ. Additionally, adding τ as a constraint leads to a large increase of the error. This was not observed in Gorce et al. (2018), as the optical depth used, $\tau = 0.058 \pm 0.012$, was higher (Planck Collaboration et al. 2016d). This might be due to the poor way reionisation is modelled and accounted for when deriving the value of the Thomson optical depth from Planck 2018 data: reionisation is considered a redshift-symmetric, quasi-instantaneous process and the impact of kinetic Sunyaev-Zel'dovich effect from reionisation on CMB data is overlooked (see Sec. 2.1). Yet, all our current results remain in the 1-σ confidence interval of $\tau_{\rm Planck}$.

The method used here consists of minimising the sum of the χ^2 value obtained for each data set. Because there are more data points for x_e and $\rho_{\rm SFR}$ than for τ, this sum naturally skews results to be more sensitive to these two data sets. Additionally, as an integrated constraint (see Sec. 2.1.1), the constraining power of τ is low compared to other data types. In this perspective, and because they cannot reproduce the high τ value they use as constraint ($\tau = 0.091 \pm 0.013$, Planck Collaboration et al. (2014)) with the sme simple χ^2 fit, Ishigaki et al. (2015) choose to use reduced χ^2: for each data set, they divide χ^2 by the number of corresponding data points, so that all data sets are given equal weights. They find that this approach leads to a large discrepancy between $\rho_{\rm SFR}(z)$ and $x_e(z)$ data points, with the best-fit model giving a star formation history flat with redshift. We therefore choose to keep raw χ^2 here.

The fact that the **all** and **orho** runs give almost identical $\rho_{\rm SFR}(z)$ and $x_e(z)$ on the range of redshifts considered seems to indicate that star formation history constrains reionisation the most. To confirm this, we perform a **norho** run, skipping constraints from star formation history. Results are shown on Fig. 2.13 for star formation history and global reionisation history. Interestingly, the constraints from star formation are dominated by the data points at $z \sim 6 - 8$, which correspond to the midpoint of reionisation and to the redshift range where we have the most x_e data points. Naturally, the confidence intervals on the fits are very wide at low redshift as no data is available to constrain it. In terms of global reionisation history, the very beginning of the process is similar to what was found for **all** and **norho**. The difference gets clearer for $z < 9$ and $x_e > 0.2$ and increases with time until giving two very different endpoints: respectively, $z_{\rm end,all} = 5.93 \pm 0.23$ and $z_{\rm end,norho} = 5.62 \pm 0.04$. Despite this discrepancy in therms of global history, the results are

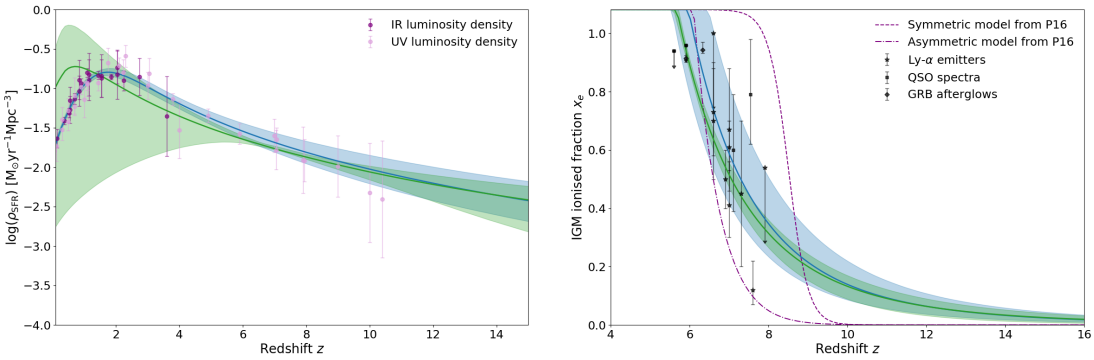

Figure 2.13: Results of fitting Eq. (2.14) to data. ML model and 95% confidence intervals are shown for the **all** (blue) and **norho** (green) runs. *Left panel:* Star formation history $\rho_{\rm SFR}(z)$ with redshift. *Right panel:* IGM ionised fraction $x_e(z)$ with redshift. Inferences are compared with results of Planck Collaboration et al. (2016d). The origin of data points is detailed in Secs. 2.2.1 and 2.2.2.

still compatible with CMB data: we find $\tau_{\rm norho} = 0.062 \pm 0.002$. However, **norho** results must be handled carefully as the MCMC algorithm does not fully converge and the resulting posterior distributions on the model parameters are extremely spread. This is likely due to the chosen parameterisation being based on the evolution of $\rho_{\rm SFR}(z)$, especially the bump in star formation at $z \sim 2-3$. When star formation data is not considered, the 4-parameter analytical expression of $\rho_{\rm SFR}(z)$ is not a good choice. Two approaches could be considered to solve this problem: firstly, to adopt a more simple parameterisation of $\rho_{\rm SFR}(z)$, focused on its evolution at $z > 5$, as proposed in Ishigaki et al. (2015); secondly, to use a parameterisation of $x_e(z)$ rather than $\rho_{\rm SFR}(z)$. However, the objective here being to combine a maximum amount of data to obtain the strongest possible constrain on reionisation, we do not perform such an analysis.

***

2.4 Chapter conclusion & discussion

Many different types of observations are available to constrain reionisation but, individually, they all have biases that prevent us from deriving a consistent history of reionisation: galaxy density observations rely on not-yet-verified extrapolations that can lead to a large overestimate of the photon budget for reionisation; measurements of the IGM ionised level are flawed with large error bars and modelling uncertainties because of a small statistical sample; and the model of reionisation included in CMB data analysis is very simplistic. A way to overcome these individual biases is to combine these three data types to derive a comprehensive history of reionisation. Using the latest results available on cosmic star formation density, ionised fraction of the IGM and Thomson optical depth, and reasonable assumptions about the high-redshift Universe, we find that reionisation is an asymmetric process driven by galaxies. It starts slowly around $z = 15$, before taking off once 20% of the IGM is ionised, and ends shortly after $z = 6$. Among all data, star formation history seems to be the most constraining for the EoR. In Chapter 4, we will discuss the limitations aforementioned, and how they can be overcome, in order to increase the precision of our constraints.

An interesting prospect to improve current constraints are observations of the 21cm signal from the Epoch of Reionisation, introduced in Sec. 1.3, with low frequency radio-telescopes such as LOFAR, MWA, HERA and the SKA. Two different approaches can be used: the first one consists of using the sky-averaged signal to construct the 21cm power spectrum as a function of frequency and so redshift. Observations can be made with a radio telescope as simple as a single dipole, looking at a sufficiently large portion of the sky for spatial fluctuations to average away. It is clear from Eq. (1.18), giving the evolution of the sky-averaged differential brightness temperature with frequency, that the shape of $x_e(z)$ will strongly impact both the shape and amplitude of the 21cm power spectrum. The second approach is to look at smaller areas of the sky to map spatial fluctuations of the brightness temperature and from it, derive an estimate of the global IGM ionised fraction. From such maps, we also get a direct image of the ongoing reionisation process in the IGM and of growing ionisation bubbles around galaxies, that is of local reionisation. In this perspective, accessing small-scale reionisation data, either through the 21cm signal or CMB observations, will give us information about the physical properties of the early IGM and light sources.

Chapter 3

Small-scale reionisation and local history

In the previous chapter, we have seen that reionisation as a global process, looking at the evolution of the IGM ionised fraction with time, can be constrained by a variety of cosmological and astrophysical observations. However, reionisation is an inhomogeneous process: as discussed in Chapter 1, all regions of the sky have not been reionised simultaneously, and the densest regions, where the light sources sit, have likely been ionised first. Depending on the nature of the IGM – notably its density, and on the nature of the sources – for example, their mass and radiation, a given region of the sky will be ionised differently: the growth rate and shape of the H II regions surrounding sources will vary. In this perspective, in this chapter, we introduce efficient statistical tools which are able to characterise the topology of reionisation on scales of a few hundreds of megaparsecs, in order to, later, use this information to constrain the physics of the early Universe. We consider two types of observations: high-multipole CMB data, with the kinetic Sunyaev-Zel'dovich effect, and 21cm tomography. Observations of the spatial fluctuations of the 21cm signal from EoR made by radiotelescopes such as HERA, MWA or the SKA are indeed expected to give maps of the ionisation state of the IGM up to redshift 25. Developing novel and efficient ways of extracting statistical information from radio observations is essential considering the amount of data that future interferometers will produce: HERA will generate about 0.2 terabytes of raw data per day, and SKA about 160 terabytes per second, i.e. the estimated global internet traffic in 2015.

3.1 First statistical moment

Statistical methods are a useful way to extract meaningful information from a large set of data but are often computationally expensive. In this first section, we consider the easiest and quickest possible statistical function, the first moment, in the case of filling fraction distributions. Depending on the ionising properties of light sources, the morphology of reionisation will be different: bright sources will produce a 'Swiss cheese' field, where large and well-defined ionising spheres are scarcely distributed throughout an homogeneous neutral background, whereas faint sources will produce many small ionised regions covering the neutral IGM.

This is illustrated in Fig. 3.1, presenting ionisation fields cut through three versions of the `rsage` simulation. Each version relies on the same underlying dark matter field, but models the relation between the physical properties of a star-forming galaxy and the fraction of ionising photons escaping it in a different way (see App. B.2 or Seiler et al. (2019) for details). In `rsage const`, the escape fraction is constant, equal to $f_{\rm esc} = 20\%$; in `rsage fej`, $f_{\rm esc}$ is roughly inversely proportional to halo mass; and in `rsage SFR`, $f_{\rm esc}$ is proportional to star formation efficiency, and so to halo mass. These simulations were kindly provided by Anne Hutter. The three snapshots considered in Fig. 3.1 are taken when the simulations are 30% ionised and are made of either fully ionised (black) or fully neutral (white) pixels. It is clear that three ionisation fields have a different morphology, and, in particular, `rsage SFR` has the largest ionised bubbles[1]. Indeed, low-mass halos hardly build up ionised regions around themselves and so there are only a few large ionised regions, corresponding to high-mass halos with a high ionising emissivity. In the lower panels of the figure, we show binary ionisation fields from three different runs of the 21CMFAST simulation, corresponding to three different values of the turnover mass $M_{\rm turn}$ (Mesinger & Furlanetto 2007; Mesinger et al. 2011). This parameter corresponds to the minimum halo mass below which the number density of halos hosting star-forming galaxies drops exponentially. The three runs have same dimensions and resolution as `rsage` – that is a box length of $L = 160$ Mpc for 256 cells, and correspond to $M_{\rm turn} = 10^8\ M_\odot$, $10^9\ M_\odot$ and $10^{10}\ M_\odot$, dubbed respectively M8, M9 and M10 (see App. B.3). Despite having the same underlying matter field, these three runs exhibit different sizes of ionised regions. Similarly to what was found for `rsage`, the simulation where only the heaviest galaxies contribute to reionisation, M10, shows the largest ionised regions on average, while M8 exhibits many small ionised regions distributed evenly throughout the neutral background. However, here, H II regions are far from spherical. Note that these six simulations will be used and compared throughout this work.

[1] As shown in Hutter et al. (2020) using bubble size distributions, this is true at any point during reionisation.

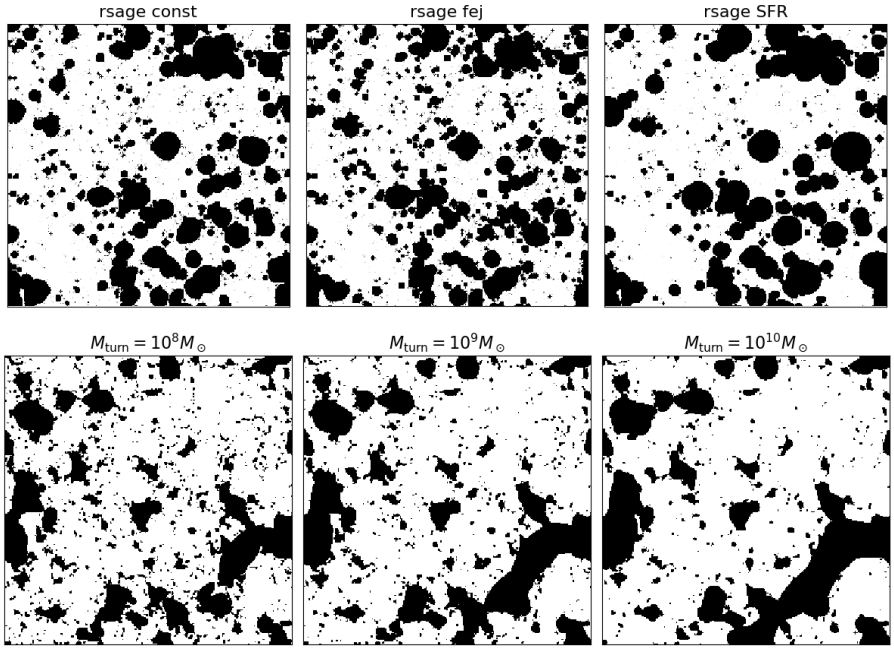

Figure 3.1: *Upper panels:* Binary ionisation fields cut through the three simulations described in Appendix B.2 at $x_e = 0.30$ (Seiler et al. 2019), illustrating how different physics lead to a different reionisation morphology. Courtesy of A. Hutter. *Lower panels:* Binary ionisation fields cut through three runs of 21CMFAST for different values of the minimal halo mass require to ionise (Mesinger & Furlanetto 2007; Mesinger et al. 2011).

3.1.1 Variance of the probability distribution of ionised pixels

The one-point statistic that comes immediately to mind when looking at the binary ionisation fields of Fig. 3.1 is the distribution of ionised pixels throughout the 3D box. Such statistics were used in Watkinson & Pritchard (2014) to compare inside-out vs. outside-in models of reionisation within the 21CMFAST simulation framework. Here, we review the results of this paper while applying the method to the `rsage` simulations[2].

Consider a 3D ionisation field filled with either fully ionised or fully neutral pixels. Using the definition of the mean of the field $\bar{x}$ (here, corresponding to the filling fraction or the global ionisation level) and normalisation properties, we find the probability distribution function of the ionised pixels to be

$$p(x) = (1 - \bar{x})\delta(x) + \bar{x}\delta(x - 1), \tag{3.1}$$

where $\delta(x)$ is the Dirac delta function. From this we can easily derive a theoretical expression for the statistical moments and cumulants of the distribution. The n-th moment μ_n

[2]Note that `rsage` assumes inside-out reionisation.

and the n-th central moment μ'_n are given by:

$$\begin{aligned}\mu_n &= \int x^n p(x)\,\mathrm{d}x = \bar{x} \\ \mu'_n &= \int (x-\bar{x})^n p(x)\,\mathrm{d}x = (-1)^n \bar{x}^n (1-\bar{x}) + (1-\bar{x})^n \bar{x} = \bar{x}(1-\bar{x})\left[(-1)^n \bar{x}^{n-1} + (1-\bar{x})^{n-1}\right]\end{aligned} \tag{3.2}$$

These can be related to the well-known variance $\mu'_2 = \sigma^2$, skewness μ'_3/σ^3 and kurtosis μ'_4/σ^4. The cumulants κ_n are derived from the moment-generating function and can be derived using the following recursion relation:

$$\kappa_n = \mu_n - \sum_{m=1}^{n-1} \binom{n-1}{m-1} \kappa_m \mu_{n-m} = \bar{x}\left[1 - \sum_{m=1}^{n-1} \binom{n-1}{m-1} \kappa_m\right].$$

For the first few, we find

$$\begin{aligned}\kappa_1 &= \mu_1 = \bar{x} \\ \kappa_2 &= \mu'_2 = \sigma^2 = \bar{x}(1-\bar{x}) \\ \kappa_3 &= \bar{x}\left(1 - 3\bar{x} + 2\bar{x}^2\right) \\ \kappa_4 &= \bar{x}\left(1 - 7\bar{x} + 12\bar{x}^2 - 6\bar{x}^3\right).\end{aligned} \tag{3.3}$$

All these statistics tend to zero as $\bar{x} \to 0$ and are symmetric under $\bar{x} \Leftrightarrow 1 - \bar{x}$. The four first theoretical cumulants are represented on Fig. 3.2 for $0 \leq \bar{x} \leq 1$ as the solid black lines. They are compared to the moments numerically computed on the different 3D snapshots available for the three `rsage` simulations, in colour. As the difference between the theoretical model and the simulations is very small in amplitude (about 0.005), we add the results of a null test as a dashed line on the figure to assess the precision of the algorithm used to numerically compute the cumulants. The null test consists of 3D boxes of same dimensions randomly filled by zeros and ones in order to achieve the desired filling fraction. We see this null test is much closer to the theoretical result than our simulations, confirming that the differences observed have a physical and not numerical origin.

As the first cumulant is equal to the mean $\bar{x}$, it is not surprising that all simulations give a perfectly identical $y = x$ curve for κ_1. Results for the higher-order cumulants are more interesting: there is a clear difference between the theoretical model and the `rsage` simulations, averaging around 10% of the theoretical value, and reaching 20% for κ_4. Interestingly, the difference is more significant in the first half of the reionisation process. In Watkinson & Pritchard (2014), the authors compare simulations with either outside-in or inside-out models of reionisation which will result in dramatically different morphologies. Here, despite having three scenarios of inside-out reionisation, we can still differentiate `rsage SFR` from the two other simulations. When performing the same analysis on maps of the differential 21cm brightness temperature computed with Eq. (1.18) for each simulation, we find that each cumulant follows the same trend with $x_{\mathrm{H\,II}}$ but with a much larger amplitude, therefore making this statistics a promising tool to constrain the escape fraction.

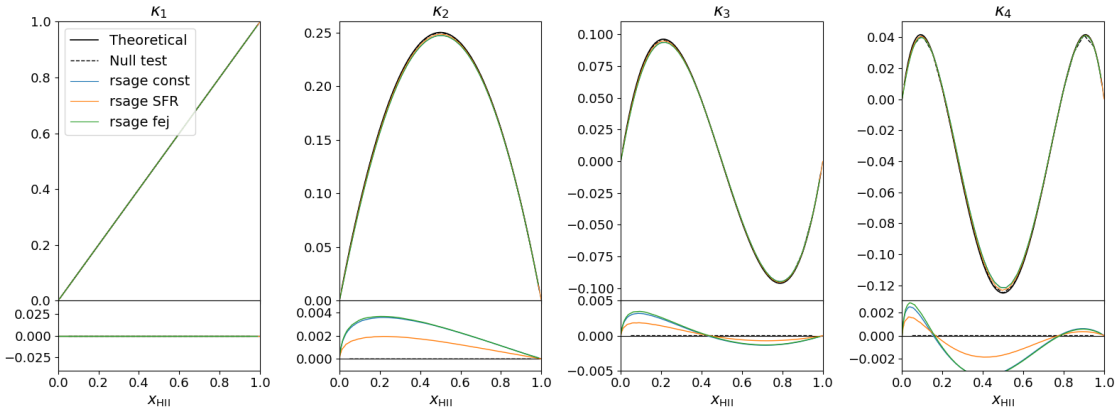

Figure 3.2: Evolution of different statistical cumulants κ_n with ionised fraction for the three `rsage` simulations (upper panels) and absolute difference with a theoretical model (lower panels).

This enhanced amplitude is due to the fact that the Dirac distribution of ionised pixels in Eq. (3.1) is now modulated by the Gaussian distribution of warm (partially neutral) pixels.

These results are all derived from 3D boxes but in practice, we will not observe 3D boxes but either a 2D image of the sky at a given redshift, or a 3D light-cone covering a range of redshifts. We do not expect these results to hold in 2D as the large uncertainty on the filling fraction, if the image is too small (see Sec. 4.1), will wash out such a slight difference in the cumulants. We therefore choose to now look at statistics based on 2D images.

3.1.2 Filling fraction distributions & local variance

Take a 3D `rsage const` box at a given redshift of filling fraction $\bar{x}$. We slice it into $N = 256$ 2D fields along a given direction, considered to be the line-of-sight, and compute the average of each slice. We therefore end up with a distribution of N filling fractions $\{x_{\rm loc,}i\}$. We repeat this process on all the snapshots available for the simulation, at different stages in the reionisation process, and present the resulting distributions in the left panel of Fig. 3.3. The distributions are initially very narrow, before getting wider as reionisation progresses and as the bubble sizes and locations become more correlated. However, they stay centred on the ionisation level of the whole box $\bar{x}$, shown as a solid vertical line. For $\bar{x} > 80\%$, the distributions are again very narrow as most pixels are fully ionised. On the right panel of Fig. 3.3, we summarise these results by plotting the evolution of the standard deviation of the $x_{\rm loc}$ distributions $\sigma_{\rm loc}$ as a function of global ionisation level $\bar{x}$ (blue solid line). We compare it with the evolution of the standard deviation of the 3D pixel distribution $\sigma_{\rm whole}$ described in the previous section, scaled by 1/10 (dashed black line). The reionisation midpoint, where the theoretical $\sigma_{\rm whole}(x) = x(1-x)$ peaks, is shown as the dotted vertical line. Interestingly, $\sigma_{\rm loc}(x)$ is slightly distorted compared to this parabola and actually reaches its maximum a short time after the midpoint, when the box is 60% ionised. This can be related to the percolation level reaching a limit point. As the distri-

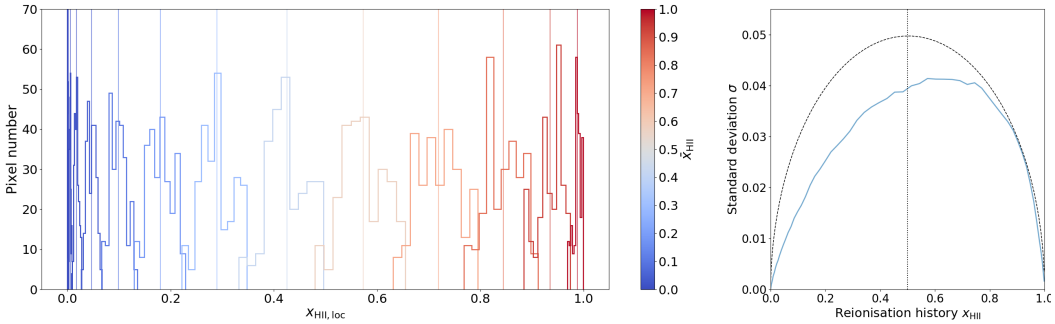

Figure 3.3: *Left panel:* Distribution of the ionisation levels of the N slices that can be carved out of the `rsage const` simulation along one direction, at different stages in the reionisation process. The solid vertical lines are the means of the corresponding whole 3D boxes, considered to be the 'true' values. *Right panel:* Evolution of the standard deviations of each distribution with global reionisation history (blue solid line), compared to the standard deviation of the distribution of ionised pixels throughout the whole box divided by 10 (dashed line).

butions at either end of the reionisation process are close to Dirac delta functions, $\sigma_{\mathrm{loc}} \to 0$ as $\bar{x} \to 0$ and $\bar{x} \to 1$. We also look at the kurtosis and skewness of the distributions to asses their non-Gaussianity, which might be a tracer of clustering in the simulation. The skewness ranges from 0 to 1 during most of the reionisation process, confirming that the distributions are symmetric around the mean value then. However, it is very high (~ 3) at the very beginning and very low (~ -2) at the very end, which corresponds to the somewhat squashed distributions seen on Fig. 3.3. The kurtosis also has values close to zero for the bulk of the process: there are fewer and less extreme outliers than there would be in an equivalent normal distribution i.e. most slices are similar. The x_{loc} distributions are therefore close to Gaussian in the middle stages of reionisation, for $0.2 < \bar{x} < 0.8$, and looking at their standard deviation will be a sufficient source of information.

We now wonder what information we can get from the evolution of σ_{loc} with ionisation level. We therefore compute the x_{loc} distributions of the other two `rsage` simulations to see if such a statistics can differentiate them. The resulting $\sigma_{\mathrm{loc}}(x)$ are shown in the upper panels of Fig. 3.4. As for `rsage const`, $\sigma_{\mathrm{loc}}(x)$ reaches its maximum at around 60% ionisation for the two additional simulations. On average, there is more variance between the `rsage SFR` slices, which corresponds to the fact that the simulation has typically larger ionised bubbles (Seiler et al. 2019). Indeed, for a given filling fraction, if the ionisation field is made of a few scarce large ionised regions, two slices randomly picked in the box are unlikely to be similar. On the contrary, if the field is made of many small ionised regions covering the neutral background, slices are likely to be very similar, and, on average, a better representation of the overall 3D field. Looking at the snapshots of Fig. 3.1, this explains why `rsage fej` is found to have the smallest σ_{loc}. `rsage const` appears to be an intermediary case.

In the lower panels of Fig. 3.4, we compare these results to what is obtained for three 21CMFAST simulations of same resolution and dimensions but different M_{turn} values,

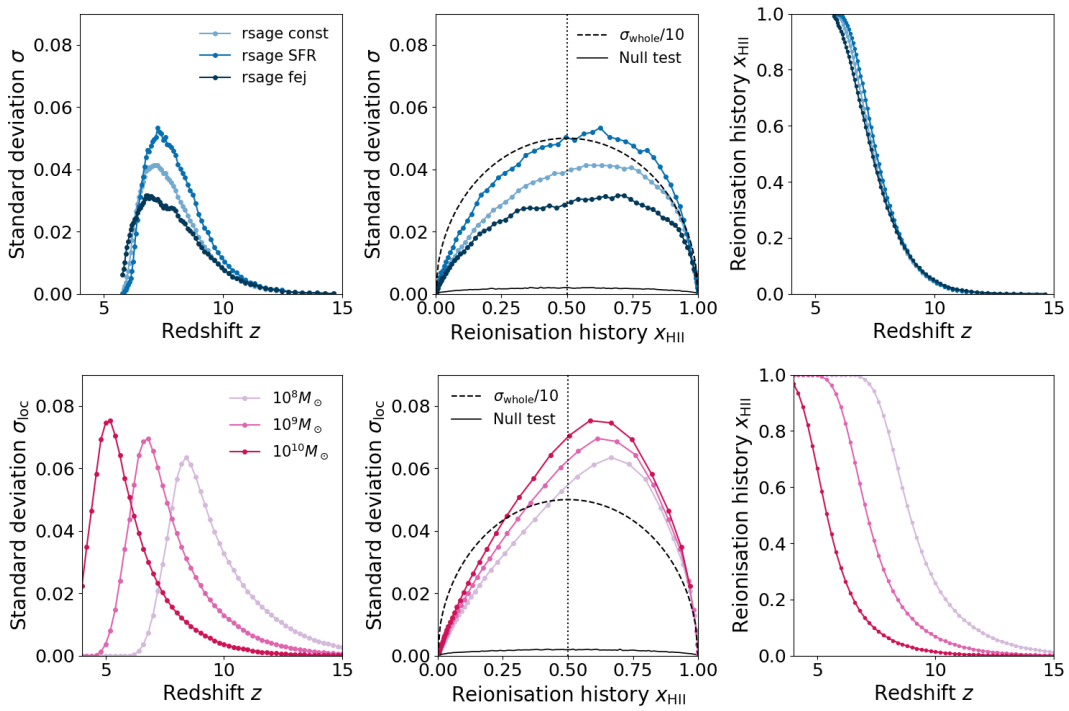

Figure 3.4: Evolution of the standard deviation on global ionisation level measured in the set of N slices that can be carved out of the simulation in one direction $\sigma_{\rm loc}$ with redshift (left panel) and ionisation level (middle panel). Here, $\sigma_{\rm whole}$ is the theoretical variance defined by $\sigma_{\rm whole}(x) = x(1-x)$. *Right panel:* Corresponding reionisation histories. Results for the three `rsage` simulations (upper panels) and the three 21CMFAST runs (lower panels) are compared.

shown in the lower panels of Fig. 3.1 and described in the previous section. Note that because of the very different ways reionisation physics is modelled in the two types of simulations (see App. B), it is irrelevant to compare results from one simulation to another. However, comparing within the same framework allows to test for the robustness of results. M10, which has the largest ionised regions on average, gives the largest variance, similarly to what we found for `rsage SFR`. On the contrary, M8 gives the lowest values of $\sigma_{\rm loc}$ and, again, the three simulations are easily distinguished. Note that the variance of the three 21CMFAST simulations also peaks around $x_{\rm H\,II} = 0.60$. For reference, we compute the local variance of a null test, consisting of a 3D box of same resolution and size as our simulations, but randomly filled with ionised pixels to reach the considered ionisation level. The resulting variance, close to zero and largely insignificant compared to what was obtained for the simulations, is shown as the black solid line in the middle panels of Fig. 3.4.

Here, in contrast to what was found with the standard deviation of pixel distributions $\sigma_{\rm whole}$ in the previous section, there is a clear difference between the `rsage fej` and `rsage const` simulations. Indeed, when looking at the distribution of filling fraction between slices, we introduce correlations between the ionised pixels of a given slice, which were overlooked in $\sigma_{\rm whole}$. Let μ_α be the filling fraction of slice α cut through a box made of

N^3 cells of value x_i such that[3]

$$\mu_\alpha = \frac{1}{N^2} \sum_{i \in \alpha} x_i. \tag{3.4}$$

Then the variances considered write

$$\begin{aligned} {\sigma_{\text{whole}}}^2 &= \langle x_i^2 \rangle - \langle x_i \rangle^2 \\ \sigma_{\text{loc}}^2 &= \langle \mu^2 \rangle - \langle \mu \rangle^2 \end{aligned} \tag{3.5}$$

where

$$\langle \mu \rangle = \frac{1}{N} \sum_\alpha \mu_\alpha = \frac{1}{N^3} \sum_\alpha \sum_{i \in \alpha} x_i = \frac{1}{N^3} \sum_{i \in \text{box}} x_i = \langle x_i \rangle$$

is the filling fraction of the whole box. The second moment writes

$$\begin{aligned} \langle \mu^2 \rangle &= \frac{1}{N} \sum_\alpha \left(\frac{1}{N^2} \sum_{i \in \alpha} x_i \right) \left(\frac{1}{N^2} \sum_{j \in \alpha} x_j \right) \\ &= \frac{1}{N} \sum_\alpha \left(\frac{1}{N^4} \sum_{i \in \alpha} \sum_{j \in \alpha} x_i x_j \right) \\ &= \frac{1}{N^5} \sum_\alpha \left(\sum_{i=j \in \alpha} x_i^2 + \sum_{i \in \alpha} \sum_{i \neq j \in \alpha} x_i x_j \right). \end{aligned}$$

The first term is similar to $\langle x_i^2 \rangle$, but the second term includes correlations between pixels within a given slice. In σ_{whole}, the correlations considered will be between two random pixels throughout the box, and the structure information will be washed out.

In this section, we have introduced a new one-point statistics, σ_{loc}, based on the distribution of the means of slices in a simulation, quick to compute, and which can give us information about the morphology of the ionisation field. The local variance makes use of sample variance, which normally is an issue when observing, to differentiate between different physical properties of ionising sources, such as the escape fraction of ionising photons or the minimal mass of star-forming galaxies. These results are pushed further in a dedicated work (Gorce et al. in prep), where the method is applied to 21cm brightness temperature maps in a bid to use these results observationally. In this work, we use 21CMMC (Greig & Mesinger 2017) to constrain astrophysical parameters related to star formation and ionising emissivity of galaxies, including M_{turn}. We show that, added to current observations such as galaxy luminosity functions and IGM ionised fraction estimated from QSO spectra, σ_{loc} greatly improves constraints on these parameters. We also look at its limitations. Indeed, because σ_{loc} is based on sample variance, small box sizes, that is small fields of view, are required to achieve satisfying results. Additionally, the quality of the constraints will depend on the resolution of the simulation (or the angular resolution of

[3]Because we are considering binary fields, $x_i = 0$ or 1.

the telescope) and on the number of slices available. We now turn to two-point statistics.

3.2 Second statistical moment: the kSZ power spectrum

When looking at extracting a maximum of information from a field, one does not stop at one-point statistics. The next step is naturally the power spectrum, or inverse Fourier transform of the two-point correlation function, a tool cosmologists are particularly fond of. The power spectrum can indeed tell us a lot about a field, although it overlooks non-Gaussian information, essential to the study of reionisation, as we will see in Sec. 3.3.

From the ionisation and density fields of the three `rsage` simulations presented above, we can derive their 21cm brightness temperature fields $\delta T_\mathrm{b}(\boldsymbol{x}, z)$, according to Eq. (1.18). On Fig. 3.5, we show the dimensionless 21cm power spectra computed from these boxes at the 40% and 60% ionisation levels (corresponding to slightly different redshifts for each simulation). It is defined as $\Delta^2_{21}(k, z) = k^3\langle|\delta_{21}(\mathbf{k}, z)|^2\rangle/2\pi^2$, where $\delta_{21}(\boldsymbol{x}, z) = \delta T_\mathrm{b}(\boldsymbol{x}, z)/\delta\bar{T}_\mathrm{b}(z) - 1$. Despite being similar, the three spectra exhibit small differences that can be related to the morphology of the ionisation field in each simulation (Mesinger et al. 2011). However, the difference is maximal on large scales (or small wavenumbers), where error bars will also be maximal because of sample variance[4]. Sample variance in the case of 21cm observations will be discussed further in Sec. 4.1. Another tool, also corresponding to a two-point statistics, has been proven to be a good tracer of not only the global history but also the morphology of reionisation: the kSZ angular power spectrum. We have seen in Sec. 1.2 how the amplitude of this spectrum, related to the scattering of CMB photons off high energy electrons, is currently used to constrain the duration and midpoint of EoR. Here, we push the relation between kSZ power spectrum and reionisation a step further by proposing a new parameterisation, not only of its amplitude, as done in previous works (Shaw et al. 2012; Battaglia et al. 2013), but also of its shape, in terms of reionisation parameters. To do so, we look at the different elements making up the kSZ signal in a simulation, described in App. B.1, and draw a simple description of the most significant elements, that we can later relate to reionisation. This work was the basis of Gorce et al. (2020), reproduced in Appendix A.3.

3.2.1 Derivation of the kSZ angular power spectrum

When CMB photons scatter off clouds of free electrons with a non-zero bulk velocity $\mathbf{v}$ relative to the CMB rest-frame, they generate temperature anisotropies along the line of

[4]Here, we only compute error bars corresponding to Poisson noise. They are too small to be visible on the figure.

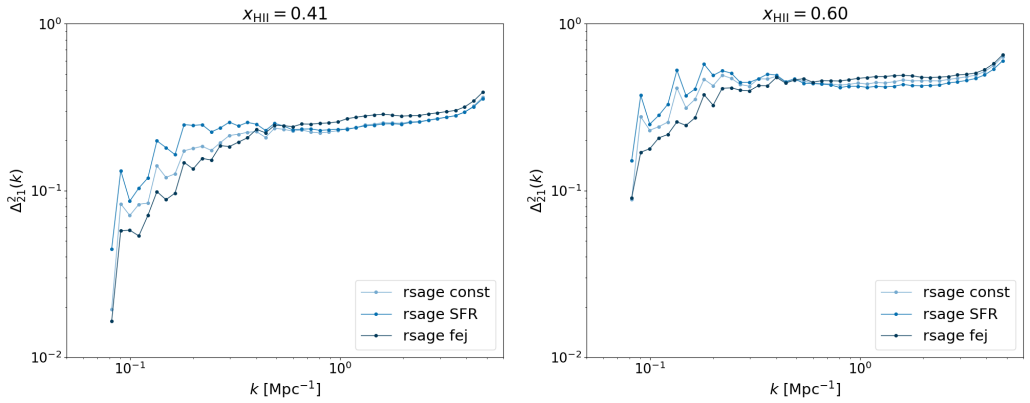

Figure 3.5: Comparison of the dimensionless power spectra of the 21cm brightness temperature fluctuations $\Delta^2_{21}(k, z)$ at $x_{\rm H\,II} = 0.40$ and $x_{\rm H\,II} = 0.60$ for the three `rsage` simulations.

sight $\hat{\mathbf{n}}$ that write

$$\delta T_{k\rm SZ}(\hat{\mathbf{n}}) = \frac{\sigma_T}{c} \int \frac{\mathrm{d}\eta}{\mathrm{d}z} \frac{\mathrm{d}z}{(1+z)} \, \mathrm{e}^{-\tau(z)} \, n_e(\boldsymbol{x}, z) \, \mathbf{v} \cdot \hat{\mathbf{n}} \, , \tag{3.6}$$

with σ_T the Thomson cross-section, c the speed of light, η the comoving distance to redshift z and τ the Thomson optical depth described in Sec. 1.2. We define the density contrast of free electrons $\delta_e(\boldsymbol{x}, z) = n_e(\boldsymbol{x}, z)/\bar{n}_e(z) - 1$. Here, we will focus on the patchy component of the kSZ signal, stemming from inhomogeneous reionisation, so we limit the integral in Eq 3.6 to a redshift range $z > z_{\rm end}$. In practice, the upper bound corresponds to the highest redshift considered in the simulation (here, $z_{\rm max} = 15$), and we find the contribution from pre-reionisation era, when the only free electrons in the IGM are leftover from recombination, to be negligible. We will now derive an expression of the angular power spectrum associated with Eq. (3.6), in order to find an easy way to model its different elements.

The density-weighted peculiar velocity of the free electrons $\mathbf{q} \equiv \mathbf{v}(1 + \delta_e) = \mathbf{v} + \mathbf{v}\delta_e = \mathbf{v} + \mathbf{q}_e$ can be decomposed into a divergence-free $\mathbf{q}_B$ and a curl-free $\mathbf{q}_E$ components. In the Fourier domain, $\tilde{\mathbf{q}} = \tilde{\mathbf{q}}_E + \tilde{\mathbf{q}}_B$. When projected along the line of sight, $\tilde{\mathbf{q}}_E$ will cancel and only the component of $\tilde{\mathbf{q}}$ perpendicular to $\mathbf{k}$, $\tilde{\mathbf{q}}_B$, will contribute to the kSZ signal (Jaffe & Kamionkowski 1998). In the small angle limit, the Limber approximation gives

$$C_\ell = \frac{8\pi^2}{(2\ell+1)^3} \frac{\sigma_T^2}{c^2} \int \frac{\bar{n}_e(z)^2}{(1+z)^2} \, \Delta^2_{B,e}(\ell/\eta, z) \, \mathrm{e}^{-2\tau(z)} \, \eta \, \frac{\mathrm{d}\eta}{\mathrm{d}z} \, \mathrm{d}z, \tag{3.7}$$

for $C_\ell \equiv T^2_{\rm CMB} \, |\delta \tilde{T}_{\rm kSZ}(k)|^2$ the amplitude of the kSZ angular power spectrum at the multipole moment ℓ such that $k \equiv \ell/\eta$. $\Delta_{B,e}$ is defined by $\Delta^2_{B,e}(k, z) \equiv k^3 P_{B,e}(k, z)/(2\pi^2)$ where $P_{B,e}$ is the power spectrum of the curl component of the momentum field such that $(2\pi)^3 P_{B,e} \, \delta(\mathbf{k} - \mathbf{k}') = \langle \tilde{\mathbf{q}}_{B,e}(\mathbf{k}) \, \tilde{\mathbf{q}}^*_{B,e}(\mathbf{k}') \rangle$. We want to expand this last term, so we write

$$\tilde{\mathbf{q}}_{B,e}(\mathbf{k}) = \int \frac{\mathrm{d}^3\mathbf{k}'}{(2\pi)^3} \, (\hat{\mathbf{k}}' - \mu\hat{\mathbf{k}}) \, \tilde{v}(k') \, \tilde{\delta}_e \left(|\mathbf{k} - \mathbf{k}'| \right) , \tag{3.8}$$

where $\mu = \hat{\mathbf{k}} \cdot \hat{\mathbf{k}}'$, so that

$$\begin{aligned}\frac{\langle \tilde{\mathbf{q}}_{B,e}(\mathbf{k})\ \tilde{\mathbf{q}}^*_{B,e}(\mathbf{k}')\rangle}{(2\pi)^3\delta_D(|\mathbf{k}-\mathbf{k}'|)} \equiv& \frac{2\pi^2}{k^3}\Delta^2_{B,e}(k,z) \\ =& \frac{1}{(2\pi)^3}\int \mathrm{d}^3k'\,[(1-\mu^2)\,P_{ee}(|\mathbf{k}-\mathbf{k}'|)\,P_{vv}(k') \\ &- \frac{(1-\mu^2)\,k'}{|\mathbf{k}-\mathbf{k}'|}P_{ev}(|\mathbf{k}-\mathbf{k}'|)\,P_{ev}(k')],\end{aligned} \tag{3.9}$$

where the z-dependencies have been omitted for simplicity. $P_{ee}(k,z) \equiv \langle|\tilde{\delta}_e(\mathbf{k},z)|^2\rangle$ is the power spectrum of the free electrons density fluctuations and P_{ev} is the free electrons density-velocity cross-spectrum. In the linear regime, we can write $\mathbf{v}(\mathbf{k}) = i\mathbf{k}\,(f\dot{a}/k)\,\tilde{\delta}(\mathbf{k})$, where a is the scale factor and f the linear growth rate defined by $f(a) = \mathrm{dln}D/\mathrm{dln}a$ for D the growth function so that

$$P_{vv}(k,z) = \left(\frac{\dot{a}f(z)}{k}\right)^2 P^{\mathrm{lin}}_{\delta\delta}(k,z) \tag{3.10}$$

where $P^{\mathrm{lin}}_{\delta\delta}$ is the linear total matter power spectrum. This expression allows us to compute the velocity power spectrum fully from linear theory and not be limited by the simulation size and resolution. We also assume for the cross-spectrum:

$$P_{ve}(k,z) \simeq b_{\delta e}(k,z)P_{\delta v}(k,z) = \frac{f\dot{a}(z)}{k}\,b_{\delta e}(k,z)P^{\mathrm{lin}}_{\delta\delta}(k,z), \tag{3.11}$$

where the bias $b_{\delta e}$ is defined by the ratio of the free electrons power spectrum over the non-linear matter power spectrum $b_{\delta e}(k,z)^2 = P_{ee}(k,z)/P_{\delta\delta}(k,z)$. Although coarse, this approximation only has a minor impact on our results: it implies variations of $\sim 0.05\ \mu\mathrm{K}^2$ in the patchy kSZ amplitude (see also Alvarez 2016). The final expression of the power spectrum of the curl component of the momentum field then writes

$$\begin{aligned}P_{B,e}(k,z) = \frac{1}{(2\pi)^3}f(z)^2\dot{a}(z)^2\int \mathrm{d}^3k'(1-\mu^2)\times \\ \left[\frac{1}{k'^2}P_{ee}(|\mathbf{k}-\mathbf{k}'|)\,P^{\mathrm{lin}}_{\delta\delta}(k',z)\ - \frac{b_{\delta e}(k',z)}{|\mathbf{k}-\mathbf{k}'|^2}\,b_{\delta e}(|\mathbf{k}-\mathbf{k}'|,z)\,P^{\mathrm{lin}}_{\delta\delta}(|\mathbf{k}-\mathbf{k}'|,z)\,P^{\mathrm{lin}}_{\delta\delta}(k',z)\right],\end{aligned} \tag{3.12}$$

which we can plug into Eq. (3.7) to find the final expression for the kSZ angular power spectrum.

3.2.2 The power spectrum of free electrons density contrast

The central component of this work is $P_{ee}(k,z)$, the power spectrum of the electron contrast density field $\delta_e(\boldsymbol{x},z)$. To get an idea of the behaviour of this object, we look at a reionisation simulation, ran according to the procedure detailed in Aubert et al. (2015), previously used in Deparis et al. (2019) and described in App. B.1. The simulation produces snapshots of the dark matter density, baryon density and ionisation fields at

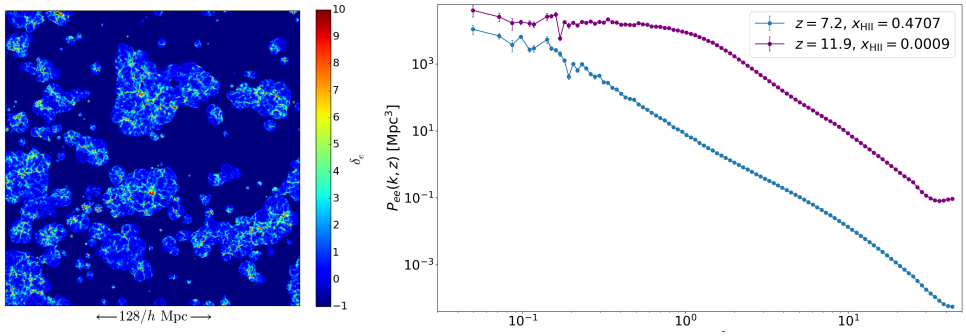

Figure 3.6: Snapshot of the electron density contrast field for the first of the six simulations, at $z = 7.15$ and $x_e = 0.47$ (left panel) and corresponding power spectrum (right panel). Additionally, the spectrum at $z = 11.9$ is shown in purple.

different redshifts. The boxes have side length $L = 128/h$ Mpc for 1024^3 cells. In the left panel of Fig. 3.6, we show $\delta_e(\boldsymbol{x}, z)$ for this simulation at $z = 7.15$, corresponding roughly to the midpoint reionisation ($x_e = 0.47$). The structure follows the distribution of ionised regions, roughly similar to bubbles, on large scales, whereas the small-scale structure seems closer to the underlying matter distribution. On the right panel, we show the power spectrum of the same box as the blue solid line, compared to the spectrum of an earlier snapshot ($z = 11.9$ and $x_e = 0.1\%$) as the purple line. Before the onset of reionisation, despite the few free electrons left over after recombination, the amplitude of P_{ee} is negligible. In the early stages of the process (purple curve), the spectrum consists of a plateau at low frequencies before the power drops off as k^{-3} on smaller scales. To translate this behaviour, we empirically choose the following parameterisation:

$$P_{ee}(k, z) = \frac{\alpha_0 \; x_e(z)^{-1/5}}{1 + [k/\kappa]^3 x_e(z)}. \tag{3.13}$$

The constant amplitude on large scales corresponds to the parameter α_0, weighted by a power of the ionisation level. The amplitude will be maximal at the very start of reionisation, when the variance in the free electron field is also maximal. It then slowly decreases as ionised regions grow and fill up the box. This constant power drops above a cut-off frequency $\kappa {x_e}^{-1/3}$ which decreases with time, following the growth of ionised bubbles. Indeed, there is no power above this frequency, meaning that there is no smaller ionised region than $r_{\rm min}(z) \equiv 2\pi x_e^{1/3}/\kappa$ at this time.

In the later stages of reionisation, the power-law structure of early times is still visible, although mixed with a shape similar to a biased matter power spectrum. Indeed, once reionisation is over and all IGM atoms are ionised, the fluctuations in free electrons density follow those of matter on large scales ($k < 1$ Mpc^{-1}). On smaller scales, gas thermal pressure induces a drop in $P_{ee}(k, z)$ compared to the dark matter. To describe this evolution at low redshifts, we choose the same parameterisation as Shaw et al. (2012), given in Eq. (3.14), to describe the gas bias $b_{\delta e}(k, z)^2 = P_{ee}(k, z)/P_{\delta\delta}(k, z)$ but adapt the parameters

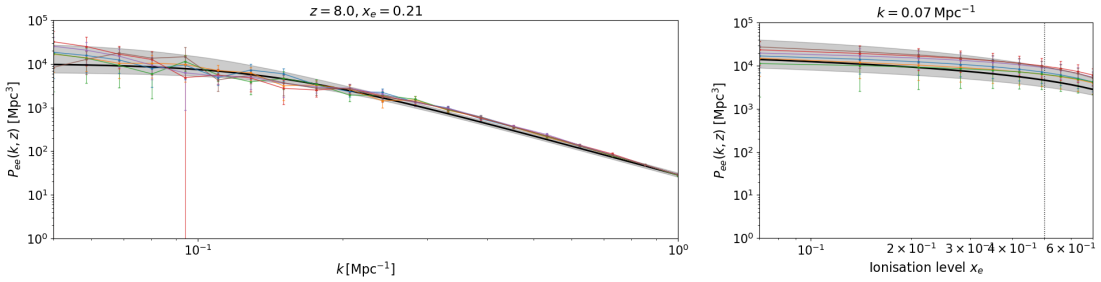

Figure 3.7: Results of fitting Eq. (3.15) to the $P_{ee}(k, z)$ spectra of our six simulations, shown as the various colour lines. Best-fit result is shown as the black solid line, with associated 68% confidence level as the shaded area.

to our simulation, which however do not cover redshifts lower than 5.5.

$$b_{\delta e}(k,z)^2 = \frac{1}{2}\left[\mathrm{e}^{-k/k_f} + \frac{1}{1+(gk/k_f)^{7/2}}\right] \tag{3.14}$$

We find $k_f = 9.4\ \mathrm{Mpc}^{-1}$ and $g = 0.5$, constant with redshift. Our values for k_f and g are quite different from those obtained by Shaw et al. (2012): for their simulations, power starts dropping between 0.05 and 0.5 Mpc^{-1} compared to $k \sim 3\ \mathrm{Mpc}^{-1}$ here. This can be explained by our simulations making use of adaptive mesh refinement, therefore resolving very well the densest regions, so that our spectra are more sensitive to the thermal behaviour of gas. This model, where k_f and g are constant parameters, is a very basic one. It will however be sufficient for this work since we focus on the patchy component of the kSZ effect, at $z \geq 5.5$. Additionally, the scales mostly contributing to the patchy kSZ signal correspond to modes $10^{-3} < k/\mathrm{Mpc}^{-1} < 1$ where P_{ee} follows the matter power spectrum, so that a precise knowledge of $b_{\delta e}(k, z)$ is not required (Gorce et al. 2020).

To account for the smooth transition of P_{ee} from the power-law of Eq. (3.13) to a biased matter power spectrum, we write the final form for the free electrons density fluctuations power spectrum as

$$P_{ee}(k,z) = [f_\mathrm{H} - x_e(z)] \times \frac{\alpha_0\ x_e(z)^{-1/5}}{1+[k/\kappa]^3 x_e(z)} +\ x_e(z) \times b_{\delta e}(k,z)^2 P_{\delta\delta}(k,z), \tag{3.15}$$

for $f_\mathrm{H} = 1 + Y_p/4X_p \simeq 1.08$, with Y_p and X_p the primordial mass fraction of helium and hydrogen respectively[5]. The total matter power spectrum $P_{\delta\delta}$ is computed using the Boltzmann integrator `CAMB` (Lewis et al. 2000; Howlett et al. 2012) for the linear terms and the `HALOFIT` procedure for the non-linear contributions (Smith et al. 2003).

We calibrate this expression on the six simulations available for this work: six simulations with identical numerical and physical parameters are produced in order to make up for the limited physical size of the box and the associated sample variance. They only differ in the random seeds used to generate the initial displacement phases, resulting in six

[5]Note that originally our simulations only include hydrogen reionisation. To account for the potential loss of kSZ power (Shaw et al. 2012), we scale the ionisation level of each snapshot by f_H such that $x_e(z) = f_\mathrm{H}\, x_{\mathrm{H\,II}}(z)$.

different configurations of structures within the simulated volumes. Eq. (3.15) is fitted to the power spectra of the six simulations on a scale range $0.05 < k/\mathrm{Mpc}^{-1} < 1.00$, corresponding to the scales which contribute the most to the signal at $\ell = 3000$ (Gorce et al. 2020), and a redshift range of $6.5 \leq z \leq 10.0$, corresponding to the core of the reionisation process ($0.07 < x_e < 0.70$). The diagonal of the covariance matrix derived from the sample of six simulations is used as error bars for each $P_{ee}(k, z)$ data point. Details of the fitting procedure can be found in Gorce et al. (2020). Fig 3.8 shows the result of the fit at a given redshift (left panel) or a given scale (right panel). We further apply the fit to the power spectra extracted from the three `rsage` simulations and the three 21CMFAST simulations described in Sec. 3.1 in order to assess how robust this very simple parameterisation is to different physics of reionisation. For the 21CMFAST simulations, we run twenty times each simulation – corresponding to a value of M_{turn}, but for different initial conditions. From these 20 realisations we derive relative error bars $\sigma(k, z)$ on $P_{ee}(k, z)$ values, corresponding to the 68% confidence level on the distribution of values for each bin. We generalise these results to `rsage`: on the scales and redshifts range considered in this section, we have $\sigma(k, z)/P_{ee}(k, z) = 10^b\,(k/k_0)^a$, where $k_0 = 1$ Mpc^{-1}. Values $a = -1.12 \pm 0.79$ and $b = -1.74 \pm 0.70$ have been found by fitting the $\sigma(k, z)$ values of the 60 simulations simultaneously. We then apply this expression to the spectra of the `rsage` simulations, as an approximation of sample variance. Finally, a last simulation is generated, with same resolution and box size as the six initial simulations but with twice as much star formation, therefore reionising earlier ($z_{\mathrm{re}} = 7.94$) but on a similar redshift interval ($\Delta z = 1.20$). The best-fit parameters, defined as the maximum likelihood parameters, are given in Table 3.1, for each of these fits.

3.2.3 Patchy kSZ angular power spectra

Once we have a value of α_0 and κ for each simulation, since we know their exact reionisation histories, we can derive their patchy kSZ angular power spectrum according to Eq. (3.7). These are shown in the middle panels of Fig. 3.8, along with the corresponding reionisation histories (left panels). For each simulation, the 68% confidence interval on the fit parameters is propagated to a 68% confidence interval shown as the shaded area around the kSZ signal derived from the best-fit parameters. Inferences are compared to the latest observational results on kSZ amplitude: using SPT data, Reichardt et al. (2020) find $\mathcal{D}_{3000}^{\mathrm{patchy}} = 3.0 \pm 1.0\ \mu\mathrm{K}^2$. All our results are compatible with this detection.

We see that despite very similar reionisation histories, the three EMMA simulations and the three `rsage` simulations give very different patchy kSZ spectra: the small error bars on $x_e(z)$ translate into a 10% error bar on the kSZ amplitude at $\ell = 2000$. Interestingly, the six initial EMMA simulations, corresponding to a *late reionisation* scenario ($z_{\mathrm{re}} \simeq 7.10$), give a very different kSZ spectrum to the *early reionisation* simulation one, despite similar physics: not only the amplitude is impacted by the changed reionisation history, but also the shape. Around $\ell \sim 3000$, the two spectra have similar values (the difference is about

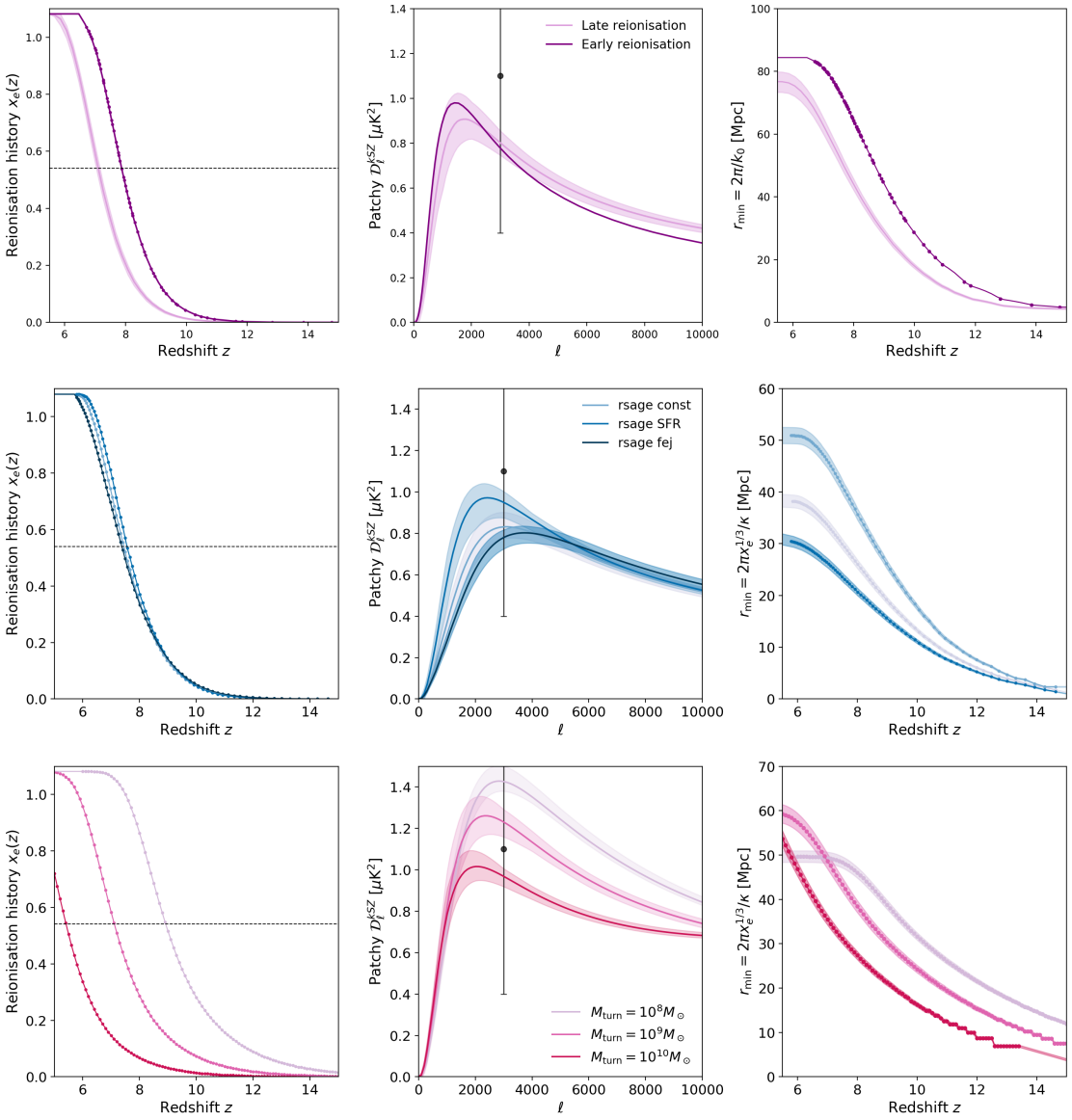

Figure 3.8: Comparison of results for the different simulations considered: respectively, EMMA, `rsage` and 21CMFAST. *Left panel:* Reionisation histories. *Middle panel:* Patchy kSZ angular power spectra. The data point corresponds to constraints from Reichardt et al. (2020). *Right panel:* Minimal size of ionised regions. Shaded areas correspond to the 68% confidence level on kSZ amplitude propagated from the probability distributions of the fit parameters.

Table 3.1: Comparison of results for the different simulations considered. $\mathcal{D}^h_{3000}$ and $\mathcal{D}^p_{3000}$ are given in μK^2 and correspond to the amplitude of the, respectively, homogeneous and patchy kSZ power spectrum at $\ell = 3000$. Δz is defined as $\Delta z = z(x_e = 0.25) - z(x_e = 0.75)$.

	EMMA		`rsage`			21CMFAST		
	Late	Early	`const`	`SFR`	`fej`	M8	M9	M10
$z_{\rm re}$	7.10	7.94	7.45	7.56	7.37	9.45	7.56	5.84
$z_{\rm end}$	5.84	6.89	5.79	5.78	5.70	7.76	6.19	4.75
Δz	1.16	1.20	1.46	1.38	1.60	2.17	1.70	1.34
τ	0.054	0.062	0.058	0.060	0.058	0.085	0.062	0.044
$\log\alpha_0$	3.93	4.10	3.12	3.47	2.87	3.30	3.58	3.79
/Mpc^3	$\pm$0.06	$\pm$0.15	$\pm$0.04	$\pm$0.04	$\pm$0.04	$\pm$0.03	$\pm$0.04	$\pm$0.04
κ	0.084	0.076	0.164	0.123	0.205	0.130	0.108	0.093
/Mpc^{-1}	$\pm$0.003	$\pm$0.009	$\pm$0.005	$\pm$0.005	$\pm$0.007	$\pm$0.003	$\pm$0.004	$\pm$0.003
$\mathcal{D}^h_{3000}$	3.39	3.86	3.57	3.57	3.56	3.58	3.21	2.84
$\mathcal{D}^p_{3000}$	0.80	0.74	0.83	0.95	0.78	1.43	1.23	0.97
$\ell^{\rm max}$	1800	1400	3100	2400	3700	2800	2300	2000

0.05 μK^2, see Table 3.1). This confirms that looking at the amplitude of the kSZ signal at $\ell = 3000$ to constrain reionisation history, as done in previous works, is far from sufficient and can lead to substantial errors. One needs to not only adapt the amplitude of the kSZ spectrum to CMB data, but also its shape. We can confirm a direct linear relation between the amplitude of the spectrum at $\ell = 3000$ and reionisation parameters such as the midpoint $z_{\rm re}$ or the duration Δz, which explains the somewhat unexpected fact that M8 exhibits much more kSZ power than M10. However, the parameters of this relation, and particularly the slope, change from one simulation to another. Therefore, there cannot be a relation giving $\mathcal{D}_{3000}$ from Δz and $z_{\rm re}$ and valid all the time, as suggested in Battaglia et al. (2013). In Table 3.1, we give the multipole $\ell^{\rm max}$ at which the kSZ spectrum reaches its maximum for each simulation. In the past, this value has been related to the characteristic size of ionised bubbles during reionisation (McQuinn et al. 2005; Iliev et al. 2007b; Mesinger et al. 2012). Using the random mean free path algorithm to estimate the bubble sizes in their simulations (Mesinger 2010), Hutter et al. (2020) confirm what we could already guess from the ionisation fields shown in Fig. 3.1: at all times, `rsage SFR` exhibits larger ionised bubbles on average than the other two simulations. Here, we notice that the `rsage SFR` simulation has the smallest value of $\ell^{\rm max}$ among the three `rsage` simulations, corresponding to the largest angular scales: this seems to confirm the relation between $\ell^{\rm max}$ and the bubble sizes. Additionally, the same conclusion can be drawn from the 21CMFAST results: M10, which shows the largest ionised bubbles compared to the two other runs (see Fig. 3.1), also has the smallest $\ell^{\rm max}$ value. In the past, this relation has been established in a purely empirical way. In the next Section, we will look for a physical interpretation of this result.

3.2.4 Physical interpretation

In this Section, we try to give a physical interpretation of the two parameters used to derive the kSZ angular power spectrum and to describe the evolution of the power spectrum of free electrons density contrast in terms of α_0 and κ. To do so, we look at an analytical derivation of $P_{ee}(k, z)$ for a toy model. Consider a box of volume $V = L^3$ filled with n fully ionised bubbles of radius R, randomly distributed throughout the neutral background, so that their centres are located at $\boldsymbol{a}_i$ for $i \in \{1, n\}$. The density of free electrons in the box follows

$$n_e(\boldsymbol{r}) = \frac{\bar{n}_e}{f} \sum_{i=1}^{n} \Theta\left(\frac{|\boldsymbol{r} - \boldsymbol{a}_i|}{R}\right), \tag{3.16}$$

where $\Theta(x)$ is the Heaviside step function, $\bar{n}_e$ is the mean number density of electrons in the box and f the filling fraction of the box (here, $f = x_e$). $\bar{n}_e/f$ is the number of electrons in one bubble divided by its volume and, ignoring overlaps, $f = 4/3\pi R^3 n/V$. Consider the electron density contrast field δ_e on which $P_{ee}(k, z)$ is built:

$$\delta_e(\boldsymbol{r}) \equiv \frac{n_e(\boldsymbol{r})}{\bar{n}_e} - 1 = \frac{1}{f} \sum_{i=1}^{n} \Theta\left(\frac{|\boldsymbol{r} - \boldsymbol{a}_i|}{R}\right) - 1, \tag{3.17}$$

represented on Fig. 3.6 for one of the six EMMA simulations used in this work. δ_e Fourier–transforms into

$$\tilde{\delta}_e(\mathbf{k}) = \frac{L^3}{n} W(kR) \sum_{i=1}^{n} \mathrm{e}^{-i\mathbf{k}\cdot\boldsymbol{a}_i}, \tag{3.18}$$

where $W(y) = (3/y^3)\,[\sin y - y\,\cos y]$ is the spherical top hat window function. Using this expression, and following Bharadwaj & Pandey (2005), the power spectrum of the electron density contrast field writes:

$$P_{ee}(\mathbf{k}) = \frac{4}{3f} \pi R^3\, W^2(kR), \tag{3.19}$$

which has units Mpc^3. Fig. 3.9 gives an example of such a power spectrum. We have generated an ionisation field made of enough bubbles of radius $R = 15$ px $= 5.5$ Mpc[6] to reach a filling fraction $f = 1\%$ in a box of 512^3 pixels and side length $L = 128/h$ Mpc. We compare the expression in Eq. (3.19) with power spectrum values computed directly from the 3D field and find a good match. The shape is very similar to the $P_{ee}(k, z)$ spectrum shown in the right panel of Fig. 3.6 for EMMA at the early stages of reionisation: despite its simplicity, this model seems to be a good description of $P_{ee}(k, z)$.

Let's look into the structure of this spectrum in more details. On very small or very

[6]The bubble radii actually follow a Gaussian distribution centred on 15 px with standard deviation 2 px.

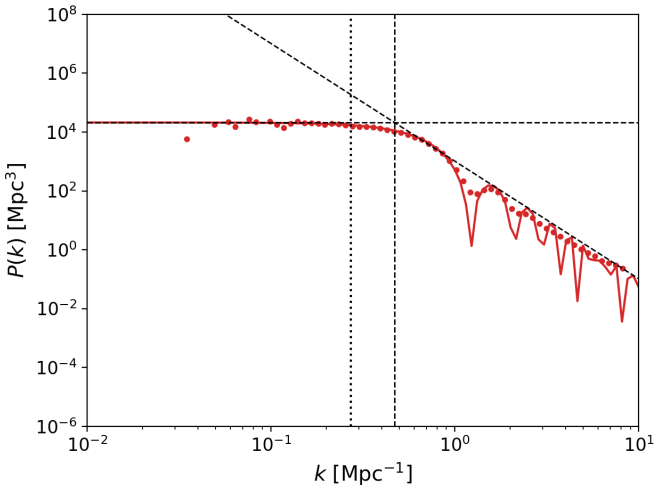

Figure 3.9: Free electrons density contrast power spectrum for a box filled with enough bubbles of radius $R = 15$ px $= 5.5$ Mpc to reach a filling fraction $f = 1\%$. Points are results of a numerical computation of the power spectrum, compared to the theoretical model (solid line). The dotted vertical line corresponds to $k = 1/R$, the dashed vertical line to $9^{1/4}/R$, the dashed horizontal line to $4/3\pi R^3/f$ and the tilted dashed line has slope k^{-4}.

large scales, the window function behaves as:

$$\begin{aligned} W(y) &\sim \frac{3}{y^3} \times \frac{y^3}{3} = 1 \quad \text{as } y \to 0 \\ W(y) &\sim \frac{3}{y^3} \times y = \frac{3}{y^2} \quad \text{as } y \to \infty. \end{aligned} \tag{3.20}$$

Thus, on small scales, the toy model power spectrum decreases as k^{-4} (see tilted dashed line on the figure). This is different to the evolution empirically chosen in Eq. (3.13), where the power to decrease as k^{-3}, because in our simulations small ionised regions will keep appearing as new sources light up, maintaining power on scales smaller than the typical bubble size. Additionally, in the simulations, the density resolution will allow correlations between regions within a given bubble, as can be seen in the δ_e field of Fig. 3.6, which will add power to the spectrum on small scales.

For $k > 9^{1/4}/R$, corresponding to the intersection point of the horizontal and tilted dashed lines on Fig. 3.9, the power starts dropping. In the parameterisation given in Eq. (3.13), the drop-off frequency roughly corresponds to $\kappa x_e^{-1/3}$, and we can therefore draw the parallel $\kappa x_e^{-1/3} \propto 1/R$. This confirms the intuition we had for a relation between the cut-off frequency and the typical bubble size (as there is no power above κ, there must be no ionised regions smaller than $1/\kappa$). Interestingly, Xu et al. (2019) find a similar feature, also related to the typical bubble size, in the bias between the H I and matter fields. On the right panels of Fig. 3.8, we show the evolution or $r_{\min}(z) \equiv 2\pi x_e(z)^{1/3}\kappa^{-1}$ as a function of redshift for each simulation. Simulations with on average larger bubbles (`rsage SFR` compared to `rsage const`, M10 compared to M8) also have higher values of $r_{\min}$ for a given ionisation level, corresponding, in turn, to smaller κ values (see Table 3.1). Now,

how can we relate κ to $\ell^{\max}$? Basic mathematics can give us a rough idea. By definition, $\ell^{\max}$ is the multipole at which C_ℓ is maximum, therefore its derivative $\mathrm{d}C_\ell/\mathrm{d}\ell = 0$ for $\ell = \ell^{\max}$. Ignoring the $k = 0$ cases, according to Eq. (3.7), this corresponds to $k = \ell/\eta$ such that $\partial P_{ee}(k, z)/\partial k = 0$, and so to scales $k < \kappa$. As a confirmation, we compute the patchy kSZ power spectrum for fixed $x_e(z)$ and α_0 but let κ values vary and find a clear linear relation between κ and $\ell^{\max}$, shown on the left panel of Fig. 3.10. Previous results on the six high-resolution simulations, `rsage` and 21CMFAST lie along this line; this relation is therefore valid for all types of simulations. Such a relationship means that a detection of the patchy power spectrum in CMB observations would give an estimate of $\ell^{\max}$, giving access to κ and consequently to the evolution of the typical bubble size.

Let's now turn to α_0. On large scales, the toy model gives $P_{ee}(k) \sim 4/3\pi R^3/f$, constant with k (dashed horizontal line on Fig. 3.9). It is inversely proportional to the filling fraction f and therefore has larger global amplitude earlier in reionisation. Drawing a parallel with our parameterisation of $P_{ee}(k, z)$ in Eq. (3.13), we have $\alpha(z) \equiv \alpha_0 x_e^{-1/5} \propto R^3/x_e(z)$. This equivalence is easy to interpret: as a measure of the amplitude of the power spectrum of the contrast density, α is a measure of the variance in the field (remember that the contrast field is defined as $\delta_e(r) + 1 = n_e(r)/\bar{n}_e$ and $\bar{n}_e \propto f$ is the mean electron number density). When the filling fraction is very small, only a very small numbers of ionised bubbles live in an otherwise neutral box, and the variance is very high. On the contrary, when the filling fraction is $\sim 50\%$, the box is filled in a rather homogeneous way, and the variance is very low. Naturally, α_0 will also depend on the bubble size: for a given filling fraction, many small bubbles will cover the neutral background more homogeneously than a few large bubbles and lead to a smaller variance, so a smaller α_0 value. This idea is similar to what was observed in Sec. 3.1 when defining σ_{loc}. This relation can also explain the correlation observed between α_0 and κ when fitting Eq. (3.15) to data (recall that $R \propto 1/\kappa$).

Since α_0 is independent of redshift, it will be a pre-factor for the left-hand side of Eq. (3.12), and we therefore expect a strong correlation between this parameter and the maximum amplitude reached by the spectrum $\mathcal{D}_{\max}$. We confirm this intuition by fixing the reionisation history and κ but varying α_0 on the range $3.0 < \log \alpha_0 < 4.4$ and comparing the resulting spectra. Results are shown on the right panel of Fig. 3.10: there is a clear linear relation between these two parameters and α_0, but in this case results for `rsage` and 21CMFAST do not follow the correlation. Interestingly, the shape of the different resulting kSZ power spectra is strictly identical (namely, $\ell^{\max}$ does not change when varying α_0), hinting at the fact that $\ell^{\max}$ depends only on κ and not α_0 or reionisation history. Therefore it will be possible to make an unbiased estimate of κ from the shape of the measured spectrum. The `rsage` simulations show that, for a similar reionisation history, a larger value of α_0 will lead to a stronger kSZ signal; but looking at 21CMFAST, we found that an early reionisation scenario can counterbalance this effect and lead to high amplitude despite low α_0 values. This corroborates the results of Mesinger et al. (2012), which find that the amplitude of the spectrum is determined by both the morphology (and so the α_0 value) and the reionisation history. Therefore, fitting CMB data to our parameterisation

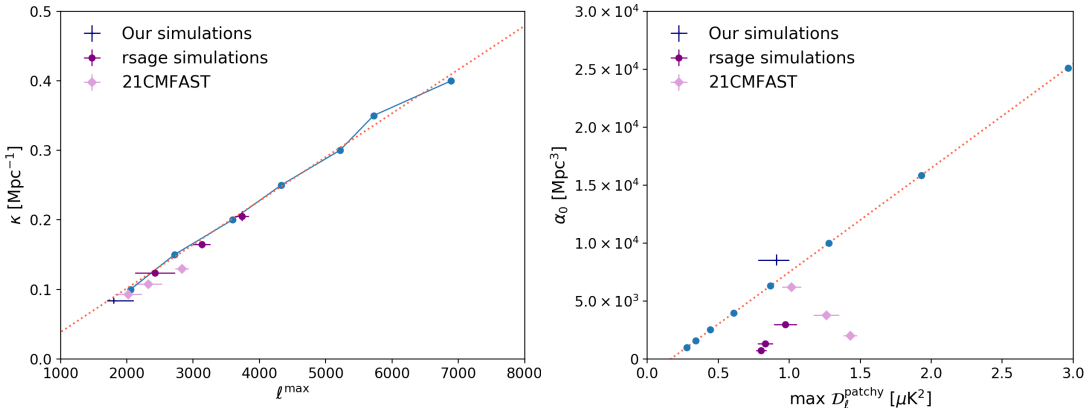

Figure 3.10: *Left panel:* Evolution of the peaking angular scale of the patchy kSZ power spectrum $\ell^{\max}$ for one given reionisation history but different values of the κ parameter. *Right panel:* Evolution of the maximum amplitude of the patchy kSZ power spectrum $\mathcal{D}_{\max}$ for one given reionisation history but different values of the α_0 parameter. On both figures, the red dotted line is the result of a linear regression and inferences are compared to results for different simulations.

will likely lead to strongly correlated values of α_0 and parameters such as Δz or $z_{\rm re}$. Other methods should be used to constrain the reionisation history and break this degeneracy, such as constraints from the value of the Thomson optical depth, or astrophysical constraints on the IGM ionised level. Conversely, 21cm intensity mapping should be able to give independent constraints on α_0.

With this new formalism, it will be possible to derive for the first time the amplitude *and* shape of the patchy kSZ power spectrum from CMB data. Here, the reionisation history is included in the determination of the shape, giving more consistent results. Indeed, currently, different prescriptions of $x_e(z)$ are used at different stages of the CMB data analysis: one is included in the kSZ template, another in the scalings giving $\mathcal{D}_{3000}$ in terms of $z_{\rm re}$ and Δz, while the tanh parameterisation of Eq 2.4 is used to derive τ. Reciprocally, measuring the kSZ signal will allow us to infer the values of the two parameters of Eq. (3.13), providing detailed information about the physics of reionisation: κ will constrain the growth of ionised bubbles with time and α_0 the evolution of the variance of the ionisation field during EoR, both being related to the ionising properties of early galaxies. The complex derivation of the kSZ signal, based on a series of integrals, leads to correlations between our parameters. For example, a high amplitude of the spectrum can be explained either by a large value of α_0 due to a high ionising efficiency of galaxies, or by an early reionisation. Such degeneracies, however, could be broken by combining CMB data with other observations: astrophysical observations of early galaxies and quasars will help grasp the global history of reionisation and constrain parameters such as Δz and $z_{\rm re}$, while 21cm intensity mapping will help understand reionisation morphology, putting independent constraints on α_0 and κ.

However, power spectra overlook the non-Gaussianity of the signal they describe, and the 21cm signal is expected to be significantly non-Gaussian during EoR, especially in the

very early and very late stages (Watkinson et al. 2017; Majumdar et al. 2018; Hutter et al. 2020). In order to take non-Gaussianity into account, one needs to jump to the next order of statistics and look at 3-point correlation functions or at their Fourier counterpart, the bispectrum.

3.3 Third statistical moment: triangle correlations and other higher-order statistics

A Gaussian random field (GRF) $g(\boldsymbol{r})$ is fully described by its first and second-order statistics, such as the mean and the variance. This is why cosmologists often look at the power spectrum of its contrast field $\delta(\boldsymbol{r}) = g(\boldsymbol{r})/\langle g \rangle - 1$, which has mean zero, so that all the information about the field is enclosed in its variance, and in turn, the power spectrum of $\delta(\boldsymbol{r})$. However, the first and second statistical moments are not sufficient to describe non-Gaussian fields such as 21cm brightness temperature maps during reionisation. In fact, a GRF and a strongly non-Gaussian field can share the same power spectrum despite having very different structures in real space. This is illustrated in Fig. 3.11, where we show two ionisation fields, one with a clear bubble structure (upper panel) and a GRF (lower panel).

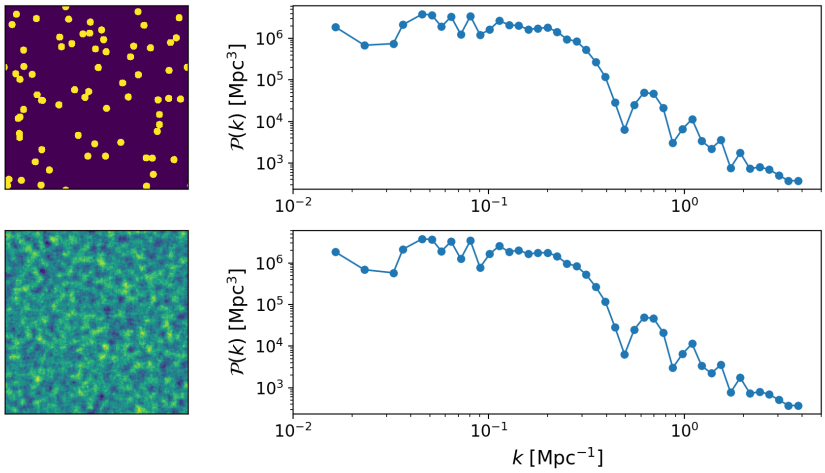

Figure 3.11: Illustration of two fields having very different real-space structures (left panels) but identical power spectra (right panels). The bottom field is a Gaussian random field.

3.3.1 The 21cm bispectrum

Some works have focused on the Fourier transform of the 3-point correlation function (3-PCF), the bispectrum, to extract information about the non-Gaussianity of the 21cm signal

during reionisation. Consider the spatial fluctuations of the 21cm brightness temperature field, given in Eq. (1.18): $\delta_{21}(\boldsymbol{r}) = \delta T_{\rm b}(\boldsymbol{r})/\langle\delta T_{\rm b}\rangle - 1$. The bispectrum $\mathcal{B}$ of this field is defined as

$$\langle\delta_{21}(\mathbf{k}_1)\,\delta_{21}(\mathbf{k}_2)\,\delta_{21}(\mathbf{k}_3)\rangle = (2\pi)^3\,\delta(\mathbf{k}_1+\mathbf{k}_2+\mathbf{k}_3)\,\mathcal{B}(\mathbf{k}_1,\mathbf{k}_2,\mathbf{k}_3) \tag{3.21}$$

where δ is the Dirac delta function and the brackets denote an ensemble average. Because the 21cm field is a real field, and due to parity invariance, the bispectrum is real (Shimabukuro et al. 2016; Majumdar et al. 2018). It measures the excess probability between three points forming a triangle in Fourier space and will therefore, in contrast to the power spectrum, depend not only on the amplitude of the $\mathbf{k}$ vectors but also their direction. For this reason, it is difficult to represent, and different works have chosen different approaches. Most authors choose to separate the shapes of the triangle the wave-vectors form.

In their work, the first one to estimate the 21cm bispectrum, Shimabukuro et al. (2016) choose to consider the amplitude of a normalised, dimensionless bispectrum $k^6|\mathcal{B}(k)|$ where the ratio of the amplitudes of the three wave-vectors varies: $k_1 = k_2 = k_3$ gives equilateral triangles, $k_1 = k_2 = 2k_3$ gives *folded* triangles and $k_3 = 10k_1 = 10k_2$ *squeezed* triangles. The authors find that the main contribution to this bispectrum is matter fluctuations and they are able to relate features in the 21cm power spectrum to some seen in the bispectrum. For example, the squeezed bispectrum will give information about small scales, related to the shorter side of the triangle; large scales, corresponding to the two larger sides; and about the correlations between the two. Therefore, $B(10k, 10k, k)$ combines the information we can extract from $P(10k)$ and $P(k)$, and includes extra information about the cross correlations between the two scales. In a follow-up paper, the authors further show that combining bispectrum with power spectrum information can give improved constraints on astrophysical parameters related to reionisation such as the virial temperature of halos or the ionising efficiency of light sources, as well as reduce the degeneracy between them (Shimabukuro et al. 2017).

However, because this approach considers the amplitude $|\mathcal{B}|$ of the bispectrum only, it overlooks the information that its sign potentially carries. In their work, Majumdar et al. (2018) therefore choose to look at the raw bispectrum, without any normalisation, and consider three different shapes of triangles, according to the geometry illustrated in Fig. 3.12. Let $\mathbf{k}_3 = -\mathbf{k}_1 - \mathbf{k}_3$ to satisfy the Dirac delta condition in Eq. (3.21) and θ the angle between $\mathbf{k}_1$ and $\mathbf{k}_2$, then

- Stretched triangles are such that $\theta < 2\pi/3$ ($1 \geq \cos\theta > 1/2$),
- Equilateral triangles such that $\theta = 2\pi/3$ ($\cos\theta = -1/2$) and
- Squeezed triangles have $\theta > 2\pi/3$ ($-1 \leq \cos\theta < -1/2$).

The authors find that the equilateral bispectrum is negative on a large k range during the EoR, and that the negative amplitude increases with the ionised fraction during the core of

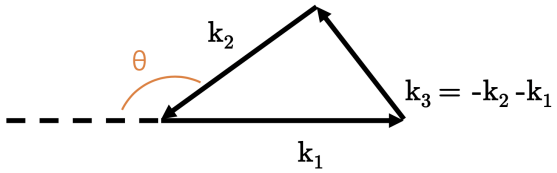

Figure 3.12: Geometry of the bispectrum in Fourier space.

the process, as the field gets further and further from a GRF. The authors further confirm that the bispectrum of isosceles triangles, mainly squeezed ones, captures correlations between small and intermediate scales, that they relate to the presence of neutral bridges or ionised tunnels in the field. For all triangle shapes, positive values of the bispectrum seem to stem from matter fluctuations, or cross correlations between the ionisation field and the matter field. Therefore during reionisation, most of the bispectrum signal stems from H I fluctuations rather than matter ones (Majumdar et al. 2018; Hutter et al. 2020).

The sign of the bispectrum is essential because it tells us about the structure of the underlying field. It can be interpreted in terms of inference patterns: in two dimensions, the bispectrum of three k-vectors forming an equilateral triangle is built upon the inference pattern of three waves with equivalent configurations, that is a spherically symmetric concentration of signal (see Lewis (2011) and Watkinson et al. (2019) for an enlightening illustration of this). In 3D, a strong signal from the equilateral bispectrum will stem from a field made of filaments with circular cross-section. Filaments with an above-average density will yield a strong positive signal, whereas under-dense filaments will yield a negative bispectrum (Watkinson et al. 2019). Similarly, the bispectrum of flattened triangles will be enhanced in the presence of filaments with an ellipsoidal cross section, that tend towards planes.

Further works choose to focus on a dimensionless bispectrum, normalised by the power spectrum in order to isolate the non-Gaussianity:

$$b(k_1, k_2, k_3) = \frac{\mathcal{B}(k_1, k_2, k_3)}{\sqrt{k_1 k_2 k_3 P(k_1) P(k_2) P(k_3)}}. \tag{3.22}$$

This new bispectrum is very efficient at tracing the morphology of the underlying field and can so be used to estimate the contribution of QSOs and X-ray binaries to X-ray heating during the cosmic dawn (Watkinson et al. 2019) or the morphology of ionised regions during EoR (Hutter et al. 2020). In particular, it is possible to relate the scale at which the equilateral bispectrum changes sign to the typical size of ionised bubbles at this time.

These results are very interesting prospects for future 21cm intensity mapping observations but are still mainly theoretical and some further work is required to understand how exactly a tool such as the bispectrum can be used with interferometric observations (Trott et al. 2019). In particular, one needs to understand the impact of foreground removal

on the non-Gaussianity of the signal (Watkinson et al. 2020). The main disadvantage of the bispectrum is its interpretation: because it is a function of three three-dimensional parameters and because it has a complex structure which holds most of the physical information, it is difficult to get a simple picture of it. In this perspective, we will now look at a custom version of its real-space counterpart, the 3-point correlation function, modified in order to be easily read and to pick up the bubbly structure of the ionisation field during reionisation.

3.3.2 The triangle correlation function of phases: definition

Let a 3D real ionisation field $x(\boldsymbol{r})$ of volume V and its direct Fourier transform $\hat{x}(\mathbf{k}) = |\hat{x}(\mathbf{k})|\,\mathrm{e}^{i\phi}$, which is a complex number with an amplitude and a phase $\phi = \arg\,[\hat{x}(\mathbf{k})]$. The power spectrum of this field is defined by

$$P(k) = \hat{x}(\mathbf{k})\,\hat{x}(-\boldsymbol{k}) = \hat{x}(\mathbf{k})\,\hat{x}^{\star}(\mathbf{k}) = |\hat{x}(\mathbf{k})|^2 \tag{3.23}$$

where the asterisk denotes the complex conjugate and we have used the symmetry of the Fourier transform of a real field. Because of this very symmetry, when computing the power spectrum of a field, we lose the information carried in the phase of the Fourier transform. Yet, phases are essential to characterise the structure of a field. Consider the two field presented in Fig. 3.11. They have the same power spectrum, meaning that the amplitude of their Fourier transforms are identical. However, the second field (lower panel) was obtained by shuffling the Fourier phases of the first one: randomising the phases removes the geometrical structure of the field. In other words, the Fourier phases of a field characterise its non-Gaussianity. In the rest of this section, we therefore choose to focus on what we call the phase factor of our field, defined by:

$$\hat{\epsilon}(\mathbf{k}) = \frac{\hat{x}(\mathbf{k})}{|\hat{x}(\mathbf{k})|} = \mathrm{e}^{i\,\arg\,[\hat{x}(\mathbf{k})]}. \tag{3.24}$$

By construction, the phase factor will have an amplitude of one, so that its 2-point correlation function (2-PCF) – and consequently its power spectrum, will vanish. The simplest statistics related to $\hat{\epsilon}(\mathbf{k})$ we can find is then its 3-PCF, which is the inverse Fourier transform of the bispectrum, defined by:

$$\mathcal{B}(\mathbf{k}, \boldsymbol{q}) = \hat{x}(\mathbf{k})\,\hat{x}(\boldsymbol{q})\,\hat{x}(-\mathbf{k}-\boldsymbol{q}), \tag{3.25}$$

and in particular for the phase factor:

$$\mathcal{B}_{\epsilon}(\mathbf{k}, \boldsymbol{q}) = \hat{\epsilon}(\mathbf{k})\,\hat{\epsilon}(\boldsymbol{q})\,\hat{\epsilon}(-\mathbf{k}-\boldsymbol{q}) = \frac{\mathcal{B}\,(\mathbf{k}, \boldsymbol{q})}{|\mathcal{B}\,(\mathbf{k}, \boldsymbol{q})\,|}. \tag{3.26}$$

Note that for a mildly non-Gaussian field, it is possible to relate the bispectrum of the phase factor with the normalised bispectrum defined in Eq. (3.22) (Wolstenhulme et al.

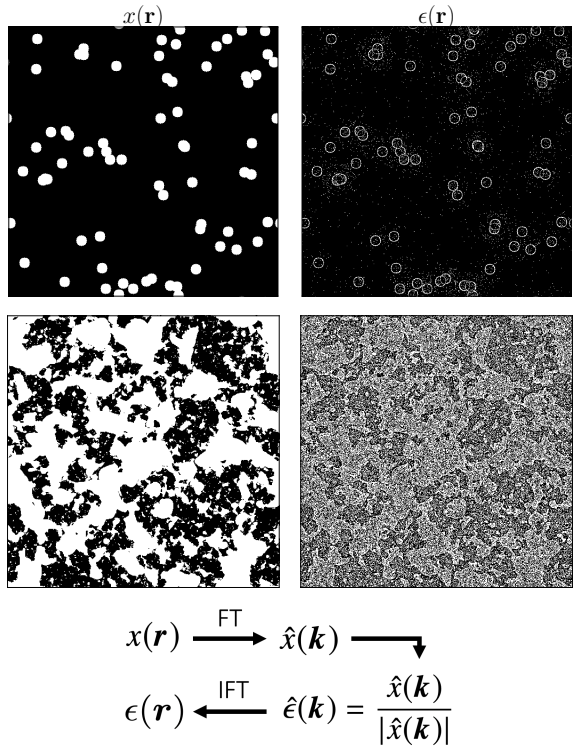

Figure 3.13: Examples of phase information in real space. Left panels represent the ionisation field $x(\boldsymbol{r})$ and the right panel the inverse Fourier transform of the corresponding phase factor $\hat{\epsilon}(\mathbf{k})$. *Top row:* Toy model with randomly distributed ionised bubbles. *Bottom row:* Output of the 21CMFAST simulation. Both boxes have 512^2 pixels and side length $L = 400$ Mpc.

2015). Fig. 3.13 illustrates how phases carry structure information by comparing a field to the inverse Fourier transform of its phase factor $\epsilon(\boldsymbol{r})$, a tracer of phase information in real space. The two fields considered are first an ionisation field made of randomly distributed ionised disks on a neutral background (top panels) and second the ionisation field extracted from a run of 21CMFAST at $z = 7.8$ and global ionised fraction $x_{\mathrm{H\,II}} = 0.54$. We see that phases mostly preserve the edges of the ionised regions.

The 3-point correlation function of the phase factor $\epsilon(\boldsymbol{r})$ is defined by

$$\Xi\left(\boldsymbol{r}, \boldsymbol{s}\right) = \frac{V^2}{(2\pi)^6} \int\int \mathrm{d}^3k \; \mathrm{d}^3q \; \mathrm{e}^{i(\mathbf{k}\cdot\boldsymbol{r}+\boldsymbol{q}\cdot\boldsymbol{s})} \frac{\mathcal{B}\left(\mathbf{k}, \boldsymbol{q}\right)}{|\mathcal{B}\left(\mathbf{k}, \boldsymbol{q}\right)|}. \tag{3.27}$$

Previous works have used modified versions of this function, for two vectors $\boldsymbol{r} = -\boldsymbol{s}$, in a bid to characterise the filamentary structure of the cosmic web (Obreschkow et al. 2013; Eggemeier et al. 2015; Wolstenhulme et al. 2015). Here, conversely, we target the bubbly structure of the ionisation field during reionisation, and therefore consider two vectors $\boldsymbol{r}$ and $\boldsymbol{s}$ forming an equilateral triangle, as it is the three-point shape closest to a sphere. In

this case, $\boldsymbol{s}$ is just $\boldsymbol{r}$ rotated by an angle $\pi/3$ so that, in 3D:

$$\begin{cases} s_x = \dfrac{1}{2}r_x - \dfrac{\sqrt{3}}{2}r_y \\ s_y = \dfrac{\sqrt{3}}{2}r_x + \dfrac{1}{2}r_y \\ s_z = r_z \end{cases}$$

where the 2D case is limited to the first two equations[7]. If we define a new vector $\boldsymbol{p}$ according to

$$\boldsymbol{p} = \begin{pmatrix} k_x + \frac{1}{2}q_x + \frac{\sqrt{3}}{2}q_y \\ k_y - \frac{\sqrt{3}}{2}q_x + \frac{1}{2}q_y \\ k_z + q_z \end{pmatrix},$$

we can rewrite $\mathbf{k}\cdot\boldsymbol{r} + \boldsymbol{q}\cdot\boldsymbol{s} = \boldsymbol{p}\cdot\boldsymbol{r}$ in Eq. (3.27). By taking the rotational average of this equation, we find in dimension D ($D = 2$ or $D = 3$)

$$\xi_3^*(r) \equiv \frac{V^2}{(2\pi)^{2D}} \int\int \mathrm{d}^D k \; \mathrm{d}^D q \; \omega\left(pr\right) \frac{\mathcal{B}\left(\mathbf{k},\boldsymbol{q}\right)}{\left|\mathcal{B}\left(\mathbf{k},\boldsymbol{q}\right)\right|}, \tag{3.28}$$

where ω is the window function corresponding to the rotational average of the exponential factor:

$$\omega(x) = \begin{cases} \dfrac{\sin\left(x\right)}{x} & \text{if } D = 3, \\ J_0(x) & \text{if } D = 2, \end{cases}$$

for $J_0(x)$ the Bessel function of the first kind of order 0. Numerically, we will need to discretise the integrals so that

$$\xi_3^*(r) = \sum_{\mathbf{k}} \sum_{\boldsymbol{q}} \omega\left(pr\right) \frac{\mathcal{B}\left(\mathbf{k},\boldsymbol{q}\right)}{\left|\mathcal{B}\left(\mathbf{k},\boldsymbol{q}\right)\right|}, \tag{3.29}$$

where we have considered our density field as a periodic 2D or 3D box with physical side length L, divided into N^D cells. Each cell has a width $\Delta x = L/N$. In Fourier space, this box transforms into a box of same dimensions (N^D) but of side length $2\pi N/L$ and spacing $\Delta k = 2\pi/L$. The largest mode $k = 2\pi/\Delta x$ has the smallest wavelength. If we assume phases are uncorrelated below a given scale, then the modes whose wavelengths are smaller than this scale will have random phases. When the resolution is improved, i.e. Δx reduced, the number of such modes increases and random phase terms are added to Eq. (3.29) so that the signal eventually diverges. Following Obreschkow et al. (2013), we introduce a cut-off $k \leq \pi/r$ on the sums of Eq. (3.29) to limit this number. Similarly, when increasing the size of the box L, we add modes with wavelength larger than the largest correlation scale within the box, and therefore add random phase terms to the sum. Because $\Delta k = 2\pi/L$, the number of modes scales as L^D and $s(\boldsymbol{r})$ diverges as $L^{3D/2}$. As discussed in Obreschkow

[7]Note that in the actual computation of the triangle correlations function, we will consider rotations not only around the z-axis but also around the other two axes.

et al. (2013), we introduce the pre-factor $(r/L)^{3D/2}$ to Eq. (3.29) to remove this divergence. These changes applied to the isotropic modified 3-PCF $\xi_3^*(r)$ define the triangle correlation function of phases (TCF):

$$s(r) = \left(\frac{r}{L}\right)^{3D/2} \sum_{k,q \leq \pi/r} \omega\left(pr\right) \frac{B\left(\mathbf{k}, \boldsymbol{q}\right)}{\left|B\left(\mathbf{k}, \boldsymbol{q}\right)\right|}. \tag{3.30}$$

$s(\boldsymbol{r})$ is a complex function but, similarly to the bispectrum, its imaginary part will sum to zero. This object was first introduced in Gorce & Pritchard (2019), reproduced in Appendix A.2. The code developed to compute the TCF is available on my GitHub page.

All these derivations have been done with $x(\boldsymbol{r})$ being the ionisation field $x_{\mathrm{H\,II}}$. If we consider the neutral field $x_{\mathrm{H\,I}}$, we have $x_{\mathrm{H\,II}} = 1 - x_{\mathrm{H\,I}}$ and $\hat{x}_{\mathrm{H\,II}}(\mathbf{k}) = -\hat{x}_{\mathrm{H\,I}}(\mathbf{k})$ which we can plug back into the equations above to find $s_{\mathrm{H\,II}}(r) = -s_{\mathrm{H\,I}}(r)$. Therefore, when applied to a mostly ionised field containing a few remote neutral islands, the correlations dominating the signal will be related to H I regions and the signal will be negative. In particular, because 21cm interferometric images trace the neutral gas in the sky, if we apply our method on 21cm brightness temperature maps, we obtain a negative signal. This also implies that during the middle stages of the reionisation process, positive and negative (respectively, H II and H I) correlations overlap, and the TCF flattens to zero.

3.3.3 The triangle correlation function of phases: application

Now that we have derived our new statistics, we will test it on ionisation fields and see what information we can extract from it. We start with toy models, where fully ionised bubbles are randomly distributed on an homogeneous neutral background, to characterise the function. Then we move on to actual reionisation simulations, such as 21CMFAST and `rsage`.

Proof of concept on toy models

We generate boxes of dimension N^2 filled with randomly distributed disks with pixel value 1 corresponding to H II regions. Because the UV photons emitted by early galaxies have a very short mean free path in the surrounding neutral IGM, the boundary between ionised and neutral regions is expected to be sharp (Liu et al. 2016), so that a binary model where ionised bubbles have $x_{\mathrm{H\,II}} = 1$ and neutral regions $x_{\mathrm{H\,II}} = 0$ is a good transcription of the reality of the IGM ionisation field[8]. Generated bubbles are allowed to overlap, and periodic boundary conditions are respected throughout the box. We then compute the triangle correlation function (TCF) in Eq. (3.30) for different correlation scales and plot the result on Fig. 3.14 for 20 realisations of a box filled with 70 binary bubbles of radius 10 (in pixel units), equivalent to $R = 7.8$ Mpc, so that the global ionised fraction of the

[8]Note that we have also tried the case where the ionised regions are 2D Gaussian distributions, in order to account for partially ionised regions. The structure of the resulting signal is roughly the same, but with weaker amplitude.

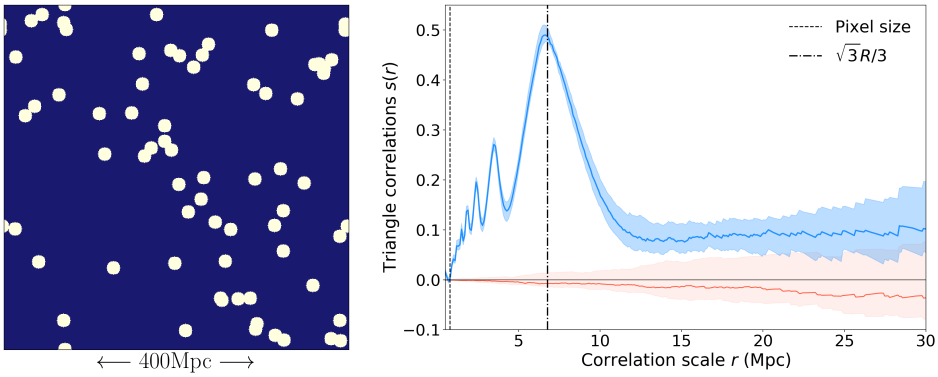

Figure 3.14: Triangle correlation function for a box of 512^2 pixels and side length $L = 400$ Mpc filled with 70 binary bubbles of radius $R = 10$ px (in blue) or filled with a Gaussian random field (in red). The shaded areas correspond to the 95% confidence interval as the function was computed for 20 different realisations of the same box.

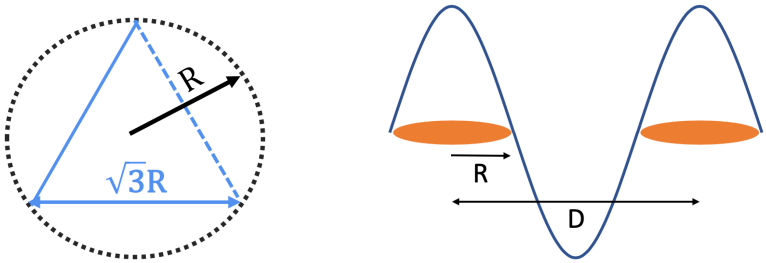

Figure 3.15: Illustration of basic geometry to understand the triangle correlation function. The right-hand sketch is adapted from Watkinson et al. (2019).

box is $x_{\mathrm{H\,II}} = 8\%$. The TCF of this field is compared to the signal obtained for 20 boxes of same dimensions but filled with a Gaussian random field.

We see a strong peak in the signal at scales $r \simeq 7$ Mpc, i.e. smaller than the radius size. We would expect the TCF to peak at $\sqrt{3}R$ as it probes equilateral triangles inscribed in the binary disks of the box, which have a side length of $\sqrt{3}R$, as illustrated on the left panel Fig. 3.15. However, the wave-vectors which give signal are the ones whose wavelength is large enough to cover a whole bubble, as illustrated on the right panel of Fig. 3.15. Such waves have $k = 2\pi/D$ with $D = 4R$, thus we probe Fourier modes with wavelength twice larger than expected, corresponding to real-space scales twice smaller than expected (Watkinson et al. 2019). The peak is therefore observed at $\sqrt{3}R/2$ (dash-dotted line on the figure). Conversely, the signal computed for the Gaussian random fields is close to zero, confirming that the TCF is an efficient tracer of non-Gaussianity, and that is because it is based on the phases of the signal.

Indeed, let's take our toy moddel and compute its 2-point correlation function, its TCF and a modified version of the TCF, which uses the full bispectrum, phases and amplitude included:

$$\Xi_3^{(1)}(r) = \left(\frac{r}{L}\right)^{3D/2} \sum_{k,q \leq \pi/r} \omega_D\,(pr)\ \mathcal{B}\,(\mathbf{k}, \boldsymbol{q})\,. \tag{3.31}$$

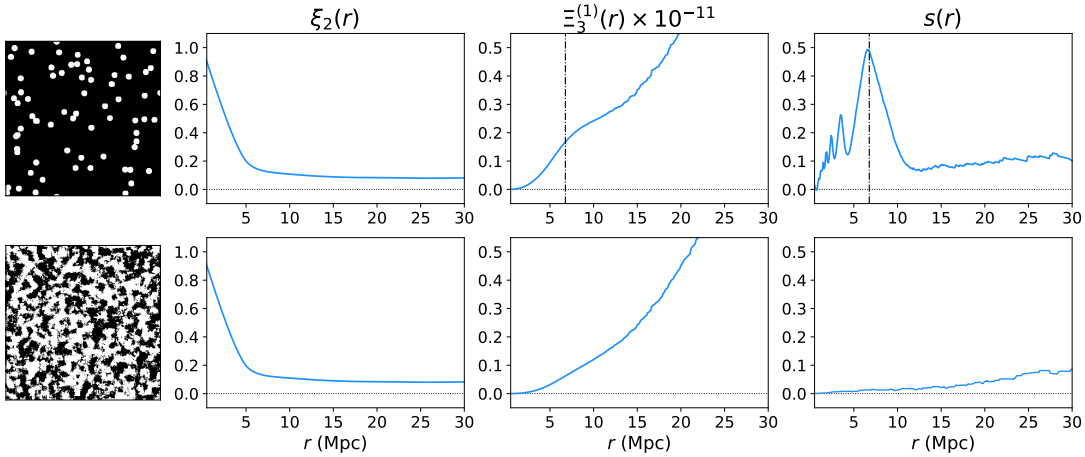

Figure 3.16: Comparison of results on phase correlations for two ionisation fields with identical power spectra and dimensions ($N = 512$, $L = 400$ Mpc) but different phase information: lower panels correspond to the field from upper panels after having reshuffled the Fourier phases. Left panels show the 2D ionisation field in real space, middle left, middle right and right panels respectively show the corresponding 2-PCF $\xi_2(r)$, the scaled modified 3-PCF $\Xi_3^{(1)}(r)$ (see Eq. 3.31), and the triangle correlation function $s(r)$. The vertical line marks $\sqrt{3}R/2$.

We then shuffle the Fourier phases of the toy model, that is replace them by random values between 0 and 2π, and compute the corresponding 2-PCF, TCF and modified 3-PCF $\Xi_3^{(1)}$. Results can be seen on the upper and lower panels of Fig. 3.16 for the toy model and its Gaussian counterpart respectively. The left panels are identical to Fig. 3.11: we see that reshuffling the phases has made the field lose all its structure and there are no bubbles any more. Because we kept the absolute value of the field unchanged, the 2-PCF in the second column are exactly identical. The modified 3-PCF of Eq. (3.31) is shown in the third column. As a statistics of order three, it includes non-Gaussian information and we can see for the toy model a slight bump at scales corresponding to the TCF bump in the fourth column. However, this information is washed out by Gaussian information, so that the 3PCF of the two fields are only slightly different. Conversely, when normalising the bispectrum by its amplitude and using the phase factor, we have kept only the non-Gaussian information so that the TCF is close to zero for the Gaussian field, but has a clearly defined structure, related to the bubbles forming the field, for the toy model.

From these preliminary results, we can already see some limitations in the use of the TCF. First, for both the toy model and the GRF, the signal is very similar for all realisations of the box at small scales, but the confidence intervals become wider at larger scales. This will remain true for any size of box, any resolution and any filling fraction. Second, we observe that the higher the filling fraction or the higher the radius, the flatter the TCF signal: bubbles overlap more and more and locating them individually to get a clear signal becomes difficult. The TCF will therefore be better at identifying bubble sizes in the very early or very late stages of reionisation, as we will see in the next paragraph.

Applications to simulations

Now that we have characterised the TCF on toy models, we apply it to more physical ionisation fields: firstly runs of the semi-numerical simulation 21CMFAST, and secondly the three `rsage` simulations used earlier in this chapter (see App. B for details). In these simulations, the bubbles are no longer randomly distributed throughout the box and correlations between the locations of ionised regions will appear in the signal. Additionally, the ionised regions will not have the perfect spherical shape they had in the toy model.

With 21CMFAST, we generate a dark matter box with sufficient resolution to obtain a H II field of 512^3 pixels and side length $L = 400$ Mpc with Planck Collaboration et al. (2016b) cosmology. The resulting reionisation history, shown in Fig 3.18, has its midpoint at $z = 7.9$ for a duration of $\Delta z = z\,(x_{\mathrm{H\,II}} = 0.10) - z\,(x_{\mathrm{H\,II}} = 0.99) = 4.9$ and gives $\tau = 0.067$. The output of the simulation is a 3D H I field but we choose to analyse 2D slices to be closer to actual observations. We also convert the given H I field into a binary H II field in order to get positive triangle correlations when most of the field is ionised and negative correlations when the sky is mainly neutral, as explained earlier. Fig. 3.17 presents the TCF of single 2D slices at redshifts $z = 12.0, 11.0, 10.0, 9.0, 8.0, 7.0, 6.4$ and 6.2 corresponding to global ionisation levels of $x_{\mathrm{H\,II}} = 0.09, 0.10, 0.18, 0.29, 0.49, 0.80, 0.97$ and 0.99 respectively, along with a picture of the corresponding H II field. For each snapshot, results are shown with variance estimated from the TCF of 20 Gaussian random fields of same dimensions: again, the signal is more significant on small scales. These errors give an idea of the reliability of the signal depending on the scale but they are incomplete. Indeed, the TCF signal will be strongest for very non-Gaussian fields at the very early or very late stages of reionisation, when isolated features such as a small number of purely ionised regions or a few leftover neutral islands are present. Consider the $z = 6.2$ slice on Fig. 3.17: the strong signal comes from the remote neutral islands seen in the field. These islands are isolated features specific to this region of the simulation and if we compute the TCF from averaging the signal over the N slices of the box, it will likely be washed out by the overall homogeneously neutral field. This prevents us from putting error bars on our results, an issue that will be further discussed in Sec. 4.1.

At high redshift, before ionised regions start percolating, we see on Fig. 3.17 that the TCF has more power at small scales but no clear peak. This is likely due to the variety of H II regions: many small ionised regions around young sources cover the neutral background relatively homogeneously and there is no typical bubble size. By looking at the signal-to-noise ratio (SNR), we can infer an upper limit on the sizes of the ionised regions: at $z = 13$, scales smaller than 8.9 Mpc contribute for 80% of the cumulative SNR; at $z = 12$ and $z = 11$, this upper limit increases respectively to 10.8 Mpc and 11.2 Mpc. The structure of the ionisation field at high redshift directly relates to the way the 21CMFAST algorithm is constructed. The angular structure of the ionised regions can be related to the use of excursion-set theory: as soon as a region has produced enough photons to ionise all its baryons, then it is considered ionised. The fact that there are many small ionised

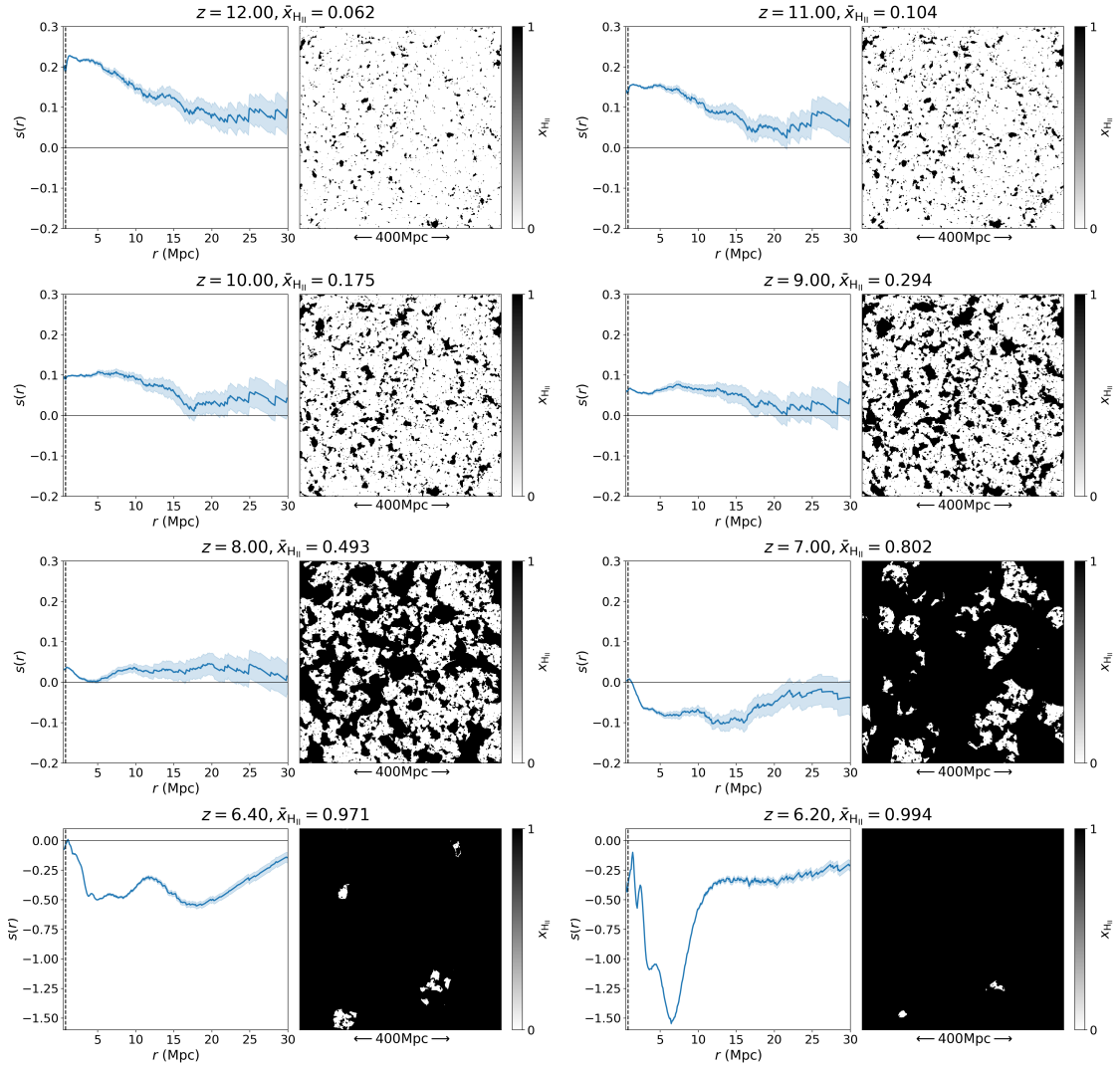

Figure 3.17: Triangle correlations for 2D slices of our simulation at various redshifts. Error bars correspond to the variance estimated from a Gaussian random field of same dimensions.

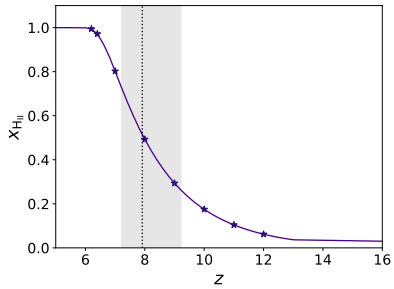

Figure 3.18: Reionisation history of our simulation. The dotted line corresponds to the midpoint of reionisation, i.e. $z = 7.9$, and the shaded region to global ionised fraction between 25% and 75%. The starred points are the stages of reionisation represented above.

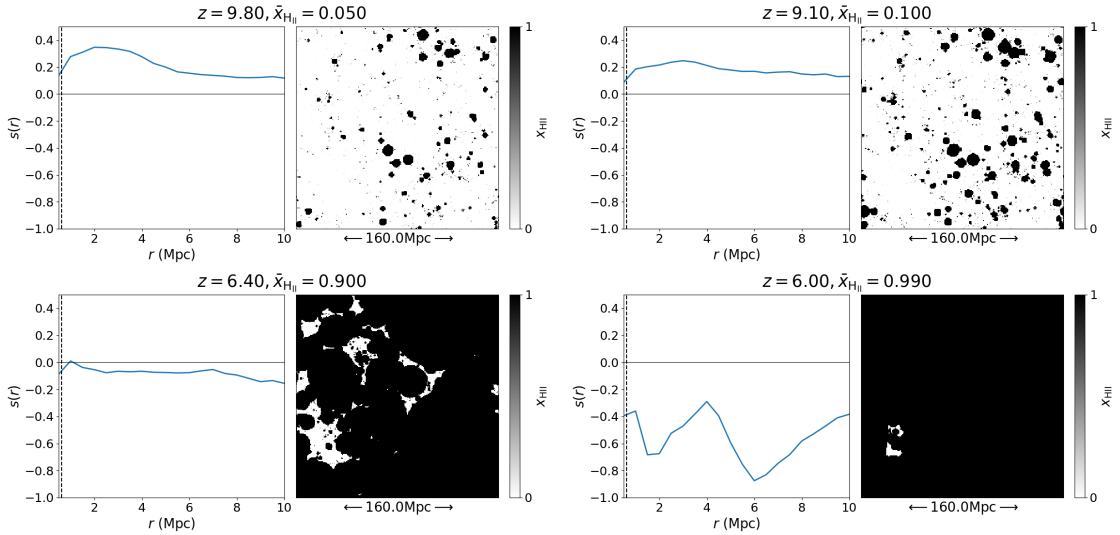

Figure 3.19: Triangle correlations for individual 2D slices of the `rsage const` simulation at various redshifts.

regions rather than a few large ones is related to the value of the M_{turn} parameter used, 10^8 $M_\odot$. Now let's turn to the `rsage const` simulation: Fig. 3.19 shows the TCF of individual slices taken at $x_{\mathrm{H\,II}} = 0.05$, 0.10, 0.90 and 0.99. Here, the high-redshift signal is still low because of the variety of ionised region sizes, but there is a visible preferred scale at $x_{\mathrm{H\,II}} = 5\%$, around $r \sim 3$ Mpc. It could also be interesting to look at simulations where reionisation is led by Active Galactic Nuclei (AGN): ionising sources are more scarce and have a better ionising efficiency, leading to a topology more similar to the toy models used above.

Later on, when the global ionisation fraction reaches values between 25% and 75%, negative signal coming from neutral regions overlaps with the positive signal from ionised regions. The TCF of our 21CMFAST simulation flattens, and cannot give information about the morphology of the field anymore. However, measuring a flat signal from actual data could be interpreted as the reionisation process being in its middle stages. For `rsage`, the signal is still mostly flat for $x_{\mathrm{H\,II}} = 0.90$, but slightly negative because the field is now mostly neutral. For $z > 7$, most of the 21CMFAST simulation is ionised and only a few remote neutral islands remain. We see on Fig. 3.17 that the sizes of these neutral islands are efficiently picked up by the TCF. For $z = 6.2$, there is a very clear negative peak at scales $r = 7.7$ Mpc which correspond to a radius size of $R = 9.2$ Mpc, once rescaled by $\sqrt{3}/2$, corresponding to the size of the neutral zone when we estimate it by eye. For $z = 6.4$, we see two clear peaks in the signal, corresponding to the two sizes of ionised regions seen in the corresponding real space field. Indeed, when we artificially cover one of the two neutral zones, and compute the TCF of the modified field, we find that the corresponding peak disappears. The first peak is spread over scales $4.6 < r < 7.8$ Mpc i.e. $5.5 < R < 9.3$ Mpc, while the second one is more narrow, centred around 20.2 Mpc. For comparison, we empirically find that we can sieve the two larger neutral islands in the field

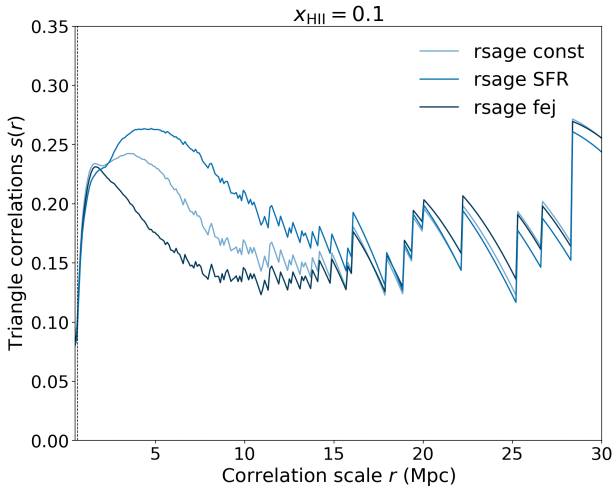

Figure 3.20: Triangle correlations averaged over 60 slices cut through the three `rsage` simulations at $x_{\rm H\,II} = 0.10$. Figure never published.

with disks of radius ~ 23 px ~ 18 Mpc; whereas the smaller ones can fit in disks whose radii range from 7 Mpc to 12 Mpc. We observe a similar behaviour in the TCF of `rsage const` at $x_{\rm H\,II} = 99\%$. However, because of the lower resolution of the simulation, the neutral islands are square-shaped and the TCF signal is noisy. This motivates a further study of how well the TCF performs compared to common BSD algorithms, presented in Gorce & Pritchard (2019).

We saw on Fig. 3.1 that the three `rsage` simulations have a very distinct morphology, with spherical ionised regions, more or less large depending on the model of $f_{\rm esc}$ used. If our previous interpretation of the TCF as a bubble size algorithm is right, these differences should be traceable with the TCF. We therefore compute the triangle correlations of 60 random slices cut through the three `rsage` simulations at $x_{\rm H\,II} = 0.10$ and show on Fig. 3.20 the mean signal for each simulation. The signal is very noisy on scales larger than 15 Mpc and identical for the three simulations, confirming that it is a numerical effect due to box size and resolution. Conversely, on correlation scales smaller than 15 Mpc, the three simulations give very different signals: `rsage SFR`, which has the largest bubbles on average, has a TCF which bumps at the largest scales ($r \sim 5$ Mpc). Then comes `rsage const` and finally `rsage fej`, similarly to what was found in the previous two sections. Interestingly, all three signals exhibit a bump in amplitude around $r \sim 1.5$ Mpc, which we interpret as the size of newly formed ionised regions. These results are given without error bars for clarity. Indeed, including the variance between the signal measured in the 60 different slices, the TCF of the three simulations overlap. That is because the box is too small and the sample variance too large. This result is a proof-of-concept, but a confirmation using a larger simulation would be useful.

In this section, we have seen that non-Gaussian information is essential to understand the reionisation process in its entirety, and in particular its morphology. Third-order

statistics, such as the 21cm bispectrum and the triangle correlation function, are an efficient tool to extract this type of information from data as they are computed directly from observed visibilities, in Fourier space. As we will explain in Sec. 4.1, because it is based on closed triangles made of the phases of the signal, the TCF in particular will benefit from reduced observational errors due to the closure phase relation. This will be a clear advantage compared to usual bubble size distribution algorithms, which require good-quality real-space data. Indeed, in the very early or very late stages of EoR, the TCF can be used to infer a typical size of ionised bubbles or neutral islands. The shape and sign of its signal can also be used to follow the global reionisation process: it will be strongly positive at high redshift, flat and close to zero in the middle stages of EoR and peaking at negative values at low redshift. If it is robust to instrumental effects such as instrument noise and resolution, was we will investigate in the next chapter, it will be an ideal tool to apply to 21cm intensity maps.

***

3.4 Chapter conclusion & discussion

In this chapter, we have seen how CMB and 21cm data can be used to learn about the morphology of reionisation and, in turn, about the physical properties of early galaxies, here represented by different versions of the `rsage` and the 21CMFAST simulations. On 21cm intensity mapping data, sample variance can be used to our benefit in a tool as simple as a one-point statistic to constrain the emissivity of light sources. More complex statistical objects, designed for the study of reionisation with interferometric data, such as the triangle correlation function of phases, can tell us about the IGM global ionisation level and typical bubble sizes. However, if 21cm observations are an exciting prospect to learn about local reionisation, it is not the only one. Small-scale CMB data, and in particular the new parameterisation of the patchy kSZ signal introduced in this chapter, can tell us about the astrophysics of the early Universe. Additionally, we have shown in Chapter 2 that observations of high-redshift galaxies and quasars, supplemented by large-scale CMB data, are essential to place constraints on the IGM ionisation level.

Another promising perspective is cross-correlations of the 21cm signal with other high-redshift data sets (Furlanetto & Lidz 2007). Indeed, cross-correlations can reduce systematic uncertainties, a major issue of 21cm observations, help confirming the cosmological origin of the signal and provide an additional insight on the nature of the sources. Many works have already focused on two-point cross-correlations between the 21cm signal and galaxy surveys such as surveys of Lyman-α emitters (LAEs). LAEs being reionisation sources, they should sit in ionised regions and have negative correlations with the 21cm signal (Vrbanec et al. 2016; Sobacchi et al. 2016). Additionally, LAE surveys, which are booming in numbers, offer precise redshift measurements (Hutter et al. 2017). Others have considered cross-correlations between the kSZ and 21cm signal, which should similarly be negative (Tashiro et al. 2011). In this case, the squared kSZ field needs to be considered to avoid signal suppression due to the random direction of the electrons proper velocities around their host cluster. This issue can be overcome by looking at the next order, fore example kSZ-kSZ-21cm correlations (La Plante et al. 2020). The increased sensitivity of futuristic small-scales CMB experiments such as CMB-S4 should also give access to spatial fluctuations in the Thomson optical depth, which could in turn be cross-correlated with the 21cm signal (Dvorkin & Smith 2009).

Nevertheless, all these new methods require good-quality 21cm data, which will be difficult to obtain because of thermal noise and instrument resolution, but also because of the poorly known foregrounds hiding the cosmological signal. Additionally, sample variance, which was used to our benefit in Sec. 3.1, will add errors to any result inferred from interferometric observations because of the limited field of view of the instrument. Finally, many model uncertainties, either on the sources of reionisation or the nature of the IGM at high redshift, can impact the constraints on the process we obtained in Chapter 2.

Chapter 4

Limitations and prospects of reionisation study

There are many exciting prospects for the study of reionisation. To only name a few, improved sensitivity in CMB-S4 experiments will allow a spotless detection of the kSZ power from reionisation, giving access to crucial information about the morphology and the timeline of the process. Additionally, current 21cm global experiments are giving the first constraints on the 21cm power spectrum and future intensity mapping experiments will give direct maps of the ionisation state of the IGM throughout cosmic history. We have seen in the previous chapter that, in order to make the most out of the upcoming data, one needs to develop new and clever statistical tools, able to handle the large amount of data produced by these experiments. However, the high degree of precision of future observations means that model uncertainties, which were previously washed out by low statistics, will now be a limiting factor in our analyses. For example, we have seen that making good use of high-ℓ observations of the kSZ power spectrum to constrain EoR requires an improved modelling of its shape and amplitude. Moreover, as these experiments are pushing their resolution to an extreme point, and looking at very faint and distant objects, instrumental effects will be a major obstacle to overcome in order to use their data.

In this chapter, we focus on the observations- and then model-related limits of the methods described in previous sections. On the observations side, we focus on the problem of sample variance for 21 observations, as well as on the impact of foregrounds and instrumental effects. We show that the tools introduced in the previous chapter, such as the triangle correlation function, are robust to some of these effects and therefore are a strategical choice for future data analysis. However, more work is still required in this

direction. We finally consider model-related uncertainties, highlighting the way the value of the Thomson optical depth measured from CMB varies depending on the nature of the data used and on the prescription chosen for the reionisation history $x_e(z)$. We come back to the results of Sec. 2.3, which combined currently available data on reionisation to give a comprehensive scenario, and assess their dependence on the poorly-known parameters used to derive a history of reionisation, such as the escape fraction of ionising photons.

4.1 Observations-related limits

In this section, we are interested in how reionisation constraints can be impacted by observational biases. They can be intrinsic biases – such as sample variance or foregrounds, or instrumental biases – such as sensitivity and resolution. We will focus on such limits in the case of 21cm observations, both because they are the most anticipated EoR-related results and because they have gigantic challenges to overcome. This does not mean however that other observations are not impacted. We have seen in Sec. 2.3 that estimating the photon budget for reionisation relied heavily on measuring the density of light sources in the early Universe and, in particular, of star-forming galaxies. Too faint and too distant objects cannot yet be observed: there are only a few points in the galaxy luminosity function at $z \geq 10$ and magnitudes fainter than $M = -15$ are not visible with current telescopes. Until the new generation of telescopes, such as the James Webb telescope, comes online, extrapolations need to be made – they will be investigated in Sec. 4.2.

4.1.1 Super-sample covariance

Sample variance is the error that comes from making a cosmological measurement from a limited region of the sky. Because this region is not representative of the whole Universe – it can be over-dense or under-dense compared to the mean for example, the corresponding measurement will be over- or under-estimated. Reproducing the same measurement on a sky patch of the same size but at a different location will lead to a different value. Reproducing the measurement on a sky patch of same size and location but different depth in redshift will lead to a different value. In other words, the density fluctuations with wavelengths larger than the size of the sky patch will not be captured.

In the case of galaxy surveys, this observational bias will translate into larger error bars on cosmological parameters. Similarly, the amplitude of the 21cm power spectrum or of the global signal will be impacted, for example if the field of view of the interferometer is too narrow (Muñoz & Cyr-Racine 2020; Kaur et al. 2020). Here, I will describe super-sample covariance (SSC) in the case of galaxy surveys, because it is the subject for which this problem has been investigated in most depth and the underlying formalism is very similar to the one dedicated to 21cm observations. Additionally, as part of the Euclid summer school I attended in 2019, I have been involved in a project aiming at evaluating the impact of sample variance on cosmological parameter estimations with the Euclid satellite (Laureijs et al. 2011), which introduced me to the problem.

Hu & Kravtsov (2003) first introduced the concept of SSC for galaxy surveys and found that the associated error on σ_8 and w was generally comparable to or greater that the shot-noise. Notably, the statistical uncertainty on w is doubled in SZ surveys limited to $z \leq 1$. In this work, the authors consider a full-sky survey and focus on the bias stemming from the limited redshift depth of the survey. Indeed, because the sky is observed in redshift bins of finite width, some large-scale modes along the line-of-sight will be missed

by observations. They do not take the limited sky coverage of the survey into account as they find that the amplitude of the bias is only weakly dependent on the survey volume. However, the increased sensitivity of future surveys, such as Euclid, will lead to a shot-noise small enough for the SSC to be the main source of error on cosmological parameters. Recent works have therefore focused on finding an efficient way to compute this deeply non-linear effect (Lacasa & Grain 2019a). The Euclid group project I am part of aims at giving a precise estimate of the SSC associated to the limited size of the survey, as until now only rough approximations were used (Lacasa et al. 2018). Firstly, we have derived the analytical expression of the partial sky SSC and implemented it in an existing fast and efficient SSC estimator, `PySSC`, developed by Fabien Lacasa (Lacasa & Grain 2019b)[1]. The next paragraph outlines the derivations and first results obtained. Secondly, we will use this covariance matrix to see the impact of associated errors on cosmological parameter estimations with Euclid. Final results are to be published by the end of the year.

Take two observables O_1 and O_2, which correspond to the integral over the line-of-sight of, respectively, o_1 and o_2, such that $O_1 = \int \mathrm{d}V_1\, o_1$ for V_1 the comoving volume per steradian. We define the super-sample covariance for these observables by (Lacasa & Grain 2019a):

$$\mathrm{Cov}_{\mathrm{SSC}}\left(O_1, O_2\right) = \iint \mathrm{d}V_1 \mathrm{d}V_2 \frac{\partial o_1}{\partial \delta_b}\left(z_1\right) \frac{\partial o_2}{\partial \delta_b}\left(z_2\right) \sigma^2\left(z_1, z_2\right). \tag{4.1}$$

$\sigma^2(z_1, z_2)$ is the variance of the background density field defined as

$$\sigma^2(z_1, z_2) = \langle \delta_b(z_1) \delta_b(z_2) \rangle = \int \frac{\mathrm{d}^3\mathbf{k}}{(2\pi)^3} \tilde{W}\left(\mathbf{k}, z_1\right) \tilde{W}^*\left(\mathbf{k}, z_2\right) P_m(k|z_{12}), \tag{4.2}$$

where $\tilde{W}$ is the Fourier transform of the survey window function. Its expression will vary if we are looking at full- or partial-sky coverage. $\partial o_1 / \partial \delta_b(z_1)$ describes how O_1 varies with changes in the background density δ_b. We take O_1 (resp. O_2) to be the angular power spectrum cross-correlating two LSS tracers A and B (resp. C and D) – typically, galaxy clustering and galaxy shear. Each is measured in a redshift bin (respectively i_z, j_z, k_z and l_z) of variable width. Let $P_{AB}(k_\ell|z)$ the 3D power spectrum at $k_\ell \equiv (\ell + 1/2)/d_c(z)$. By definition, $o_{AB} = W^A_{i_z}(z) W^B_{j_z}(z) P_{AB}\left(k_\ell|z\right)$ (resp. o_{CD}), and if we assume that the derivatives $\partial o_i / \partial \delta_b$ vary slowly with redshift compared to $\sigma^2(z_1, z_2)$, we can rewrite Eq. (4.1) for the two power spectra as

$$\begin{aligned} \mathrm{Cov}_{\mathrm{SSC}}(P_{AB}, P_{CD}) \simeq & \frac{\partial P_{AB}}{\partial \delta_b}\left(z_1\right) \frac{\partial P_{CD}}{\partial \delta_b}\left(z_2\right) \times \\ & \iint \mathrm{d}V_1\, \mathrm{d}V_2\; W^A_{i_z}(z_1) W^B_{j_z}(z_1) W^C_{k_z}(z_2) W^D_{l_z}(z_2)\, \sigma^2\left(z_1, z_2\right), \end{aligned} \tag{4.3}$$

where $W^A_{i_z}(z)$ is the window function of observable A corresponding to redshift bin i_z. It

[1] Available at `https://github.com/fabienlacasa/PySSC`. The `partialsky` branch gathers the results of this project.

is non-zero over the width of the redshift bin, and has unit [probe unit] $\cdot$ sr/(Mpc/h). We have

$$\frac{\partial P_{AB}}{\partial \delta_b}(z) = \frac{\int \mathrm{d}V\ W_{i_z}^A(z) W_{j_z}^B(z)\, \partial P_{AB}/\partial\delta_b\,(k_\ell|z)}{I^{AB}(i_z, j_z)} \tag{4.4}$$

where $I^{AB}(i_z, j_z) \equiv \int \mathrm{d}V\ W_{i_z}^A(z) W_{j_z}^B(z)$. Let R_ℓ^{AB} the effective relative response of the considered power spectrum:

$$\frac{\partial P_{AB}}{\partial \delta_b}(k) \equiv R^{AB}(k)\, P_{AB}(k). \tag{4.5}$$

For the matter power spectrum, R is constant with redshift and can be computed from perturbation theory or estimated from simulations (Lacasa & Grain 2019a). Then

$$\begin{aligned}\frac{\partial P_{AB}}{\partial \delta_b}(z) \times I^{AB}(i_z, j_z) &= \int \mathrm{d}V\ W_{i_z}^A(z) W_{j_z}^B(z)\, \partial P_{AB}/\partial\delta_b\,(k_\ell|z) \\ &= \int \mathrm{d}V\ W_{i_z}^A(z) W_{j_z}^B(z)\, R^{AB}(k_\ell)\, P_{AB}(k_\ell, z) \\ &\equiv R_\ell^{AB}\, C_\ell^{AB}(i_z, j_z)\end{aligned}$$

where in the last step we used the Limber approximation, wich gives

$$C_\ell^{AB}(i_z, j_z) = \int \mathrm{d}V\ W_{i_z}^A(z) W_{j_z}^B(z) P_{AB}(k_\ell|z)\,. \tag{4.6}$$

Finally, we define the matrix $S_{i_z,j_z;k_z,l_z}^{A,B;C,D}$ which is the dimensionless volume-averaged (co)variance of the background matter density contrast by

$$S_{i_z,j_z;k_z,l_z}^{A,B;C,D} \equiv \int \mathrm{d}V_1 \mathrm{d}V_2\ \frac{W_{i_z}^A(z_1)\, W_{j_z}^B(z_1)}{I^{AB}(i_z, j_z)} \frac{W_{k_z}^C(z_2)\, W_{l_z}^D(z_2)}{I^{CD}(k_z, l_z)} \sigma^2(z_1, z_2) \tag{4.7}$$

and the covariance simply rewrites

$$\begin{aligned}&\mathrm{Cov}_{\mathrm{SSC}}\left(C_\ell^{AB}(i_z, j_z), C_{\ell'}^{CD}(k_z, l_z)\right) \approx \\ &\qquad R_\ell^{AB} C_\ell^{AB}(i_z, j_z) \times R_{\ell'}^{CD} C_{\ell'}^{CD}(k_z, l_z) \times S_{i_z,j_z;k_z,l_z}^{A,B;C,D}.\end{aligned} \tag{4.8}$$

Full sky coverage In the case of full sky coverage, the variance of the background density field is simply (Lacasa & Rosenfeld 2016):

$$\sigma^2(z_1, z_2) = \frac{1}{2\pi^2} \int k^2 \mathrm{d}k\ P_m(k|z_{12})\, j_0(kr_1)\, j_0(kr_2), \tag{4.9}$$

where r_i is the comoving distance to redshift z_i and j_0 the spherical Bessel function. Given that the angular matter power spectrum can be written as

$$C_\ell^m(z_1, z_2) = \frac{2}{\pi} \int k^2 \mathrm{d}k\ P_m(k|z_{12})\, j_\ell(kr_1)\, j_\ell(kr_2), \tag{4.10}$$

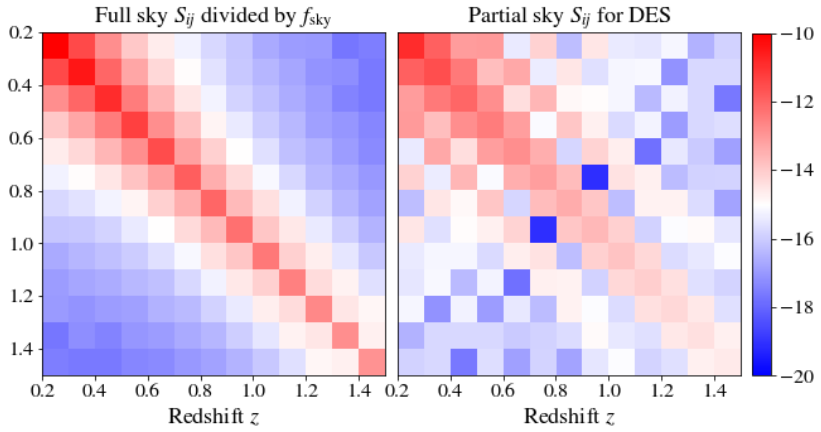

Figure 4.1: S_{ij} matrices for DES and top-hat redshift bins. *Left panel:* Result for a full-sky coverage, rescaled by f_{SKY}. *Right panel:* Results for a partial-sky coverage with the correct survey mask.

we can write σ^2 as its monopole

$$\sigma^2 = \frac{1}{4\pi} C^m_{\ell=0}(z_1, z_2). \tag{4.11}$$

By injecting this expression in Eq. (4.7), we have

$$S^{A,B;C,D}_{i_z,j_z;k_z,l_z} = \frac{1}{4\pi} C_{\ell=0}(X, Y), \tag{4.12}$$

where

$$X(\hat{n}) = \frac{\int \mathrm{d}V \; W^A_{i_z}(z) W^B_{j_z}(z) \; \delta_m(r\hat{n})}{\int \mathrm{d}V \; W^A_{i_z}(z) W^B_{j_z}(z)} \tag{4.13}$$

so that

$$\begin{aligned} C_{\ell=0}(X, Y) = \int \mathrm{d}V_1 \mathrm{d}V_2 \, k^2 \mathrm{d}k \; & \frac{W^A_{i_z}(z_1) W^B_{j_z}(z_1)}{\int W^A_{i_z}(z_1) W^B_{j_z}(z_1)} \frac{W^C_{k_z}(z_2) W^D_{l_z}(z_2)}{\int W^C_{k_z}(z_2) W^D_{l_z}(z_2)} \\ & \times P^m(k|z_1, z_2) \; j_0(kr_1) j_0(kr_2). \end{aligned} \tag{4.14}$$

Here, $\hat{n}$ is a unit vector describing the position on the sky plane. An example of such a matrix is shown on the left panel of Fig. 4.1. The survey considered here is the Dark Energy Survey (DES, The Dark Energy Survey Collaboration 2005), for top-hat redshift bins spanning the range $0.1 \leq z \leq 1.5$ with width 0.1. We only show correlations between auto-spectra ($A = B$, S_{ij}), compared to the general case of the S_{ijkl} matrix defined above. Lacasa & Grain (2019b) find that, for Euclid specifications, when looking at photometric galaxy clustering in a redshift bin $0.9 < z < 1.0$, all cosmological constraints are heavily impacted by the SSC, σ_8, n_S and w in particular, adding a 5% bias to their estimated value. Barreira et al. (2018) find similar results for weak lensing.

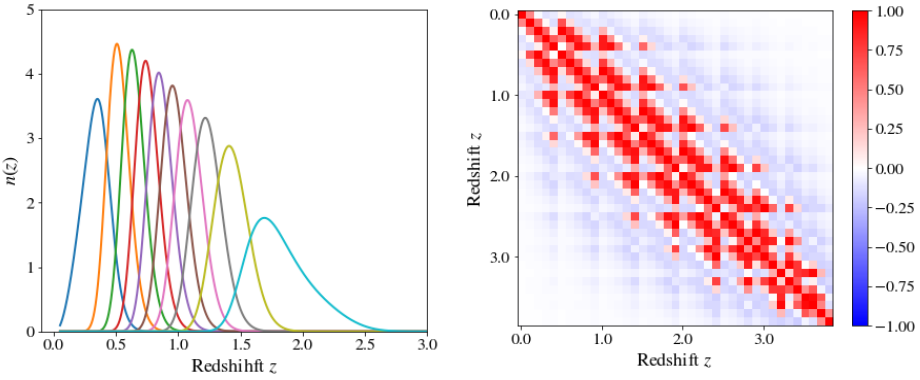

Figure 4.2: *Left panel:* Photometric redshift bins for Euclid specifications. *Right panel:* Correlation matrix corresponding to the super sample covariance for the Euclid survey mask.

Partial sky coverage In previous works, the impact of partial sky coverage on the SSC was estimated by rescaling the full-sky covariance by a factor f_{SKY}^{-1}, where $f_{SKY} \equiv \Omega_S/4\pi$ is the fraction of the sky covered by the survey and Ω_S its solid angle. In Fig. 4.1, we compare the S_{ij} matrices obtained when considering a full-sky coverage rescaled by f_{SKY} and when accurately estimating the partial sky SSC using the survey mask, in the case of DES. Despite the fact that in both matrices, auto-correlations between redshift bins (along the diagonal) dominate, the structure is very different. Averaged over all the bins, the relative difference between the two matrices is about 6% and culminates on the diagonal, where it reaches 10%. The corners, corresponding to correlations between the highest and lowest redshifts, present a difference of about 12%. Dividing the full-sky SSC by f_{SKY} will therefore lead to underestimating cross-bins correlations.

Consider a survey with partial sky coverage. Its mask is represented by a window function $\mathcal{M}$, which has zero value outside the survey and is independent of redshift. It is split into a radial and an angular part, such that $\mathcal{M}(\mathbf{x}) = \mathcal{M}_r(z)\,\mathcal{M}(\hat{\mathbf{n}})$. The covariance of the background mode is (Lacasa et al. 2018):

$$\sigma^2\,(z_1, z_2) = \frac{1}{\Omega_{\rm S}^2} \sum_\ell (2\ell+1)\, C_\ell(\mathcal{M})\, C_\ell^{\rm m}\,(z_1, z_2)\,,$$

where $C_\ell^{\rm m}$ is the matter angular power spectrum and $\Omega_{\rm S} = 4\pi f_{\rm SKY}$ the survey solid angle. As for the full-sky case, we can see the S_{ijkl} matrix as a C_ℓ of a non-physical field X, which kernel is the product of the window functions $W^A W^B$. This time, however, multipoles larger than 0 will contribute to the SSC:

$$S^{A,B,C,D}_{i_z,j_z,k_z,l_z} = \frac{1}{\Omega_S^2} \sum_\ell (2\ell+1) C_\ell(X,Y) C_\ell(\mathcal{M}). \tag{4.15}$$

When considering the full-sky limit of Eq. (4.15) ($f_{SKY} \to 1$ and $C_{\ell>0}(\mathcal{M}) = 0$), we retrieve the full-sky matrix given in Eq. (4.12).

We compute the partial sky SSC for the Euclid mask, and the redshift bins corresponding to its photometric instruments. Results are shown on Fig. 4.2, in terms of the

correlation matrix $C_{ij} = S_{ij}/\sqrt{S_{ii}S_{jj}}$. It is interesting to see that correlations exist between the different redshifts bins, and that the structure of the correlation matrix is very different from the one obtained for the full-sky SSC. Despite Euclid's mask covering a large fraction of the sky (about 50%), going from full-sky to partial-sky SSC increases the associated errors on w, Ω_m and σ_8 by 20% to 115%, depending on the tracer used (weak lensing or galaxy clustering). At this level, the SSC bias is comparable to the shot-noise.

In Sec. 3.1, we have made use of the sample variance to learn about the physics underlying reionisation. We have looked at deliberately small simulation sizes and found that, for statistically larger ionised bubbles during reionisation, corresponding to more ionising-efficient sources, the variance in the filling fractions measured in 2D slices throughout a 3D box was larger. However, this variance can be an issue when trying to estimate parameters such as the global IGM ionised fraction from a limited field of view. Using very large simulations (of side length $L = 1.8$ Gpc), Muñoz & Cyr-Racine (2020) show that the global signal measured from 2D slices $T_{21}^{\rm obs}(z)$ fluctuates at the percent level around the true value $\bar{T}_{21}(z)$, averaged over the entire 3D simulation. Since, in practice, only one of these slices will be available at a given frequency, the SSC will bias measurements of the global signal. The authors derive a theoretical sample variance, similar to the one defined in Eq. (4.2), and given by

$$\sigma_{21}^2(z) = \langle |T_{21}^{\rm obs}(z)|^2 \rangle - \bar{T}_{21}(z)^2 = \int \frac{{\rm d}^3\boldsymbol{k}}{(2\pi)^3}\, P_{21}(k,z)\, W_z^2(\boldsymbol{k}), \tag{4.16}$$

where P_{21} is the power spectrum of the 21cm brightness temperature fluctuations $\delta T_{\rm b}$. This variance is similar to the $\sigma_{\rm loc}$, defined empirically and introduced in Sec. 3.1, but additionally accounts for the error due to the depth of observations. Muñoz & Cyr-Racine (2020) choose to focus on this latter contribution and find that, in an extreme case designed to reproduce the amplitude of the EDGES signal (Bowman et al. 2018), σ_{21} can exceed the thermal noise. For fiducial models, the SSC-related error is $\sigma_{21}(z = 16.8) = 0.03$ mK – about 10 times below the thermal noise. This error on the 21cm global temperature propagates to parameter estimations to the same level of precision. Looking at correlations between different redshift bins, they find that the sample variance-induced error is halved for a distance of 60 Mpc between bins, hinting that observations should be limited to lightcones of similar depth. When considering the impact of the limited field of view, scaled to their simulation side length, the variance increases ten-fold to $\sigma_{21}(z = 16.3) = 0.6$ mK, in agreement with our previous results. Such an error is much more concerning for the precision of measurements. This could be an issue for experiments such as LOFAR, which has a field of view of $5\times5\,{\rm deg}^2$, corresponding to about 900 Mpc at $z = 16.3$ and SKA, which field of view of 327 arcmin at a nominal frequency of 110 MHz corresponds to $L \sim 1$ Gpc, both smaller than the simulation used in Muñoz & Cyr-Racine (2020). When looking at lower redshifts, corresponding to the core of the reionisation process, the sample variance will be even larger and must therefore not be ignored (Gorce et al. in prep). However,

we expect this result to be largely dependent on the cell resolution of the simulation considered. Therefore we generate a 21CMFAST simulation box for $M_{\rm turn} = 10^9\ M_\odot$, side length $L = 480$ Mpc and cell size $\Delta x = 0.625$ Mpc, closer to the specifications of SKA-*Low*. At a nominal frequency of 110 MHz, the telescope is indeed expected to have an angular resolution of 11 arcsec, i.e. between 0.45 and 0.55 Mpc on the redshift range $5 \leq z \leq 13$. We divide this initial large simulation into subcubes of decreasing size, until $L = 15$ Mpc. We compute the local variance obtained from the ionisation and 21cm brightness temperature fields of all the subcubes and compare their values. The maximum signal is reached for the smallest box size, and reaches values as high as ~ 6 mK. The maximum amplitude, taken at $x_e = 0.60$, decreases drastically with box size. In the case of 21cm fluctuations, the decrease follows

$$\sigma_{\mathrm{loc},\delta T_\mathrm{b}} \sim 1.3 \text{ mK} \times \left(\frac{L}{100 \text{ Mpc}}\right)^{-0.8}. \tag{4.17}$$

The field of view of SKA-*Low* corresponds to $L = 760, 840, 900, 940$ and 970 Mpc at, respectively, $z = 5, 7, 9, 11$ and 13. For $z = 7$, this gives ~ 0.24 mK.

From an empirical point of view, looking at 21CMFAST boxes of increasing size, Kaur et al. (2020) find that box sizes of at least 200 Mpc are necessary to estimate the power spectrum of 21cm fluctuations during the EoR without bias, after including thermal noise for 1000 hours of observations with SKA-*Low* and removing foregrounds. At earlier times, however, corresponding to the Cosmic Dawn and in which the redshift $z = 16.8$ considered by Muñoz & Cyr-Racine (2020) lies, simulations of up to $L = 300$ Mpc underestimate the power on large scales by $\sim 8\%$ on average. It therefore seems that the power spectrum is less sensitive to sample variance than the global signal. In general, to be conservative, box sizes not smaller than 1 Gpc, or corresponding fields of view, should be used to reach sufficient precision on both estimators.

4.1.2 Impact of foregrounds and instrumental effects on 21cm observations

The 21cm signal is a forbidden transition of the neutral hydrogen atom, however significant on cosmological scales because of the abundance of hydrogen in the Universe. At low redshift, it is mostly visible inside galaxies. At higher redshift, it can help trace the Epoch of Reionisation, as the IGM transitions from mostly neutral to ionised. However, because of the distance, the signal observed today from EoR is very faint, of the order of a few tens of mK. Instrumental effects, such as thermal noise, will greatly temper with this signal. The distance also means that many objects standing between the neutral atoms emitting 21cm radiation and us will interfere with our detection of the signal. These foregrounds, expected to have a brightness temperature of a few K, are made of several components which we will outline below. A detailed review of such foregrounds is beyond the scope of this work, but we refer the interested reader to Jelić et al. (2008) and Chapman & Jelić (2019) for more details.

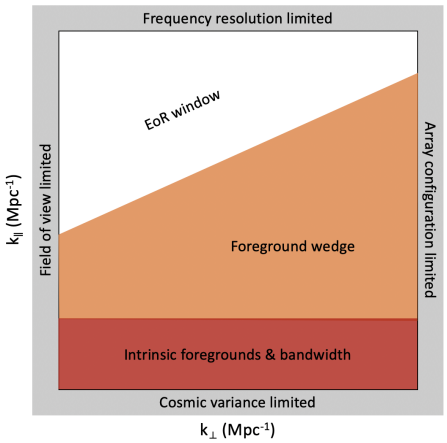

Figure 4.3: Illustration of the foreground wedge in the $(k_\perp, k_\parallel)$ plane.

Foregrounds

Emissions within the Milky Way are expected to be the main contributor to foregrounds. Galactic synchrotron emission, which arises from the interaction between relativistic free electrons from the interstellar medium (ISM) and the Galactic magnetic field, has the most significant contribution. It is expected to have a smooth dependence with frequency, determined empirically using galactic radio surveys (Jelić et al. 2008). Another 1% of the total foregrounds will stem from the bremsstrahlung due to the scattering of ions off each other inside the Milky Way. The resulting emission spectrum, corresponding to thermal emission from an optically thin region, is well modelled by a spectral index of 2.1 (Westerhout 1958; Bennett et al. 1992). Another contribution comes from synchrotron emission of supernovae remnants (Alfvén & Herlofson 1950). Despite their large amplitude, the problem posed by galactic foregrounds can be overcome by carefully choosing the area of the sky targeted by the interferometer, for example, outside the galactic plane. As these foregrounds smooth spectral dependency is well understood, in contrast to the 21cm signal from reionisation, their spectrum will be easy to subtract. Extragalactic foregrounds represent the remaining 27% of the total foregrounds and are more difficult to model (Jelić et al. 2008). They include radio galaxies, observed as very bright point sources in the sky (Fanaroff & Riley 1974) and emission from the intercluster medium of galaxy clusters, expected to be high at the low frequencies considered for EoR because of a steep spectrum (Feretti 2005; Feretti et al. 2012).

Different methods can be used to remove or at least reduce the contribution of these foregrounds to the observed signal. The first one, called 'foreground avoidance', relies on the fact that the combination of the spectrally smooth structure of the foregrounds and of chromaticity leads to the foregrounds mostly contaminating a wedge-like region of the cylindrical $(k_\perp, k_\parallel)$ plane. This is the plane formed by wave-vectors perpendicular and parallel to the line of sight, respectively. This structure is illustrated on Fig. 4.3. At low $k_\perp$, errors increase because of the limited field-of-view of the instrument, while frequency

resolution limits the sensitivity at large $k_{\parallel}$. Cosmic variance limits access to the smallest $k_{\parallel}$ modes, as well as the limited bandwidth and foregrounds. Moving towards higher $k_{\perp}$, the foregrounds leak out to higher $k_{\parallel}$ in a wedge-like shape. The rest of the Fourier plane allows a clean measurement of the 21cm signal in what is called the 'EoR window' (Datta et al. 2010; Liu et al. 2014). This method is currently used by experiments such as HERA. It has the advantage of not requiring an advanced modelling of foregrounds, but as our knowledge of foregrounds improves, more and more are included to models, leading the EoR window to shrink and significantly limiting the modes that can be used.

The second technique used falls under the name of 'foreground removal' techniques. Parametric methods rely on the smooth frequency dependence of foregrounds compared to the cosmological signal and look to fit spectra indices to data (Jelić et al. 2008). However, as the cosmological signal is very weak relative to the contamination of foregrounds, polynomials of a too high order are likely to over-fit the data and suppress the residual signal. Conversely, if the order of the polynomial is too low, foregrounds will contaminate the residual signal. Non-parametric methods can avoid this caveat, with the added advantage that they make no assumption on the shape of the foregrounds signal as they allow the data to dictate their functional form. Examples of such methods include FastICA (Chapman et al. 2012) and GMCA (Chapman et al. 2013), the latter being used by LOFAR to recover upper limits on the 21cm power spectrum (Patil et al. 2017). The collaboration has now switched to another method, called GPR for Gaussian process regression, and based on Bayesian optimisation. It was used in their latest results, giving $\Delta^2_{21} < (73)^2$ mK^2 (2σ) at $k = 0.075\ h\text{cMpc}^{-1}$ (Mertens et al. 2020). One of the lowest upper limits on the cylindrical 21cm power spectrum so far is given by Trott et al. (2020), finding 1.8×10^3 mK^2 (2σ) at $k = 0.14\ h\text{Mpc}^{-1}$ and $z = 6.5$ with 110 hours of MWA data. In this work, the authors use CHIPS (the Cosmological HI Power Spectrum estimator, Trott et al. 2016). CHIPS uses realistic instrumental and foreground models to form an optimal estimator of the power spectrum, weighting the data in order to maximise the likelihood of unbiased signal.

If these methods have been tested and approved when applied to the 21cm power spectrum, their impact on the non-Gaussianity of the signal is still discussed. Some works have looked at recovering maps of the ionisation field after removing foregrounds, confirming that we should be able to recover the phases of the signal, especially with the GMCA algorithm (Chapman et al. 2013). However, the recent works of Watkinson et al. (2020) show that on large scales, EoR structures are completely swamped by those of the foregrounds, preventing us from applying foreground avoidance techniques to recover the 21cm bispectrum but giving reasonably good results with non-parametric techniques. Instrumental errors, on the other hand, are found to largely corrupt the observed bispectrum, questioning its potential use for parameter estimation. In the following paragraph, we assume that foregrounds have been efficiently removed from the signal, and look at the impact of effects such as thermal noise and resolution on non-Gaussian estimators.

Instrumental effects

Consider 2D ionisation maps similar to the ones studied in Sec. 3.3, but with added beam smoothing and noise corresponding to observations by the core of SKA1-*Low*, its central area (with larger baselines), and by LOFAR. We want to know if it is still possible to recover the triangle correlations signal, presented in Sec. 3.3. We pick three simulated fields: the first is a toy model made of 70 bubbles of radius $R = 10$ px, assumed to correspond to a redshift $z = 9$. The two others are extracted from the 21CMFAST runs considered in Sec. 3.3 at redshifts $z = 6.2$ and 6.4, where the triangle correlation function (TCF) signal gave a good estimation of the sizes of neutral islands. The clean maps are shown, in this order, on the left panels of Fig. 4.4. We convert each one of them into a brightness temperature map according to Eq. (1.18) with Planck 2016 cosmology (Planck Collaboration et al. 2016b).

The resolution of 21-cm tomographic data will be first limited by the angular resolution of the interferometer considered. The full width at half maximum (FWHM) of the point source function of an interferometer is given by (in radians)

$$\theta = 1.22 \times \frac{\lambda}{b_{\max}}, \tag{4.18}$$

where $\lambda = 21\text{cm} \times (1 + z)$ is the redshifted 21cm wavelength and $b_{\max}$ is the maximum baseline of the interferometer. For LOFAR, SKA1-*Low* core and SKA1-*Low* central respectively, we take $b_{\max} = 3.5$, 1.0 and 3.4 km. We convolve the clean δT_b maps with a Gaussian kernel of FWHM $\theta\, d_{\rm c}(z)$ for $d_{\rm c}(z)$ the comoving distance at the redshift (i.e. frequency) considered. The resulting images for SKA central are shown in the second column of Fig. 4.4. Because they have similar maximum baselines, the angular resolution of SKA central is close to the one of LOFAR. For SKA core, much smaller baselines lead to the smoothing blurring the shape of the ionised bubbles to an extreme point, and our method will perform poorly. Finally, realistic thermal noise is simulated with the OSKAR[2] software, courtesy of Emma Chapman. This noise is added to our three fields, and results for SKA core, SKA central are LOFAR are shown, respectively, in the last three columns on the figure. We choose 1000 hours of integration time, but recent works have shown that as few as 324 hours of observations with SKA can be sufficient to differentiate between different reionisation models (Binnie & Pritchard 2019). Note that these results have been previously published in Gorce & Pritchard (2019).

The lower panels of Fig. 4.4 present the signal resulting from computing the TCF of each of the fields, with different levels of instrumental effects considered. The error bars correspond to the variance of the TCF computed for a Gaussian random field of same dimensions. The first column, corresponding to triangle correlations for a clean field, gives the reference signal in which we identify the reference peaking scale, shown as a dotted blue line on each plot[3]. It will later be compared to the scale picked up on corrupted data. As

[2] `https://github.com/OxfordSKA/OSKAR`

[3] For the $z = 6.4$ 21CMFAST field (lower row), there are two scales picked up. The larger one is well

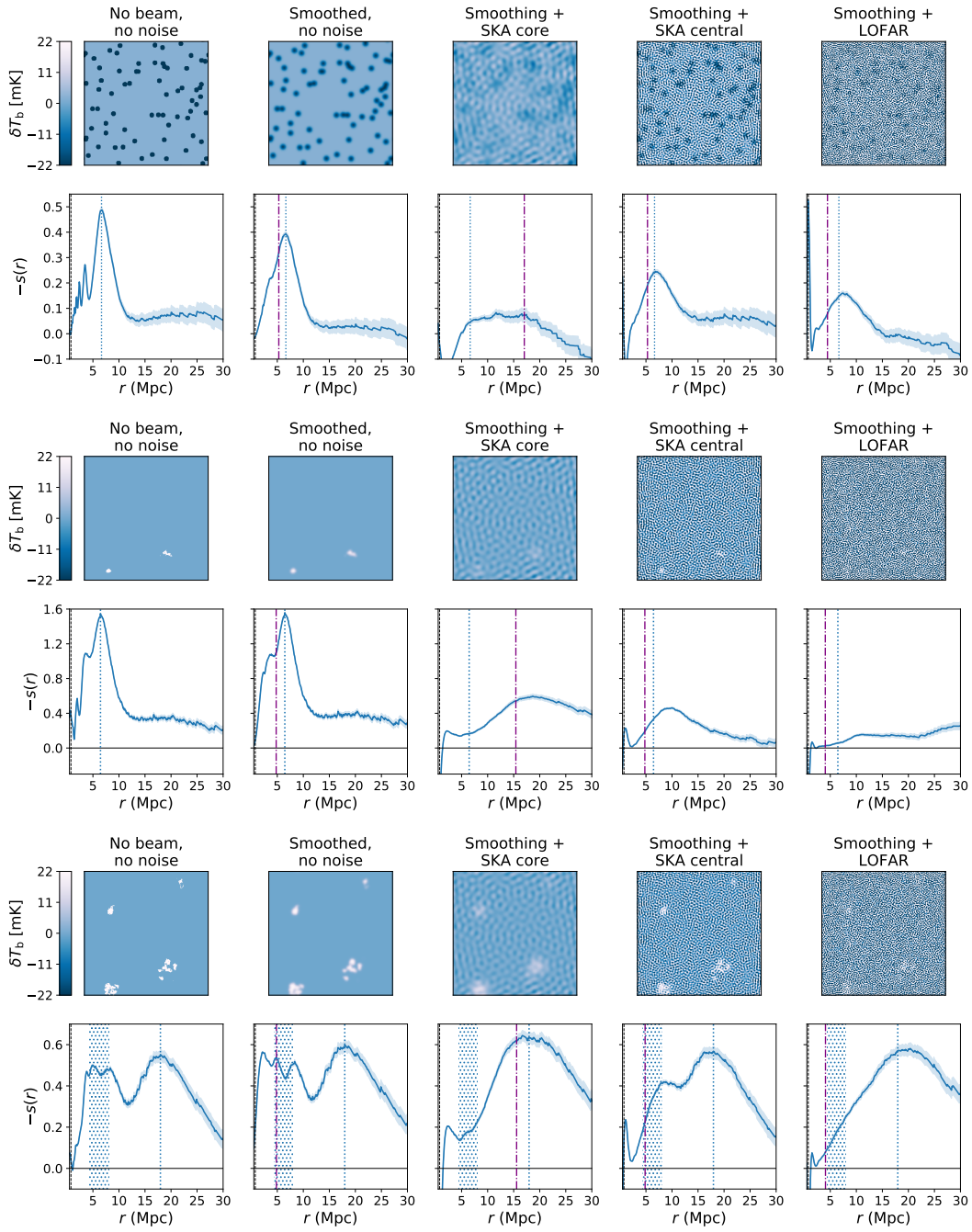

Figure 4.4: Comparison of phase correlations for a 2D brightness temperature map with dimensions $N = 512$, $L = 400$ Mpc for different types of thermal noise. From left to right: the clean signal, the field smoothed by a Gaussian beam corresponding to the angular resolution of SKA central, and the clean field with added smoothing and noise from, respectively, SKA1-*Low* core, SKA1-*Low* central and LOFAR. The dotted blue lines (regions) indicate the peaking scale found on the clean field (left panel) and the purple dash-dotted lines the smoothing scale of the corresponding experiment. From top to bottom: toy model, 21CMFAST simulation at $z = 6.2$ and $z = 6.4$. Error bars correspond to the variance estimated from a Gaussian random field of same dimensions.

Table 4.1: Peaking scales (Mpc) for a toy model with different types of observational effects: smoothing due to angular resolution and noise.

	True radius	Clean signal	Smoothed signal	Smoothing + noise	Smoothing scale
LOFAR	7.8	6.7	6.6	7.4	4.5
SKA1-*Low* core	7.8	6.7	8.2	–	17.0
SKA1-*Low* central	7.8	6.7	6.7	6.9	5.3

can be seen on the images, the beam smoothing introduces a pattern that could be picked up by the TCF, we therefore show as dash-dotted lines on each plot the smoothing scale of the corresponding experiment. Values for the toy model are given in Table 4.1. The TCF obtained on the field corresponding to SKA core observations is almost flat because of the low angular resolution that blurs the ionised regions edges. It actually seems to peak at the smoothing scale. On the other hand, instrumental effects from SKA central and LOFAR applied to the toy model still allow the TCF to exhibit a clear peak at a scale close to the one found with clean signal (see Table 4.1 for details): we can recover the bubble size with a 1 Mpc precision. Naturally, increasing the integration time improves results further. For 21CMFAST maps, the LOFAR sensitivity is not sufficient to recover the TCF signal: at $z = 6.2$ the signal is mostly flat, and although there is a clear peak for the $z = 6.4$ map, it cannot resolve the two characteristic scales. SKA central gives better results, with the two peaks visible. Applying the same tests to 21CMFAST boxes at higher redshifts, we find that, because there is no clear characteristic scale in the field (see Sec. 3.3), the TCF peaks at the smoothing scale corresponding to the telescope considered. The sign of the signal, which traces the advancement of the reionisation process, is however well recovered.

Instrument calibration

Precise radio observations suffer from requiring a good instrumental calibration to separate the 21cm signal from foregrounds. This is one of the main challenges of upcoming experiments. Using the TCF can however allow to overcome this issue, because it is based on the phases of the measured visibilities[4]. Consider the visibility V_{ij}^{m} measured between two antennae i and j at a given frequency ν. It will have contributions from the cosmological signal V_{ij}^{true}, but also from the amplitude and phase errors of each antenna, modelled by a complex gain $G_i = |G_i|\,\mathrm{e}^{i\phi_i}$, such that:

$$V_{ij}^{\mathrm{m}} = G_i G_j^{*}\, V_{ij}^{\mathrm{true}} = |G_i G_j|\,\mathrm{e}^{i(\phi_i - \phi_j)}\, V_{ij}^{\mathrm{true}}, \tag{4.19}$$

where $*$ denotes a complex conjugate. The amplitude of this gain stems from beam specific effects such as mirror reflectivity, detector sensitivity or local scintillation whereas the phase term can originate either from telescope errors or from external effects such as

defined, but we use an interval 6.2 ± 1.6 Mpc for the smaller one.

[4]We have seen in Sec. 1.3 that, in the flat-sky approximation, the visibilities are a direct image of the Fourier transform of the sky patch observed.

atmospheric turbulence (Levrier et al. 2006; Monnier 2007). If we combine the signal from three antennae forming a closed triangle to form a bispectrum, we avoid this phase error and we will be left only with the phases of the true signal. Indeed, consider now three baselines ij, jk and ki observing at ν, the bispectrum of their complex visibilities is

$$\begin{aligned}\mathcal{B}_{ijk} &= V_{ij}^{\mathrm{m}}\, V_{jk}^{\mathrm{m}}\, V_{ki}^{\mathrm{m}} \\ &= |G_i G_j G_k|^2\ \mathrm{e}^{i(\phi_i-\phi_j)}\, \mathrm{e}^{i(\phi_j-\phi_k)}\, \mathrm{e}^{i(\phi_k-\phi_i)}\ V_{ij}^{\mathrm{true}}\, V_{jk}^{\mathrm{true}}\, V_{ki}^{\mathrm{true}} \\ &= |G_i G_j G_k|^2\ V_{ij}^{\mathrm{true}}\, V_{jk}^{\mathrm{true}}\, V_{ki}^{\mathrm{true}}.\end{aligned} \tag{4.20}$$

The different phase terms cancel each other out, so that the phase of the measured bispectrum is the phase of the true bispectrum. This is called the closure phase relation. In our previous results, we worked in two dimensions, so that the three vectors considering to form a triangle lie in the same plane on the sky, perpendicular to the line-of-sight, and are measured at the same frequency: the closure relation holds. This means that we will be able to apply the TCF to observational data without worrying about calibration errors. For an example of the use of bispectrum closure phases in interferometry, we refer the reader to Thyagarajan et al. (2018). In this work, the authors compare the bispectrum phase spectra – the phases of $\mathcal{B}_{ijk}$, coming from different components of a simulated signal: a single point-source, diffuse foregrounds and H I fluctuations from the EoR. They show that a quantitative relationship exists between the EoR signal strength and the whole bispectrum phase power spectra.

In practice, there are some limitations to the use of the closure relation. First, only a limited number of triangles can be constructed from the array of antennae of a telescope, therefore some information will be lost compared to simple baseline measurements. This should be easy to overcome as Monnier (2007) show that with as little as 40 antennae, we are able to recover 95% of the phase information. The 296 antennae of the SKA1-*Low* central array and the 48 antennae of LOFAR allow to recover respectively 99.3% and 95.8% of it. Additionally, keeping only the modes forming closed triangles in data analysis will worsen the sparsity of observations and discarding amplitude information will lead to higher noise levels: Readhead et al. (1988) find that the noise level of a phase-only observation will be at least twice higher than a map made from full visibility data. The authors also show that, because the bispectrum is a triple product, there will be additional noise terms compared to single baseline observations, corresponding to cross-products. Indeed, if the same signal is measured on different time intervals, the observed bispectrum will not only be the product of three complex numbers V_{ij} anymore, but of the sum of each observation on each time interval. Then the cross terms combining signals integrated on different time intervals will give incoherent phase terms that can be assimilated to noise. This extends to the spatial domain: in a redundant array there will be contributions not only from the baselines chosen to form a closed triangle, but also from identical (parallel) baselines which are not part of a triangle. This noise can however be reduced to a good signal-to-noise ratio if enough frames are used in the integration. Finally, polarisation leakage or cross coupling

of antennae, called closure errors, can lead to a departure from the closure relation (Carilli et al. 2018).

Despite these limitations, closure phases are a major advantage of the TCF compared to other solutions found in the literature to analyse the non-Gaussianity of the 21cm signal, and in particular estimate the characteristic size of ionised regions from 21cm maps. In contrast to ordinary bubble size algorithms such as granulometry (Kakiichi et al. ????), Minkowski functionals (Gleser et al. 2006; Chen et al. 2018; Bag et al. 2018), or the friend-of-friends (Iliev et al. 2007a) and spherical average (Zahn et al. 2007) algorithms which require to reconstruct real-space images, the TCF is built on Fourier data and so can make direct use of measured visibilities.

At the moment, many effects stand between us and a clean detection of the 21cm signal, both for Gaussian and non-Gaussian components. This explains why the current best constraints on the 21cm power spectrum are only upper limits: they are noise-limited. Improving our knowledge of foregrounds is essential to be left only with the cosmological signal, but a precise simulation of instrumental effects is also necessary. The observational strategies used to gather data will also be essential to tackle issues such as sparsity, corresponding to the fact that being able to measure only a discrete range of modes reduces data quality. A huge amount of work is put into answering these questions at the moment, and developing data analysis tools which take these issues in consideration, such as the TCF, is essential if one wants to be able to use them.

4.2 Model-related limits

Reionisation is a process difficult to model and simulate because of the numerous parameters and scales involved. If the process starts on atomic scale, through the simple ionisation of a neutral atom by a photon with sufficient energy, it ends up reaching cosmological scales, until the ionisation front covers the entire IGM. We have seen in Sec. 2.2 that, if only a few equations are sufficient to describe the evolution of the ionisation level of the IGM with time, they rely on many different parameters, most of them being poorly defined or constrained. We have also seen that current constraints depend on these models: from the Gunn-Peterson troughs observed in a series of $z \sim 6$ quasars, Fan et al. (2006b) were quick to conclude that the IGM had to be about 99.98% ionised at the time. However, later works have questioned these results, pointing at the existence of a proximity zone around the quasar, more ionised than the global IGM, and at the danger of generalising results obtained around a single quasar, likely sitting inside an over-dense region of the IGM, to the entire Universe (Mesinger 2010). Additionally, constraining the photon budget for reionisation by looking at Lyα forests in quasar spectra requires a detailed modelling

of the underlying physics, which is not yet achieved (Wise 2019).

In this section, we first look at the impact a rough description of the reionisation process can have on CMB results. Then, we look at more detailed model uncertainties, related to the parameters used in Sec. 2.2, such as the escape fraction of ionising photons.

4.2.1 Different data and different parameterisations in CMB analysis

For now, the way CMB data is mainly used to constrain reionisation is through the Thomson optical depth τ, which is an integrated measurement of the density of free electrons along the line-of-sight. It is considered homogeneous on the sky plane, and therefore constrained as a single parameter, in addition to the other cosmological parameters of the base Λ-CDM model such as Ω_b, Ω_c or n_S. The inferred value of τ will depend on the data used to constrain it: using the temperature and E-mode polarisation anisotropies, auto- and cross-spectra (TT, TE, EE + lowE), Planck Collaboration et al. (2018) find $\tau = 0.054 \pm 0.07$ while including BAO leads to a marginally higher value of $\tau = 0.056 \pm 0.007$. Even if these variations are small, they lead to significant changes in resulting reionisation histories, with derived parameters such as the redshift midpoint moving from $z_{\rm re} = 7.10^{+0.87}_{-0.73}$ for TT, TE, EE + lowE to $z_{\rm re} = 7.82 \pm 0.71$ when adding BAO. The baseline results are TT, TE, EE + lowE + lensing as adding the lensing information allows to break the degeneracy between the normalisation of the initial power spectrum A_S and τ (Planck Collaboration et al. 2016a). This data set gives $\tau = 0.054 \pm 0.07$ and $z_{\rm re} = 7.67 \pm 0.73$. To reduce these uncertainties, Liu et al. (2016) suggest using 21cm power spectrum measurements to infer an independent value of τ and break the degeneracy, allowing an improved precision on the other cosmological parameters, mainly A_S itself and the sum of neutrino masses.

The fact that a small difference in τ leads to a difference of a few hundred thousand years on $z_{\rm re}$ is to be related to the underlying $x_e(z)$ parameterisation used. Indeed, to compute τ, one needs to assume a reionisation history $x_e(z)$ (see Eq. 2.1). In standard Boltzmann solvers used to compute theoretical predictions in CMB data analysis such as the `CAMB` code[5] for Planck (Lewis et al. 2000; Howlett et al. 2012), the reionisation scenario used is a step-like transition, given in Eq. (2.4), where the global ionised fraction jumps from 10% to 75% over a (fixed) redshift interval of $\Delta z = 1.73$ (Planck Collaboration et al. 2016b). As the shape is fixed, the only parameter allowed to change is $z_{\rm re}$, corresponding to a shift in the reionisation history. Because τ is derived as an integral of $x_e(z)$, a small variation in its value will require a large shift in $z_{\rm re}$. However, this step-like transition, that we will refer to as the *tanh* parameterisation thereafter, does not match simulations and observations well. Instead, according to QSO and galaxy luminosity function observations, as well as to simulations, we expect the ionisation fraction to slowly rise when the first sources light up, before taking off as soon as about 20% of the IGM is ionised (Robertson et al. 2015; Gorce et al. 2018; Aubert et al. 2018). This evolution is better transcribed by

[5] Available at `https://camb.info`.

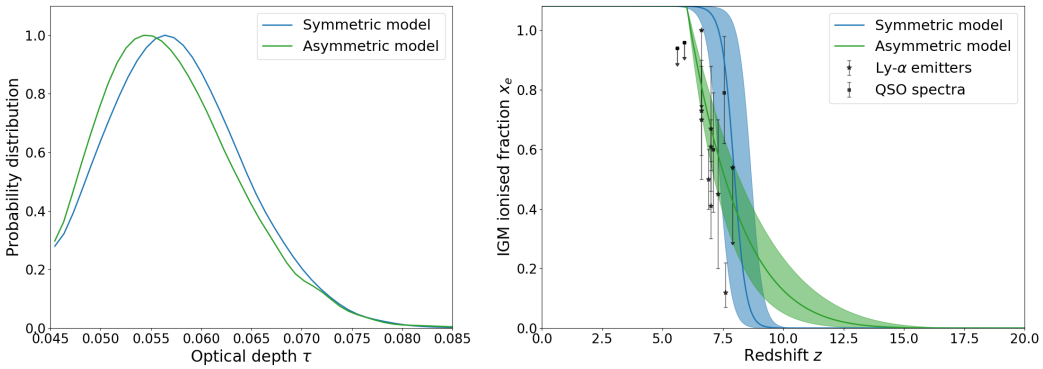

Figure 4.5: Results when fitting a symmetric (blue) and asymmetric (green) model of reionisation to CMB data (TT + TE + EE + lowE + lensing + BAO). *Left panel:* Posterior distribution for the Thomson optical depth. *Right panel:* Resulting reionisation histories.

a redshift-asymmetric parameterisation such as the power-law given in Eq. (2.5) (Douspis et al. 2015). Actually, an asymmetric reionisation history seems to also be favoured by CMB data: Miranda et al. (2017) and Heinrich & Hu (2018) actually find that Planck 2015 EE data favours an extended ionised tail at $z > 15$, incompatible with the *tanh* model. These results extend to Planck 2018 EE data, however to a weaker level (Qin et al. 2020b).

Naturally, the choice of the $x_e(z)$ parameterisation used will impact the inferred value of τ. With Planck 2018 data (Planck Collaboration et al. 2018), we modify `CAMB` to use the asymmetric parameterisation of $x_e(z)$[6] and find, using TT + TE + EE + lowE + lensing + BAO data, $\tau = 0.056 \pm 0.007$ in contrast to $\tau = 0.057 \pm 0.007$ obtained with the native hyperbolic tangent. These results translate to, respectively, $z_{\rm re} = 7.60 \pm 0.54$ and $z_{\rm re} = 7.96 \pm 0.64$, as can be seen on Fig. 4.5. Similarly, Qin et al. (2020b) confront the results of using the *tanh* model on Planck 2018 low-ℓ EE data, to a non-parametric one (the reionisation history resulting from a 21CMFAST run). They add as a constraint an upper limit on the neutral hydrogen fraction at $z = 5.9$, $x_{\rm H\,I} < 0.06 \pm 0.05$ (1σ), measured from the dark fraction in QSO spectra (McGreer et al. 2015). They find $\tau = 0.053^{+0.008}_{-0.007}$ for *tanh* and $\tau = 0.055^{+0.008}_{-0.006}$ for the astrophysical model. The asymmetric distribution of the latter corresponds to asymmetric reionisation histories: they have, respectively, $x_{\rm H\,I} > 0.925$ (1σ) and $x_{\rm H\,I} > 0.849$ (1σ) at $z = 10$. The authors argue that the difference is too small to be significant, so that using the symmetric model, and then τ as a summary statistics to constrain EoR history and astrophysical parameters is sufficient. In other words, there is no need to include a better parameterisation of $x_e(z)$ in `CosmoMC`. However, their very results show that when allowing an asymmetric parameterisation, CMB data can help constrain the onset of reionisation and therefore tell us about the birth of light sources. Additionally, the kSZ effect is an important source of information about reionisation found in CMB data: Planck Collaboration et al. (2016d) show that adding high-ℓ data from SPT to Planck 2015 data shifts the inferred optical depth from 0.058 ± 0.012 to 0.054 ± 0.012. We have seen in Sec. 3.2 that the measured kSZ power will be sensitive to the details

[6] Note that $z_{\rm end}$ is fixed to 5.5 and only $z_{\rm re}$ varies.

of reionisation history, therefore requiring a precise modelling of reionisation within the theoretical framework.

The choice made by Qin et al. (2020b), that is using an empirical $x_e(z)$, derived from a simulation, avoids the limitations due to the choice of a parameterisation, namely its lack of flexibility. However, current data on IGM neutral fraction does not justify the use of non-parametric reconstructions of the ionisation history, and, in particular, not the ones based on redshift bins (Hazra et al. 2019). Planck Collaboration et al. (2016d) showed that a model as extreme as a double reionisation (where x_e goes through two phases of increase and decrease) leads to differences on the EE spectrum that are washed out by cosmic variance. Similarly, the two x_e parameterisations mentioned above tuned to match the same τ value, lead to differences of less than 4% at $\ell < 10$. Allowing too many parameters to vary in these models will therefore lead to poorly constrained parameters: using CMB data alone, Planck Collaboration et al. (2016d) only obtain upper limits on the duration of reionisation[7] Δz.

This shows again that the key to break the degeneracies and reduce error bars on reionisation parameters is to combine data from different sources. For example, if the value of τ is mostly sensitive to the temperature and polarisation power spectrum on very large scales ($\ell < 30$), the kSZ power spectrum will be constrained by the information contained at high multipoles ($\ell > 1000$), providing an additional and independent constraint. So far, τ and the amplitude of the kSZ power at $\ell = 3000$ $\mathcal{D}_{3000}$ are derived with independent reionisation models. The former is derived from the *tanh* parameterisation of `CAMB` and the latter is based on a template derived from a specific simulation with a completely different reionisation history. Current results therefore show no correlation between the two parameters, despite the fact that they are made of the same ingredient – the distribution of free electrons along the line-of-sight. Until now, data did not allow for better than upper limits on $\mathcal{D}_{3000}$ but SPT recently claimed the first detection of the signal (Reichardt et al. 2020), showing that statistical uncertainties are decreasing and will soon allow us to constrain the amplitude *and* shape of the spectrum – following, for example, the framework described in Sec. 3.2. This new precision will let us not only increase the precision on inferred reionisation parameters, but also uncover the physical correlations relating them and that were, until now, missed.

It is useful to mention that τ is actually not homogeneous throughout the sky as currently assumed when deriving its averaged value. The inhomogeneity of cosmic reionisation means that there will be small variations in the optical depth along different lines of sight: this related to the $x_e(1 + \delta_b)$ term in its derivation (see Eq. 2.1). These variations impact the CMB temperature and polarisation anisotropies, namely correlating polarised E and B-modes (Roy et al. 2020a) and impacting the relation between the optical depth and the reionisation parameters (Liu et al. 2016). If the related error is too small to impact current constraints on parameters such as $z_{\rm re}$ from τ, these fluctuations should be measurable

[7] Corresponding to the redshift interval when the IGM goes from 10% to 99% ionised.

with CMB-S4 experiments (Dvorkin & Smith 2009). Given the faintness of the signal, one needs to develop robust estimators to observe it, for example, cross-correlations with 21cm mapping to improve the signal-to-noise ratio (Meerburg et al. 2013). So far, only toy models have been used to forecast observations (Roy et al. 2020b) and these forecasts need to be pushed further, using more accurate models and simulations of reionisation, as well as looking into the impact of foregrounds removal techniques on the potential measurements.

4.2.2 Galaxy physical properties: The escape fraction of ionising photons

Let's now turn to astrophysical considerations. In Sec. 2.2, we have outlined how one can derive a reionisation history from a star formation history and a few simple parameters. Some of these parameters were related to cosmology, such as the number density of hydrogen nuclei at a given redshift, and some others were related to the nature of the ionising sources themselves. When looking at the global ionisation rate, one needs first to know the density of existing galaxies and how luminous they are. Because current observations do not allow us to see the faintest galaxies and the highest redshifts, extrapolating is inevitable. In particular, the luminosity function of galaxies is extrapolated up to a magnitude $M_{\rm lim}$, above which we expect a drop in number. $M_{\rm lim}$ corresponds to the faintest galaxies that have not been observed but that we expect to contribute to reionisation. It will by definition have a very arbitrary value, with big consequences on the reionisation photon budget. The second question to answer to derive the ionisation rate is what types of photons early galaxies emit: Do these photons have sufficient energy to ionise an hydrogen atom? Are they likely to reach the neutral atoms of the IGM? The parameter $f_{\rm esc}$ characterises the answer to the latter. Its value will depend on the nature of the galaxies – for example, their mass or their star formation rate. The nature of the IGM at this time is also an important factor: if it is dense, that is if its clumpiness $C_{\rm H\,II}$ is large, the ionising front is likely to stall.

Because they are defined as averaged values, we do not expect observations to give precise estimates of the parameters $f_{\rm esc}$ and $C_{\rm H\,II}$. While high-resolution numerical simulations can help, the required scales to resolve all their physical dependencies simultaneously, along with a potential redshift evolution, is for now unrealistic. It is therefore essential to provide self-consistent constraints on them, analyse their joint dependencies, and evaluate their impact on our current models of reionisation. Conversely, reionisation observables such as the Thomson optical depth or the ionisation level of the IGM, may be able to constrain these parameters and tell us about the physics of the early Universe. Unless stated otherwise, the results of the two following sections were published in Gorce et al. (2018).

The escape fraction of ionising photons

An essential parameter when looking at how early galaxies reionised the IGM is the fraction of ionising photons that escape their host galaxy and reach the surrounding neu-

tral IGM $f_{\rm esc}$. In Sec. 2.2, we have introduced this parameter as constant, equal to 20%, independent of the galaxy properties, their age, and redshift. We have however pointed out that, if this value is compatible with current data, it might be over simplistic, and in particular is much larger than the escape fractions measured in low-redshift galaxies (Steidel et al. 2001; Iwata et al. 2009). Additionally, the example of the three `rsage` simulations considered throughout this work demonstrates that different prescriptions for the halo-mass or star-formation dependency of $f_{\rm esc}$ impact the reionisation history and morphology. Reciprocally, because the escape fraction can vary with metallicity or stellar binary interactions, constraining $f_{\rm esc}(z)$ could improve our knowledge of high-redshift stellar population models (Price et al. 2016). In this perspective, we will complement the analysis done in Sec. 2.3 by now allowing the escape fraction to vary when fitting the 4-parameter model of the star formation history $\rho_{\rm SFR}(z)$ in Eq. (2.14) to astrophysical constraints from quasar spectra and Lyα galaxies, the Thomson optical depth measured by Planck (Planck Collaboration et al. 2018) and galaxy luminosity functions.

Let's first consider $f_{\rm esc}$ constant with redshift, and add it as a fifth parameter of the fit, free to vary between 0 and 1. As before, we use the Gelman-Rubin test to check the convergence of our sampling chains (Gelman & Rubin 1992). All following values are given with a 1σ confidence interval. Fig. 4.6 shows the best-fit reionisation histories, when all constraints are considered or when x_e data from quasar spectra and Lyα galaxies is skipped, along with the resulting posterior distributions for $f_{\rm esc}$. The former is in good agreement with data: we find $z_{\rm re} = 6.88 \pm 0.21$ and $z_{\rm end} = 5.69 \pm 0.10$, leading to $\tau = 0.060 \pm 0.002$. The resulting escape fraction is $f_{\rm esc} = 0.17 \pm 0.03$, showing that data is compatible with a value of the escape fraction slightly lower than the commonly used value of 20%. When x_e data is not used to constrain the fit, the required value of the escape fraction is lower ($f_{\rm esc} = 0.14 \pm 0.07$) in order to slightly delay reionisation and achieve smaller values of τ, in better agreement with Planck data ($\tau = 0.056 \pm 0.08$). $f_{\rm esc}$ is only involved in the $\dot{n}_{\rm ion}$ calculation of Eq. (2.7) and not in the one of star formation rate. The four parameters of the $\rho_{\rm SFR}$ model will therefore be fixed by star formation history data while $f_{\rm esc}$ will vary to match the x_e data and the Thomson optical depth. This is why we find a best-fit star formation history similar to what was obtained when $f_{\rm esc}$ was fixed. However, the star formation rate largely depends on what is assumed for galaxy luminosity functions, and in particular the limit magnitude $M_{\rm lim}$ to which they are extrapolated. If it is too low, it will need to be balanced by a high escape fraction in order to achieve reionisation. We therefore consider correlations between $M_{\rm lim}$ and $f_{\rm esc}$ in the following paragraph.

Photons from different ranges of energy are subject to different physical phenomena and thus escape more or less easily from their host galaxy. For instance, dust extinguishes ionising, Lyα and UV continuum photons similarly, but only ionising photons are also absorbed by neutral hydrogen clumps. Thus, at high redshift, when there is few dust around the galaxy, photons of all energy ranges escape as easily; on the contrary, at low

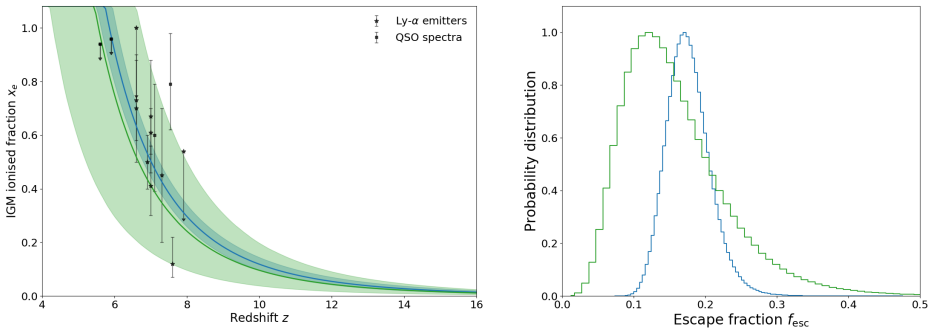

Figure 4.6: Results when fitting a constant $f_{\rm esc}$ to data. *Left panel:* Reionisation history. Data points come from quasars and Lyα emitters constraints (see Sec. 2.2). *Right panel:* Posterior distribution for $f_{\rm esc}$. ML models (continuous lines) are shown for the case where all constraints are used (blue), and when x_e constraints are skipped (green). Shaded areas correspond to the 95% confidence intervals.

redshift, ionising photons experience more difficulties to escape than others (Yajima et al. 2014). Previous works have looked at ways to constrain a redshift-evolution of $f_{\rm esc}$ with data, using parametric (Kuhlen & Faucher-Giguère 2012) or non-parametric (Mitra et al. 2012; Price et al. 2016) methods. Here, we choose the following power-law:

$$f_{\rm esc}(z) = \alpha \left(\frac{1+z}{8} \right)^{\beta}. \tag{4.21}$$

α is the value of $f_{\rm esc}$ at $z = 7$, where most of the x_e data points are located. We take $\beta > 1$ to ensure an increase with redshift and set a maximum of 1 for the $f_{\rm esc}$ value, corresponding to the extreme case of all ionising photons escaping. We perform an MCMC maximum likelihood sampling of the 2 parameters of Eq. (4.21), the convergence being ensured by the Gelman-Rubin test. As mentioned before, the star formation history plays no role in constraining $f_{\rm esc}$ and when the four parameters of the $\rho_{\rm SFR}(z)$ model are included in the fit, their resulting posterior distributions are the same for all our runs. In the following results, we therefore fix $a = 0.0145$, $b = 3.20$, $c = 2.63$ and $d = 5.69$, their maximum likelihood value when they are included in the fit.

When considering x_e data points and τ as constraints, we find $\alpha = 0.15 \pm 0.007$ (1σ) and $\beta < 1.83$ at 95% confidence. Fig. 4.7 shows results for the reionisation history (left panel) and $f_{\rm esc}(z)$ (right panel), for a fit using x_e data and one ignoring them. Overall, the low τ value given by Planck does not require a high ionising emissivity and so, when all constraints are considered, $f_{\rm esc}$ ranges from 5% to 30% throughout the reionisation process for a mean of 0.20 ± 0.02, to compare to what was obtained when $f_{\rm esc}$ was considered constant with redshift ($f_{\rm esc} = 0.17 \pm 0.03$). The best-fit reionisation history is more extended than it was for our fiducial model (here, $\Delta z = 2.74 \pm 0.24$; it was $\Delta z = 2.00 \pm 0.11$ when $f_{\rm esc}$ was fixed) because large values of $f_{\rm esc}$ at high redshift allow for reionisation models to start earlier and get closer to x_e data points but still end by $z = 5$. High-redshift data points, on the star formation history or the IGM ionisation level, for instance given by

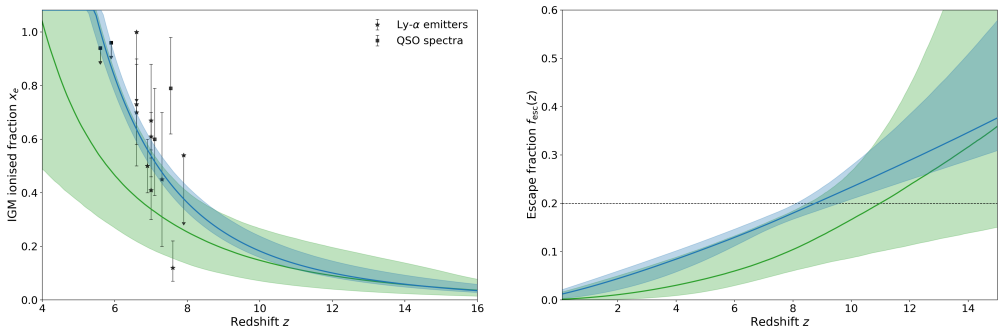

Figure 4.7: Results when fitting $f_{\rm esc}$ to data. *Left panel:* Reionisation history. *Right panel:* Best-fit models for $f_{\rm esc}$ with redshift. ML models (continuous lines) are shown for the case when all constraints are used (blue) and when x_e constraints are skipped (green). Shaded areas correspond to the 95% confidence intervals.

JWST, will therefore be necessary to constrain the value of $f_{\rm esc}$ and its potential evolution with redshift. An extended reionisation yields larger τ values ($\tau = 0.067 \pm 0.003$), still within the 95% confidence interval of Planck. As before, ignoring priors on the IGM ionisation level delays reionisation to reach values of the optical depth closer to Planck results, and a lower escape fraction is then sufficient. However, the difference is of order only 0.05. This corroborates the results of Price et al. (2016), stating that $f_{\rm esc}$ is not very sensitive to the value of the Thomson optical depth. Using a similar power-law to model $f_{\rm esc}(z)$ and allowing $C_{\rm H\,II}$ and $\xi_{\rm ion}$ to vary while skipping constraints on the IGM ionisation level from quasar spectra and Lyα galaxies, Price et al. (2016) find slightly smaller values of the escape fraction ($f_{\rm esc}(z = 8) < 0.10$) but which show a steeper increase with redshift ($\beta > 3$). This is because of the high values of τ the authors use as constrain, which trigger an early reionisation ($z_{\rm re} \sim 8$) and because most of the constraints are absorbed by $\xi_{\rm ion}$ rather than $f_{\rm esc}$. This shows that, again, our results must be considered with caution as we expect a correlation between the escape fraction and other parameters. In particular, we look at the joint dependency of $f_{\rm esc}$ and the star formation rate amplitude, via the parameter $M_{\rm lim}$, in the next paragraph.

Influence of the magnitude limit

In order to study the influence of the choice of magnitude limit on our results, we adopt a modified version of the parameterisation of the UV luminosity density $\rho_{UV}(z)$ given in Eq. (2.15):

$$\rho_{\rm UV}(z) = \frac{2\,\rho_{\rm UV}(z = z_\star)}{10^{a(z-z_\star)} + 10^{b(z-z_\star)}} \tag{4.22}$$

We choose this parameterisation instead of the one previously used for $\rho_{\rm SFR}(z)$ because the galaxy luminosity functions used here are limited to redshifts $3.8 \leq z \leq 10.4$, after cosmic noon and a simple double power-law will be enough to describe the decrease in star formation on $z > 3$. The inflexion point chosen is $z_\star = 7.9$, which corresponds to one of the redshifts where we have galaxy luminosity data, with reasonable error bars, and to the

core of the reionisation process[8]. We sample the two parameters a and b, along with $f_{\rm esc}$ and $M_{\rm lim}$. For each iteration of the fit, we compute $\rho_{UV}(z)$ for the sampled value of $M_{\rm lim}$ from the Schechter parameters derived in McLure et al. (2013); Schenker et al. (2013); Bouwens et al. (2015b); Ishigaki et al. (2015); Oesch et al. (2015); Livermore et al. (2017)[9], fixing the value of $\rho_{UV}(z = z_\star)$. The $\rho_{UV}(z)$ model corresponding to the sampled values of a and b is then compared to these data points and combined with the sampled $f_{\rm esc}$ value to compute $x_e(z)$ and confront it to the x_e data points and Planck's τ. We end up with three χ^2 values which are summed to give the final χ^2 that the algorithm is looking to minimise. $f_{\rm esc}$ is allowed to vary between 0 and 1 and $M_{\rm lim}$ between -17 to -10, where -16 is the detection limit of current observations (Bouwens et al. 2015b; Ishigaki et al. 2018) and -10 is the magnitude of the smallest haloes forming stars (Faucher-Giguère et al. 2011). $M_{\rm lim} = -17$ is therefore a very conservative case, with very few ionising photons produced, whereas $M_{\rm lim} = -10$ is a very optimistic case, leading to a very comfortable photon budget for reionisation. Note that these results have never been published, and aim at further the results of Gorce et al. (2018), presented in Appendix A.1.

The best-fit parameters, yielding the smallest χ^2, are $a = 0.05 \pm 0.03$, $b = 0.42 \pm 0.07$, $\log \rho_{UV}(z = z_\star)/\mathrm{ergs\,s^{-1}Hz^{-1}Mpc^{-3}} = 26.1 \pm 0.2$, $f_{\rm esc} = 0.21 \pm 0.10$ and $M_{\rm lim} = -13.1 \pm 1.7$, so that $\tau = 0.055 \pm 0.001$. Freeing $M_{\rm lim}$ allows to reconcile x_e data and Planck's τ value compared to the previous paragraph. Fig. 4.8 shows the resulting reionisation histories on the left panel, and the joint posterior distribution of $f_{\rm esc}$ and $M_{\rm lim}$ with 1, 2 and 3σ contours, confirming the assumed strong correlation between these two parameters. In order to match observations, a low value of the escape fraction will require extrapolating galaxy luminosity functions to faint luminosities. This corroborates the results of Gorce et al. (2018), where we found, confronting our fits to data derived for typical values of the magnitude limit ($M_{\rm lim} = -17$, -13 and -10), that the most conservative case required extremely large values of the escape fraction ($f_{\rm esc} \sim 0.6 - 0.8$ for $M_{\rm lim} = -17$). In particular, values such as $f_{\rm esc} = 20\%$ require $M_{\rm lim} \geq -14$ (remember, $M_{\rm lim} = -13$, shown as a black cross on the figure, was used in the previous sections). Similarly, considering a varying value of $M_{\rm lim}$ with redshift, Price et al. (2016) find that it varies in order to balance the increasing value of $f_{\rm esc}$ with redshift allowed by their model and give optical depths compatible with Planck. Current observations do not go to fainter luminosities that $M \sim -15$, we therefore still require galaxies that have not been yet observed to derive a consistent history of reionisation. Observations of faint and high-redshift galaxies by the James Webb Space Telescope (JWST, Gardner et al. 2006) are highly anticipated, in order to confirm or infirm the contribution of these galaxies to reionisation.

Ishigaki et al. (2018) find a similarly shaped 2D distribution function of $f_{\rm esc}$, $\log \rho_{UV}(z = z_\star)$ and $M_{\rm lim}$, leading to $M_{\rm lim} < -14$ and $f_{\rm esc} = 0.17^{+0.07}_{-0.03}$. In their work, the authors fit a, b, $z_\star$, $f_{\rm esc}$ and $M_{\rm lim}$ to their own data on luminosity density. They also add the optical depth from the previous Planck results ($\tau = 0.058 \pm 0.012$, Planck Collaboration et al.

[8]When $z_\star$ is added as a free parameter, we obtain very similar results on $x_e(z)$.
[9]This corresponds to 24 data points on the range $3.8 \leq z \leq 10.4$.

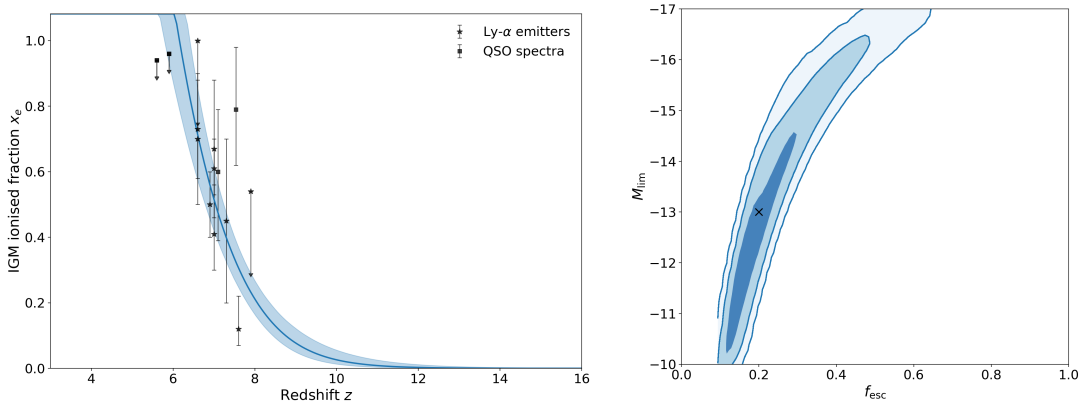

Figure 4.8: Results of adding the magnitude limit $M_{\rm lim}$ and the escape fraction $f_{\rm esc}$ to our fits. *Left panel:* Reionisation histories. The best-fit scenario when all constraints are used is shown as the solid blue line, along with its 95% confidence interval. *Right panel:* 2D posterior distribution of $M_{\rm lim}$ and $f_{\rm esc}$ with 1, 2 and 3σ confidence levels. The cross shows fiducial values used in Sec. 2.3.

(2016d)) and x_e measurements from quasar spectra and Lyα galaxies as constraints. Here, combining different datasets on luminosity functions allows to give more than an upper limit on $M_{\rm lim}$.

As mentioned before, these results depend on the value assumed for $\xi_{\rm ion}$, the Lyman continuum photons production efficiency, which is used with $f_{\rm esc}$ to derive the IGM ionisation rate $\dot{n}_{\rm ion}(z)$ from UV luminosity densities. Here, we have used $\xi_{\rm ion} = 10^{53.14}$ s$^{-1}M_{\odot}^{-1}$yr (Robertson et al. 2015) and we consider that the uncertainties obtained for $f_{\rm esc}$ include those on $\xi_{\rm ion}$. We expect that, once data on star formation history at earlier times is available, we will be able to improve constraints on the magnitude limit.

4.2.3 IGM physical properties: The clumping factor of ionised hydrogen

Another key-parameter of the reionisation process is the clumping factor of ionised hydrogen in the IGM $C_{\rm H\,II}$. It is related to the characteristic recombination time: the more matter is aggregated in clumps, the easier for ionised atoms to recombine in these very same clumps. However, as mentioned in Sec. 2.2, a precise estimate of its value is difficult to obtain. On the simulation side, estimating $C_{\rm H\,II}$ requires getting a sufficient precision for the gas distribution, a correct topology of ionised and neutral matter, and an accurate model of the evolution of gas clumps themselves during the reionisation process (Mao et al. 2020; Chen et al. 2020). Most recent studies use values ranging from 1 to 6 at the redshifts of interest, i.e. for $6 \lesssim z \lesssim 30$ (Sokasian et al. 2003; Iliev et al. 2006; Raičević & Theuns 2011; Shull et al. 2012; Robertson et al. 2015; Finkelstein et al. 2015; Bouwens et al. 2015a). Other works look at a redshift-dependent evolution (Iliev et al. 2007a; Pawlik et al. 2009; Haardt & Madau 2012; Finlator et al. 2012; Sobacchi & Mesinger 2014), because at low redshift, most of the ionised hydrogen is located in matter haloes, whose increasing overdensity implies a large $C_{\rm H\,II}$ (Furlanetto & Oh 2005; Sobacchi & Mesinger

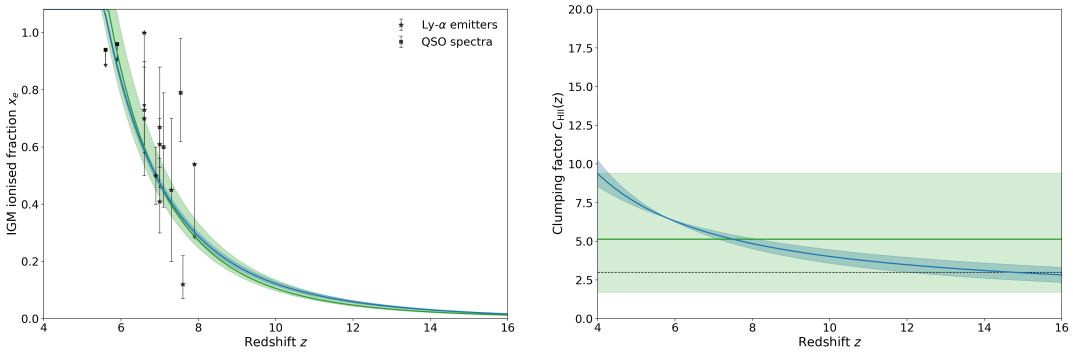

Figure 4.9: Results when considering a 2-parameter model for $C_{\rm H\,II}$. *Left panel:* Reionisation history. *Right panel:* Redshift-evolution of $C_{\rm H\,II}(z)$. Best-fit models, along with their 95% confidence intervals, are shown when all data sets are used as constraints for the redshift-evolution (in blue) or when $C_{\rm H\,II}$ is constant (in black).

2014). Because $C_{\rm H\,II}$ is closely related to the physics of the IGM, it is not only interesting to see the impact of its value on our models of reionisation, but also to see what we could learn about the properties of the high-redshift IGM with precise reionisation observations.

In this perspective, we now add the clumping factor as a fifth parameter to the $\rho_{\rm SFR}(z)$ fit, free to vary between 0 and 100. Because $C_{\rm H\,II}$ is involved only in the calculation of the evolution equation of the ionisation level (Eq. 1.7) as the competing term related to recombinations, star formation history data points do not constrain its value significantly, but rather a, b, c and d. Results are shown, for the posterior distributions of $x_e(z)$ and $C_{\rm H\,II}$, on Fig. 4.9 in green. When all data sets are included in the fit, we find $C_{\rm H\,II} = 4.98 \pm 1.97$, which is within the range of values used in the literature. Despite this wide posterior distribution, the corresponding range of reionisation histories is quite narrow with $z_{\rm re} = 6.86 \pm 0.10$. It seems that the exact value of $C_{\rm H\,II}$ only slightly impacts the reionisation history and, conversely, it will not be possible to constrain the clumpiness of the IGM from global reionisation constraints. Additionally, the resulting Thomson optical depths are very close to the distribution obtained when $C_{\rm H\,II}$ is fixed to 3: $\tau = 0.060 \pm 0.001$ to be compared with $\tau_{C_{\rm H\,II}=3} = 0.064 \pm 0.001$. Because the Thomson optical depth only sets loose constraints on reionisation history, we find that x_e measurements are essential to constrain $C_{\rm H\,II}$. When skipped, because of the wide error bars on $\rho_{\rm SFR}(z)$ at high redshift, the only constrain ensuring reionisation to happen is the Thomson optical depth. Therefore $C_{\rm H\,II}$ is poorly constrained: the peak likelihood corresponds to $C_{\rm H\,II} = 17.0$ but with a tail extending to 100 (3σ). These high values lead to a high recombination rate, which is not balanced sufficiently by star formation, so that reionisation happens later ($z_{\rm re} = 5.82 \pm 0.75$), leading to $\tau = 0.047 \pm 0.008$. Conversely, skipping or keeping the τ constraint gives almost identical results as long as x_e data is used.

We now model a redshift-evolution of $C_{\rm H\,II}$ with a simple power-law inspired by the

results of Haardt & Madau (2012):

$$C_{\mathrm{H\,II}}(z) = 1 + a\left(\frac{z}{7}\right)^b, \tag{4.23}$$

where $1+a$ is the value of $C_{\mathrm{H\,II}}$ at $z=7$, that is around the midpoint of reionisation. It is generally admitted that the clumping factor only decreases with z, so we set the uniform priors $a > 0$ and $b < 0$. Addtionally, its formal definition is $C_{\mathrm{H\,II}} = \langle n^2_{\mathrm{H\,II}}\rangle / \langle n_{\mathrm{H\,II}}\rangle^2 = 1 + \delta_{\mathrm{H\,II}}$, if we define the overdensity of ionised hydrogen as $\delta_{\mathrm{H\,II}} = (n_{\mathrm{H\,II}} - \langle n_{\mathrm{H\,II}}\rangle) / \langle n_{\mathrm{H\,II}}\rangle$. Before the onset of reionisation, most of the hydrogen is neutral so that H II fluctuations are very weak: $\delta_{\mathrm{H\,II}}(z \to \infty) = 0$: $b < 0$ ensures that $C_{\mathrm{H\,II}} \to 1$ as $z \to \infty$. Finally, according to this definition, $C_{\mathrm{H\,II}}(z)$ is infinite at $z = 0$. If it reaches too large values at low redshift, recombinations will take over ionisation and the IGM will be either never fully ionised or x_e will reach 1 and then decrease again. To avoid these unphysical behaviours, we require H I reionisation to end before the one of He II, therefore before $z = 4$. Because $C_{\mathrm{H\,II}}$ is not involved in the calculation of ρ_{SFR} but only of the recombination time, star formation history data have no influence over its value so we constrain our runs by x_e and τ_{Planck} only – the ρ_{SFR} parameters are fixed to their best-fit values in Sec. 2.3.

The maximum likelihood is reached for $a = 3.49 \pm 0.49$ and $b = -0.87 \pm 0.43$, resulting in $\tau = 0.061 \pm 0.002$. The best-fit $C_{\mathrm{H\,II}}(z)$ and $x_e(z)$ are shown on Fig. 4.9 in blue. We see the redshift-evolution of $C_{\mathrm{H\,II}}$ allows an even better constrained reionisation history, with $z_{\mathrm{re}} = 6.88 \pm 0.26$. However, data does not require a strong evolution during reionisation: it increases from 2.5 at $z = 15$ to 10 at $z = 4$. In fact, the slope b is poorly constrained and values ranging from -1.5 to 0 lead to similar reionisation histories. We note a strong correlation between the parameter a in the model, which corresponds to $C_{\mathrm{H\,II}}(z=7) - 1$ and τ: higher values of a, and therefore of $C_{\mathrm{H\,II}}$ at the midpoint of reionisation, lead to lower τ values, as a higher recombination rate delays reionisation. This is a promising way to constrain $C_{\mathrm{H\,II}}$ independently of other parameters. Interestingly, there was no correlation noted between τ and $C_{\mathrm{H\,II}}$ when the latter was taken constant with redshift.

Data seems to require values of the IGM clumping factor larger than the constant $C_{\mathrm{H\,II}} = 3$, often used in the literature, mainly to match the low Thomson optical depth measured by Planck. However, this value relies on an outdated model of reionisation included in `CosmoMC`, and correctly including reionisation within the CMB data analysis framework will likely lead to larger optical depths (see Planck Collaboration et al. 2016d, and previous section). Values $C_{\mathrm{H\,II}} \leq 10$ all yield similar reionisation histories, in good agreement with measurements of the global IGM ionisation level from quasars and Lyα galaxies, and within the confidence intervals of Planck results. Therefore any $C_{\mathrm{H\,II}}$ on this range will be a good first approximation. If a redshift-evolution is not favoured, it can still be useful to include it to our models because of the high correlation noted between the value of $C_{\mathrm{H\,II}}$ around the midpoint of reionsation and τ.

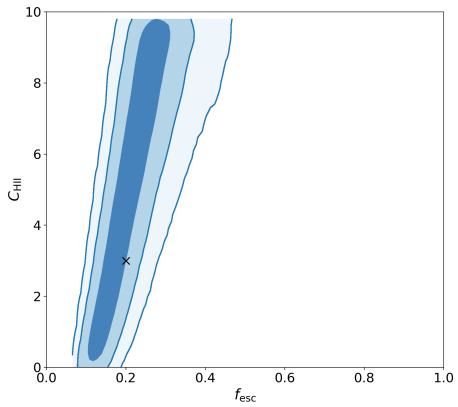

Figure 4.10: Posterior distribution for $f_{\rm esc}$ and $C_{\rm H\,II}$ when they are added to the fit on $\rho_{\rm SFR}(z)$. Contours correspond to the 1-, 2- and $3-\sigma$ confidence levels. The cross shows the fiducial values used in Sec. 2.3.

Joint dependency of $f_{\rm esc}$ and $C_{\rm H\,II}$

Now that we have studied the impact of $f_{\rm esc}$ and $C_{\rm H\,II}$ separately, we look at how their values are correlated and add them to the four parameters of the $\rho_{\rm SFR}(z)$ model in Eq. (2.14). In agreement with previous results that showed data only weakly favours a redshift-evolution for these two parameters, we take them constant. $f_{\rm esc}$ is allowed to vary between 0 and 1, and a flat prior $C_{\rm H\,II} \in [0, 10]$ is added on $C_{\rm H\,II}$[10]. The six parameters have maximum likelihood values similar to previous results: we find $a = 0.0145$, $b = 3.21$, $c = 2.62$ $d = 5.68$, $f_{\rm esc} = 0.22 \pm 0.06$ and $C_{\rm H\,II} = 5.73 \pm 2.81$. The larger error bars on $C_{\rm H\,II}$ seem to indicate that the uncertainty on $f_{\rm esc}$ has been absorbed by them. We show the 2D posterior distribution of $f_{\rm esc}$ and $C_{\rm H\,II}$ on Fig. 4.10, when all three data sets are used. Ishigaki et al. (2015) find a similar behaviour, with however $f_{\rm esc}$ values larger by about 0.10 for all $C_{\rm H\,II}$, resulting into low τ values, around 0.040. Here, the resulting ionisation histories are also close to what was obtained when $f_{\rm esc}$ and $C_{\rm H\,II}$ were fixed. In particular, the evolution of the ionised level of the IGM and thus the derived value of τ remain quite well constrained ($\tau = 0.060 \pm 0.002$) and in agreement with Planck.

As a conclusion, we have seen that the quality of the observations currently available, as well as the high number of parameters involved when deriving a model reionisation history do not allow to derive clear joint dependencies between the astrophysical parameters at stake. We have found that for the escape fraction, a value $f_{\rm esc} \simeq 20\%$ is sufficient to achieve reionisation, in good agreement with data, as long as $M_{\rm lim} > -13$. The clumping factor is loosely constrained by data, and any value on the range $1 < C_{\rm H\,II} < 10$ will lead to reionisation histories in good agreement with data. Indeed, all our analyses, where different sets of parameters were allowed to vary, led to similar reionisation histories, confirming the validity of a model where reionisation starts around $z = 15$ and is ended by $z_{\rm end} = 5.5$, with

[10]When $C_{\rm H\,II}$ is allowed to take any value between 0 and 100, the preferred value is about 40 and the recombination rate is so high that an escape fraction of 80% is required to achieve reionisation.

a midpoint around $z_{\rm re} = 7.5$. Improved observations, namely at high redshift, should allow to reduce the observed degeneracies and to use reionisation observables to learn about the physics of the early Universe.

***

4.3 Chapter conclusion & discussion

This chapter has highlighted the model- and observations-related issues we encounter with current data, as well as the ones we will have to overcome with future data, in particular 21cm. For each of the problems listed, we have assessed the related error and found that, sometimes, for example for astrophysical parameters such as the IGM clumpiness, their impact on EoR constraints was only weakly significant. This will be useful as it is currently not possible to run simulations of sufficient precision, or to observe a sufficient number of high-redshift objects, to know these parameters well. It will, however, also be problematic, since the information we can get on the nature of the IGM at high redshift from global reionisation observations is consequently limited.

Considering high-impact factors, we have looked for ways to avoid or suppress the associated errors and some of the statistical tools introduced in Chapter 3 are found to be particularly robust to instrumental effects. The triangle correlation function, for instance, benefits from reduced calibration errors thanks to the use of closure phases, and is found to be weakly sensitive to the instrumental resolution and thermal noise of experiments such as SKA. Additionally, some of the model-uncertainties mentioned in this chapter are expected to be lifted with future observations. With the sensitivity of JWST, we expect to observe the faint-end of galaxy luminosity functions, therefore avoiding unphysical extrapolations and confirming their anticipated contribution to reionisation. JWST's deep-sky observations should also tell us about the density of galaxies at redshifts $z > 10$, which, as we have seen, will in turn help constrain a potential evolution of the escape fraction with redshift. Increased simulation sizes and resolution, accounting for more and more physical effects, will also tell us about objects that are not currently observable, and improve our global picture of EoR.

Finally, the sample variance, which was used to our benefit in Sec. 3.1, is an intrinsic observational issue that one cannot avoid, and must therefore be modelled. In this perspective, we have introduced the super-sample covariance, a theoretical derivation of the impact of sample variance on cosmological parameter inference. This derivation, which for the first time accounts for the limited size of surveys such as Euclid, can be extended to observations of the 21cm global signal.

Chapter 5

Conclusions

In this thesis, I have looked at reionisation history, from a global and then local perspective. At both levels, I have developed, and made available for the community, analysis methods robust to model- and observations-related limitations, specific to the study of the Epoch of Reionisation (EoR). Indeed, despite this period covering a few billion years of the history of the Universe, it is poorly known and a lot of work is required before being able to use the next generation of observational data. Once this data is available, my tools will give reliable constraints on reionisation in general, and on the physical properties of the high-redshift IGM and galaxies in particular.

As the second major phase transition of the Universe after recombination, the EoR is firstly interesting as a global process. In this work, I have given a reference, comprehensive history where reionisation is an asymmetric process, starting slowly around $z = 15$, before accelerating when 20% of the IGM is ionised, and ending before $z = 5$. In this simple scenario, based on a few reasonable assumptions about the high-redshift Universe, reionisation is driven by galaxies. This result is obtained by combining, for the first time, all the observational data available today, from quasar spectra and galaxy luminosity functions to CMB optical depth. Despite very different cosmological and astrophysical origins, these observations are consistent and give a coherent picture of the process. However, fully reionising the IGM requires high-redshift and faint galaxies which have not yet been observed. In this perspective, the deep-sky observations of the James Webb Space Telescope (JWST, Gardner et al. 2006) are highly anticipated. These results are essential for reionisation study as star formation is a direct tracer of the ionising photon budget with cosmic time. Additionally, the quality of current data on the IGM ionised fraction x_e is low, both because of modelling uncertainties on the nature or environment of the source, and because of the small size of the data sample. Wide surveys such as the space-based Euclid (Laureijs et al. 2011) and Nancy Grace Roman telescopes (previously named WFIRST, Green et al. 2012)[1], or the ground-based Vera Rubin telescope (previously name LSST, LSST Science

[1]Euclid will cover about seven times larger sky area than the Roman telescope, while the imaging of the latter will be about 2.5 magnitudes deeper than Euclid.

Collaboration et al. 2009), will provide an unprecedented amount of imaging data for studies of faint light sources: together, these telescopes will cover about 2 200 $\deg^2$ of deep observations of the sky. Simulations estimate that the Rubin telescope alone will discover about 1 000 quasars at $z > 7$ (Ivezić 2018), while the fifth phase of the Sloan Digital Sky Survey (SDSS, York et al. 2000) will target over 400 000 sources, primarily black holes. Follow-ups by JWST will, in turn, give their optical and infrared spectra, from which we can infer x_e. Observations of a wide number of luminous objects by these telescopes will be helped by improved methods to locate quasars in large data sets, such as Bayesian model comparison and machine learning techniques (Mortlock 2014; Richards et al. 2015). The number of observed Lyman-α galaxies is also expected to be greatly improved.

Deriving a global reionisation history from astrophysical observations includes modelling a number of astrophysical objects and processes which are not always well understood. In this work, I have given a clear picture of what information is missing, and what type of observations will be needed to improve results. For example, JWST's sensitivity, limited to a handful of narrow but deep fields, will allow observations of dim objects and tell us about the high-z and faint-end of galaxy luminosity functions. This, in turn, will constrain the value of a global escape fraction of ionising photons $f_{\rm esc}$, averaged over galaxy properties, as well as its potential redshift-evolution. Conversely, the global reionisation history seems to be only weakly sensitive to the nature of the IGM during the process, and in particular to averaged parameters such as its overall clumpiness $C_{\rm H\,II}$. To further constrain such parameters, as well as the properties of early galaxies, we will need to turn to more local measurements, such as 21cm intensity mapping.

In this perspective, I have introduced tools designed to efficiently extract information about reionisation from 21cm intensity mapping data. Efficient analysis methods are essential considering the amount of data 21cm experiments produce: the Hydrogen Reionization Array (HERA, DeBoer et al. 2017) will generate about 0.2 terabytes of raw data per day, and the Square Kilometre Array (SKA, Koopmans et al. 2015) about 160 terabytes per second, the estimated global internet traffic in 2015. I have presented a quick and easy-to-compute one-point statistic, dubbed local variance. Applied to narrow lightcones, it can tell us both about the global reionisation history and the physical properties of early galaxies while making use of what is normally considered an observational bias: the sample variance. A more complex object described here is the triangle correlation function of phases (TCF), based on the phases of the 21cm bispectrum, and benefiting from reduced calibration errors thanks to the closure phase relation. The TCF is designed to trace the shape and evolution of H II regions during reionisation. Because these two objects are robust to instrumental effects such as the angular resolution and thermal noise of, for example, SKA1-*Low*, they are not limited to theoretical studies and can be used on actual observations. However, a limitation not investigated in details here is foreground removal. Indeed, observations of the cosmological 21cm signal are likely to be spoilt by foregrounds 10 to 100 times larger in amplitude. More work is required to improve our modelling of

these foregrounds and, in turn, remove them accurately from data. In the case of intensity mapping, the impact of foregrounds on the non-Gaussian part of the 21cm signal needs to be assessed, despite pessimistic first works (Watkinson et al. 2020). A way to overcome poor signal-to-noise ratios and to confirm the cosmological origin of a measured signal is to use cross-correlations, for example between 21cm and kSZ (Jelić et al. 2010; Tashiro et al. 2011; La Plante et al. 2020), 21cm and τ (Meerburg et al. 2013; Roy et al. 2020b), or 21cm data and Lymanα emitters (Carucci et al. 2017; Hutter et al. 2017). If these cross-correlations can be computed at the power spectrum level, higher-order statistics such as the TCF are also an interesting prospect.

On a shorter timescale, clean measurements of the 21cm power spectrum are expected in the coming years. Lowest upper limits, noise- and systematics-limited, are currently bouncing back and forth between the Low Frequency Array in the Netherlands (LOFAR, van Haarlem et al. 2013a) and the Murchison Widefield Array in Australia (MWA, Tingay et al. 2013). Results from HERA in South Africa and the Giant Metrewave Radio Telescope in India (GMRT, Paciga et al. 2011), are also highly anticipated. Additionally, the sky-averaged global 21cm signal will give us information about the global history of the process, and in particular its onset via the birth of the first stars. It is targeted by single antenna experiments such as the Experiment to Detect the Global EoR Signature (EDGES, Bowman et al. 2008), the Shaped Antenna measurement of the background RAdio Spectrum 2 (SARAS 2, Singh et al. 2018). EDGES, in particular, has claimed the first detection of this signal in 2018 (Bowman et al. 2018). Although not yet confirmed, if true, this result would require us to rethink our picture of the Cosmic Dawn (Barkana 2018).

Improved observations of the CMB, both on large and small scales, are also an exciting perspective for learning about the EoR. Satellites such as LiteBird (Hazumi et al. 2012), scheduled to launch in 2027, should reach the cosmic variance limit on the Thomson optical depth $\sigma(\tau) = 0.002$ – today, Planck's results have a precision of $\sigma(\tau) = 0.007$ (Planck Collaboration et al. 2018). The primary target of LiteBird is the polarisation B-modes of the CMB, which will be contaminated by secondary anosotropies stemming from patchy reionisation (Mukherjee et al. 2019). Observing this polarised signal is also the aim of, for example, the Background Imaging of Cosmic Extragalactic Polarization (BICEP, Keating et al. 2003) and POLARBEAR (Kermish et al. 2012). Because of the very high sensitivity required to observe B-modes on large scales, these experiments will also improve reionisation constraints based on the low-ℓ parts of the TT, TE and EE spectra.

To this day, small-scale CMB observations essentially allow to constrain reionisation as a whole, and in an inconsistent manner: different prescriptions are used to describe reionisation at different stages of the analysis, and the main model is a step-like reionisation history, very different from the results of observations and simulations (Aubert et al. 2015; Gorce et al. 2018). I have therefore introduced a new parameterisation of the patchy kinetic Sunyaev Zel'dovich (kSZ) angular power spectrum in terms of reionisation which can be directly added to the CMB data analysis pipeline. The complicated physics involved in

the kSZ signal are summarised in this quick and easy-to-forward-model formalism, based on two parameters related to the nature of the IGM and of early galaxies. With this parameterisation, it will be possible to measure for the first time the accurate amplitude and shape of the kSZ power spectrum from reionisation. However, extracting information about reionisation from high-ℓ CMB data requires a good knowledge of the late-time, homogeneous part of the kSZ signal, as well as an efficient removal of foregrounds with multi-frequency analysis. Current data, obtained with the latest generations of the Atacama Cosmology Telescope (ACT, Kosowsky 2003) and the South Pole Telescope (SPT, Ruhl et al. 2004), and combined with Planck large-scale data, have mostly given upper limits on the amplitude of the patchy kSZ signal and rely on inconsistent and outdated models of reionisation. After 5 years of observations of 1 500 deg^2 of the sky with the SPT-3D camera, the noise levels are expected to be significantly reduced, resulting in substantially lower uncertainties on the measured temperature power spectrum for $\ell > 1000$. Additionally, the Simons Observatory (SO, Ade et al. 2019) and CMB-S4 experiments (Abazajian et al. 2016) will extend these measurement to larger sky areas, with reduced noise, and on more frequency bands, improving foreground removal. Forecasts therefore expect a detection of the amplitude of the patchy kSZ signal at $\ell = 3000$ at the 0.2 μK^2 level with SO (Ade et al. 2019), whereas the most recent claimed detection by SPT has a 1.0 μK^2 uncertainty (Reichardt et al. 2020). Depending on its mean value, future CMB experiments should also be able to detect spatial fluctuations in the Thomson optical depth τ (Roy et al. 2018), allowing cross correlations with 21cm data (Meerburg et al. 2013; Roy et al. 2020b).

Reciprocally, a better knowledge of reionisation will allow to put strong priors on τ or $x_e(z)$ in CMB analysis and reduce the remaining degeneracies between cosmological parameters and τ. A high precision measurement of the reionisation bump will also help in detecting potential B-modes, once systematics and foregrounds are removed.

Other observational probes of the EoR exist and have not been used in this work. We have mentioned in Sec. 2.2 the possibility of constraining the ionising rate of the IGM using the luminosity functions (LF) of Lyα emitters. If the experiments described above will push the observed LF to fainter magnitudes and higher redshift, there is still a lot of uncertainty on the underlying modelling of the physics involved (Santos 2004). Another option is to look at the evolution of the IGM thermal state. Indeed, the IGM will be photo-heated to a few 10^4 K by reionisation[2], before gradually cooling with expansion. Because of this slow cooling process, the low density IGM gas retains some thermal memory of when and how it was ionised (Miralda-Escudé & Rees 1994). Different models of reionisation will lead to different thermal histories: for example, earlier reionisation scenarios lead to a cooler IGM at low redshift. Most current measurements of the IGM temperature are obtained by analysing the shapes of the absorption lines in the Lyα forest of quasar spectra

[2] $T = 2 \times 10^4$ K is considered to be the mean temperature around a newly formed atom (Loeb & Furlanetto 2013).

(Hiss et al. 2018), but newer methods, using the Lyα flux power spectrum, have recently been proposed (Boera et al. 2019). New observations of quasars and Lyα galaxies by the experiments mentioned above will therefore also help increase the significance of such measurements.

Finally, simulations are an ideal way of reaching scales and redshifts which are not accessible through observations. Today, most simulations, of different degrees of complexity, vary the physical properties and density of early light sources in order to reproduce observations. Models which match the observations will therefore tell us what is required for reionisation to happen the way we observe it today. However, the most complex and physically accurate simulations are limited by computing power, and do not reach scales larger than a few hundreds of megaparsecs (Gnedin 2014; Ocvirk et al. 2016; Pawlik et al. 2017). Post-processing cosmological hydrodynamical or dark matter only simulations with radiative transfer is a cheaper alternative, as the required resolution can be coarser (Mellema et al. 2006; Trac & Cen 2007; Ciardi et al. 2012; Hutter et al. 2014; Iliev et al. 2014). On the other hand, semi-numerical simulations, despite making coarse approximations, can reach gigaparsecs sizes (Furlanetto et al. 2004a; Mesinger & Furlanetto 2007; Thomas et al. 2009; Ghara et al. 2015). Because they are quick to compute, it is possible to sample various realisations, corresponding to different astrophysical parameters, and confront them to data in an MCMC approach (Greig & Mesinger 2017). All these methods are expected to make a lot of progress in the coming years, as computational power will be greatly improved.

Reionising the IGM involves many different physical processes, on a wide range of scales. This is both a curse, since it makes it difficult to have a comprehensive picture of the process, and a blessing, since many different types of observations can help constraining it. The EoR is related to many fundamental questions about the high-redshift Universe, from the density and clumpiness of the IGM to the astrophysics of luminous objects, such as the formation of the first stars, the impact of radiative feedback on star formation or black hole growth, and the nature of early galaxies and (mini-)quasars. Indeed, constraining the onset of reionisation tells us about the properties of these galaxies, which are the building blocks of galaxies observed today and hence can confirm, or infirm, current models of galaxy formation and evolution. All of this makes the study of reionisation a priority of cosmology, with many observational and modelling challenges to overcome, that I am happy to have contributed to and excited to keep doing so.

Appendix A

Published journal articles

A.1 Observational constraints on key-parameters of cosmic reionisation history

This article was the result of a work started as a Master student. It aims at combining all the data currently available to constrain the reionisation process as a whole and derive a comprehensive scenario. A similar approach is adopted in Sec. 2.3, however, the results are not the same as the ones of the paper as the observational data used has been updated. This work also investigates the impact of the exact value of some parameters used when deriving reionisation history from measurements, which are poorly known. These results make up most of Secs. 4.2.2 and 4.2.3. All the results presented in this article, and the ones related to the article presented in this thesis, are the result of my personal work. It was published in August 2018 in Astronomy & Astrophysics.

Astronomy & Astrophysics manuscript no. Article
September 3, 2018

Observational constraints on key-parameters of cosmic reionisation history

A. Gorce[1,2], M. Douspis[1], N. Aghanim[1], and M. Langer[1]

[1] Institut d'Astrophysique Spatiale, Université Paris-Sud, CNRS, UMR8617, 91405 Orsay, France
e-mail: adelie.gorce@ias.u-psud.fr
[2] Department of Physics, Blackett Laboratory, Imperial College, London SW7 2AZ, U.K.

Received *********; accepted *******

ABSTRACT

We discuss constraints on cosmic reionisation and their implications on a cosmic star formation rate (SFR) density $\rho_{\rm SFR}$ model; we study the influence of key-parameters such as the clumping factor of ionised hydrogen in the intergalactic medium (IGM) $C_{\rm H\,II}$ and the fraction of ionising photons escaping star-forming galaxies to reionise the IGM $f_{\rm esc}$. Our analysis has used SFR history data from luminosity functions, assuming that star-forming galaxies were sufficient to lead the reionisation process at high redshift. We have added two other sets of constraints: measurements of the IGM ionised fraction and the most recent result from Planck Satellite about the integrated Thomson optical depth of the cosmic microwave background (CMB) $\tau_{\rm Planck}$. Our analysis shows that a reionisation beginning as early as $z \geq 14$ and persisting until $z \sim 6$ is a likely scenario.
We also considered various possibilities for the evolution of $f_{\rm esc}$ and $C_{\rm H\,II}$ with redshift, and confront them with observational data cited above. We conclude that, if the model of a constant clumping factor is chosen, the fiducial value of three is consistent with observations; even if a redshift-dependent model is considered, the resulting optical depth is strongly correlated with $C_{\rm H\,II}$ mean value at $z > 7$, an additional argument in favour of the use of a constant clumping factor. Similarly, a constant value of the escape fraction is favoured over a redshift-dependent model. When added as a fit parameter, we find $f_{\rm esc} = 0.19 \pm 0.04$. However, this result strongly depends on the choice of magnitude limit in the derivation of $\rho_{\rm SFR}$. Our fiducial analysis considers faint galaxies ($M_{\rm lim} = -13$) and the result is a well constrained escape fraction of about 0.2, but when $M_{\rm lim} = -17$, the number of galaxies available to reionise the IGM is not sufficient to match the observations, so that much higher values of $f_{\rm esc}$, approaching 70%, are needed.

Key words. Cosmology: dark ages, reionisation, first stars – Cosmology: cosmic background radiation – Galaxies: high-redshift – Galaxies: evolution – Galaxies: formation

1. Introduction

Around redshift $z \simeq 1090$, during the recombination era, protons paired with free electrons to form neutral atoms: the ionisation level of the intergalactic medium (IGM) fell to 0.0001 % and remained at this level for several billions of years (Peebles 1968; Zel'dovich et al. 1969; Seager et al. 2000). Nevertheless, observations of the Gunn-Peterson effect (Gunn & Peterson 1965) in quasar spectra inform us that at $z \sim 6$, 99.96 ± 0.03 % of the IGM hydrogen atoms are ionised (Fan et al. 2006). What happened in the meantime, during the Epoch of reionisation (EoR), is an essential source of information about the evolution of the Universe, the formation of large cosmic structures and the properties of early galaxies, to cite only a few. Thanks to improved observations of the cosmic microwave background (CMB), luminosity functions of galaxies, damping wings of quasars and Ly-α emissions (e.g. Schenker et al. 2013; Schroeder et al. 2013; Madau & Dickinson 2014; Planck Collaboration et al. 2016b), more and high quality data are available. Now the generally accepted scenario is that first star-forming galaxies reionised neutral regions around them between $z \simeq 12$ and $z \simeq 6$ and then the ionised regions progressively overlapped (e.g. Aghanim et al. 1996; Becker et al. 2015) so that IGM neutral hydrogen fraction rapidly decreased until quasars took over to reionise helium from $z \simeq 3 - 4$ (Mesinger 2016).
Yet, some doubts remain about the sources of reionisation: some support the hypothesis that quasars could have led the process (Madau & Haardt 2015; Khaire et al. 2016; Grazian et al. 2018) but star-forming galaxies are often preferred. For instance, Robertson et al. (2015) argue that they were sufficient to maintain the IGM ionised at $z \sim 7$. The most recent value of the integrated Thomson optical depth, deduced from observations of the CMB, equals $\tau_{\rm Planck} = 0.058 \pm 0.012$ and is obtained considering an instantaneous reionisation at $z_{\rm reio} = 8.8 \pm 0.9$ ended by $z = 6$ (Planck Collaboration et al. 2016b). It is much lower than previous observations by the Wilkinson Microwave Anisotropy Probe (WMAP) $\tau_{\rm WMAP} = 0.088 \pm 0.014$ for $z_{\rm reio} = 10.5 \pm 1.1$ (Hinshaw et al. 2013). This decrease, according to Robertson et al., reduces the need for a significant contribution of high-redshift galaxies and allows them to extrapolate galaxies luminosity functions for $10 \lesssim z \leq 30$.
Like Robertson et al. (2015), a number of recently published papers assume redshift-independent values of the escape fraction of ionising photons $f_{\rm esc}$ and of the clumping factor $C_{\rm H\,II}$ (Bouwens et al. 2015a; Ishigaki et al. 2015; Greig & Mesinger 2017), which is a questionable hypothesis. The escape fraction depends on numerous astrophysical parameters and, for this reason, it is often a generalised, global and redshift-independent value that is used, for an order of magnitude of 0.1. Some simulations give expressions of $f_{\rm esc}$ as a function of redshift (Haardt & Madau 2012; Kuhlen & Faucher-Giguère 2012) or of various parame-

ters such as halo mass or star formation rate (Wise et al. 2014; Paardekooper et al. 2015), but these models are rarely combined with observational constraints, aiming to deduce a certain history of reionisation. The situation is similar for the clumping factor: its evolution with redshift can be considered in simulations through various models (e.g. Mellema et al. 2006; Pawlik et al. 2009; Sobacchi & Mesinger 2014), but these are rarely compared with observations. We must, however, refer to Price et al. (2016) who constrain parametrised models of the escape fraction $f_{\rm esc}\,(z)$ with Thomson optical depth and low multipole E-mode polarisation measurements from Planck Collaboration et al. (2016b), SDSS BAO data and galaxy observations for $3 \lesssim z \lesssim 10$.

We first describe in Sect. 2 the observables of the reionisation process we will use throughout the analysis: the cosmic star formation rate density, the ionised fraction of the IGM and the Thomson optical depth, for which observational data is available – described in Sect. 3; as well as the two key-parameters of this study, the escape fraction of ionising photons and the clumping factor of IGM ionised hydrogen. Then we look in Sect. 4 for the redshift-evolution we will further consider for the star formation rate (SFR) density, extrapolating luminosity functions at $z \gtrsim 10$. Doing this, we study the impact of our observational constraints on $\rho_{\rm SFR}$. Investigations are then made on the escape fraction value and on how observations can constrain it: we try several parametrisations out – a redshift-independent one, where $f_{\rm esc}$ is free to vary in $[0.1, 0.4]$, and a power-law function of z. We proceed the same for $C_{\rm H\,II}$, but this time considering several possible parametrisations of its evolution with redshift, mainly from Iliev et al. (2007) and Pawlik et al. (2009). We conclude with a discussion of our results in Sect. 5, including a test of different values for the magnitude limit, and a summary in Sect. 6.

Throughout this paper, all cosmological calculations assume the flatness of the Universe and use the Planck cosmological parameters (Planck Collaboration et al. 2016a): $h = 0.6774$, $\Omega_{\rm m} = 0.309$, $\Omega_{\rm b}h^2 = 0.02230$ and $Y_{\rm p} = 0.2453$. Unless otherwise stated, all distances are comoving.

2. Observables of reionisation

2.1. Drawing the history of reionisation

Clues about the reionisation process can be derived from various observables. Under the assumption that star-forming galaxies provided the majority of the photons which ionised the IGM, the star formation rate density, $\rho_{\rm SFR}$, can logically give precious information about the EoR. Values of SFR density with redshift are deduced from luminosity functions (LF) of star-forming galaxies. LF can be observed down to a certain magnitude, but needs to be extrapolated to consider the contribution of unobserved fainter galaxies. Equation 1 shows how the comoving ionisation rate $\dot{n}_{\rm ion}$ is computed from the LF.

$$\begin{aligned}\dot{n}_{\rm ion} &= \int_{M_{\rm lim}}^{\infty} \phi(M_{\rm UV})\, f_{\rm esc}(M_{\rm UV})\, \xi_{\rm ion}(M_{\rm UV})\, {\rm d}M_{\rm UV} \\ &\simeq \langle f_{\rm esc}\, \xi_{\rm ion}\rangle \int_{M_{\rm lim}}^{\infty} \phi(M_{\rm UV})\, {\rm d}M_{\rm UV} \\ &\simeq f_{\rm esc}\, \xi_{\rm ion}\, \rho_{\rm SFR}. \end{aligned} \quad (1)$$

The final expression directly relates $\rho_{\rm SFR}$ to the cosmic reionisation rate $\dot{n}_{\rm ion}$, in units of photons per unit time per unit volume, and is the version we will use in our models. We see that the choice of $M_{\rm lim}$ is fundamental as it directly impacts the value of $\rho_{\rm SFR}$. Bouwens et al. (2015a) state that faint galaxies must contribute to the total UV radiation from galaxies but, assuming they do not form efficiently for lower luminosities (see Rees & Ostriker 1977; Mac Low & Ferrara 1999; Dijkstra et al. 2004), Robertson et al. choose to use $M_{\rm lim} = -13$ rather than $M_{\rm lim} = -17$, a choice we will discuss in this paper.

Two important parameters are used in Eq. 1: $f_{\rm esc}$ and $\xi_{\rm ion}$. They describe the fact that only a limited amount of the photons produced by star-forming galaxies eventually end up ionising the IGM: first, they need to have sufficient energy – above the Ly-α limit, and second, they must escape their host galaxy and reach the IGM. The first condition is conveyed by $\xi_{\rm ion}$, the quantity of Lyman continuum photons produced per second and per unit SFR for a typical stellar population. According to Robertson et al. (2015), we take $\xi_{\rm ion} = 10^{53.14}$ Lyc photons s^{-1} M$_\odot^{-1}$ yr. The second condition is conveyed by $f_{\rm esc}$, the fraction of ionising radiation coming from stellar populations which is not absorbed by dust and neutral hydrogen within the host galaxy and so does contribute to the process. We note that in Eq. 1 we chose to consider values of $f_{\rm esc}$ and $\xi_{\rm ion}$ averaged over magnitude, i.e. the effective values.

Aiming to reproduce observations on the star formation history from $z \sim 30$ to $z \sim 1$, we choose the four-parameter model suggested by Robertson et al. (2015), updated from Madau & Dickinson (2014, Sect. 5, Eq. 15) and described in Eq. 2 below. According to data, $\rho_{\rm SFR}(z)$ follows a first rising phase, over $3 \lesssim z \lesssim 15$, which is expressed in our parametrisation by an evolution $\rho_{\rm SFR}(z) \propto (1+z)^{b-d}$, up to a peaking point around $z \sim 1.8$, that is, when the Universe was around 3.6 Gyr old. It then declines as $\rho_{\rm SFR}\,(z) \propto (1+z)^{b}$ until $z = 0$. To stay consistent with observations, we set $b > 0$ and $b - d < 0$.

$$\rho_{\rm SFR}(z) = a \frac{(1+z)^b}{1 + \left(\frac{1+z}{c}\right)^d}. \quad (2)$$

In order to put our results in perspective, we consider different values of the magnitude limit for our study and therefore use another parametrisation of the star formation history, suggested by Ishigaki et al. (2015) and designed to reproduce the rapid decrease of $\rho_{\rm UV}(z)$ from $z \sim 8$ towards higher redshifts and but not the bump on luminosity density observed around $z \sim 2$

$$\rho_{\rm UV}(z) = \frac{2\,\rho_{\rm UV}(z=8)}{10^{a(z-8)} + 10^{b(z-8)}}. \quad (3)$$

Here, $\rho_{\rm UV}(z = 8)$ is a normalisation factor, and a and b characterise the slope of $\rho_{\rm UV}(z)$. This model is more adapted to the study of reionisation in itself, as the process is known to end before $z = 4$ and so before the star formation bump. However we cannot limit our analysis to this late-redshift model since the former carries more information about the reionisation history and is therefore more interesting when considering a large amount of free parameters. We note that for $M_{\rm lim} = -10$ and $M_{\rm lim} = -17$, we use $\xi_{\rm ion} = 10^{25.2}$ erg^{-1} Hz, following Ishigaki et al. (2015).

Other observations can lead to estimations of the fraction of ionised IGM $Q_{\rm H\,II}$, also called filling factor, which relates to the SFR density via Eq. 4. In this equation, the time-related evolution of $Q_{\rm H\,II}$ depends on two contributions: an ionisation source term, proportional to $\dot{n}_{ion}$, and a sink term due to the competition of recombination. $t_{\rm rec}$ is the IGM recombination time defined in Eq. 5 and $\langle n_{\rm H}\rangle$ is the mean hydrogen number density, defined by $\langle n_{\rm H}\rangle = \frac{X_{\rm p}\Omega_{\rm b}\rho_{\rm c}}{m_{\rm H}}$, with $\rho_{\rm c}$ the critical density of the Universe.

$$\dot{Q}_{H_{II}} = \frac{\dot{n}_{\rm ion}}{\langle n_{\rm H}\rangle} - \frac{Q_{\rm H\,II}}{t_{\rm rec}}, \quad (4)$$

$$\frac{1}{t_{\rm rec}} = C_{\rm H\,II}\,\alpha_{\rm B}(T)\left(1+\frac{Y_{\rm p}}{4X_{\rm p}}\right)\langle n_{\rm H}\rangle\,(1+z)^3. \quad (5)$$

In Eq. 5, $X_{\rm p}$ and $Y_{\rm p}$ are the primordial mass fraction of Hydrogen and Helium respectively. $\alpha_{\rm B}(T)$ is the case B recombination coefficient at a fiducial IGM temperature of $T = 20\,000$ K, often considered as the mean temperature around a newly ionised atom. This value is consistent with measurements at $z \sim 2-4$ (Lidz et al. 2010) but has been estimated to $T \lesssim 10^4$ K at $z \sim 5-6$ (Becker et al. 2011; Bolton et al. 2012). It fluctuates by a factor of between one and two, depending on the spectrum of the sources and on the time passed since reionisation (Hui & Haiman 2003). Yet, $\alpha_{\rm B}$ is expressed as $\alpha_{\rm B}(T) \approx 2.6\times10^{-13}\,T_4^{-0.76}$ cm^3 s^{-1} with $T_4 = T/10^4$ K (Osterbrock 1989), in other words, it is a weak function of T so that its variations do not affect our results significantly. We note that, rather than case A, we considered case B recombinations in order to exclude recombinations to the ground state and because we consider that ionisations and recombinations are distributed uniformly throughout the IGM, so that each regenerated photon soon encounters another atom to ionise (Loeb & Furlanetto 2013, Sect. 9.2.1). The clumping factor $C_{\rm H\,II}$ expresses how ionised hydrogen nuclei are distributed throughout the IGM. $C_{\rm H\,II}$ and $t_{\rm rec}$ are inversly proportional: the more the matter is aggregated in clumps, the easier for ionised atoms to recombine in these very same clumps.
To compare with the evolution derived from Eq. 4, we considered two parametrisations of the time evolution of the filling factor $Q_{\rm H\,II}$, that we will then use to calculate the integrated Thomson optical depth from data. The first depicts the reionisation process as a step-like and instantaneous transition with a hyperbolic tangent shape (Eq. 6). The second is a redshift-asymmetric parametrisation, described in Eq. 7, inspired by Douspis et al. (2015). It uses a power-law defined by two parameters i.e. the redshift at which reionisation ends $z_{\rm end}$ and the exponent α:

$$Q_{\rm H\,II}(z) = \frac{f_{\rm e}}{2}\left[1+\tanh\left(\frac{y-y_{\rm re}}{\delta y}\right)\right], \quad (6)$$

$$Q_{\rm H\,II}(z) = \begin{cases} f_{\rm e} & \text{for } z < z_{\rm end}, \\ f_{\rm e}\left(\frac{z_{\rm early}-z}{z_{\rm early}-z_{\rm end}}\right)^{\alpha} & \text{for } z > z_{\rm end}. \end{cases} \quad (7)$$

where $y(z) = (1+z)^{\frac{3}{2}}$, $y_{\rm re} = y(z = z_{\rm re})$ for $z_{\rm re}$ the redshift of instantaneous reionisation and $\delta y = \frac{3}{2}(1+z)^{\frac{1}{2}}\,\delta z$. $z_{\rm early}$ corresponds to the redshift around which the first emitting sources form, and at which $Q_{\rm H\,II}(z)$ is matched to the residual ionised fraction ($\overline{\rm x} = 10^{-4}$). To be consistent with observations, which give $Q_{\rm H\,II}(z \leq 6.1) \simeq 1$ with very low uncertainty (McGreer et al. 2015), we choose $z_{\rm end} = 6.1$. Furthermore, when comparing our findings with the Planck results we set $z_{\rm re}$ at equal to 8.8, $z_{\rm early} = 20$, and also $\alpha = 6.6$ (Planck Collaboration et al. 2016b).

Observations of CMB satellites allow us to estimate the Thomson optical depth τ, integrated over the electron column density to the last scattering surface. It expresses the fraction of photons scattered along the line of sight by free electrons and thus is a direct indicator of the global ionisation rate of the IGM. It is related to the two previously described observables $Q_{\rm H\,II}$ and $\rho_{\rm SFR}$ via Eq. 8, where c is the speed of light in vacuum, $\sigma_{\rm T}$ the Thomson scattering cross-section, $H(z)$ the Hubble constant and $f_{\rm e}$ the number of free electrons per Hydrogen nucleus. We have assumed that Helium is doubly ionised at $z \leq 4$ (Kuhlen & Faucher-Giguère 2012) and thus have $f_{\rm e} = 1 + \eta Y_{\rm p}/4X_{\rm p}$ with $\eta = 2$ for $z \leq 4$ and $\eta = 1$ for $z > 4$.

$$\tau(z) = c\,\langle n_{\rm H}\rangle\,\sigma_{\rm T}\int_0^z f_{\rm e}\,\frac{Q_{\rm H\,II}(z')}{H(z')}\,(1+z')^2\,{\rm d}z' \quad (8)$$

2.2. Configuring the key-parameters of reionisation

Among the various parameters cited in Sect. 2.1, two key-parameters of the reionisation history are still under a lot of investigations: the escape fraction and the clumping factor. As mentioned before, $f_{\rm esc}$ expresses the fraction of the ionising radiation produced by stellar populations which is not absorbed by dust and neutral hydrogen within its host galaxy, and thus contributes to the ionisation of the IGM. In our approach, it is an effective value, averaged over stochasticity, halo mass dependencies in the source populations and, most importantly, over all sources considered in the Universe. This averaged value is hard to compare with observations of lone galaxies or haloes, which usually give much lower values. For instance, Steidel et al. (2001) and Iwata et al. (2009) estimate the escape fraction of some $z \sim 3$ galaxies to be $\gtrsim 1\%$. On the contrary, overall values of $f_{\rm esc}$ can be derived from simulations but are still highly uncertain. According to Finkelstein et al. (2015) and to agree with Ly-α forests measurements (Bolton & Haehnelt 2007), it should not be higher than 0.13; Fernandez et al. (2013) use a value of 0.1 from a simulation; Robertson et al. (2015) deduce from their analysis that, in order to have star-forming galaxies driving the reionisation process at high redshift, $f_{\rm esc}$ must equal at least 0.2; Inoue et al. (2006) find that, if recent values of the escape fraction can be as low as $f_{\rm esc} = 0.01$ at $z \sim 1$, $f_{\rm esc}$ increases quickly with redshift to reach 10% at $z \gtrsim 4$. Finally, Dunlop et al. (2013) assure that, considering the spectral energy distributions observed from high-redshift galaxies, it should be $\approx 0.1-0.2$. Yoshiura et al. (2017) summarise results on $f_{\rm esc}$ by saying that if it is generally acknowledged that, among all dependencies, the escape fraction decreases with the mass of the galaxy, there is a variance within one or two orders of magnitude among simulations results. For instance, a simulation from Yajima et al. (2014), on which assumptions of Robertson et al. (2015) are based, shows that, amidst all types of photons produced in star-forming galaxies (Ly-α, UV-continuum and ionising photons), the escape fraction of ionising photons is the only one which seems to depend neither on the redshift nor on the galaxy properties: it keeps a constant value of 0.2 with time, that we use for our first analysis.

However, photons from different ranges of energy are subject to different physical phenomena and thus escape more or less easily from their host galaxy. For instance, dust extinguishes ionising, Ly-α and UV continuum photons similarly, but only ionising photons are also absorbed by neutral hydrogen clumps. Thus, at high redshifts, when there is little dust around the galaxy, photons of all energy ranges escape as easily; on the contrary, at low redshift, ionising photons experience more difficulties to escape than others (Yajima et al. 2014). We can then infer an increase of $f_{\rm esc}$ with redshift that we parametrise in Eq. 9, defined for $z \geq 4$ and inspired by Kuhlen & Faucher-Giguère (2012); Chisholm et al. (2018). This evolution corresponds to either an evolution of the SFR of galaxies themselves and its associated feedback, or by a redshift evolution in the make up of the galaxy population. Here, owing to the UV spectral slope constraints, we set a maximum of 1 for the $f_{\rm esc}$ value, corresponding to a situation where

all ionising photons escape.

$$f_{\rm esc}(z) = \alpha \left(\frac{1+z}{5}\right)^{\beta}. \quad (9)$$

In this parametrisation, also close to the one used in Price et al. (2016), α is the value of $f_{\rm esc}$ at $z = 4$ and $\alpha\beta/5$ of its derivative at $z = 4$, redshift at which we expect the hydrogen ionising background to be dominated by star-forming galaxies (Kuhlen & Faucher-Giguère 2012). We take β positive in order to have an increasing escape with redshift, as anticipated earlier.

The second key-parameter of the reionisation process which we are going to investigate is the clumping factor of ionised hydrogen in the IGM $C_{\rm H\,II}$, used in Eq. 5. It expresses how ionised hydrogen nuclei are gathered in heaps throughout the IGM. This parameter is essential because it is the growth of these clumps that allows the reionisation front to progress in the IGM and because competing recombinations will predominantly take place there. A precise estimate of $C_{\rm H\,II}$ can be difficult to obtain. Simulations do indeed have several obstacles to overcome: getting a sufficient precision for the gas distribution, a correct topology of ionised and neutral matter, and an accurate model of the evolution of gas clumps themselves during the reionisation process. Besides, $C_{\rm H\,II}$ is often first defined on a single ionisation bubble and then summed on all bubbles to get the global volume-averaged value used here: the simulation must consider an extremely wide range of scales (Loeb & Furlanetto 2013, Sec. 9.2).

Most recent studies use values ranging from one to six at the redshifts of interest, i.e. for $6 \lesssim z \lesssim 30$ (Sokasian et al. 2003; Iliev et al. 2006; Raičević & Theuns 2011; Shull et al. 2012; Robertson et al. 2015; Finkelstein et al. 2015; Bouwens et al. 2015a). Other studies predict a redshift-dependent evolution (Iliev et al. 2007; Pawlik et al. 2009; Haardt & Madau 2012; Finlator et al. 2012; Sobacchi & Mesinger 2014), justified by the fact that during the late stages of EoR, ionisation fronts penetrate into increasingly overdense regions of the IGM, which have higher recombination rates and so drive a rapid increase of $C_{\rm H\,II}$ (Furlanetto & Oh 2005; Sobacchi & Mesinger 2014). In our study, besides constant values of $C_{\rm H\,II}$, we consider two parametrisations son the redshift range $3 \leq z \leq 30$[1] :

$$C_{\rm H\,II}(z) = \alpha + a\left(\frac{z}{8}\right)^{b}, \quad (10)$$

$$C_{\rm H\,II}(z) = a\,{\rm e}^{\,b\,(z-8)\,+\,c\,(z-8)^2}. \quad (11)$$

The first expression comes from Haardt & Madau (2012). We update it in order to have $a = C_{\rm H\,II}(z = 8) - \alpha$ because $Q_{\rm H\,II}$ is close to 0.5 at $z = 8$. The second one comes from Mellema et al. (2006) and Iliev et al. (2007) and shows a different behaviour: it is convex and has a minimum at $z_{\rm min} = -b/2c$. As explained earlier, it is generally admitted that the clumping factor only decreases with z, and therefore we set $z_{\rm min} \gtrsim 30$ so that $C_{\rm H\,II}$ does not reach its minimum on our analysis range. For the same reason, a and b from Eq. 10 have to be of opposite signs and more precisely we take $a > 0$ and $b < 0$ in order to have $C_{\rm H\,II}(z) \underset{z\to 0}{\longrightarrow} +\infty$.

The formal definition of the clumping factor is (Bouwens et al. 2015a; Robertson et al. 2015): $C_{\rm H\,II} = \langle n_{\rm H\,II}^2\rangle / \langle n_{\rm H\,II}\rangle^2 = 1 + \delta_{\rm H\,II}$, if we define the overdensity of ionised Hydrogen as $\delta_{\rm H\,II} = (n_{\rm H\,II} - \langle n_{\rm H\,II}\rangle)/\langle n_{\rm H\,II}\rangle$. Long before the EoR, most of the Hydrogen was neutral so that fluctuations in the ionised Hydrogen overdensity were very weak. In this perspective, we consider in our models that $\delta_{\rm H\,II}(z \to \infty) = 0$ and so take $C_{\rm H\,II}(z = 100) = 1$.

[1] We assume that $C_{\rm H\,II}$ is the same for H II and He III on this range.

3. Data

The SFR density can be estimated via the observed infrared and rest-frame UV LFs. We use the luminosity densities and SFR densities compiled by Robertson et al. (2015), computed from Madau & Dickinson (2014), Schenker et al. (2013), McLure et al. (2013), Oesch et al. (2015) and Bouwens et al. (2015a). Robertson et al. also use HST Frontier Fields LF constraints at $z \sim 7$ by Atek et al. (2015) and at $z \sim 9$ by McLeod et al. (2015). Estimates of Madau & Dickinson (2014) derived from Bouwens et al. (2012) are updated with newer measurements by Bouwens et al. (2015a). For the calculation of $\rho_{\rm SFR}$, as a start, luminosity functions of star-forming galaxies are extended to UV absolute magnitudes of $M_{\rm lim} = -13$. Then we compared this with results for minimal and maximal magnitude limits $M_{\rm lim} = -17$ and $M_{\rm lim} = -10$. We note that if Robertson et al. (2015) express $\rho_{\rm SFR}$ in $\rm M_\odot\ yr^{-1}\ Mpc^{-3}$, Ishigaki et al. (2015) use UV luminosity units, i.e. ergs $\rm s^{-1}\ Hz^{-1}\ Mpc^{-3}$. In order to compare results, we used the conversion factor used in Bouwens et al. (2015a) and first derived by Madau et al. (1998):

$$\rm L_{UV} = \frac{SFR}{M_\odot\,yr^{-1}} \times 8.0 \times 10^{27}\ ergs\,s^{-1}\,Hz^{-1}.$$

UV luminosity densities used in this work are the ones detailed in Ishigaki et al. (2015), namely they come from Schenker et al. (2013); McLure et al. (2013); Bouwens et al. (2007, 2014, 2015b); Oesch et al. (2015).
Observations related to the ionised fraction of the IGM $Q_{\rm H\,II}$ used as constraints to our fits include the Gunn-Peterson optical depths and the dark-gap statistics measured in $z \sim 6$ quasars (McGreer et al. 2015), damping wings measured in $z \sim 6 - 6.5$ quasars (Schroeder et al. 2013) and the prevalence of Ly-α emission in $z \sim 7 - 8$ galaxies (Schenker et al. 2013; Tilvi et al. 2014; Faisst et al. 2014). We note that in the figures, further data points, not used as constraints in the fit, are displayed to use as comparison. These include observations of Lyman-α emitters (Konno et al. 2017; Ouchi et al. 2010; Ota et al. 2008; Caruana et al. 2014), of near-zone quasars (Mortlock et al. 2011; Bolton et al. 2011) and of a gamma-ray burst (Chornock et al. 2014).
Last, we consider estimations of the Thomson optical depth derived from Planck Satellite observations: $\tau_{\rm Planck} = 0.058 \pm 0.012$ for a redshift of instantaneous reionisation $z_{\rm reio} = 8.8 \pm 0.9$ (Planck Collaboration et al. 2016b). We compare it to the asymptotic value τ obtained from our model calculations at high redshift.

4. Results

4.1. Cosmic star formation history

Since we are interested in the reionisation history both up to and beyond the limit of the current observational data, we adopt the four-parameter model from Eq. 2 into a Monte Carlo Markov chain (MCMC) approach. We perform a maximum likelihood (ML) determination of the parameter values assuming Gaussian errors on a redshift range of [0, 30], extrapolating current observations on star formation history from $z = 10.4$ to $z = 30$. We

fit to the star formation data described in Sect. 3 and then compute the range of credible reionisation histories for every value of the $\rho_{\rm SFR}$ model parameters by solving the differential equation of Eq. 4. Filling factor data is used as an additional observational prior for the fit. Finally, we evaluated the Thomson optical depth as a function of z via Eq. 8 and compare its 'asymptotic' value, at $z = 30$, to $\tau_{\rm Planck} = 0.058 \pm 0.012$ (Planck Collaboration et al. 2016b) as a last constraint on the fit. Because we want to know what observable constrains reionisation history the most, all constraints are not always used: the run **ALL** uses all three sets of data as constraints; **NOQ** skips $Q_{\rm H\,II}$ data; **NORHO** skips star formation data, and **ORHO** uses only star formation history in the fit.

In this first step, we adopt the fiducial, constant with redshift values $f_{\rm esc} = 0.2$, $\log_{10}\xi_{\rm ion} = 53.14$ [Lyc photons $\rm s^{-1} M_\odot^{-1}$ yr] and $C_{\rm H\,II} = 3$ (e.g. Pawlik et al. 2009; Shull et al. 2012; Robertson et al. 2013, 2015). Results are summarised in Fig. 1 and in Table 1. Fig. 2a shows resulting star formation history and Fig. 2b resulting reionisation history. We find that star formation history constrains reionisation the most: both figures show that **ALL** and **ORHO** runs give similar evolutions and close ML values for a, b, c, and d (see Table 4). We note that our constraints with **ORHO** and **ALL** are dominated by the $\rho_{\rm SFR}$ data points at a redshifts of approximately five and the fixed functional form assumed for $\rho_{\rm SFR}(z)$; they are fully consistent with Robertson et al. (2015). On the contrary, for **NORHO**, the shape of $\rho_{\rm SFR}(z)$ is changed and reionisation begins much later, around $z \sim 12$ rather than $z \sim 15$ for other runs. **NORHO** results must be handled carefully as its parameters probability density functions (PDFs) are extremely spread-out; the **NORHO** line drawn on figures corresponds to the median values of parameters. All we can conclude is that, when star formation history constraints are skipped, there is a much wider range of possible scenarios.

Interestingly, Fig. 2b shows that for each run considering star formation history constraints, the process begins as early as $z = 15$. This is hardly compatible with WMAP results which stated that, if we consider reionisation as instantaneous, it should occur at $z_{\rm reio} \simeq 10.5 \pm 1.1$ (Hinshaw et al. 2013) and so cannot begin before $z = 12$. Observations also have an influence on the Thomson optical depth values, as **NORHO** gives a slightly lower value of τ (0.053 ± 0.003 compared to 0.061 ± 0.001 for **ALL**). Yet, all results remain in the 1-σ confidence interval of $\tau_{\rm Planck}$.

In the rest of the study we used the **ALL** run as our definitive parametrisation for $\rho_{\rm SFR}$ evolution with redshift: definitive parameters for Eq. 2 are ($a = 0.146$, $b = 3.17$, $c = 2.65$, $d = 5.64$) from Table 1. ML parameters for other runs can be found in Table 4.

Table 1: ML model parameters for a model using all three sets of constraints.

a	b	c	d	τ
0.146	3.17	2.65	5.64	0.0612
±0.001	±0.20	±0.14	±0.141	±0.0013

4.2. Escape fraction of ionising photons $f_{\rm esc}$

In order to study the role of the escape fraction in this analysis we chose, as detailed in Sect. 2.2, to first consider it as a fifth parameter of the fit – on top of (a, b, c, and d) from Eq. 2, free to vary between 0 and 0.4. We name **ALL** the run which uses $\rho_{\rm SFR}$, $Q_{\rm H\,II}$ and τ constraints, and **NOQ** the one that

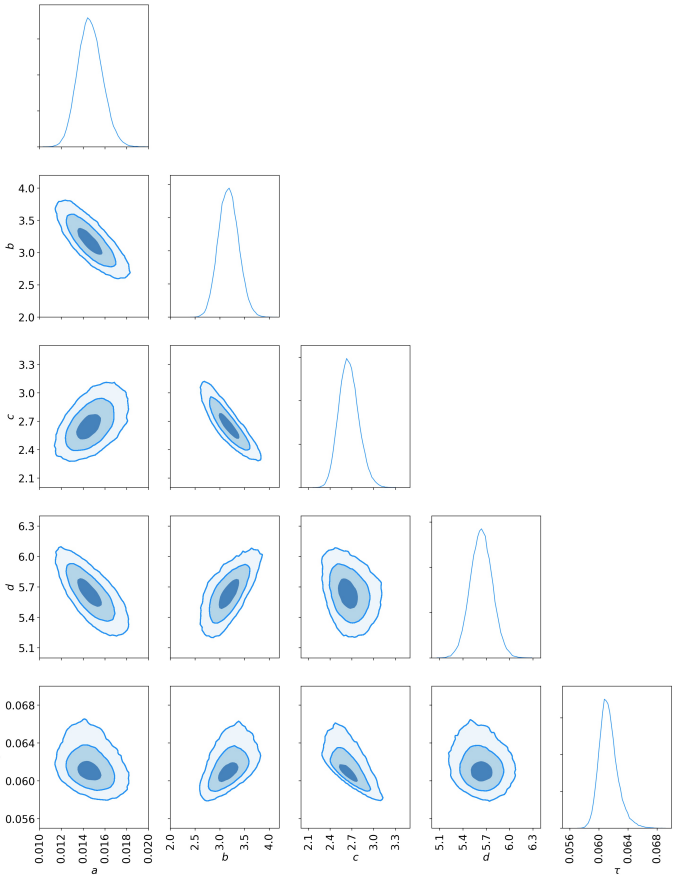

Fig. 1: Results of the MCMC analysis for the **ALL case**. The contours show the 1, 2, 3 σ confidence levels for a, b, c, d and the derived parameter τ.

skips ionisation level constraints. $f_{\rm esc}$ is involved only in the $\dot{n}_{\rm ion}$ calculation of Eq. 1 and not in the one of $\rho_{\rm SFR}$ so that star formation history takes no part in the computation of $f_{\rm esc}$. This explains why for all runs, results on the SFR density are close to the ones of Sect. 4.1 (see Tables 4 and 5 for details). For **ALL**, we get ML parameters ($a = 0.0147$, $b = 3.14$, $c = 2.69$, $d = 5.74$). Figure 3 shows that $Q_{\rm H\,II}$ constraints have a strong influence on $f_{\rm esc}$: confidence intervals are much wider for **NOQ** than for **ALL** (see Table 5). Besides, the **NOQ** PDF of $f_{\rm esc}$ is almost flat: standard deviation is equal to 0.079, that is, around 30% of the mean value and two times more than for **ALL**. For now, we chose to use $f_{\rm esc} = 0.19 \pm 0.04$, in other words, the median value of the escape fraction for the **ALL** run, when a redshift-independent value is needed for $f_{\rm esc}$. The full triangle plot for the **ALL** case is shown Fig. A.1 in Appendix.

We now turn to the possibility of a redshift evolution in $f_{\rm esc}$ for $z \in [4, 30]$. We perform an MCMC maximum likelihood sampling of the two-parameter parametrisation described in Eq. 9. For the reasons explained above on the lack of relation between $\rho_{\rm SFR}$ and $f_{\rm esc}$, we do not use star formation data as a constraint any more and assume that the time evolution of the SFR density follows Eq. 2 using parameters (a, b, c, d) resulting from Sect. 4.1. We used parameters corresponding to the set of constraints that is used on $f_{\rm esc}$: if only τ priors are considered here, we use (a, b, c, and d) resulting from a **NOQ** run (see Table 4 for values).

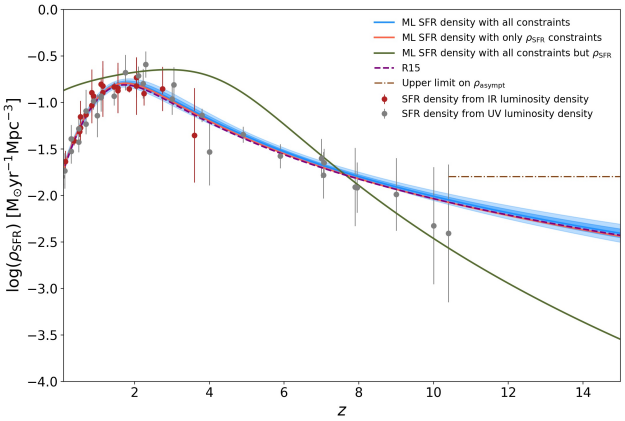

(a)

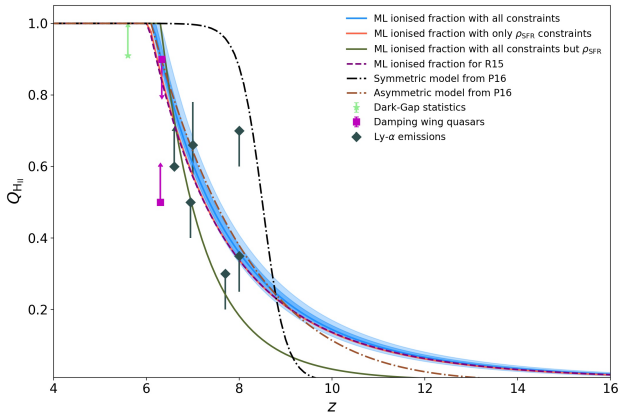

(b)

Fig. 2: (a) Star formation rate density $\rho_{\rm SFR}$ with redshift. Data points are determined from infrared (plotted in red) or ultraviolet (in grey) luminosity densities (Sect. 3). Maximum likelihood parametrisations (continuous lines) are shown for various set of constraints: blue when all constraints are used; coral when only data on star formation are used; green when τ and reionisation history data are used. The 68% confidence interval on $\rho_{\rm SFR}$ (light blue region) is drawn for the blue model. We note that the interval, corresponding to statistical uncertainties, is very narrow. These inferences are compared with a model forced to reproduce results from Robertson et al. (2015), cited as R15 in the legend, drawn as the purple dotted line. The horizontal dashed-dotted line corresponds to the upper limit on a hypothetical constant value of $\rho_{\rm SFR}$ for $z > 10.4$ (Section 5.2). (b) Ionised fraction of the IGM $Q_{\rm H\,II}$ with redshift for same models as (a). Details on the origin of data points are given in the legend and Sect. 3. Inferences are also compared with the two evolutions used in Planck Collaboration et al. (2016b, cited as P16) to model the reionisation process: a redshift-symmetric hyperbolic tangent as the brown dashed-dotted line and a redshift-asymmetric power-law in black.

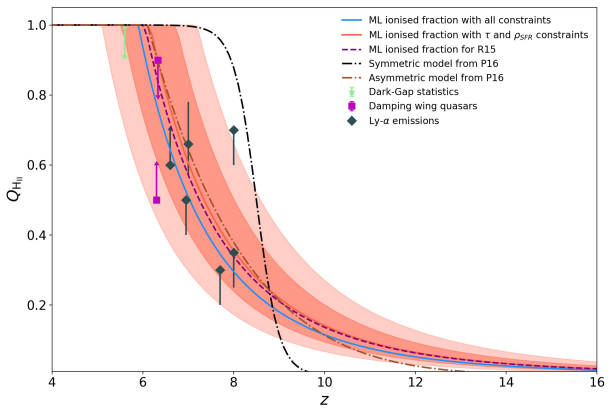

Fig. 3: Ionised fraction of the IGM $Q_{\rm H\,II}$ with redshift when $f_{\rm esc}$ is introduced as a parameter. Details on the origin of data points are given in the legend. ML models (continuous lines) are shown for various set of constraints: blue when all constraints are used, coral when $Q_{\rm H\,II}$ constraints are skipped, for which the 68% and 95% confidence intervals are drawn in salmon. These inferences are compared with a model forced to reproduce results from Robertson et al. (2015, R15, purple dotted line) and with the two evolutions used in Planck Collaboration et al. (2016b, P16): redshift-symmetric as the dashed-dotted brown line and redshift-asymmetric in black.

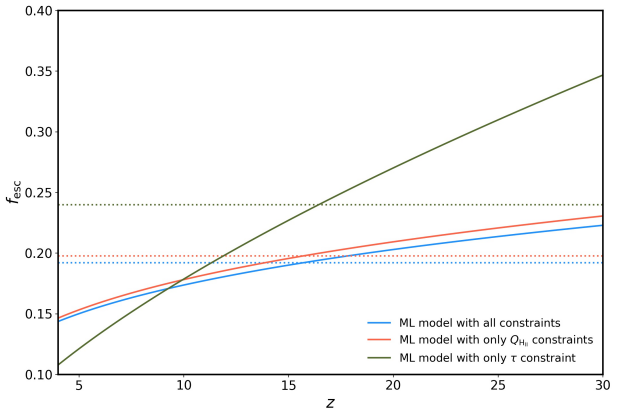

Fig. 4: Possible evolutions of $f_{\rm esc}$ with redshift. ML models are shown for various set of constraints: blue when all constraints are used; coral when τ constraints are skipped; green when $Q_{\rm H\,II}$ constraints are skipped. Horizontal dotted lines represent the mean value of $f_{\rm esc}$ over $4 \leq z \leq 30$ for the model of the corresponding colour.

We find that priors on the IGM ionisation level have a much stronger influence on results than the Thomson optical depth. Indeed, Fig. 4 shows that ML evolutions using both $Q_{\rm H\,II}$ and τ constraints or only $Q_{\rm H\,II}$ are very similar: mean values for $z \geq 4$ are similar by $\sim 3\%$ and in both cases, the evolution with redshift is rather weak, as values range from 0.15 around $z \sim 4$ to 0.24 around $z \sim 30$. We note that if Mitra et al. (2015) draw a similar conclusion of an almost constant $f_{\rm esc}$ value with redshift from their modelling, they obtain lower values of the escape fraction with an average of about 10% in the redshift range six to nine. For **NOQ**, the optical depth remains surprisingly close to other models and to $\tau_{\rm Planck} = 0.058 \pm 0.012$, around 0.061. The difference is apparent in the evolution of the ionised fraction, as reionisation begins and ends later, around $z = 6$ rather than $z = 6.4$ in this case; on the contrary, when $Q_{\rm H\,II}$ data is used, the history tends to be the same as in previous analysis. Our

results when only $\tau_{\rm Planck}$ constraints are considered are quite similar to those of Price et al. (2016) in which authors study the evolution of $f_{\rm esc}$ with redshift. They mainly use constraints from $\tau_{\rm Planck}$, concluding to a strong increase of $f_{\rm esc}$ from about 0.15 to about 0.55, depending on the observational constraints used. ML parameters for Eq. 9 when all constraints are considered are ($\alpha = 0.14 \pm 0.02, \beta = 0 \pm 0.3$) and give a mean value for $f_{\rm esc}$ of about 0.20, which is extremely close to the 0.19 ± 0.04 found when considering the escape fraction constant with redshift (see Table 5 for details).

4.3. Clumping factor of ionised hydrogen in the IGM $C_{\rm H\,II}$

Following the definition of Sect. 2.2, we now investigate the constraints on $C_{\rm H\,II}$ set by observations. As we did in Sect. 4.2 for $f_{\rm esc}$, we added $C_{\rm H\,II}$ as a fifth parameter of the fit on $\rho_{\rm SFR}$ using Eq. 2, apart from (a, b, c, d). It is free to vary between zero and ten, the order of magnitude of fiducial values most commonly used in publications (e.g. Shull et al. 2012; Robertson et al. 2013, 2015). Here again, we call **ALL** the run using all constraints in the fit, and **NOQ** the one that skips $Q_{\rm H\,II}$ constraints.
After performing the MCMC ML sampling of the five parameters (see Table 4 for details), we get a quite spread PDF for $C_{\rm H\,II}$ with **ALL**: the standard deviation is equal to 1.85 for a median value of 4.56. Even with such a wide range of possible values, the range of possible reionisation histories remains very narrow and the Thomson optical depth PDF is almost exactly the same as when we take $C_{\rm H\,II} = 3$: $\tau_{\rm ALL} = 0.0570 \pm 0.0019$ to be compared with $\tau_{C_{\rm H\,II}=3} = 0.0612 \pm 0.0013$ (see Table 2 and Fig. A.2 in Appendix). Besides, for **NOQ**, the range of possible reionisation histories is wider than for **ALL**: the width of the 95% confidence area is about 0.6 when ML reionisation model is halfway through ($Q_{\rm H\,II} = 0.5$) for **NOQ** but 0.16 for **ALL**. We also note that for **NOQ** τ takes lower values ($\tau_{\rm NOQ} = 0.0561 \pm 0.0064$) but remains, as others, in the 1-σ confidence interval of $\tau_{\rm Planck}$. This confirms that IGM ionisation level data are compatible with Planck observations and that the value of $C_{\rm H\,II}$ constrains only slightly the reionisation history.

We now successively test the two redshift-dependent models of the clumping factor given in Eq. 10 and 11. $C_{\rm H\,II}$ is not involved in the calculation of $\rho_{\rm SFR}$ but only of the recombination time. Thus, as for $f_{\rm esc}$, star formation history data have no influence over it: the **ALL** run is now constrained by $Q_{\rm H\,II}$ and $\tau_{\rm Planck}$ only. We also note that, for low values of z (precisely for $z \leq 6.8$), $Q_{\rm H\,II}$ becomes higher that 1 in our calculations, which is physically irrelevant so we ignore results in this range.

Once again, IGM reionisation level data constrain results more than $\tau_{\rm Planck}$. The redshift-evolution of $C_{\rm H\,II}$ and $Q_{\rm H\,II}$ for the two parametrisations presented in Sect. 2.2 and for **ALL** runs are shown in Figs. 5a and 5b. We see on the left panel that there are a lot of possible output evolutions for both models but this does not translate in significant variations of $Q_{\rm H\,II}(z)$ whose 68% confidence intervals are found to be very narrow. All scenarios remain quite close, with reionisation beginning around $z = 16$ and ended by $z = 6$. This means that, as in previous paragraph where $C_{\rm H\,II}$ was assumed constant with redshift, its exact value has no significant impact on the reionisation history. In fact, variations in $C_{\rm H\,II}$ have some impact on the computed Thomson optical depth: as seen in Table 2, higher values of $C_{\rm H\,II}$ allow for a lower value of τ – consistent with Eqs. 5 and 8. All values remains in the 1-σ confidence interval of $\tau_{\rm Planck}$.

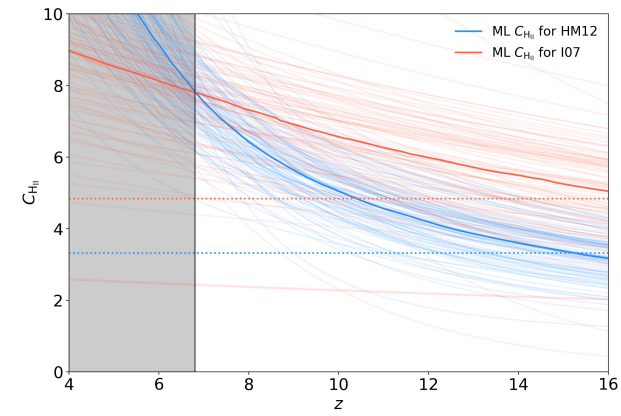

(a)

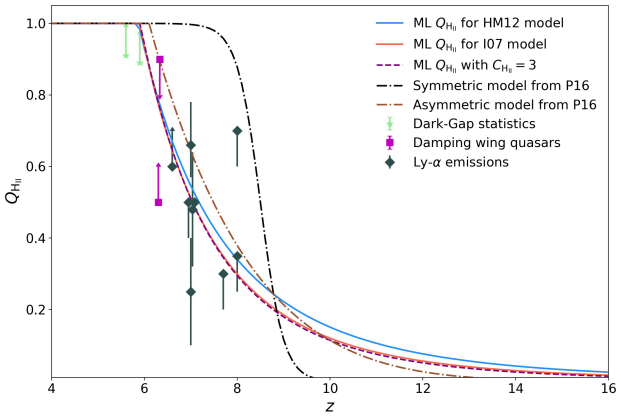

(b)

Fig. 5: (a) Possible evolutions of $C_{\rm H\,II}$ with redshift. ML models are shown for the two models of Sect. 2.2: blue for the first, coral for the second. Dotted horizontal lines correspond to the mean value of $C_{\rm H\,II}(z)$ for $z > 6.8$, where outputs of the model are used in calculations, for the model of the corresponding colour. The vertical line is located at $z = 6.8$. Lines of lighter colours represent various outputs of the sampling of the corresponding model. (b) Redshift evolution of $Q_{\rm H\,II}$ for the same models of $C_{\rm H\,II}(z)$. Inferences are compared to a result with $C_{\rm H\,II}(z) = 3$ in purple dashed line, and to the theoretical models of Planck Collaboration et al. (2016b): a redshift-symmetric model in black and a redshift-asymmetric model in brown.
References. HM12: Haardt & Madau (2012) or Eq. 10. I07: Iliev et al. (2007) or Eq. 11.

Finally, it seems that the fiducial constant value often used in papers,$C_{\rm H\,II} = 3$, and which lies between the mean values of our models (~ 3 for **HM12**, 1.8 for **I07**, and 4.5 for **Free**), is a reasonable choice. More generally, and in accordance with Bouwens et al. (2015a), as long it remains in a range of [1.4,8.6], which is the 95% confidence interval of $C_{\rm H\,II}$ from first paragraph (**Free** fit), results are consistent with the three sets of constraints available. This result corroborates the work of Price et al. (2016), who also note that their analysis is almost completely independent of the clumping factor over the prior range $1 < C_{\rm H\,II} < 5$.

Table 2: Resulting Thomson optical depths for various evolutions of $C_{\rm H\,II}$ with redshift.

Model	$\langle\tau\rangle$	σ
$C_{\rm H\,II} = 3$	0.0612	0.0013
Free	0.0570	0.0019
HM12	0.0604	0.0020
I07	0.0579	0.0027

References. Free: Model with $C_{\rm H\,II}$ as a fifth parameter, varying in [1, 10]; HM12: Haardt & Madau (2012), Eq. 10; I07: Iliev et al. (2007), Eq. 11.

4.4. Varying both $f_{\rm esc}$ and $C_{\rm H\,II}$

Now we have studied the impact of $f_{\rm esc}$ and $C_{\rm H\,II}$ separately, we set the evolution of $\rho_{\rm SFR}(z)$ according to Eq. 2, using parameters a, b, c, and d resulting from the analysis of Sect. 4.1. We performed an MCMC maximum likelihood sampling of the two parameters $f_{\rm esc}$ and $C_{\rm H\,II}$, considered constant with redshift. The first is allowed to vary between 0.001 and 1, the other between one and seven. We show parameter distributions for f_{esc} and $C_{\rm H\,II}$ in Fig. 6. We constrain the fit with all three data sets.

If we consider the median value of each parameter distribution as its maximum likelihood value, we find $f_{esc} = 0.193 \pm 0.026$ and $C_{\rm H\,II} = 4.43 \pm 1.11$. We see results are pretty similar to the previous analysis: if the escape fraction is well constrained, with a standard deviation of about 13%, the clumping factor can take a much wider range of values, between 3 and 5.5. We note that there seems to be a strong upper bound for the escape fraction around 0.26, which we can compare to the asymptotic value of f_{esc} when it is allowed to change with redshift (see Fig. 4). Because parameters take values close to previous results, the resulting ionisation histories are also close to the ones observed in Fig. 2b and are hence in good agreement with observations.

Finally, we considered the case when the four parameters describing the evolution of $\rho_{\rm SFR}(z)$ are set free in the same time as $f_{\rm esc}$ and $C_{\rm H\,II}$, using all datasets. We assumed the same prior as Price et al. (2016) on $C_{\rm H\,II}$ considering values between one and five. The full triangle plot is shown in Fig. A.3 and best fit parameters are reported in Table 4. The values found are in agreement with previous runs, with an undetermined value of $C_{\rm H\,II}$ at the 2σ level. As in Price et al. (2016) the degeneracy between $f_{\rm esc}$ and $C_{\rm H\,II}$ and the current data do not allow to constrain strongly all free parameters. However the evolution of the filling factor (Fig. 7) and thus the derived value of τ remain quite well constrained ($\tau = 0.058 \pm 0.002$) and in agreement with Planck ($\tau_{\rm Planck} = 0.058 \pm 0.012$).

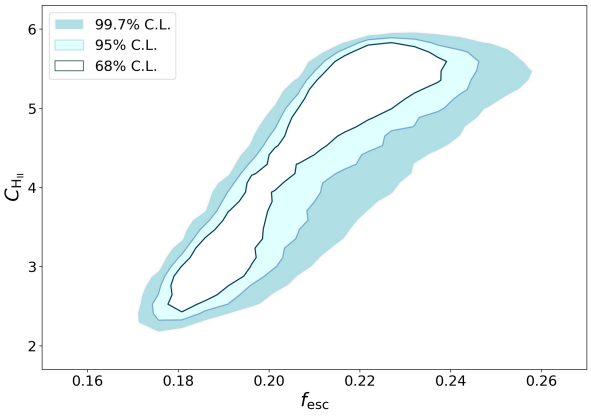

Fig. 6: MCMC distribution for f_{esc} and $C_{\rm H\,II}$ when both are taken as fit parameters (other parameters fixed). The escape fraction is allowed to vary between 0.1% and 100%, the clumping factor between one and seven.

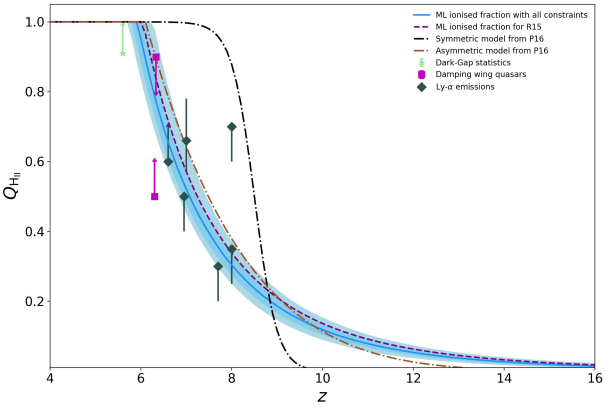

Fig. 7: Redshift evolution of $Q_{\rm H\,II}$ when all parameters $(a, b, c, d, f_{esc}, C_{\rm H\,II})$ are free and all datasets used. Fig. A.3 show the corresponding constraints on assumed parameters.

5. Discussion

5.1. Influence of the magnitude limit

In order to study the influence of the choice of magnitude limit on our results, we adopt the model of Eq. 3 into an MCMC approach similar to Sect. 4. We fit the model to our three data sets adapted to the corresponding magnitude limit as described in Section 3. $M_{\rm lim} = -17$ and $M_{\rm lim} = -10$ correspond to the analysis performed in Ishigaki et al. (2015), and $M_{\rm lim} = -13$ corresponds to Robertson et al. (2015).

We compute the star formation and reionisation histories compatible with the three sets of observational data, for the maximum likelihood parameters (here, median values) of the parametrisation in Eq. 3 and for the three $M_{\rm lim}$ values. Results can be found in Figs. 8a and 8b where two cases have been considered: $f_{\rm esc}$ fixed, taken to have the value used in corresponding references (left panels) and $f_{\rm esc}$ allowed to vary between 0 and 1 (right panels). In both cases, the effect of the two additional sets of data used as constraints here, $Q_{\rm H\,II}$ and $\tau_{\rm Planck}$, which were not used in Ishigaki et al. (2015), is to lower the quantity of ionising sources needed at high redshift to reach a fully ionised IGM by $z \sim 6$. We note, however, that here the values of some parameters were taken from Ishigaki et al. (2015) and hence quite different from the ones used in Sect. 4.1. For instance, Ishigaki et al. found $C_{\rm H\,II}$ values of 1.9 and 1.0 for respectively $M_{\rm lim} = -17$ and $M_{\rm lim} = -10$ whereas we used $C_{\rm H\,II} = 3$ before and consequently in the analysis for $M_{\rm lim} = -13$.

However this comparison illustrates the systematic uncertainties on reionisation history due to the choice in the magnitude limit, but also in $f_{\rm esc}$ and $C_{\rm H\,II}$ values. We see these are much wider than the statistical uncertainties observed in Fig. 2b while still being reasonable. In particular, they mainly concern high redshifts. Indeed, we see in Fig. 8b that the 68% confidence interval on star formation histories widens with redshift. However, few observations are available on this redshift range so we

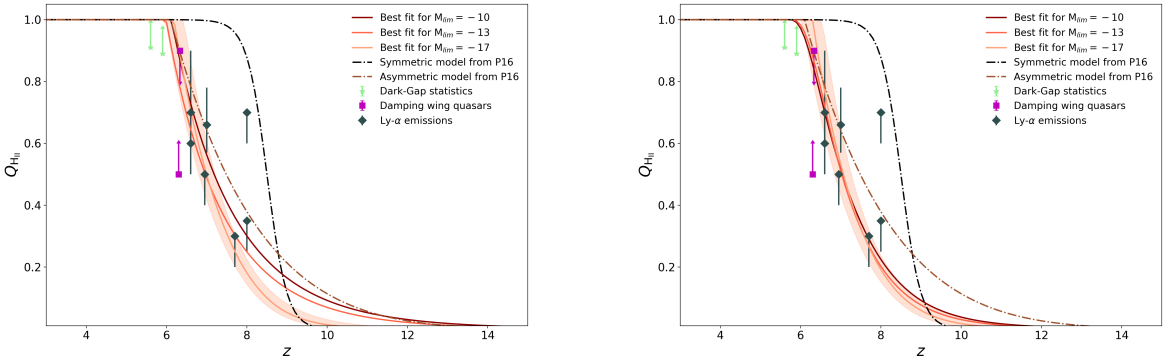

(a)

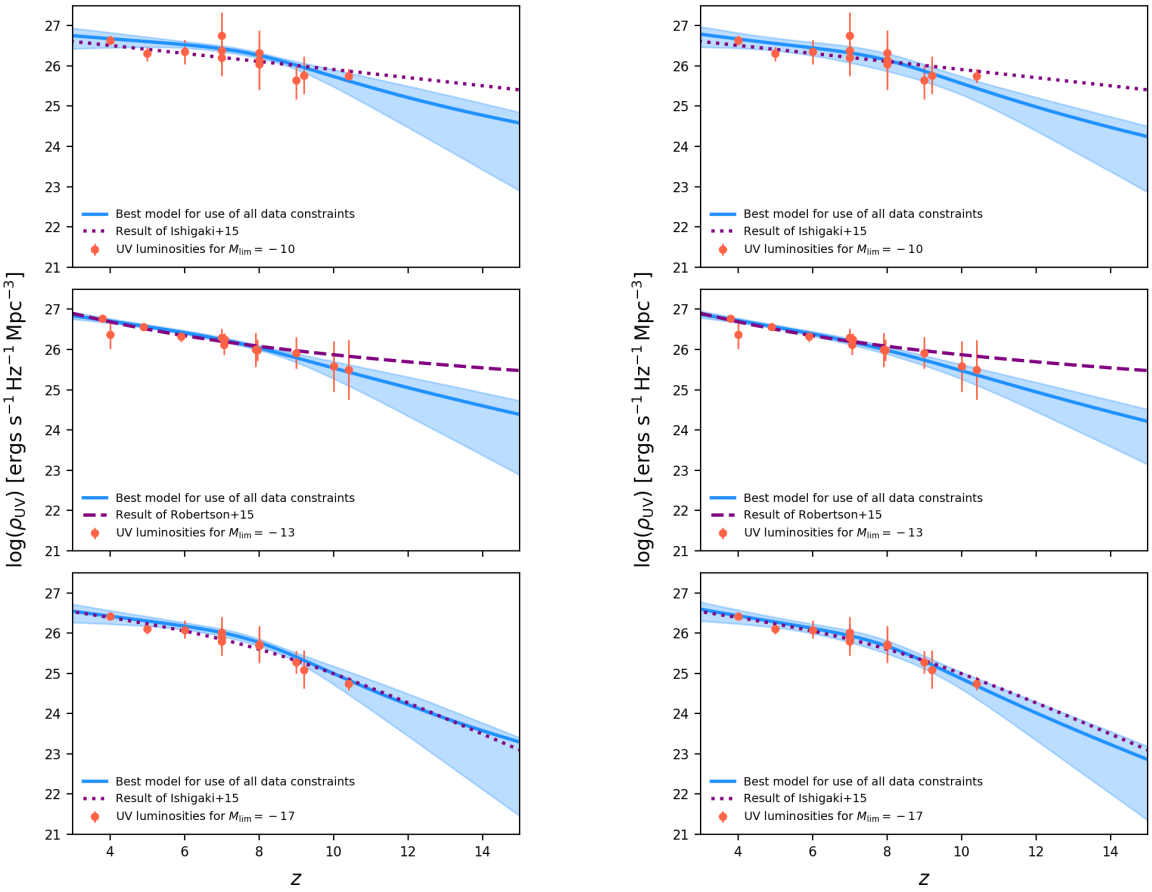

(b)

Fig. 8: (a) Redshift evolution of $Q_{\rm H\,II}$ for various choices of the magnitude limit in luminosity data: brown for $M_{\rm lim} = -10$, orange for $M_{\rm lim} = -13$ and beige for $M_{\rm lim} = -17$. The light orange region represents the 68% confidence level for the worst case scenario, i.e. $M_{\rm lim} = -17$. Left panel: escape fraction fixed to the values used by corresponding references. Right panel: escape fraction varying between zero and one. (b) UV luminosity density $\rho_{\rm UV}$ with redshift in logarithmic scale for three values of the magnitude limit: $M_{\rm lim} = -10$ in the upper panel, $M_{\rm lim} = -13$ in the middle panel and $M_{\rm lim} = -17$ in the lower panel. Data points are from Ishigaki et al. (2015) or adapted from Robertson et al. (2015). Maximum likelihood parametrisations corresponding to Eq. 3 (continuous lines) are shown for fits using all observational constraints. The 68% confidence interval is represented as the light blue region. These results are compared with a model forced to reproduce results from corresponding references, drawn as the purple lines. Left panel: escape fraction fixed. Right panel: escape fraction allowed to vary between zero and one.

may expect that once data on earlier times is available, we will be able to improve constraints on the magnitude limit. In this perspective we can mention the work of Mason et al. (2018), who derived a new constraint on reionisation history from sim-

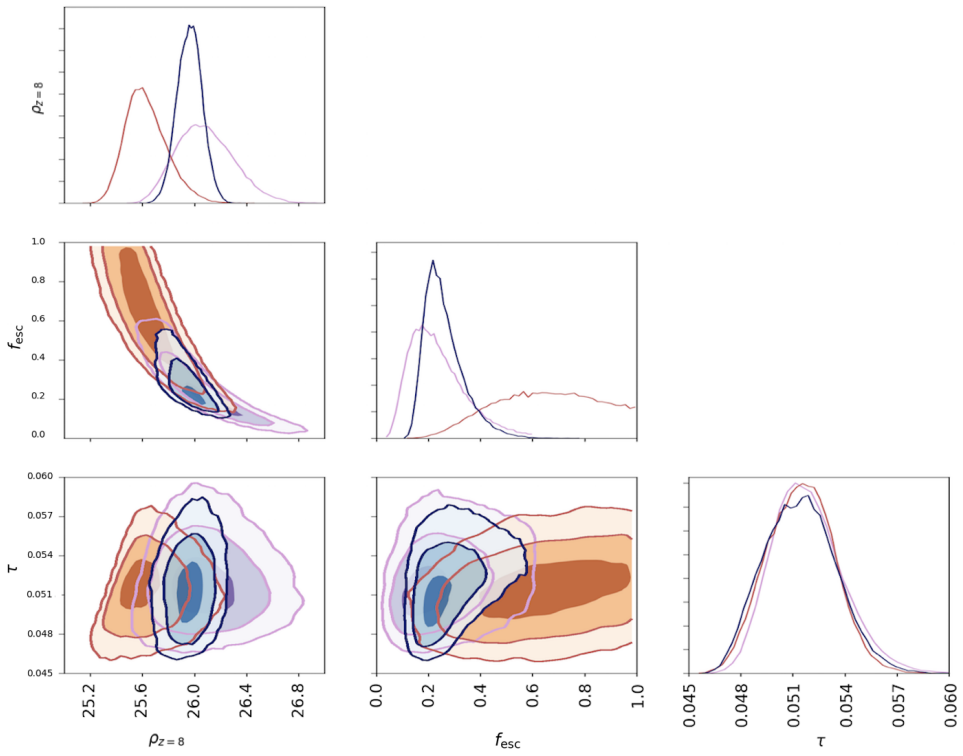

Fig. 9: Result of the MCMC analysis for the parametrisation described in Eq. 3 with f_{esc} added as a fitting parameter. Here, all three sets of observational data were used as constraints. The contours show the 1-, 2- and 3 − σ confidence levels for $\log(\rho_{z=8})$, f_{esc} and the derived parameter τ. Colours correspond to the different values of the magnitude limit used in the analysis: purple for $M_{lim} = -10$, blue for $M_{lim} = -13$ and orange for $M_{lim} = -17$. These results can be compared to reionisation histories displayed in Fig. 8a and 8b.

ulations and models of the effects of IGM radiative transfer on Lyman-α emissions. They find an IGM ionised fraction at $z \sim 7$ of $x_{H\,II} = 0.41^{+0.15}_{-0.11}$ in better agreement with our model for $M_{lim} = -17$ (see Fig. 8a).

From a different point of view, Price et al. (2016) consider a varying value of M_{lim} with redshift, and find that M_{lim} varies in order to match the value of τ_{Planck} and to balance the increasing value of f_{esc} with redshift allowed by their model. Here we find that, overall, the model combines star formation history and ionised fraction with difficulties when $M_{lim} = -17$. Indeed, Fig. 9 shows the probability distribution functions of the parameters $\log(\rho_{SFR})$ and f_{esc} and the corresponding distribution of derived optical depths for the three choices of magnitude limit. We see that for $M_{lim} = -17$ the value of f_{esc} is not well constrained and tends to be high. For lower values of the escape fraction, the reionisation process needs to start way earlier than in most of our results in order to have enough radiation to fully ionise the IGM and to reach a sufficient value of τ. In fact, leaving the escape fraction as a free parameter balances the uncertainty in the choice of M_{lim}: Fig. 8a shows a narrower range of uncertainties when we do not fix f_{esc}, confirming the correlation mentioned in Price et al. (2016).

5.2. Reionisation sources at $z > 10$

Some doubts remain about the sources of reionisation: if Robertson et al. (2015) found that star-forming galaxies are sufficient to lead the process and to maintain the IGM ionised at $z \sim 7$ – assuming $C_{H\,II} = 3$ and $f_{esc} = 0.2$, their analysis extrapolates luminosity functions between $z \simeq 10$ and $z \simeq 30$, overlooking the possibility that other sources may have taken part in the early stages of reionisation process. Besides, they argue that low values of the Thomson optical depth reduce the need for a significant contribution of high-redshift galaxies and Planck Collaboration et al. (2016b) give much lower values than WMAP did (Hinshaw et al. 2013): $\tau_{Planck} = 0.058 \pm 0.012$ vs. $\tau_{WMAP} = 0.088 \pm 0.014$. Thus, now that we have investigated the possibility of this extrapolation, we chose to try the one of a constant SFR at $z \gtrsim 10$.

We performed an MCMC maximum likelihood sampling of the 4-parameter model of $\rho_{SFR}(z)$ in Eq. 2 and add as a fifth parameter the the value of SFR density at $z > 10.4$, our last data point corresponding to a redshift of 10.4. We refer to it as ρ_{asympt} and chose to use all observations cited in Sect. 2.1 as constraints. Final values of parameters a, b, c, and d are close to the ones from Sect. 4.1. We find that there is a strong correlation between ρ_{asympt} and τ, because of the direct integration in Eq. 8 and so expect higher values of the optical depth for high values of ρ_{asympt}. Yet, τ values are limited by $Q_{H\,II}$ data points and they have more impact on the global scenario. Indeed, models where $Q_{H\,II}$ equals 30% as soon as $z = 10$ are allowed, whereas it is closer to 20% at the same redshift when ρ_{SFR} is extrapolated. The correlation observed in our model parameters likelihood functions between ρ_{asympt} and τ had already been noticed by Robertson et al. (2015), as a correlation between τ and the averaged value of ρ_{SFR} for $z > 10$. A linear regression gives

$$\langle \rho_{SFR} \rangle_{z>10.4} = 0.51\,\tau - 0.026\ [\mathrm{M_\odot\,yr^{-1}\,Mpc^{-3}}], \quad (12)$$

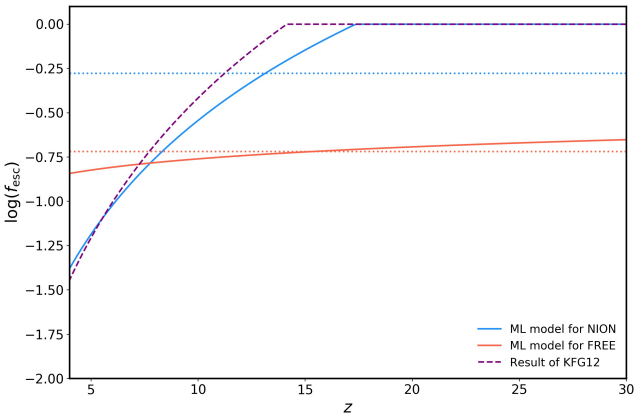

Fig. 10: Evolution of $f_{\rm esc}$ with redshift when $\dot{n}_{\rm ion}$ data points are used. ML models are shown for various set of constraints: blue when all constraints are used (**NION**); coral when $\dot{n}_{\rm ion}$ constraints are skipped (**FREE**). Horizontal dashed lines represent the mean value of $f_{\rm esc}$ over $4 \leq z \leq 30$ for the model of the corresponding colour. Inferences are compared to results of Kuhlen & Faucher-Giguère (2012, KFG12, purple dashed line).

with a correlation coefficient $r = 0.98$.

In this parametrisation, $\rho_{\rm asympt}$ can take very low values (down to 10^{-4} [$M_\odot\,{\rm yr}^{-1}\,{\rm Mpc}^{-3}$]) meaning that reionisation sources are almost completely absent at $z > 10$. It also has an upper limit of 0.016 [$M_\odot\,{\rm yr}^{-1}\,{\rm Mpc}^{-3}$]. This is close to the redshift-independent evolution of $\rho_{\rm SFR}$ ($\simeq 10^{-1.5}$ [$M_\odot\,{\rm yr}^{-1}\,{\rm Mpc}^{-3}$]) considered by Ishigaki et al. (2015) for $z > 3$ in order to reproduce $\tau_{2014} = 0.091^{+0.013}_{-0.014}$ (Planck Collaboration et al. 2014), when usual decreasing models only gave them $\tau \simeq 0.05$. We can compare Sect. 4.1 results with this upper limit in Figure 2a. Despite the wide range of possible values for $\rho_{\rm asympt}$, all results are consistent with our data and in particular, optical depths always remain in the 68% confidence interval of $\tau_{\rm Planck}$.

5.3. How are $f_{\rm esc}$, $\dot{n}_{\rm ion}$ and $\rho_{\rm SFR}$ correlated?

We expect a correlation between the amplitude a of the star formation rate density parametrisation Eq. 2 and the escape fraction. Indeed, $f_{\rm esc}$ takes no part in the estimation of $\rho_{\rm SFR}$ but they both take part in the calculation of $\dot{n}_{\rm ion}$ in Eq. 1 and then in the integration of $Q_{\rm H\,II}$ in Eq. 4. Thus, they must be constrained by the same data, so that the parameter a can be a proxy for variations in the escape fraction value. To investigate this possible correlation, we plotted the distributions of $a \times f_{\rm esc}$ for various sets of constraints and in different models: with (**PAR**) and without (**CST**) the escape fraction as a fifth fit parameter and with all constraints.We find that **CST** gives a lower value than **PAR** with a relative difference of 2.8%. This hints at a correlation between a and $f_{\rm esc}$ but more tests are needed to confirm or infirm this result.

To further investigate the link between $f_{\rm esc}$, $\dot{n}_{\rm ion}$ and $\rho_{\rm SFR}$, we considered values of the reionisation rate at various redshifts, used in Kuhlen & Faucher-Giguère (2012) and Robertson et al. (2013), and inferred from measurements and calculations of Faucher-Giguère et al. (2008); Prochaska et al. (2009); Songaila & Cowie (2010). We call **NION** the run using these new constraints – in addition to the others – and **FREE** the one skipping them, corresponding to **ALL** from Sect. 4.2.

Table 3: Comparison between our results and data points on the cosmic reionisation rate from Kuhlen & Faucher-Giguère (2012, KFG12).

z	$\dot{n}_{\rm ion}$ [10^{50} s^{-1} Mpc^{-3}]		
	KFG12	NION	FREE
4.0	$3.2^{+2.2}_{-1.9}$	3.9 ± 0.7	$13.7^{+3.9}_{-5.1}$
4.2	$3.5^{+2.9}_{-2.2}$	4.0 ± 0.7	$12.6^{+3.5}_{-4.5}$
5.0	4.3 ± 2.6	4.1 ± 0.5	$9.3^{+2.3}_{-2.6}$

We compare in Table 3 values of the reionisation rate at various redshifts for **NION**, **FREE** and Kuhlen & Faucher-Giguère (2012). **NION** gives results close to data points, increasing with z, whereas **FREE** values are significantly higher and decrease with redshift. This difference in the evolutions of $\dot{n}_{\rm ion}(z)$ is directly linked to $f_{\rm esc}(z)$. We see in Fig. 10 that $f_{\rm esc,FREE}$ is almost constant with redshift and therefore $\dot{n}_{\rm ion}(z)$ decreases on this redshift range: because $f_{\rm esc}$ values remains quite high, there is no need for many ionising sources at high redshift. On the contrary, when the constraints on $\dot{n}_{\rm ion}$ are included in the fit, the reionisation rate takes overall lower values (see Table 3) so that $f_{\rm esc,NION}$ has to take higher values at high redshift (saturating to 1 for $z \geq 15$) to compensate for the lack of ionising sources. However, this is still hardly sufficient and we find that for **NION**, the reionisation process needs to start as early as at $z = 8$ to fully ionise the IGM, with $Q_{\rm H\,II} = 1$ being reached later than others models, around $z = 5.5$. This behaviour leads to a high value of $\tau = 0.082$, at the edge of the 3-σ confidence interval of $\tau_{\rm Planck}$ and therefore hardly compatible with observational results (Planck Collaboration et al. 2016b). Removing the constraints on the filling factor, $f_{\rm esc}$ remains low on the whole redshift range (< 20). We then get values of the optical depth in agreement with Planck (0.058 ± 0.011) but reionisation does not end before $z \sim 4$. Thus, the estimations on the reionisation rate from Faucher-Giguère et al. (2008); Prochaska et al. (2009); Songaila & Cowie (2010) are compatible with one observable at a time: either the ionisation level – leading to a higher value of τ –, or the Thomson optical depth – so that reionisation ends around $z \sim 4$ – , but cannot match all observations in a coherent way.

6. Conclusions

We used the latest observational data available on reionisation history, i.e. cosmic star formation density, ionised fraction of the IGM and Thomson optical depth derived from Planck observations to find that they are all compatible with a simple and credible scenario where reionisation begins around $z = 15$ and ends by $z = 6$. Among all data, star formation history seems to be the most constraining for the EoR.

An investigation of various parametrisations of the escape fraction of ionising photons has lead us to conclude that it is very well constrained by observations: when considered constant with redshift, values allowed by the fit range from 20% to 28%; when considered redshift-dependent, from $f_{\rm esc}(z = 4) \simeq 17\%$ to $f_{\rm esc}(z = 30) \simeq 26\%$ following a low increase with z. The fiducial constant value of 20% often used in papers seems then to be perfectly consistent with our data. However, one must keep in mind that these results strongly depend on the hypothesis we make about the magnitude limit as a lower value of $M_{\rm lim}$ will require higher values of $f_{\rm esc}$ and vice versa. While the constraints on τ are unaffected by the assumption on $M_{\rm lim}$, the confidence range on $f_{\rm esc}$ is enlarged for $M_{\rm lim} = 10$. Furthermore, our differ-

Table 4: ML parameters from the fit on $\rho_{\rm SFR}$ with various parameters and constraints.

Ref.	Constraints			$\rho_{\rm SFR}$ parameters				Other parameters	
	$\rho_{\rm SFR}$	$Q_{\rm H\,II}$	$\tau_{\rm Planck}$	a	b	c	d	$f_{\rm esc}$	$C_{\rm H\,II}$
ALL	✓	✓	✓	0.0146 ± 0.0011	3.17 ± 0.20	2.65 ± 0.14	5.64 ± 0.14	–	–
	✓	✗	✗	0.0145 ± 0.0011	3.20 ± 0.22	2.63 ± 0.15	5.68 ± 0.19	–	–
NORHO	✗	✓	✓	0.0129 ± 0.343	0.458 ± 0.970	5.69 ± 1.65	7.14 ± 1.90	–	–
	✓	✓	✗	0.0147 ± 0.0011	3.17 ± 0.21	2.66 ± 0.14	5.63 ± 0.14	–	–
NOQ	✓	✗	✓	0.0145 ± 0.0011	3.22 ± 0.22	2.61 ± 0.15	5.66 ± 0.19	–	–
ALL	✓	✓	✓	0.0147 ± 0.0011	3.14 ± 0.21	2.69 ± 0.15	5.74 ± 0.19	0.193 ± 0.037	–
NOQ	✓	✗	✓	0.0146 ± 0.0011	3.18 ± 0.21	2.65 ± 0.15	5.70 ± 0.19	0.213 ± 0.079	–
ALL	✓	✓	✓	0.0146 ± 0.0011	3.18 ± 0.21	2.65 ± 0.15	5.67 ± 0.19	–	4.56 ± 1.85
NOQ	✓	✗	✓	0.0145 ± 0.0012	3.20 ± 0.22	2.63 ± 0.15	5.69 ± 0.19	–	5.10 ± 2.74
ALL*	✓	✓	✓	0.0147 ± 0.0011	3.14 ± 0.21	2.69 ± 0.15	5.75 ± 0.19	0.20 ± 0.05	3.50 ± 1.10

Notes. *: Prior on $f_{\rm esc}$ and $C_{\rm H\,II}$ are different for comparison with Price et al. (2016) – see text for details.

Table 5: ML parameters for the fits on $f_{\rm esc}(z)$ and $C_{\rm H\,II}(z)$ in, respectively, Sect. 4.2 and 4.3.

Model	Reference	$Q_{\rm H\,II}$	$\tau_{\rm Planck}$	Model parameters			
				α	β		
$f_{\rm esc}(z)$	KFG12	✓	✓	0.14 ± 0.02	0 ± 0.29		
		✓	✗	0.15 ± 0.02	0 ± 0.30		
		✗	✓	0.11 ± 0.09	0 ± 0.78		
				α	a	b	c
$C_{\rm H\,II}(z)$	HM12	✓	✓	0.74 ± 0.29	5.74 ± 1.07	-1.21 ± 0.58	–
		✓	✗	0.79 ± 0.29	5.56 ± 1.09	-1.30 ± 0.69	–
	I07	✓	✓	–	7.29 ± 1.63	-0.042 ± 0.030	$0 \pm 2.4 \times 10^{-4}$
		✓	✗	–	7.11 ± 1.17	-0.046 ± 0.058	$0 \pm 6.3 \times 10^{-4}$

References. KFG12: Kuhlen & Faucher-Giguère (2012); HM12.1 & HM12.2: Haardt & Madau (2012); I07: Iliev et al. (2007).

ent sets of observations seem to be in tension with each other for $M_{\rm lim} = -17$ or for values of $f_{\rm esc} \lesssim 10\%$.

On the contrary, the clumping factor of ionised hydrogen in the IGM can take a wide range of different values without impacting the reionisation observables significantly. For instance, when take $C_{\rm H\,II}$ as a redshift-independent parameter, its relative standard deviation is 41% whereas it is at most 7.6% for $Q_{\rm H\,II}(z)$[2]. The result is the same when we consider that $C_{\rm H\,II}$ depends on redshift: a great variety of possible evolutions gives the same scenario in terms of ionisation level. There is no greater impact on Thomson optical depth values, which vary of a maximum of a few percent compared to $\langle\tau\rangle_{C_{\rm H\,II}=3}$ and always remains in the 1-σ confidence interval of $\tau_{\rm Planck}$. Observational constraints are thus extremely robust to variations of the clumping factor. We nevertheless find a correlation between the averaged value of $C_{\rm H\,II}$ for $z \in [6.8, 30]$ and τ: the linear fit

$$\langle C_{\rm H\,II}\rangle_{z>6.8} = -350\,\tau + 24.4 \tag{13}$$

provides a good description of their connection[3]. This supports the use of a redshift-independent clumping factor to study the EoR. A possible choice, consistent with observations, would then be $C_{\rm H\,II} = 3$, the fiducial value often used in papers, because it lies in the range of the ML $C_{\rm H\,II}$ values found in Sect. 4.3.

Last, a quick study on the possible reionisation sources at $z \gtrsim 10$ showed that there is no need for exotic sources such as early quasars (Madau & Haardt 2015) or for an artificial increase in star formation density at high redshift (Ishigaki et al. 2015). When their luminosity functions are extrapolated, a hypothesis still recently strongly supported by Livermore et al. (2017), star-forming galaxies provide enough photons to have a fully ionised IGM at $z = 6$.

Acknowledgements. The authors thank B.E. Robertson for kindly providing us with his compilation of star formation rate densities. They thank the referee for useful comments. This research made use of Astropy, a community-developed core Python package for Astronomy (Astropy Collaboration et al. 2013, 2018); matplotlib, a Python library for publication quality graphics (Hunter 2007) and emcee, an implementation of the affine invariant MCMC ensemble sampler (Foreman-Mackey et al. 2013). This work was partly supported by Programme National de Cosmologie et Galaxies (PNCG). AG acknowledges financial support from the European Research Council under ERC grant number 638743-FIRSTDAWN as well as from an STFC PhD studentship.

[2] Reached at $z = 6.2$.

[3] Here, the model from Eq. 10 was considered.

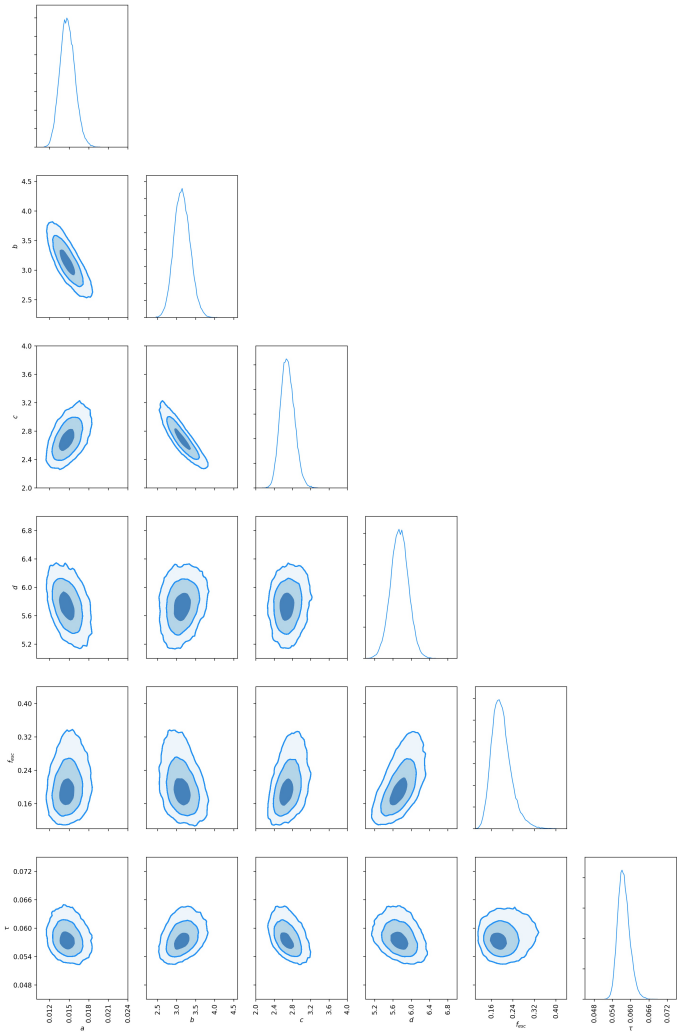

Fig. A.1: Results of the MCMC analysis for the ALL case when f_{esc} is added as a free parameter. The contours show the 1, 2, and 3 σconfidence levels for a, b, c, d, $f_{esc,}$ and the derived parameter τ.

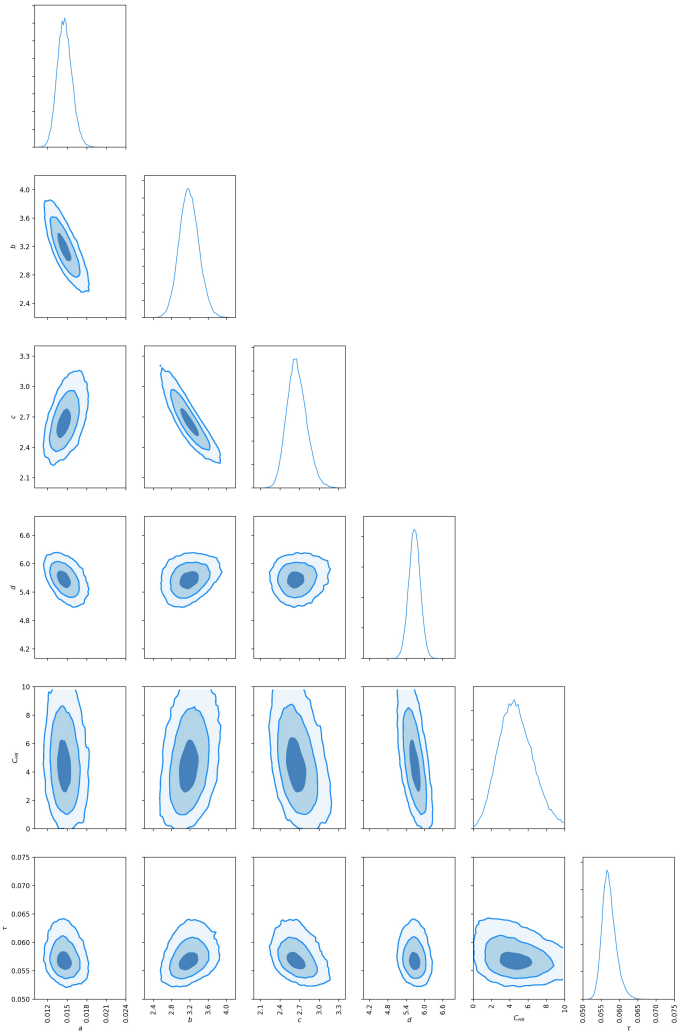

Fig. A.2: Results of the MCMC analysis for the ALL case when C_{HII} is added as a free parameter. The contours show the 1, 2, and 3 σ confidence levels for a, b, c, d, $C_{HII,}$ and the derived parameter τ.

Appendix A: MCMC multidimensional plots

We show in this appendix the additional triangle plots of the runs ALL corresponding to the studies with f_{esc} as additional free parameter (see Section 4.1), with C_{HII} as additional free parameter (see Section 4.3), and finally with both free (see Section 4.4).

References

Aghanim, N., Desert, F. X., Puget, J. L., & Gispert, R. 1996, A&A, 311, 1
Astropy Collaboration, Price-Whelan, A. M., Sipőcz, B. M., et al. 2018, ArXiv e-prints [arXiv:1801.02634]
Astropy Collaboration, Robitaille, T. P., Tollerud, E. J., et al. 2013, A&A, 558, A33
Atek, H., Richard, J., Kneib, J.-P., et al. 2015, ApJ, 800, 18
Becker, G. D., Bolton, J. S., Haehnelt, M. G., & Sargent, W. L. W. 2011, MNRAS, 410, 1096
Becker, G. D., Bolton, J. S., Madau, P., et al. 2015, MNRAS, 447, 3402
Bolton, J. S., Becker, G. D., Raskutti, S., et al. 2012, MNRAS, 419, 2880
Bolton, J. S. & Haehnelt, M. G. 2007, MNRAS, 382, 325
Bolton, J. S., Haehnelt, M. G., Warren, S. J., et al. 2011, MNRAS Letters, 416, L70
Bouwens, R. J., Bradley, L., Zitrin, A., et al. 2014, ApJ, 795, 126
Bouwens, R. J., Illingworth, G. D., Franx, M., & Ford, H. 2007, ApJ, 670, 928
Bouwens, R. J., Illingworth, G. D., Oesch, P. A., et al. 2015a, ApJ, 811, 140
Bouwens, R. J., Illingworth, G. D., Oesch, P. A., et al. 2015b, ApJ, 803, 34
Bouwens, R. J., Illingworth, G. D., Oesch, P. A., et al. 2012, ApJ, 752, L5
Caruana, J., Bunker, A. J., Wilkins, S. M., et al. 2014, MNRAS, 443, 2831
Chisholm, J., Gazagnes, S., Schaerer, D., et al. 2018, ArXiv e-prints [arXiv:1803.03655]
Chornock, R., Berger, E., Fox, D. B., et al. 2014, ArXiv e-prints [arXiv:1405.7400]
Dijkstra, M., Haiman, Z., Rees, M. J., & Weinberg, D. H. 2004, ApJ, 601, 666
Douspis, M., Aghanim, N., Ilić, S., & Langer, M. 2015, A&A, 580, L4
Dunlop, J. S., Rogers, A. B., McLure, R. J., et al. 2013, MNRAS, 432, 3520
Faisst, A. L., Capak, P., Carollo, C. M., Scarlata, C., & Scoville, N. 2014, ApJ, 788, 87
Fan, X., Strauss, M. A., Becker, R. H., et al. 2006, AJ, 132, 117
Faucher-Giguère, C.-A., Lidz, A., Hernquist, L., & Zaldarriaga, M. 2008, ApJ, 688, 85
Fernandez, E. R., Dole, H., & Iliev, I. T. 2013, ApJ, 764, 56
Finkelstein, S. L., Ryan, Jr., R. E., Papovich, C., et al. 2015, ApJ, 810, 71
Finlator, K., Oh, S. P., Özel, F., & Davé, R. 2012, MNRAS, 427, 2464
Foreman-Mackey, D., Hogg, D. W., Lang, D., & Goodman, J. 2013, PASP, 125, 306
Furlanetto, S. R. & Oh, S. P. 2005, MNRAS, 363, 1031
Grazian, A., Giallongo, E., Boutsia, K., et al. 2018, ArXiv e-prints [arXiv:1802.01953]
Greig, B. & Mesinger, A. 2017, MNRAS, 465, 4838

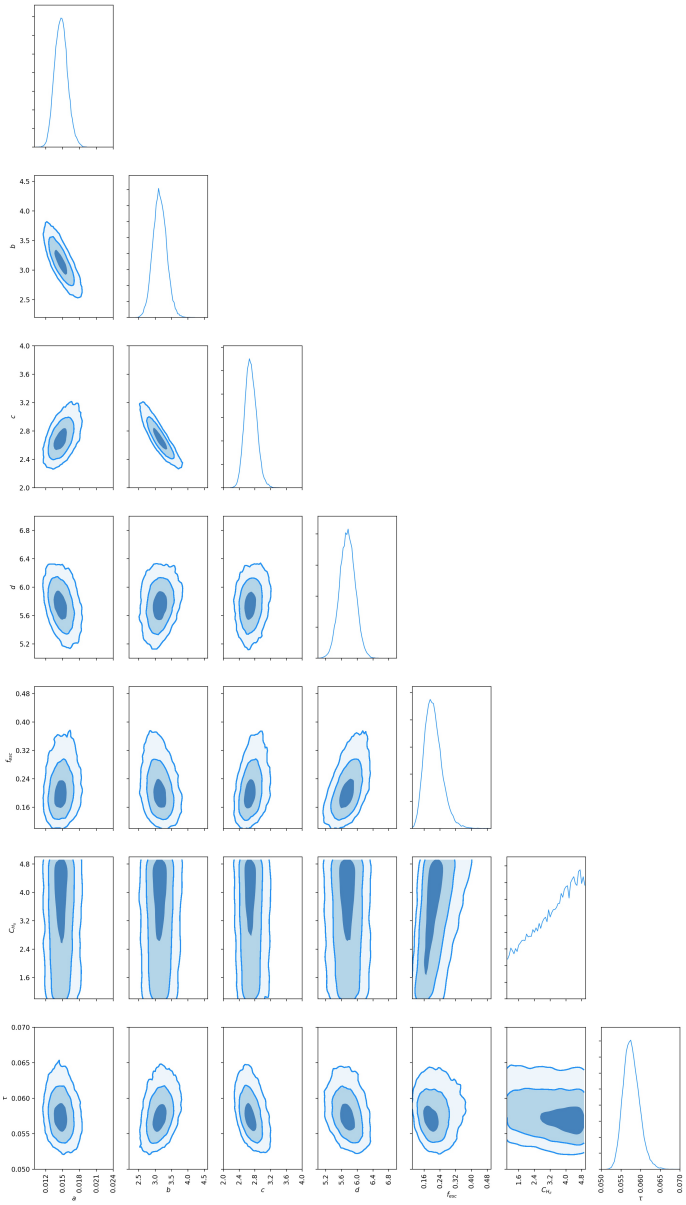

Fig. A.3: Results of the MCMC analysis for the ALL case when both f_{esc} and C_{HII} are added as a free parameter. The contours show the 1, 2, and 3 σ confidence levels for a, b, c, d, f_{esc}, $C_{\mathrm{H\,II}}$, and the derived parameter τ.

Gunn, J. E. & Peterson, B. A. 1965, ApJ, 142, 1633
Haardt, F. & Madau, P. 2012, ApJ, 746, 125
Hinshaw, G., Larson, D., Komatsu, E., et al. 2013, ApJS, 208, 19
Hui, L. & Haiman, Z. 2003, ApJ, 596, 9
Hunter, J. D. 2007, Computing In Science & Engineering, 9, 90
Iliev, I. T., Mellema, G., Pen, U.-L., et al. 2006, MNRAS, 369, 1625
Iliev, I. T., Mellema, G., Shapiro, P. R., & Pen, U.-L. 2007, MNRAS, 376, 534
Inoue, A. K., Iwata, I., & Deharveng, J.-M. 2006, MNRAS, 371, L1
Ishigaki, M., Kawamata, R., Ouchi, M., et al. 2015, ApJ, 799, 12
Iwata, I., Inoue, A. K., Matsuda, Y., et al. 2009, ApJ, 692, 1287
Khaire, V., Srianand, R., Choudhury, T. R., & Gaikwad, P. 2016, MNRAS, 457, 4051
Konno, A., Ouchi, M., Shibuya, T., et al. 2017, Publications of the Astronomical Society of Japan [arXiv:1705.01222]
Kuhlen, M. & Faucher-Giguère, C.-A. 2012, MNRAS, 423, 862
Lidz, A., Faucher-Giguère, C.-A., Dall'Aglio, A., et al. 2010, ApJ, 718, 199
Livermore, R. C., Finkelstein, S. L., & Lotz, J. M. 2017, ApJ, 835, 113
Loeb, A. & Furlanetto, S. 2013, The First Galaxies in the Universe (Princeton University Press)
Mac Low, M.-M. & Ferrara, A. 1999, ApJ, 513, 142
Madau, P. & Dickinson, M. 2014, ARA&A, 52, 415
Madau, P. & Haardt, F. 2015, ApJ, 813, L8
Madau, P., Pozzetti, L., & Dickinson, M. 1998, ApJ, 498, 106
Mason, C. A., Treu, T., Dijkstra, M., et al. 2018, ApJ, 856, 2
McGreer, I. D., Mesinger, A., & D'Odorico, V. 2015, MNRAS, 447, 499
McLeod, D. J., McLure, R. J., Dunlop, J. S., et al. 2015, MNRAS, 450, 3032
McLure, R. J., Dunlop, J. S., Bowler, R. A. A., et al. 2013, MNRAS, 432, 2696
Mellema, G., Iliev, I. T., Pen, U.-L., & Shapiro, P. R. 2006, MNRAS, 372, 679
Mesinger, A., ed. 2016, Astrophysics and Space Science Library, Vol. 423, Understanding the Epoch of Cosmic Reionization
Mitra, S., Choudhury, T. R., & Ferrara, A. 2015, MNRAS, 454, L76
Mortlock, D. J., Warren, S. J., Venemans, B. P., et al. 2011, Nature, 474, 616
Oesch, P. A., Bouwens, R. J., Illingworth, G. D., et al. 2015, ApJ, 808, 104
Osterbrock, D. E. 1989, Astrophysics of gaseous nebulae and active galactic nuclei (University Science Books)
Ota, K., Iye, M., Kashikawa, N., et al. 2008, ApJ, 677, 12
Ouchi, M., Shimasaku, K., Furusawa, H., et al. 2010, ApJ, 723, 869
Paardekooper, J.-P., Khochfar, S., & Dalla Vecchia, C. 2015, MNRAS, 451, 2544
Pawlik, A. H., Schaye, J., & van Scherpenzeel, E. 2009, MNRAS, 394, 1812
Peebles, P. J. E. 1968, ApJ, 153, 1
Planck Collaboration et al. 2014, A&A, 571, A16
Planck Collaboration et al. 2016a, A&A, 594, A13
Planck Collaboration et al. 2016b, A&A, 596, A108
Price, L. C., Trac, H., & Cen, R. 2016, ArXiv e-prints [arXiv:1605.03970]
Prochaska, J. X., Worseck, G., & O'Meara, J. M. 2009, ApJ, 705, L113
Raičević, M. & Theuns, T. 2011, MNRAS, 412, L16
Rees, M. J. & Ostriker, J. P. 1977, MNRAS, 179, 541
Robertson, B. E., Ellis, R. S., Furlanetto, S. R., & Dunlop, J. S. 2015, ApJ, 802, L19
Robertson, B. E., Furlanetto, S. R., Schneider, E., et al. 2013, ApJ, 768, 71
Schenker, M. A., Robertson, B. E., Ellis, R. S., et al. 2013, ApJ, 768, 196
Schroeder, J., Mesinger, A., & Haiman, Z. 2013, MNRAS, 428, 3058
Seager, S., Sasselov, D. D., & Scott, D. 2000, ApJS, 128, 407
Shull, J. M., Harness, A., Trenti, M., & Smith, B. D. 2012, ApJ, 747, 100
Sobacchi, E. & Mesinger, A. 2014, MNRAS, 440, 1662
Sokasian, A., Abel, T., Hernquist, L., & Springel, V. 2003, MNRAS, 344, 607
Songaila, A. & Cowie, L. L. 2010, ApJ, 721, 1448
Steidel, C. C., Pettini, M., & Adelberger, K. L. 2001, ApJ, 546, 665
Tilvi, V., Papovich, C., Finkelstein, S. L., et al. 2014, ApJ, 794, 5
Wise, J. H., Demchenko, V. G., Halicek, M. T., et al. 2014, MNRAS, 442, 2560
Yajima, H., Li, Y., Zhu, Q., et al. 2014, MNRAS, 440, 776
Yoshiura, S., Hasegawa, K., Ichiki, K., et al. 2017, MNRAS, 471, 3713
Zel'dovich, Y. B., Kurt, V. G., & Syunyaev, R. A. 1969, Soviet Journal of Experimental and Theoretical Physics, 28, 146

A.2 Studying the morphology of reionisation with the triangle correlation function of phases

This article looks at making use of the phases of the 21cm signal, which are overlooked when the power spectrum is considered. It introduces a new statistical tool, the triangle correlation function (TCF), based on these phases and build in order to pick up the spherical structure of ionised regions during reionisation. Sec. 3.3 summarises most of the results of this paper, with a discussion about the robustness of the TCF to instrumental effects such as noise and resolution in Sec. 4.1. In this article, you will find two discussions that were not included in the thesis: a comparison of the TCF as a bubble size estimator to other bubble size distribution algorithms, and a detailed discussion of the choice of phase information with respect to full (amplitude and phase) information. All the results of this paper are the product of my work. The runs of OSKAR used to simulate instrumental effects were kindly provided by Emma Chapman. This article was published in August 2019 in the Monthly Notices of the Royal Astronomical Society.

MNRAS **000**, 1–18 (2019) Preprint 4 September 2019 Compiled using MNRAS LATEX style file v3.0

Studying the morphology of reionisation with the triangle correlation function of phases

Adélie Gorce,[1,2]★ and Jonathan R. Pritchard,[1]†
[1]*Department of Physics, Blackett Laboratory, Imperial College London, SW7 2AZ, U.K.*
[2]*Institut d'Astrophysique Spatiale, CNRS/Université Paris-Sud, Université Paris-Saclay, bâtiment 121, Université Paris-Sud, 91405 Orsay Cedex,*

Accepted XXX. Received YYY; in original form ZZZ

ABSTRACT

We present a new statistical tool, called the triangle correlation function (TCF), inspired by the earlier work of Obreschkow et al. (2013). It is derived from the 3-point correlation function and aims to probe the characteristic scale of ionised regions during the Epoch of Reionisation from 21cm interferometric observations. Unlike most works, which focus on power spectrum, i.e. amplitude information, our statistic is based on the information we can extract from the phases of the Fourier transform of the ionisation field. In this perspective, it may benefit from the well-known interferometric concept of closure phases. We find that this statistical estimator performs very well on simple ionisation fields. For example, with well-defined fully ionised disks, there is a peaking scale, which we can relate to the radius of the ionised bubbles. We also explore the robustness of the TCF when observational effects such as angular resolution and noise are considered. We also get interesting results on fields generated by more elaborate simulations such as 21CMFAST. Although the variety of sources and ionised morphologies in the early stages of the process make its interpretation more challenging, the nature of the signal can tell us about the stage of reionisation. Finally, and in contrast to other bubble size distribution algorithms, we show that the TCF can resolve two different characteristic scales in a given map.

Key words: methods: statistical – cosmology: dark ages, reionization, first stars – theory – large-scale structure of Universe

1 INTRODUCTION

During the Epoch of Reionisation (EoR), from $z \sim 20$ to $z \sim 6$, early light sources ionised the hydrogen and helium atoms of the Intergalactic Medium (IGM). The information currently available on this period comes from indirect observations such as the redshift evolution of the density of star-forming galaxies, thought to be a major source of reionisation and estimated through UV luminosity densities (Bouwens et al. 2015; Ishigaki et al. 2015; Robertson et al. 2015); the integrated Thomson optical depth from Cosmic Microwave Background (CMB) observations (Planck Collaboration et al. 2016b, 2018); and from estimates of the averaged neutral fraction of the IGM obtained via the damping wings of quasars (Greig et al. 2017, 2018), surveys of Lyman-α emitters (Konno et al. 2014; Schenker et al. 2014; Mason et al. 2018) or gamma-ray bursts afterglows (Totani et al. 2014). Although these observations keep improving, in terms of both redshift and precision, they are still not sufficient to draw a precise history of reionisation. Many uncertainties remain on various aspects of the reionisation process such as the emissivity of early galaxies or the level of clumpiness in the IGM (Bouwens et al. 2017; Gorce et al. 2018). Interferometric measurements of the 21cm signal will potentially allow for maps of H I regions in the sky to give us a sense of both the topology and morphology of the reionisation process. To optimise the signal-to-noise ratio of current radio interferometers such as the Murchison Widefield Array (MWA)[1], the Precision Array to Probe the Epoch of Reionization (PAPER)[2] and the Low Frequency Array (LOFAR)[3], many works focus on statistical estimators such as the n-point correlation functions (n-PCF) and in particular the power spectrum ($n = 2$). To make the most out of upcoming observations, especially of 21cm tomographic imaging – a key science goal of the future Square Kilometer Array (SKA)[4], it is useful to look at higher-order statistics.

★ E-mail: aeg15@ic.ac.uk (AG)
† E-mail: j.pritchard@imperial.ac.uk (JRP)

[1] http://www.mwatelescope.org
[2] http://eor.berkeley.edu
[3] http://www.lofar.org
[4] http://www.skatelescope.org/

Previous works have focused on the use of the bispectrum, i.e. the Fourier transform of the 3-PCF to learn about the non-Gaussianity of the reionisation signal (Watkinson et al. 2017; Majumdar et al. 2018; Watkinson et al. 2019; Trott et al. 2019). Because they include both amplitude and phase information, the n-PCF ($n \geq 3$) will not complement the information carried by the 2-PCF as well as a correlation function solely based on the Fourier phases, such as the one we describe in this paper.

1.1 Phase information

Consider an ionisation field $x(\boldsymbol{r})$ with values ranging from 0 (neutral) to 1 (fully ionised). The visibilities observed by radio interferometers give information in Fourier space, so it is useful to expand $x(\boldsymbol{r})$ with a Fourier series,

$$x(\boldsymbol{r}) = \sum \hat{x}(\boldsymbol{k})\, e^{i\,\boldsymbol{k}\cdot\boldsymbol{r}}. \tag{1}$$

Each $\hat{x}(\boldsymbol{k})$ is a complex number which can be decomposed into an amplitude $|\hat{x}(\boldsymbol{k})|$ and a phase term $\Phi_{\boldsymbol{k}}$, so that $\hat{x}(\boldsymbol{k}) = |\hat{x}(\boldsymbol{k})|\, e^{i\,\Phi_{\boldsymbol{k}}}$. When the power spectrum $\mathcal{P}(k) = |\hat{x}(\boldsymbol{k})|^2$ of the field is considered, all the information contained in the phases is lost. If $x(\boldsymbol{r})$ is a pure Gaussian random field (GRF), then the phases are uniformly distributed on the interval $[0, 2\pi]$ (Watts et al. 2003) and the power spectrum is sufficient to fully describe the field. Conversely, non-Gaussianity is traceable to the phases. In this work, we estimate the amount of information that can be extracted from phases to add to the usual power spectrum studies. Eventually, we want to use phases to learn about the structure of an ionisation field and extract a characteristic length, such as the average radius of ionised bubbles. In this perspective, we develop a new statistical estimator, derived from the 3-point correlation function and solely based on phases, called the triangle correlation function (TCF). It is similar to the line correlation function introduced by Obreschkow et al. (2013) to study elongated structures in dark matter fields. To consider phase information only, we compute statistics from the phase factor $\hat{\epsilon}(\boldsymbol{k})$ defined as

$$\hat{\epsilon}(\boldsymbol{k}) = \frac{\hat{x}(\boldsymbol{k})}{|\hat{x}(\boldsymbol{k})|} = e^{i\,\Phi_{\boldsymbol{k}}}. \tag{2}$$

By construction, the phase factor has an amplitude of one, so that its 2-PCF and power spectrum will vanish. The simplest correlation function related to $\hat{\epsilon}(\boldsymbol{k})$ is then its 3-PCF.

The top left panel of Fig. 1 shows an ionisation field made of randomly distributed ionised discs on a neutral background. The top right panel corresponds to the inverse Fourier transform of its phase factor $\hat{\epsilon}(\boldsymbol{k})$, a tracer of phase information in real space. We see that phases mostly preserve the edges of the ionised regions: they will provide information about the structure of the field. The same exercise is done in the lower panels of Fig. 1 but for an ionisation field extracted from the semi-numerical 21CMFAST simulation (Mesinger & Furlanetto 2007) at $z = 7.8$ and global ionised fraction $x_{\mathrm{H\,II}} = 0.54$ (details on the simulation parameters can be found in Section 4.3). We see that the more complex structure of the ionisation field in this simulation is reflected in a more complex phase map. The boundaries between neutral and ionised regions are not as definite as they were for the toy model above. It will therefore be more difficult to extract information about the structure of this field from its phases.

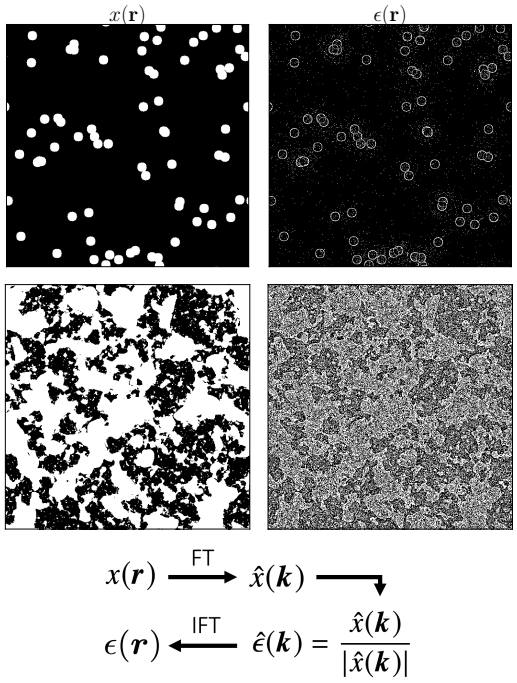

Figure 1. Examples of phase information in real space. Left panels represent the ionisation field $x(\boldsymbol{r})$ and the right panel the inverse Fourier transform of the corresponding phase factor $\hat{\epsilon}(\boldsymbol{k})$. *Top row:* Toy model with randomly distributed ionised bubbles. *Bottom row:* Output of the 21CMFAST simulation. Both boxes have 512^2 pixels and side length $L = 400$ Mpc.

To this day, little work has been done regarding phase information in the EoR, mostly because of the lack of a solid statistical framework to do so. Thyagarajan et al. (2018) have shown that the 21cm signal from EoR can be detected in bispectrum phase spectra, and mention a potential use of their results for H I intensity mapping experiments. Most of the existing work is related to the study of galaxy clustering: although the initial conditions to matter distribution in the Universe are Gaussian, the growth of cosmic structures will lead to some non-linearity and the distributions of both amplitudes and phases will be altered (Watts et al. 2003; Levrier et al. 2006). By characterising this alteration, one hopes to learn about the formation of cosmic structures and possibly about the properties of dark matter (Obreschkow et al. 2013, see also follow-up papers Wolstenhulme et al. 2015; Eggemeier et al. 2015; Eggemeier & Smith 2017). We will discuss the benefits of phases compared to amplitude information in more details in Section 6.

1.2 Current estimators of the size of ionised regions during reionisation

Characterising the morphology and topology of H II regions at different times through 21cm tomography is essential to the study of reionisation. For now, two types of metrics have been proposed to do so: Minkowski functionals (Gleser et al. 2006; Lee et al. 2008; Bag et al. 2018; Chen et al. 2018) and bubble size distributions (BSD). Using

Minkowski functionals on tomographic images, one can learn about the topology of the reionisation process at a given time, for example the level of percolation or the shape of ionised regions. When the ionised regions largely overlap, there will likely form a unique extended percolated zone pierced by neutral tunnels (Bag et al. 2018; Elbers & van de Weygaert 2018). Bubble size distributions allow for more quantitative results as they give a direct estimate of the size of ionised regions. To derive BSD, three main methods can be found in the literature: the friend-of-friends algorithm (FOF), based on the connections between ionised regions (Iliev et al. 2006); the spherical average method (SPA), which looks for the largest spherical volume which can cover an ionised region and exceed a given ionisation threshold (Zahn et al. 2007); and the mean-free-path method (RMFP), based on Monte-Carlo Markov Chain (MCMC) techniques and implemented in the semi-numerical simulation 21CMFAST (Mesinger & Furlanetto 2007; Mesinger et al. 2011). The RMFP algorithm proceeds as follows: it picks a random ionised pixel, stores its distance to the closest neutral pixel in a random direction and stack these distances, measured for many pixels, in a histogram. A thorough comparison of these methods is made in Lin et al. (2016) for simulated clean 21cm maps and in Giri et al. (2018a) for maps including observational effects. A new method, which the authors call *granulometry*, has been recently presented in Kakiichi et al. (2017). The idea is to successively sieve a binary field with a spherical hole of increasing radius R. Depending on how many ionised pixels are sieved, one can build the probability distribution of H II regions sizes. In their work, the authors prove that granulometry should perform well on future SKA observations, as long as the correct observing strategies are chosen. Lin et al. (2016) have also extended to 3D the well-known watershed algorithm: it connects same value pixels to find isodensity lines which they interpret as the edges of characteristic structures. Note that all these methods require real space data whereas the TCF can be used directly in Fourier space.

We first describe in Section 2 the 21cm signal, on which the simulated observations we use are based. In Section 3, we develop the mathematical formalism leading to the definition of the triangle correlation function, and in particular the definitions of n-point correlation functions and poly-spectra. In Section 4, we apply the TCF to simulated ionisation fields,from toy models to outputs of the 21CMFAST simulation. We relate our method to observations, and in particular to the closure phase relation, in Section 5. Finally, we discuss various aspects of our results: we first give evidence for the benefits of phase information in Section 6 and then consider computational performance in Section 7. Conclusions can be found in Section 8.

2 THE 21CM SIGNAL

The neutral hydrogen 21cm line corresponds to the spin-flip transition of an electron between the two hyperfine levels of the ground state of the H I atom. As a tracer of neutral hydrogen, it is naturally a very interesting observable to learn about the EoR. For the last decades, many efforts have been made to design experiments capable of detecting this signal, despite its low amplitude, the presence of strong foregrounds and huge calibration challenges. Seen with respect to a radio background, the CMB, the evolution of the observed differential 21cm brightness temperature writes (Pritchard & Loeb 2012):

$$\begin{aligned}\delta T_\mathrm{b} &= 27\mathrm{mK} \times x_{\mathrm{H\,I}}(1+\delta_b)\frac{\Omega_\mathrm{b}h^2}{0.023}\sqrt{\frac{0.15}{\Omega_\mathrm{m}h^2}}\sqrt{\frac{1+z}{10}}\left(1-\frac{T_\mathrm{CMB}}{T_\mathrm{S}}\right)\\ &\simeq 27\mathrm{mK}\ x_{\mathrm{H\,I}}(1+\delta_b)\frac{\Omega_\mathrm{b}h^2}{0.023}\sqrt{\frac{0.15}{\Omega_\mathrm{m}h^2}}\sqrt{\frac{1+z}{10}}\end{aligned} \tag{3}$$

where δ_b is the baryon overdensity and T_S the spin temperature, which characterises the relative populations of the two spin states. During the late stages of reionisation, it is expected that the spin temperature will dominate the CMB temperature because of its coupling to the kinetic temperature of the gas, and we can make the approximation of the second line. With this approximation, we can map the 21cm signal on the sky and, thanks to Eq. 3, interpret cold spots, i.e. regions where the signal is weaker than average, either as ionised or underdense regions; and hot spots as neutral or overdense regions. Being able to differentiate underdense from ionised regions in brightness temperature measurements is a major challenge of 21cm tomography (Giri et al. (2018a), see also Giri et al. (2018b) for an efficient way to do so). In this work however, we consider segmented data, converted into binary ionisation fields. Because of redshift, a photon emitted with a wavelength of 21cm during the EoR ($6 \lesssim z \lesssim 35$) will reach us today with a frequency $40 \lesssim \nu \lesssim 200$ MHz i.e. the frequency range that the new generation of radio interferometers, such as MWA, PAPER, LOFAR and SKA, are expected to probe.

3 THE TRIANGLE CORRELATION FUNCTION OF PHASES

For a real ionisation field $x(\boldsymbol{r})$ of volume V in dimension D, the n-point correlation function (n-PCF) measures the correlations between n points, described as $n-1$ vectors $\{\boldsymbol{r}_i\}$, $i = 1, \dots n-1$. It is defined as:

$$\Xi_n(\boldsymbol{r}_1, ..., \boldsymbol{r}_{n-1}) = \frac{1}{V}\int_V \mathrm{d}^D r \prod_{j=1}^{n-1} x(\boldsymbol{r}+\boldsymbol{r}_j), \tag{4}$$

where $\boldsymbol{r}_n = 0$. If we average this definition over all possible rotations, we obtain the isotropic n-PCF ξ_n. As can be seen in Eq. 4, the n-PCFs are convolutions and it will be easier to compute them in Fourier space. The Fourier transform of the n-PCF is called the n^th poly-spectrum P_n such that

$$P_n(\boldsymbol{k}_1, \dots \boldsymbol{k}_{n-1}) = \hat{x}(\boldsymbol{k}_1)\dots\hat{x}(\boldsymbol{k}_{n-1})\,\hat{x}\left(-\Sigma\boldsymbol{k}_j\right) \tag{5}$$

and

$$\begin{aligned}\Xi_n(\boldsymbol{r}_1, \dots \boldsymbol{r}_{n-1}) = \left[\frac{V}{(2\pi)^D}\right]^{n-1}\int \mathrm{d}^D k_1\, \mathrm{e}^{i\boldsymbol{k}_1\cdot\boldsymbol{r}_1}\ \dots\\ \times\int \mathrm{d}^D k_{n-1}\, \mathrm{e}^{i\boldsymbol{k}_{n-1}\cdot\boldsymbol{r}_{n-1}}\ P_n(\boldsymbol{k}_1, \dots \boldsymbol{k}_{n-1}).\end{aligned} \tag{6}$$

For $n = 2$, P_2 is called the power spectrum $\mathcal{P}(\boldsymbol{k})$ and for $n = 3$, we have the bispectrum $\mathcal{B}(\boldsymbol{k}, \boldsymbol{q})$ such that

$$\mathcal{P}(\boldsymbol{k}) = \hat{x}(\boldsymbol{k})\,\hat{x}(-\boldsymbol{k}) = |\hat{x}(\boldsymbol{k})|^2, \tag{7a}$$

$$\mathcal{B}(\boldsymbol{k}, \boldsymbol{q}) = \hat{x}(\boldsymbol{k})\,\hat{x}(\boldsymbol{q})\,\hat{x}(-\boldsymbol{k}-\boldsymbol{q}), \tag{7b}$$

where in the first equation we have used the fact that, because $x(\boldsymbol{r})$ is a real field, its Fourier transform verifies $\hat{x}(-\boldsymbol{k}) = \hat{x}^*(\boldsymbol{k})$. Note that we can also write the bispectrum in terms of three k-vectors $(\boldsymbol{k}_1, \boldsymbol{k}_2, \boldsymbol{k}_3)$ forming a closed triangle i.e $\boldsymbol{k}_1 + \boldsymbol{k}_2 + \boldsymbol{k}_3 = 0$.

Consider the 3-point correlation function (3-PCF), i.e. the inverse Fourier transform of the bispectrum:

$$\Xi_3(\boldsymbol{r}, \boldsymbol{s}) = \frac{V^2}{(2\pi)^{2D}} \iint \mathrm{d}^D k\ \mathrm{d}^D q\ \mathrm{e}^{i(\boldsymbol{k}\cdot\boldsymbol{r} + \boldsymbol{q}\cdot\boldsymbol{s})}\,\mathcal{B}(\boldsymbol{k}, \boldsymbol{q}). \tag{8}$$

To study filamentary structures in matter fields, Obreschkow et al. (2013, hereafter O13) consider the 3-PCF in Eq. 8 for $\boldsymbol{r} = -\boldsymbol{s}$ i.e. three equidistant points forming a straight line. Because here we look for spherical structures, we will consider two vectors $\boldsymbol{r}$ and $\boldsymbol{s}$ forming an equilateral triangle, as it is the three-point shape closest to a sphere. In this case, $\boldsymbol{s}$ is just $\boldsymbol{r}$ rotated by an angle $\pi/3$:

$$\begin{cases} s_x = \dfrac{1}{2} r_x - \dfrac{\sqrt{3}}{2} r_y \\ s_y = \dfrac{\sqrt{3}}{2} r_x + \dfrac{1}{2} r_y \\ s_z = r_z \end{cases} \tag{9}$$

where the 2D case is limited to the first two equations[5]. Let

$$\boldsymbol{p} = \begin{pmatrix} k_x + \frac{1}{2} q_x + \frac{\sqrt{3}}{2} q_y \\ k_y - \frac{\sqrt{3}}{2} q_x + \frac{1}{2} q_y \\ k_z + q_z \end{pmatrix}, \tag{10}$$

then we can write $\boldsymbol{k}\cdot\boldsymbol{r} + \boldsymbol{q}\cdot\boldsymbol{s} = \boldsymbol{p}\cdot\boldsymbol{r}$ in Eq. 8. If we choose to consider the phase factor of the bispectrum rather than its full form (see Eq. 2), we find the modified 3-PCF in dimension D

$$\Xi_3^*(\boldsymbol{r}) = \frac{V^2}{(2\pi)^{2D}} \iint \mathrm{d}^D k\,\mathrm{d}^D q\ \mathrm{e}^{i\boldsymbol{p}\cdot\boldsymbol{r}}\,\frac{\mathcal{B}(\boldsymbol{k}, \boldsymbol{q})}{|\mathcal{B}(\boldsymbol{k}, \boldsymbol{q})|}. \tag{11}$$

Note that, according to Eggemeier et al. (2015), the phase factor of the bispectrum can be directly related to the normalised bispectrum defined in Watkinson et al. (2017) and later used in Watkinson et al. (2019) and Trott et al. (2019). Assuming ergodicity, a rotational average of the above expression gives the isotropic modified 3-PCF:

$$\xi_3^*(r) \equiv \frac{V^2}{(2\pi)^{2D}} \iint \mathrm{d}^D k\ \mathrm{d}^D q\ \omega_D(pr)\,\frac{\mathcal{B}(\boldsymbol{k}, \boldsymbol{q})}{|\mathcal{B}(\boldsymbol{k}, \boldsymbol{q})|}, \tag{12}$$

where ω_D is the window function defined by

$$\omega_D(x) = \begin{cases} \dfrac{\sin(x)}{x} & \text{if } D = 3, \\ J_0(x) & \text{if } D = 2, \end{cases} \tag{13}$$

[5] Note that in the actual computation of the triangle correlation function, we will consider rotations not only around the z-axis but also around the other two.

for $J_0(x)$ the Bessel function of the first kind and order 0. Numerically, we will need to discretise the integral as

$$\xi_3^*(r) = \sum_{\boldsymbol{k}} \sum_{\boldsymbol{q}} \omega_D(pr)\,\frac{\mathcal{B}(\boldsymbol{k}, \boldsymbol{q})}{|\mathcal{B}(\boldsymbol{k}, \boldsymbol{q})|}, \tag{14}$$

for a periodic box with physical side length L, divided into N^D cells. Each cell has a width $\Delta x = L/N$. In Fourier space, this box transforms into a box of same dimensions (N^D) but of side length $2\pi N/L$ and spacing $\Delta k = 2\pi/L$. The largest mode $k = 2\pi/\Delta x$ has the smallest wavelength. If we assume phases are uncorrelated below a given scale, then the modes whose wavelengths are smaller than this scale will have random phases. When the resolution is improved, i.e. Δx reduced, the number of such modes increases and random phase terms are added to Eq. 14 so that the signal eventually diverges. Following O13, we introduce a cut-off $k \leq \pi/r$ on the sums of Eq. 14 to limit this number. Similarly, when increasing the size of the box L, we add modes with wavelength larger than the largest correlation scale within the box, and therefore add random phase terms to the sum. Because $\Delta k = 2\pi/L$, the number of modes scales as L^D and $s(\boldsymbol{r})$ diverges as $L^{3D/2}$. As discussed in O13, we introduce the prefactor $(r/L)^{3D/2}$ to Eq. 14 to remove this divergence. These changes applied to the isotropic modified 3-PCF $\xi_3^*(r)$ define the triangle correlation function of phases:

$$s(r) = \left(\frac{r}{L}\right)^{3D/2} \sum_{k,q\,\leq\,\pi/r} \omega_D(pr)\,\frac{\mathcal{B}(\boldsymbol{k}, \boldsymbol{q})}{|\mathcal{B}(\boldsymbol{k}, \boldsymbol{q})|}. \tag{15}$$

The imaginary part of $s(\boldsymbol{r})$ is zero therefore we only consider its real part in the following sections.

All these derivations have been done with $x(\boldsymbol{r})$ being the ionisation field $x_{\mathrm{H\,II}}$. If we consider the neutral field $x_{\mathrm{H\,I}}$, we have $x_{\mathrm{H\,II}} = 1 - x_{\mathrm{H\,I}}$ and $\hat{x}_{\mathrm{H\,II}}(\boldsymbol{k}) = -\hat{x}_{\mathrm{H\,I}}(\boldsymbol{k})$ which we can plug back into the equations above to find $s_{\mathrm{H\,II}}(r) = -s_{\mathrm{H\,I}}(r)$. Therefore when applied to a mostly ionised field containing a few remote neutral islands, the correlations dominating the signal will be related to H I regions and the signal will be negative. In particular, because 21cm interferometric images trace the neutral gas in the sky, if we apply our method on 21cm brightness temperature maps, we obtain the exact same signal as for the corresponding ionisation field, but with a reversed sign. This also implies that during the middle stages of the reionisation process, positive and negative (respectively, H II and H I) correlations overlap, and the TCF flattens down.

4 APPLICATION TO SIMULATED IONISATION FIELDS

We generate boxes of N^2 cells filled with randomly distributed ionised disks. Although the derivations performed in Section 3 are valid for a two or three-dimensional ionisation field, we now limit our work to 2D boxes, as they are closer to what one would observe with a radiotelescope. These boxes are binary: an ionised region will have pixels of value 1, whereas a neutral zone will be filled by zero pixels. Because the UV photons emitted by early galaxies have a very short mean free path in the surrounding neutral IGM, the boundary between ionised and neutral regions is expected to be sharp, and such a binary model is acceptable (Furlanetto et al. 2004a). Each simulated box has periodic

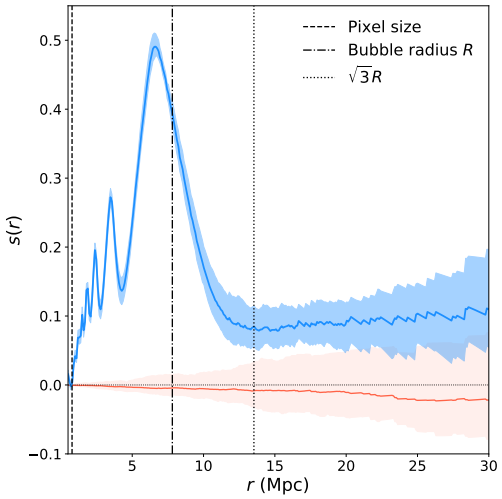

Figure 2. Triangle correlation function for a box of 512^2 pixels and side length $L = 400$ Mpc filled with 70 binary bubbles of radius $R = 10$ (pixel units). The shaded area corresponds to the 95% confidence interval as the function was computed for 30 different realisations of the same box. The triangle correlations of 30 Gaussian random fields of same dimensions are represented as the red line (mean value) and matching shaded area (95% confidence interval).

boundary conditions and ionised regions are allowed to overlap[6]. In a more realistic field, we would expect the ionised bubbles to be clustered around overdense regions rather than randomly distributed but we choose to first ignore this effect, as we will later consider it when applying our method to the 21CMFAST simulation. For each box, we compute the triangle correlation function as defined in Eq. 15 for a range of correlation scales r. We compare the resulting plot with the known size of the ionised bubbles filling the box. The programme we developed to compute these correlations is publicly available online[7].

4.1 Picking up characteristic scales

Fig. 2 shows the TCF computed for 30 realisations of a 2D box of 512^2 pixels and side length $L = 400$ Mpc filled with 70 binary bubbles of radius $R = 10$ (in pixel units) i.e. about 7.8 Mpc. The solid line is the mean value for all 30 boxes, and the shaded area represents the 95% confidence interval. Although the signal is very similar for all realisations of the box at small correlation scales, there is more variance at larger scales, as r gets closer to L. To see if this scattering is a numerical or physical effect, we compute the triangle correlations of 30 boxes of same dimensions, but with random Fourier phases; the result is added in red to the figure. In this case, the mean signal is close to zero but variance can still be seen at large scales. Interestingly, Eggemeier & Smith (2017) note the same scatter in the line correlation function $\ell(\boldsymbol{r})$ of density fields. The line correlation function is the 3-PCF of Fourier phases for three equidistant points aligned in real space (Obreschkow et al. 2013). Through its analytical derivation, they trace this scatter back to the Gaussian part of the covariance matrix of $\ell(\boldsymbol{r})$. From another point of view, we see that the mean signal flattens out when many realisations of the same box are considered. This suggests that the power seen on large scales corresponds to correlations between three points located in separate bubbles and so traces a form of correlation in the bubble locations. Because our simulation randomly distributes bubbles in the box, it is then only natural that these correlations would average out. The remaining non-zero value on large scales decreases as we increase the number of bubbles in the box and therefore can be assimilated to shot noise. Note that the oscillations on the left side of the peak are due to the sharp edges of the bubbles: when symmetrical Gaussian distributions are used instead of binary bubbles, or once the field is smoothed by a given angular resolution, they vanish. We refer the interested reader to Watkinson et al. (2017) and Majumdar et al. (2018), where the authors discuss the various problems induced by solid spheres in the bispectrum. Finally, a comparison of numerical results with an analytical derivation of the TCF for a similar toy model can eb found in Appendix A.

The triangle correlation function probes equilateral triangles inscribed in the ionised discs of the box, and simple geometry shows that these have a side length of $\sqrt{3}R$, a scale at which we would expect $s(r)$ to peak. On Fig. 2, there is a clear peak in the signal, but at $r \simeq 6.7$ Mpc $< \sqrt{3}R$. To check the physical meaning of this peak, we generate many boxes of same dimensions and fill each one of them with 50 binary bubbles of a given radius. Results are gathered in the upper panel of Fig. 3: the TCF peak shifts to larger scales as bubbles increase in size. We plot the peaking scale $r_{\rm peak}$ as a function of the bubble radius R in the lower panel of Fig. 3, where the error bars correspond to the 95% confidence interval for 10 realisations of the same box. Points are closely aligned, and a MCMC fit to a linear relation gives the following results, where both $r_{\rm peak}$ and R are in Mpc and the uncertainty corresponds to the standard deviation on sampled parameters:

$$r_{\rm peak} = (0.838 \pm 0.015)\ R + (-0.028 \pm 0.099)\,. \qquad (16)$$

We trace this shift between the peaking scale and the expected peak ($\sqrt{3}R$) back to the window function: when we take $\omega_D(x) = 1$ in Eq. 15 to compute the TCF, the signal has a shape similar to what is found for the correct window function, but is stretched over the x-axis, so that it peaks at a scale $R \leq r_{\rm peak} \leq \sqrt{3}R$.

Here, we chose to work with a binary field, with no partially ionised regions where $0 < x_{\rm H_II} < 1$. To see if our results hold when such regions exist, as there would be if X-ray photons significantly contributed to reionisation (Visbal & Loeb 2012) or if some observed regions are unresolved, we perform the same test but for symmetric 2D Gaussian distributions centred on the bubble radius R. The box dimensions are the same as before. As for binary bubbles, we observe a peak in the triangle correlation function at scales slightly smaller than $\sqrt{3}R$. A linear relation can still well describe the correlation between $r_{\rm peak}$ and R but there is more scatter around the model. This is mostly due to the peaks being difficult to locate: on average, the signal is much flatter for Gaussian than for binary bubbles.

[6] When they overlap, the maximum pixel value is set to 1, since it is a proxy for ionised level.
[7] https://github.com/adeliegorce/Triangle_correlations

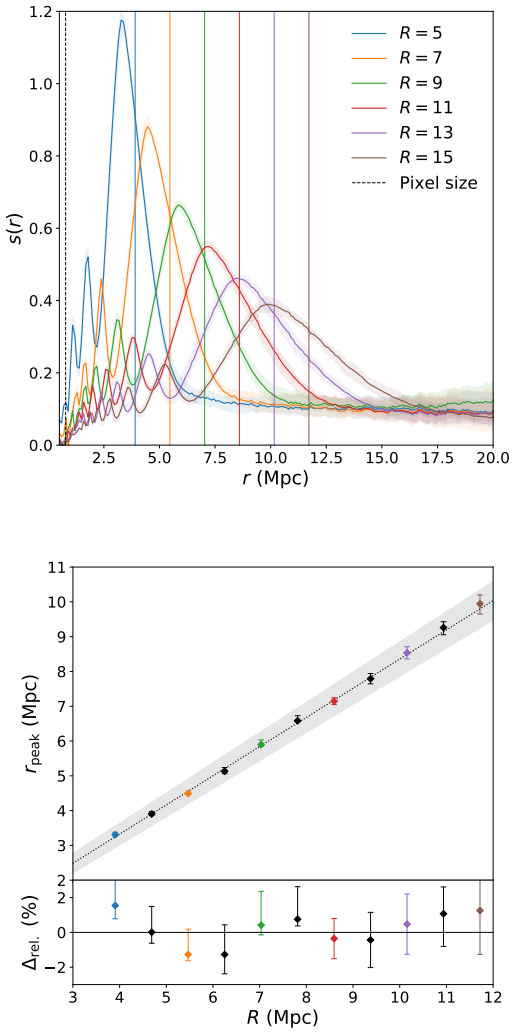

Figure 3. *Upper panel:* Triangle correlation function for 2D boxes 512 pixels, with box side length $L = 400$ Mpc and filled with 50 binary bubbles of different radii (see legend, in pixel units). Vertical lines are R for the box of the corresponding colour. *Lower panel:* Relation between the scale at which the triangle correlation function peaks $r_{\rm peak}$ and the size of the bubbles in the corresponding box R. The dotted line the maximum likelihood linear relation between the two with 95% confidence interval as the shaded area. The lower panel gives the relative distance to this result for each point.

Note that we checked that these results are independent of the number of bubbles in the box. Similarly to what O13 find, the number of bubbles (or filling fraction) will only impact the amplitude of the signal, not its shape. Indeed, for a given radius, the amplitude of the signal will decrease as the number of bubbles – and so the filling fraction of the box, increases. This is likely due to the fact that increasing the number of bubbles increases the number of different translations between objects within the box and so randomises the phase terms (Eggemeier et al. 2015). In general, we find that as long as the filling fraction does not exceed 60%, there is still a clear peak in the signal and we can infer a characteristic scale. This corresponds to the fact that in the late

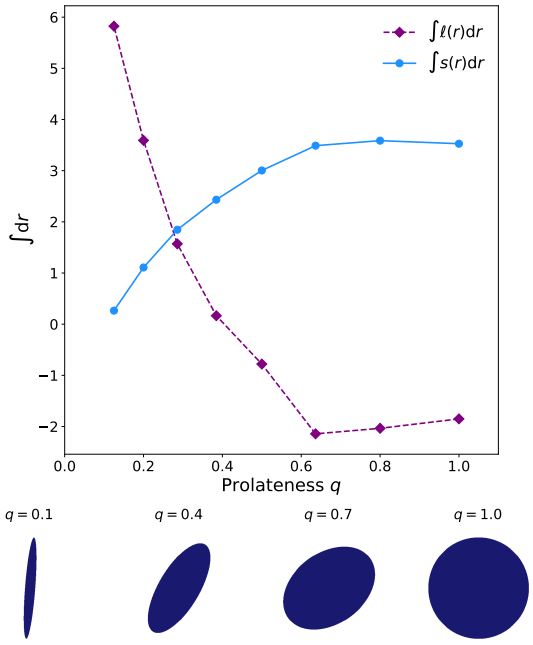

Figure 4. Evolution of the integral of the line (dashed purple) and triangle (solid blue) correlation functions with the prolateness of shapes filling up the considered box. Dimensions of studied boxes are again $N = 512$ and $L = 400$ Mpc.

stages of the reionisation process, the ionised regions have largely overlapped and they have no characteristic shape and size anymore. We can compare these results to those of Bharadwaj & Pandey (2005) who, through a more observational approach, relate the bispectrum of H I fluctuations to the correlations between the visibilities measured at three different baselines of an interferometer. They generate the same kind of toy models as us and find that their signal increases with the size of the ionised regions, but overlaps prevent their method from being used in the mid-stages of reionisation ($x_{\rm H\,II} \geq 0.5$).

4.2 Further tests

The TCF seems to correctly pick up the characteristic scale of spherical regions in an ionisation field. Because we want to use this method directly on Fourier data, for which no real space image will be available, we need to ensure that the peaking scale corresponds to spherical regions only. In their work, O13 define the line correlation function (LCF), which is analogous to our triangle correlation function but for two vectors $\boldsymbol{r}$ and $\boldsymbol{s}$ aligned ($\boldsymbol{s} = -\boldsymbol{r}$). Therefore $\ell(\boldsymbol{r})$ probes elongated rather than spherical structures and writes:

$$\ell(r) = \left(\frac{r}{L}\right)^{3D/2} \sum_{k,q \leq \pi/r} \omega_D\left(|\boldsymbol{k}-\boldsymbol{q}|r\right) \frac{\mathcal{B}(\boldsymbol{k},\boldsymbol{q})}{|\mathcal{B}(\boldsymbol{k},\boldsymbol{q})|}, \tag{17}$$

where the window function has not changed compared to our expression but is now a function of $|\boldsymbol{k}-\boldsymbol{q}|r$. O13 find the LCF to be close to flat when there are only spherical structures in the field considered (see their Figs. 3 and 4). To check the significance of each correlation function, we compute both of them for fields filled with bubbles of various

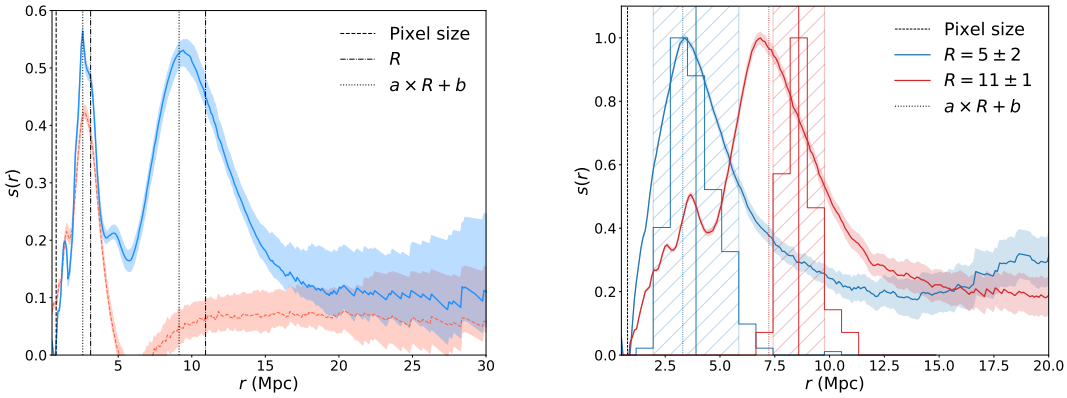

(a) (b)

Figure 5. *(a)* Triangle correlation function for 10 realisations of a box filled with 20 binary bubbles of radius 14 and 60 of radius 4 (in pixel units). Box dimensions are $N = 512^2$ and $L = 400$ Mpc. Vertical dashed-dotted lines correspond to the two bubble radii, the vertical dotted lines to the radii scaled by the linear relation from Eq. 16. Triangle correlations for 60 binary ellipses of the same dimensions are represented by the orange dashed line. *(b)* Triangle correlation function for 10 realisations of boxes filled with binary bubbles whose radii are selected from a log-normal distribution to reach a filling fraction of $\bar{x}_{\rm H\,II} = 0.09$. Box dimensions are $N = 512^2$ and $L = 400$ Mpc. The TCF (scaled to 1, solid lines) is compared to the actual distribution of radii, extracted directly from the simulation and shown as a histogram. Hatched areas correspond to $R \pm \sigma$. Vertical solid (resp. dotted) lines correspond to the radius (resp. radius scaled by the linear relation from Eq. 16).

sizes and compare the results. We find that the LCF also picks up the bubble size, with a peak located at roughly the same correlation scales as for triangle correlations, but with a much weaker amplitude. To push the comparison further, we compute the TCF and the LCF for 2D boxes filled with more or less stretched binary ellipses. We define the prolateness q of an ellipse as the ratio of its semi-minor axis to its semi-major axis so that an ellipse with prolateness $q = 1$ is a flat disk. Fig. 4 shows the evolution of the integral of the two correlation functions as a function of the prolateness of the objects in the box [8]. As $q \to 1$, the triangle correlations signal increases, while the line correlations signal decreases, even reaching negative values for $q > 0.4$. On the contrary, for $q = 0.1$, the TCF is close to zero and the LCF shows very strong signal. This confirms that the TCF mostly picks up spherical structures and therefore can safely be used to infer characteristic bubble sizes directly from Fourier data.

In reality, the reionisation process will not be as homogeneous as our toy models: it is unlikely that all ionised bubbles should have the same radius at a given redshift. It would therefore be useful if the triangle correlation function could differentiate between bubbles of different radii. To test for this, we generate a box of 512^2 pixels and side length $L = 400$ Mpc, filled with 20 binary disks of radius 14 px and 60 of radius 4 px. Results are displayed on Fig. 5a for 20 realisations of this box. We can clearly distinguish two peaks, which seem to match the bubble radii (dash-dotted vertical lines), once scaled by the coefficients of Eq. 16 (dotted vertical lines). Note that this result holds when we replace the binary bubbles by Gaussian disks. To ensure that the scales picked up by our function correspond to two different sizes of bubbles and not to the length and width of elongated structures, we compute the triangle correlations of a box filled with 60 binary ellipses of the same dimensions as the bubbles above i.e. a semi-major axis $\alpha = 14$ px and a semi-minor axis $\beta = 4$ px. The resulting TCF, shown as an orange dashed line on the figure, differs largely from the TCF of discs. There is only one clear peak, corresponding to scales close to the semi-minor axis: because it probes equilateral triangles, the function seems to pick up elongated ellipses as rows of discs of radius β. The possibility to discern two peaks in the TCF in the presence of different bubble sizes will be limited by two factors. First, the number of bubbles, as we have seen that too many or too few objects leads to a weak signal. We find that when the ratio of large over small bubble numbers exceeds 10 or drops below 0.1, one of the two peaks flattens out. Second, the separation between the two radii: the TCF peaks of bubbles with $R = 6$ px and $R = 10$ px will overlap into one single wide peak and we will not be able to differentiate them anymore.

Analytic derivations predict a log-normal distribution for the bubble sizes during reionisation, which becomes increasingly peaked as bubble grow and merge (Furlanetto et al. 2004b). This first result has been confirmed by many authors looking at simulations (McQuinn et al. 2007; Zahn et al. 2007; Lin et al. 2016). Let two boxes where the bubble centres are randomly distributed, but the radius sizes are sampled from a log-normal distribution. Because we generate the box, we know the exact distribution of bubble radii within and we want the TCF to trace it. On Fig. 5b, we compare the TCF (solid line) with the actual radius distribution (histogram) for 2 different bubble size distributions: on centred on $R = 5$ px with variance 2 px, corresponding to the early stages of EoR, and one with $R = 11$ px with variance 1 px, corresponding to later stages. The number of bubbles is adjusted to reach a filling fraction $x_{\rm H\,II} = 0.09$. Overall, there is a reasonably good match between the two. We see that as the mean radius increases, the discrepancy between peaking scale and real bubble size grows in a way

[8] Note that we integrate only on the correlation range 0.5 Mpc $\leq r \leq$ 20 Mpc where the signal is more reliable (see Sec. 4.1).

that the linear relation of Eq. 16 cannot fully compensate for. Note that results are similar for a Gaussian distribution of the bubble sizes.

4.3 Results on 21CMFAST simulation

Now that our method has been tested and characterised on toy models, we apply it to more physical ionisation fields, extracted from the semi-numerical simulation of reionisation 21CMFAST[9] (Mesinger & Furlanetto 2007; Mesinger et al. 2011). We choose 21CMFAST because, thanks to relatively short executing times, it gives a large flexibility in parametrisation. It also includes an implementation of the random mean free path algorithm to estimate the bubble size distribution of data cubes, which we can compare to our estimator. Note that an important difference with the toy models is that the bubble locations are no longer random, and the TCF might pick up correlations between the bubble centres on large scales. The 21CMFAST code first generates a high-redshift linear density field which is then evolved to lower redshifts using linear theory and the Zel'dovich approximation. The ionisation field is extracted from this density field using excursion-set theory for haloes with virial temperature $T > 10^4$ K. We use this code to generate a box with sufficient resolution to obtain a H I field of 512^3 pixels and side length $L = 400$ Mpc for the following cosmology: $\Omega_m = 0.308$, $\Omega_b = 0.049$ and $H_0 = 67.74$ km.s^{-1}Mpc^{-1} (Planck Collaboration et al. 2016a). The resulting reionisation history has its midpoint at $z = 7.9$ for a duration of $\Delta z = z(x_{\rm H\,II} = 0.10) - z(x_{\rm H\,II} = 0.99) = 4.9$ and gives an integrated Thomson optical depth of $\tau = 0.067$ (see Fig. 7).

The output of the simulation is a 3D H I field but we choose to analyse 2D slices to be closer to actual observations. We also convert the given H I field into a binary H II field in order to get positive triangle correlations when most of the field is ionised and negative correlations when the sky is mainly neutral (see Eq. 7b for $x_{\rm H\,I} = 1 - x_{\rm H\,II}$ and discussion at the end of Sec. 3), in continuity with previous sections. Fig. 6 presents the TCF of 2D slices at redshifts $z = 12.0, 11.0, 10.0, 9.0, 8.0, 7.0, 6.4$ and 6.2 corresponding to global ionisation levels of $x_{\rm H\,II} = 0.09, 0.10, 0.18, 0.29, 0.49, 0.80, 0.97$ and 0.99 respectively, along with a picture of the corresponding H II field. For each simulation, results are shown with variance estimated from the TCF of 20 Gaussian random fields (GRF) of same dimensions. This indicates that the signal is more significant at small scales, a point already mentioned in Section 4.1 and gives an idea of how well this field differs from a GRF. However, these errors will not take into account the non-Gaussian nature of the field if the 2D slice considered is not representative of the overall field, especially at high redshifts where the signal is highly non Gaussian. Indeed, consider the $z = 6.2$ slice on Fig. 6: the small ionised regions seen in the field are isolated features. If we compute triangle correlations for more realisations of this simulation, it is unlikely that the exact same feature will appear in the field and so in the TCF. Therefore there will be more variance on small scales than the error bars on the Figure. Ideally, one would find a theoretical expression for the covariance of the TCF, but we keep this derivation for future work.

At high redshift, in what is often referred to as the *pre-overlap phase*, we see on the TCFs of Fig. 6 that there is more power at small scales but no clear peak. This is likely due to the variety of H II regions: many small ionised regions around young sources parcel the neutral background out. However, by looking at the signal-to-noise ratio (SNR), we can infer an upper limit on the sizes of the ionised regions: at $z = 13$, scales smaller than 8.9 Mpc (after conversion with Eq. 16) contribute for 80% of the cumulative SNR; at $z = 12$ and $z = 11$, this upper limit increases respectively to 10.8 Mpc and 11.2 Mpc. The structure of the ionisation field at high redshift directly relates to the way the 21CMFAST algorithm is constructed and particularly to the use of excursion set theory. In excursion-set theory, when the average density of a region exceeds a given threshold, it collapses to form a halo. When applied to reionisation, the threshold additionally considers ionising photons production: if the region has produced a sufficient number of ionising photons with respect to its mass and volume, then it is considered ionised. Because of this, the ionisation field in the early stages of reionisation will have many very small sources rather than a few efficient sources. It would be interesting to compute the TCF of other reionisation simulations, in particular simulations with more efficient escape fractions (Seiler et al. 2019). This also includes simulations where reionisation is led by Active Galactic Nuclei (AGN): ionising sources are more scarce and have a better ionising efficiency, leading to a topology more similar to the toy models used in Sec. 4.1. In this perspective, our method may be able to differentiate between different reionisation scenarios. Such a study goes beyond the scope of this work but we refer the interested reader to Watkinson et al. (2019), where the authors use the bispectrum as a probe for non-Gaussianities due to X-ray heating.

Later on, when the global ionisation fraction reaches values between 25% and 75%, negative signal coming from neutral regions overlaps with the positive signal from ionised regions. The TCF flattens, and therefore cannot give information about the morphology of the field. However, measuring a flat signal from actual data could be interpreted as the reionisation process being in its middle stages. For $z > 7$, most of the sky is ionised and only a few remote neutral islands remain. This is the *post-overlap phase*. We see on Fig. 6 that the sizes of these neutral islands are efficiently picked up by the TCF. For $z = 6.2$, there is a very clear negative peak at scales $r = 7.7$ Mpc which correspond to a radius size of $r' = 9.2$ Mpc once the linear relation in Eq. 16 is applied as a correction. If we roughly estimate the size of the neutral zones, we find that they are about ~ 11 px ~ 8.6 Mpc in radius, which is very close to the estimation given by triangle correlations. For $z = 6.4$, we see two clear peaks in the signal, corresponding to the two sizes of ionised regions seen in the corresponding real space field. The first peak is spread over scales $4.6 < r < 7.8$ Mpc i.e. $5.5 < r' < 9.3$ Mpc, while the second one is more narrow, centred around 20.2 Mpc. For comparison, we find that we can sieve the two larger neutral islands in the field with disks of radius ~ 23 px ~ 18 Mpc; whereas the smaller ones can fit in disks whose radii range from 7 Mpc to 12 Mpc. This motivates a further study of

[9] http://github.com/andreimesinger/21cmFAST

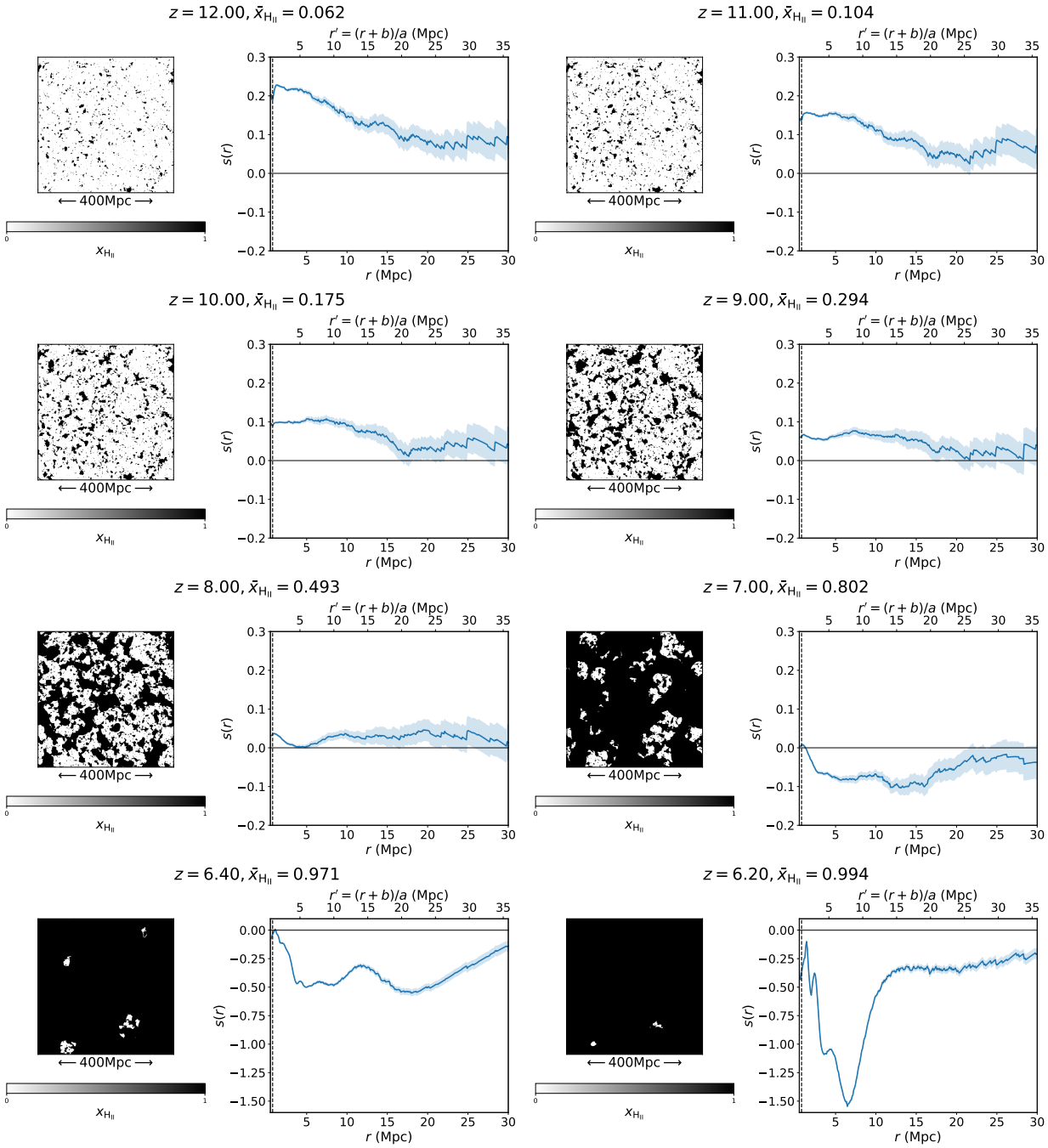

Figure 6. Triangle correlations for 2D slices of our simulation at various redshifts. The upper x-axis is the lower one scaled by the linear relation in Eq. 16. Error bars correspond to the variance estimated from a Gaussian random field of same dimensions.

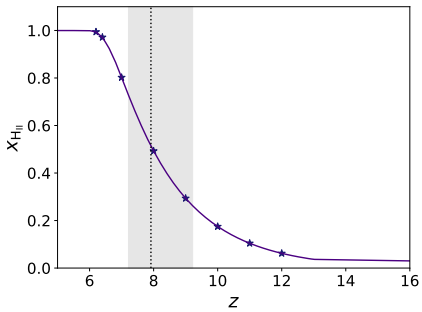

Figure 7. Reionisation history of our simulation. The dotted line corresponds to the midpoint of reionisation, i.e. $z = 7.9$, and the shaded region to global ionised fraction between 25% and 75%. The starred points are the stages of reionisation represented above.

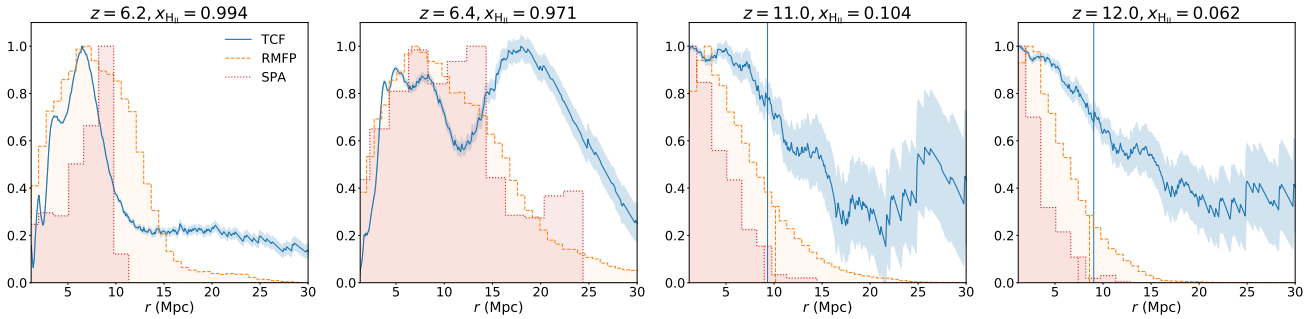

Figure 8. Comparison of different methods to estimate the size of neutral (for $z = 6.2$ and 6.4) or ionised ($z \geq 11$) regions in our 21CMFAST simulation. Error bars correspond to the variance estimated from a Gaussian random field of same dimensions.

Table 1. Peaking scale (in Mpc) for different methods to obtain the bubble size distribution of realisations of the 21CMFAST simulation at different redshifts.

z	$x_{\rm H\,II}$	TCF	RMFP	SPA
13.0	0.036	< 8.9	2.01	< 5.9
12.0	0.062	< 10.8	2.34	< 7.4
11.0	0.010	< 11.2	3.12	< 8.9
6.4	0.971	6.2 & 20.2	7.0	13.9
6.2	0.994	7.7	7.0	9.4

how well the TCF performs compared to common BSD algorithms.

Let's consider the spherical average (SPA) and the random mean free path (RMFP) methods. Note that these two algorithms need to be applied to real space images whereas the TCF is used on Fourier data. We choose not to compare our results to the friend-of-friends algorithm (Iliev et al. 2006) because it considers overlapping bubbles as a unique large ionised region, which is fundamentally different from our approach. We use versions of SPA and RMFP implemented by the authors of Giri et al. (2018a)[10]. Recall that the SPA algorithm looks for the largest sphere around each ionised region whose ionisation level exceeds a given threshold, here chosen to be $x_{\rm H\,II} = 0.5$. RMFP, on the other side, relies on MCMC: it looks for the first neutral cell encountered in a random direction starting from an ionised pixel and records the length of the ray to build a histogram. The SPA and RMFP outputs are probability distributions of radii.Results can be seen on Fig. 8 for $z = 6.2, 6.4, 11.0$ and 12.0 and are detailed in Table 1. For clarity, we plot $-s(r)$ in the first two panels to have a positive signal for all redshifts. At low redshift, our method mostly agree with the other BSDs, although the TCF exhibits a narrower peak; we are also able to clearly distinguish between two characteristic scales for $z = 6.4$, whereas SPA et RMFP only give one most likely scale, apparently corresponding to the smaller neutral regions. At higher redshift, the SPA distributions tend to $r \sim 0$ Mpc and we choose to compare values of quantiles rather than maximum likelihood values: at $z = 11$, according to SPA, there is a 80% probability that the ionised regions have a radius smaller than 13.3 Mpc; similarly, scales < 11.2 Mpc represent 80% of the cumulative SNR for the TCF. These upper limits, computed for both $z = 11$ and $z = 12$, are shown as vertical lines on Fig. 8. RMFP gives a maximum likelihood radius of 3.12 ± 0.78 Mpc (the error corresponding to the bin size), therefore the most quantitative result. For all three methods, the upper limit increases as redshift decreases, which corresponds to ionised regions growing with time. Note that the upper limit given by SPA is the lowest: our results corroborate those of Lin et al. (2016), who argue that SPA is heavily biased towards smaller bubble radii than the actual bubble sizes. Indeed, they find that for a single bubble of radius R, the SPA probability distribution peaks at $R/3$. On the contrary, they find the RMFP method to be unbiased and to peak at the correct bubble size. Note that on the two right panels of Fig. 8, we see some signal at large scales. This can be related to statistical noise on one side – we analyse a unique slice of the simulation; and to the potential correlations between separate bubbles, which are not randomly distributed anymore.

Overall, our estimator performs well with respect to comparable BSD algorithms. However, for this method to be an useful tool in the analysis of upcoming radio observations, a deeper analysis, including the study of different types of reionisation simulations, would be required. In practise, we would also use this method as a forward modelling process, and compare triangle correlations from observations to a set of predicted signals for different types of ionisation fields. We keep the construction of such a database for future work.

5 RELATION TO OBSERVATIONS

5.1 Visibilities and closure phases

When gathering data with an interferometer, the signal will be measured for pairs of antennae separated by a baseline D. The measurement is made in terms of a complex visibility $V(u, v)$, where u and v are the projection of the baseline in wavelength units on the plane perpendicular to the vector $\boldsymbol{s}_0$ pointing to the phase reference position, i.e. the centre of the field to be imaged. In Eq. 3, the brightness temperature depends on the position in the sky $\boldsymbol{r}$ where the signal is observed: $\delta T_{\rm b}(\boldsymbol{r}, z) \propto x_{\rm H\,I}(\boldsymbol{r}, z)$. $\delta T_{\rm b}$ is the intensity I_ν of the 21cm signal observed through the interferometer for a given frequency ν (i.e. for a given red-

[10] `tools21cm` are found on https://github.com/sambit-giri/tools21cm.

shift, since $\nu = \nu_{21\mathrm{cm}}/(1+z)$)[11]. In what follows, we will use $I_\nu(\boldsymbol{r}) = \bar{I}_\nu\, x_{\mathrm{H\,I}}(\boldsymbol{r}, z)$ and $\delta T_\mathrm{b}(\boldsymbol{r}, z)$ interchangebly. If the interferometer probes a sufficiently small region of the sky compared to the beam width of the antennae, we can approximate this region by a flat plane. Then the source intensity distribution is a function of two real spatial variables (l, m) and the van-Cittert theorem tells us that the complex visibility is the 2D inverse Fourier transform of the intensity, corrected by the normalised average effective collecting area $A(l, m)$ of the two antennae (Thompson et al. 2017):

$$A(l,m)\, I_\nu(l,m) = \sqrt{1-l^2-m^2} \iint V(u,v)\, \mathrm{e}^{2i\pi\,(ul+vm)}\, \mathrm{d}u\, \mathrm{d}v, \tag{18}$$

that we can re-write as

$$V(u,v) = \hat{A}^\star(u,v) * \hat{I}_\nu(u,v) \tag{19}$$

where $*$ denotes a convolution, $\hat{A}$ and $\hat{I}_\nu$ are respectively the 2D Fourier transforms of A and I_ν and we define $A^\star = A/\sqrt{1-l^2-m^2}$. Note that this approximation introduces a phase error that may need to be taken into account when applying our method, based on phase information. Because $A(l, m)$ is a measurable instrumental characteristic, if we know our instrument sufficiently well, we can deconvolve the measured complex visibilities by $\hat{A}^\star$ and obtain, after correcting for the different pre-factors, the $\hat{x}(\boldsymbol{k})$ terms to compute the triangle correlation function.

One of the interests methods based on phase information is that the phases of the measured visibilities, combined in a bispectrum, will not be sensitive to errors related to calibration (Jennison 1958; Monnier 2007). Consider the visibility V_{ij}^m measured between two antennae i and j at a given frequency ν. It will have contributions from the true visibility V_{ij}^true, coming from the cosmological signal, but also from the amplitude and phase errors of each antenna, modelled by a complex gain $G_i = |G_i|\, \mathrm{e}^{i\phi_i}$, such that:

$$\begin{aligned} V_{ij}^\mathrm{m} &= G_i G_j^*\, V_{ij}^\mathrm{true}, \\ &= |G_i G_j|\, \mathrm{e}^{i(\phi_i-\phi_j)}\, V_{ij}^\mathrm{true}, \end{aligned} \tag{20}$$

where $*$ denotes the complex conjugate. The amplitude of this gain will come from beam specific effects such as mirror reflectivity, detector sensitivity or local scintillations whereas the phase term can originate either from telescope errors or from outside effects such as atmospheric turbulence (Levrier et al. 2006; Monnier 2007). If we combine the signal from three antennae forming a closed triangle, we can avoid this phase error and we will be left only with what is called the closure phase. Indeed, consider three baselines ij, jk and ki observing at the same given frequency ν. We can write the bispectrum of their complex visibilities as

$$\begin{aligned} \mathcal{B}_{ijk} &= V_{ij}^\mathrm{m}\, V_{jk}^\mathrm{m}\, V_{ki}^\mathrm{m} \\ &= |G_i G_j G_k|^2\, \mathrm{e}^{i(\phi_i-\phi_j)}\, \mathrm{e}^{i(\phi_j-\phi_k)}\, \mathrm{e}^{i(\phi_k-\phi_i)}\, V_{ij}^\mathrm{true}\, V_{jk}^\mathrm{true}\, V_{ki}^\mathrm{true} \\ &= |G_i G_j G_k|^2\, V_{ij}^\mathrm{true}\, V_{jk}^\mathrm{true}\, V_{ki}^\mathrm{true}, \end{aligned} \tag{21}$$

[11] We assume the instrument to have narrow bandpass filters and so to probe exactly ν rather than a frequency band centred on ν.

where in the last step, the different phase terms cancel each other out: the phase of the measured bispectrum is the phase of the true bispectrum. By construction, the bispectrum $\mathcal{B}(\boldsymbol{k}, \boldsymbol{q})$ in Eq. 7b considers a closed triangle configuration, for three vectors $\boldsymbol{k}$, $\boldsymbol{q}$ and $-\boldsymbol{k}-\boldsymbol{q}$. Because we choose to work in two dimensions, the three vectors lie in the same plane on the sky, perpendicular to the line-of-sight, and are measured for the same frequency so that the closure relation holds. We will then be able to use our method on observational data without worrying about calibration errors. For an example of the use of bispectrum closure phases in interferometry, we refer the reader to Thyagarajan et al. (2018). In this work, the authors compare the bispectrum phase spectra, i.e. the phases of the bispectrum $\mathcal{B}_{ijk}$ in Eq. 21, coming from different components of a simulated signal, i.e. a single point source, diffuse foregrounds and H I fluctuations from the EoR and demonstrate that a quantitative relationship exists between the EoR signal strength and the whole bispectrum phase power spectra.

These properties are a major benefit of our technique compared to other solutions found in the literature to estimate the characteristic size of ionised regions from interferometric data as these always require to reconstruct the real-space image corresponding to observations. Indeed, our method can directly use as input the complex visibilities observed by an interferometer, and if we choose to use closure phases, results will be independent of antenna-based calibration and calibration errors. However, in practise, there are some limitations to the use of the closure relation.

First, only a limited number of triangles can be constructed from the array of antennae of a telescope, therefore some information will be lost compared to simple baseline measurements. Monnier (2007) count that for an array made of N antennae, there are $n = \binom{N}{3} = N(N-1)(N-2)/6$ possible closed triangles, $\binom{N}{2}$ independent Fourier phases and $\binom{N-1}{2}$ independent closure phases. Therefore the amount of phase information recovered from closure phases is

$$\frac{\binom{N-1}{2}}{\binom{N}{2}} = \frac{(N-1)(N-2)}{2} \times \frac{2}{N(N-1)} = \frac{N-2}{N} = 1 - \frac{2}{N}. \tag{22}$$

With as little as 40 antennae, we are able to recover 95% of the phase information but 1000 antennae are not enough to reach 99.9%. Note that for the 296 antennae of the SKA1-*Low* central array and the 48 antennae of LOFAR, we recover respectively 99.3% and 95.8% of the phase information from closure phases. However, even if almost all the phase information is recovered, Readhead et al. (1988) find that the noise level of a phase-only observation will still be at least twice higher than a map made from full visibility data, because when ignoring amplitudes, half of the signal is lost. Additionally, Readhead et al. (1988) show that because the bispectrum is a triple product, there will be new sources of noise compared to single baseline observations. First, if the same signal is measured on different time intervals, the observed bispectrum will not only be the product of three complex numbers V_{ij} anymore, but of the sum of each observation on each time interval:

$$\mathcal{B}_{ijk} = \left(\sum_m V_{ij,\tau_m}\right) \times \left(\sum_m V_{jk,\tau_m}\right) \times \left(\sum_m V_{ki,\tau_m}\right), \tag{23}$$

where V_{ij,τ_m} is the visibility measured for baseline ij on time

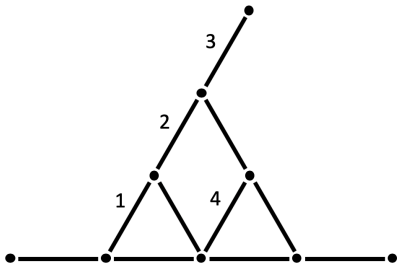

Figure 9. Example of a redundant array of antennae.

interval τ_m. Then the cross terms combining signals integrated on different time intervals (e.g. V_{ij,τ_m} and V_{jk,τ_l}) will give incoherent phase terms that can be assimilated to noise. The second potential source of noise mentioned by Readhead et al. (1988) corresponds to the same kind of reasoning, but in the spatial domain: if we consider the triangle formed by three baselines (ij, ik, kl), then on a redundant array there will be contributions not only from the $ij + jk + kl = 0$ triangles but also from identical baselines who are not part of a triangle. See the example on Fig. 9 of a redundant array: all numbered vectors correspond to the same baseline but only 1, 2 and 4 form triangles. When probing ijk triangles, the measured bispectrum will take the sum of the four signals as the visibility corresponding to this baseline (e.g. $V_{ij} = V_1 + V_2 + V_3 + V_4$) and additional cross terms, irrelevant to closure phases because they include V_3, will arise. Readhead et al. (1988) show however than these two types of noise can be reduced to a sensible signal-to-noise ratio if enough frames are used in the integration. Similarly, Carilli et al. (2018) mention that some instrumental effects such as polarisation leakage or cross coupling of antennae, called "closure errors" can lead to a departure from the closure relation.

Finally, the limited number of triangles one can construct from N given antennae will limit the sampling of (u, v) space and worsen the sparsity of observations. Applying our method to sparse data goes beyond the scope of this work, but it would be interesting to see how triangle correlations perform with this additional difficulty. For now, we will limit ourselves to noisy data sets. We refer the interested reader to Trott et al. (2019), where the authors compute the normalised bispectrum defined in Watkinson et al. (2019) from the closed triangle visibilities of MWA Phase II.

5.2 Instrumental effects

To see how our method performs when applied to actual observations, we now add instrumental effects to our ionisation maps: beam smoothing and noise corresponding to observations by the core of SKA1-*Low*, its central area, and by LOFAR. We pick three simulated ionisation fields: the first comes from the toy models described in Section 4. It is made of 70 bubbles of radius $R = 10$ px, and assumed to correspond to a redshift $z = 9$. The two others are extracted from 21CMFAST at redshifts $z = 6.2$ and 6.4. They are shown, in this order, on the left panels of Fig. 10. We first convert each one of them into a brightness temperature map according to Eq. 3 with the following cosmology: $\Omega_m = 0.309$, $\Omega_b = 0.049$ and $H_0 = 67.74$ km.s^{-1}Mpc^{-1}.

Table 2. Peaking scales (Mpc) for a toy model with different types of observational effects: smoothing due to angular resolution and noise for an integration time of 1000 h. Actual radius size is 7.8 Mpc.

	Clean signal	Smoothed signal	Smoothing + 1000h	Smoothing scale
LOFAR	6.7	6.6	7.4	4.5
SKA1-*Low* core	6.7	8.2	–	17.0
SKA1-*Low* central	6.7	6.7	6.9	5.3

The resolution of 21-cm tomographic data will be first limited by the angular resolution of the interferometer considered. The full width at half maximum (FWHM) of an interferometer is given by (in radians):

$$\theta_{\rm AR} = \frac{\lambda}{b_{\rm max}}, \tag{24}$$

where λ is the redshifted 21cm wavelength i.e. $\lambda = 21\text{cm}\times(1+z)$ and $b_{\rm max}$ is the maximum baseline of the interferometer. We have $b_{\rm max} = 3500$, 1000 and 3400 m for LOFAR, SKA1-*Low* core and SKA1-*Low* central respectively. To account for this effect, we convolve the δT_b map with a Gaussian kernel of FWHM $\theta_{\rm AR} d_c(z)$, with $d_c(z)$ the comoving distance at the redshift (i.e. frequency) considered. For SKA central, we get the second-to-left panels on the figure – note that because they have similar maximum baselines, the angular resolution of SKA central is close the one of LOFAR. For SKA core, because $b_{\rm max}$ is much smaller, the smoothing blurs the shape of the ionised bubbles to an extreme point, and our method will perform poorly. Finally, we simulate realistic instrumental noise by using the measurement equation software OSKAR[12].

Fig. 10 presents the results: the first column corresponds to triangle correlations for a clean field. We identify the peaking scale for this clean field in order to compare it to the scale picked on corrupted data later on and indicate it as a dotted blue line on each plot. Note that for the third field (21CMFAST at $z = 6.4$), there are two scales picked up. The larger one is well defined, whereas we use an interval 6.2 ± 1.6 Mpc for the smaller one. On the figure, the second column is for the field smoothed with the angular resolution of SKA1-*Low* central; and the last three for the smoothed signal with instrumental noise from each of the three experiments considered (respectively SKA1-*Low* core, central and LOFAR) and 1000 hours of integration time. We choose 1000h as it is the most commonly used value in the literature, but recent works have shown that as few as 324h of observations with SKA can be sufficient to differentiate between different reionisation models (Binnie & Pritchard 2019). The dash-dotted lines on each plot mark the smoothing scale of the corresponding experiment, whose values are given in Table 2. One can see that results with SKA core are not satisfying because of a too low angular resolution that blurs the edges of the ionised regions: the signal is mostly flat or seems to pick up the smoothing scale. However, results for SKA central and LOFAR prove very satisfactory on the toy model (first row), with a clear peak at a scale close

[12] https://github.com/OxfordSKA/OSKAR

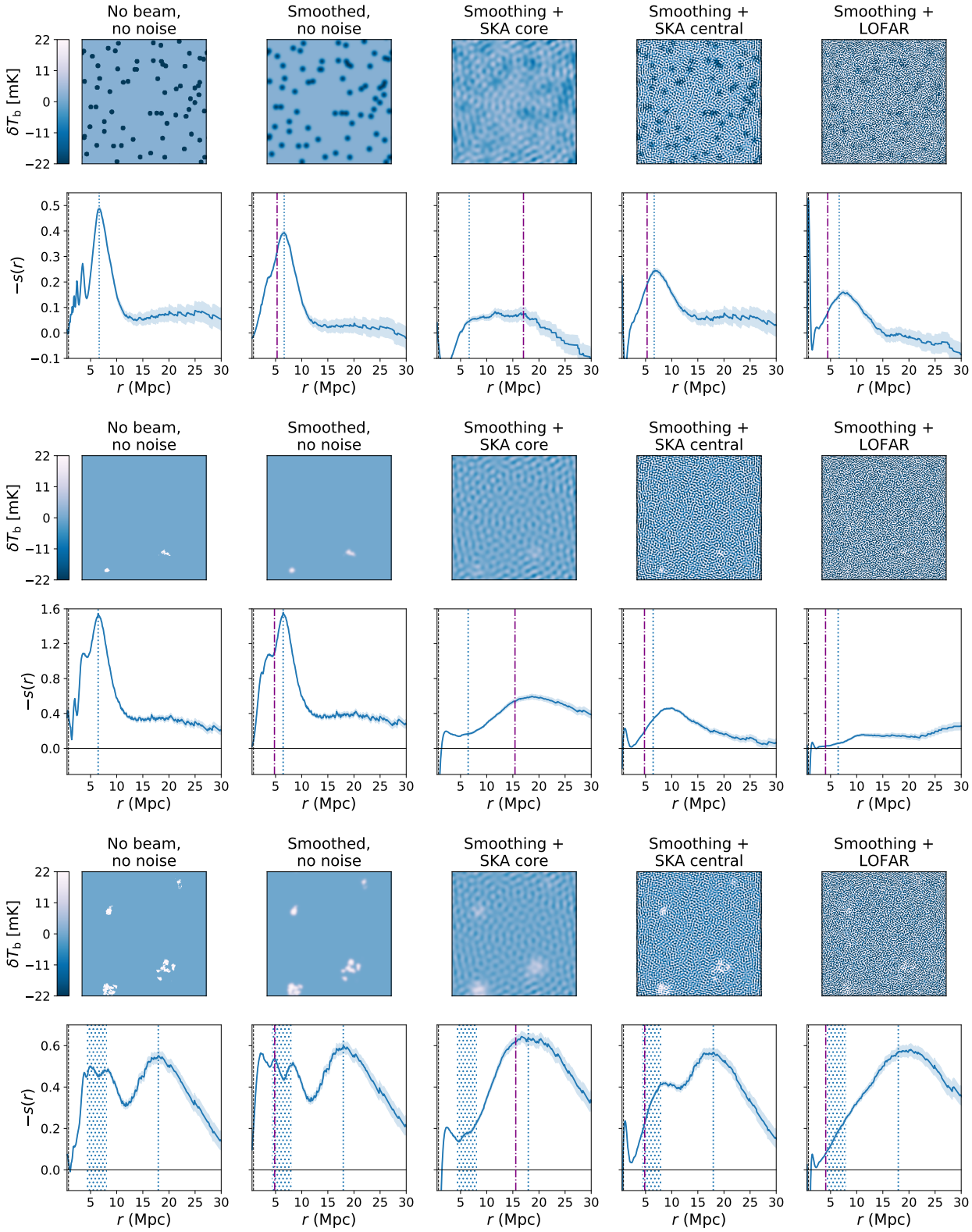

Figure 10. Comparison of phase correlations for a 2D brightness temperature map with dimensions $N = 512$, $L = 400$ Mpc for different types of instrumental noise. From left to right: the clean signal, the field smoothed by a Gaussian beam corresponding to the angular resolution of SKA central, and the clean field with added smoothing and noise from each experiment, respectively SKA1-Low core, SKA1-Low central and LOFAR. In each case, the integration time is 1000 hours. Note that $s(r)$ was computed on δT_b maps, derived from the neutral field, hence the signal is mostly negative; for readability here we have represented $-s(r)$. The dotted blue lines (regions) indicate the peaking scale found on the clean field (left panel) and the purple dash-dotted lines the smoothing scale of the corresponding experiment. From top to bottom: toy model of 70 R = 10px binary bbbles, 21CMFAST simluation at $z = 6.2$ and $z = 6.4$ respectively. Error bars correspond to the variance estimated from a Gaussian random field of same dimensions.

to the one found with clean signal (see Table 2 for details): applying the linear relation of Eq. 16 to the peaking scale could give a good approximation of the actual size of ionised regions in the image. When the integration time is increased, we get for both LOFAR and SKA1-*Low* central a peaking scale even closer to the one found for clean signal. Unfortunately, the LOFAR sensitivity does not allow to extract much information from the 21CMFAST maps: at $z = 6.2$ the signal is mostly flat, and although there is a clear peak for the $z = 6.4$ map, it cannot resolve the two characteristic scales, however picked up when accounting for SKA central sensitivity. Note that for each plot, the error bars correspond to the variance of the TCF computed for a GRF of same dimensions. We have also tried our statistic on 21CMFAST boxes at higher redshifts, and we find that, because there is no clear characteristic scale in the field (see Section 4.3), the TCF peaks at the smoothing scale corresponding to the telescope considered (listed in Table 2). There is however no risk of misinterpretation of this peak since real data would be deconvolved from telescope properties such as angular resolution before being analysed.

In all the work above, we assumed that foreground pollution was completely removed from the data cubes: Chapman et al. (2015) presented efficient foreground removal techniques that will produce good quality 21cm maps. However, foreground residuals could still impact our results. A precise instrumental calibration is usually required to separate the 21cm signal from foregrounds and is one of the main challenges of upcoming experiments although as mentioned before, it seems that bispectrum phases and therefore our results would be unaffected by calibration errors (Thyagarajan et al. 2018).

6 WHY PHASE INFORMATION?

In order to see if our phase-only estimator truly supplements power spectrum information, we generate a 2D ionisation field made of 70 binary disks of radius $R = 10$ px $= 7.8$ Mpc and compute its 2-point correlation function and its TCF. We then shuffle its Fourier phases – replace them by random phases ranging from 0 to 2π, and compute the corresponding 2-PCF and TCF. Results can be seen on the upper and lower panels of Fig. 11 respectively. On the left panels, we see that reshuffling the phases has made the field lose all its structure: there are no bubbles any more. Because we kept the absolute value of the field unchanged, the 2-PCFs in the second column are exactly identical. However, the extra information carried by phases is clearly visible when comparing the TCFs on the right-hand panels: there is almost no signal for the field with random phases whereas the field with structured phases exhibits a clear peak.

For completeness, we compute three different types of triangle correlations encompassing more or less phase information and compare results on Fig. 12. We do so for three boxes filled with 70 binary bubbles: the first (upper panel) with bubbles of radius $R = 7$, the second (middle panel) $R = 9$ and the third (lower panel) $R = 12$.

(i) The first type of triangle correlations considered is the one we have used so far, defined in Eq. 15 as a modified inverse Fourier transform of the phase factor of the bispectrum (blue solid line on Fig. 12).

(ii) The second uses the full bispectrum, amplitude included (purple dashed line on Fig. 12):

$$\Xi_3^{(1)}(r) = \left(\frac{r}{L}\right)^{3D/2} \sum_{k,q \leq \pi/r} \omega_D\,(pr)\ \mathcal{B}\,(\boldsymbol{k},\boldsymbol{q})\,. \tag{25}$$

(iii) The third only uses the amplitude of the bispectrum (green dotted line on Fig. 12):

$$\Xi_3^{(2)}(r) = \left(\frac{r}{L}\right)^{3D/2} \sum_{k,q \leq \pi/r} \omega_D\,(pr)\ |\mathcal{B}\,(\boldsymbol{k},\boldsymbol{q})\,|. \tag{26}$$

We see that the main advantage of the phase-only TCF is that, compared to statistics using bispectrum amplitude, the peaking scale is much better defined. It is also less sensitive to the filling fraction than the two other functions: in the bottom panel, where bubbles are larger and the filling fraction higher, phase correlations still exhibit a well-defined peak whereas the other two flatten.

7 COMPUTATIONAL PERFORMANCE

In Sec. 4.3 we compared the results of different methods to derive a bubble size distribution or equivalent, but we did not mention computational performance. Note that our code has been parallelised via OpenMP (OpenMP Architecture Review Board 2013) in order to reduce computing times: because most of the code consists of sums, i.e. nested loops, the parallelisation is very efficient. Three parameters will play an essential role in determining the computing time necessary to evaluate triangle correlations:

(i) The number N of pixels in the box.
(ii) The range of correlations scales r for which we compute the triangle correlations: because of the limits of our sum ($\sum_{k\leq\pi/r}$, see Eq. 15), there will be more terms to sum over for smaller scales. Therefore, in this work, we have chosen to compute triangle correlations for $0.5\ \text{Mpc} \leq r \leq 30\ \text{Mpc}$.
(iii) The box side length L, because it determines the sampling of k-cells: for smaller Δk, there will be more modes with norm smaller than π/r and hence more terms to sum over.

Most of the boxes analysed in this work had 512^2 pixels for a side length $L = 400$ Mpc and triangles correlations were computed for $r/\text{Mpc} \in [0.5, 30]$, for an average computation time of 180 minutes on 20 cores. For comparison, the SPA algorithm, as implemented by Giri et al. (2018a), takes about half an hour to run on a 3D box with same side length and sampling; whereas RMFP, as implemented in 21CMFAST, only takes a couple minutes. Therefore more work is required to improve the computational efficiency of our algorithm further and so its usability. An approach similar to the one presented in the Appendix of Eggemeier et al. (2015), where the nested sums in Eq. 15 are replaced by rotational averages in real space, could greatly improve computation times.

8 CONCLUSIONS

Following the work of O13, we have constructed a new statistical tool, based on phase information only and called the triangle correlation function (TCF), which can be used

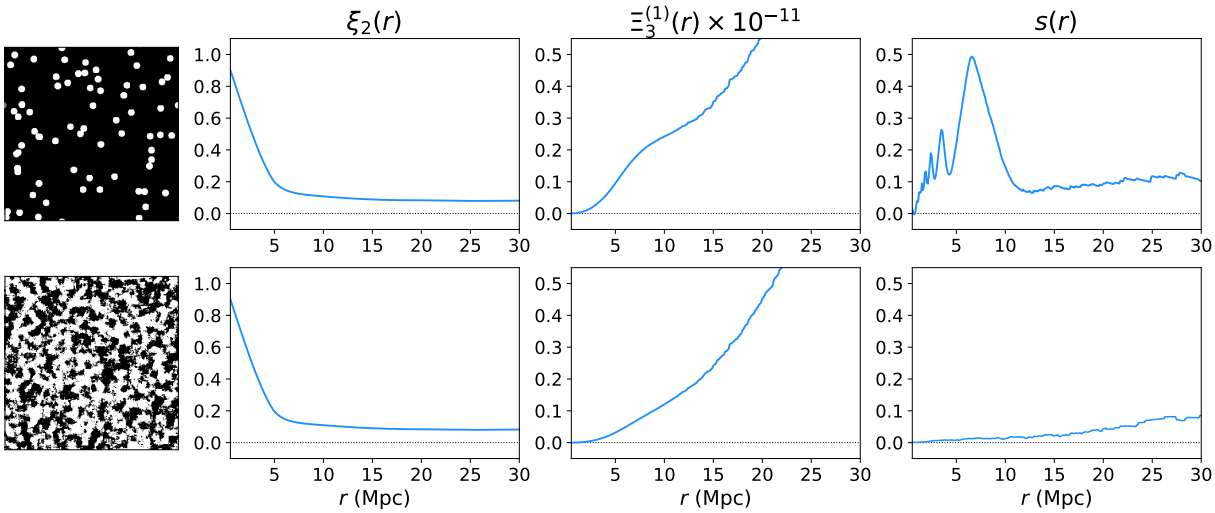

Figure 11. Comparison of results on phase correlations for two ionisation fields with identical power spectra and dimensions ($N = 512$, $L = 400$ Mpc) but different phase information: lower panels correspond to the field from upper panels after having reshuffled the Fourier phases. Left panels show the 2D ionisation field in real space, middle left, middle right and right panels respectively show the corresponding 2-PCF $\xi_2(r)$, the scaled modified 3-PCF $\Xi_3^{(1)}(r)$ (see Eq. 25), and the triangle correlation function $s(r)$.

to determine the characteristic scale of ionised regions on 21cm interferometric data from the Epoch of Reionisation. Indeed, if we plot this function over a range of correlation scales for simple fields, made of perfectly spherical fully ionised regions on a neutral background, we find a peaked signal, and the peaking scale can be directly related to the actual size of the bubbles. From such toy models, we have derived important properties for the TCF: it can differentiate between ionised regions of different sizes, and distinguish spherical from elongated structures. We have also found its results to be more reliable on scales smaller than about a twentieth of the physical side length of the field studied, as the finite size of the box implies more sample variance at larger scales. To see if our method can be applied to observational data, we have confronted the TCF with ionisation fields corrupted by instrumental noise or angular resolution from LOFAR or SKA, and we have found that it still performs well at giving the characteristic scale of ionised regions, as long as the integration time is sufficient – here, we have worked with 1000 hours. By comparing results for 3-PCF including amplitude information to $s(r)$, we also proved that a statistical tool using phase information only will be more efficient at picking up the characteristic scale of spherical structures in a field than a correlation function also using information from the bispectrum amplitude. Indeed, the phase-only function is more peaked, allowing a better identification of the characteristic scale. Moving on to the more elaborate reionisation simulation 21CMFAST (Mesinger & Furlanetto 2007), we have found that our method gives a good estimation of the size of remote neutral islands at the very end of the reionisation process. In particular, and contrarily to other BSD algorithms such as RMFP and SPA, it is able to resolve two characteristic scales in a field. In the early stages of the simulation, because there are many very small ionised regions covering the neutral background, the signal is dominated by Poisson noise, and there is no clear characteristic scale to pick up. Therefore, for fields with a very low global ionised fraction, we rather use our method to infer an upper limit on the size of ionised regions. Note that during the *overlap* phase, positive correlations from ionised regions overlap with negative signal from neutral zones and the signal flattens out: an absence of signal can be interpreted as reionisation being in its middle stages and so we can learn about the duration of the process. In general, it will be more difficult to extract phase information from non binary ionisation field because of the more complex structure of the field, which is reverberated in the phase information: Fig. 1 compares the real-space phase information of one of our toy models with $\epsilon(\boldsymbol{r})$ for one of our 21CMFAST boxes. These results, on both toy models and more elaboration simulations, hold when instrumental effects such as telescope angular resolution and instrumental noise are added to clean maps.

Apart from noise and instrumental resolution, there will be some other important questions to solve before applying our method to true 21cm tomographic data. Kakiichi et al. (2017) proved that the cold spots in 21cm tomographic images trace H II regions more efficiently at low redshift ($z \leq 7$) and high filling fraction ($x_{\rm H\,II} \geq 0.4$): earlier in the reionisation process, cold spots due to a local underdensity rather than ionisation are more frequent (see Sec. 2). Corroborated with the fact that the TCF performs well on remote neutral islands at the end of the reionisation process, we can expect to get good results on low redshift data. However, correctly identifying ionised regions in 21cm observations i.e. transforming a map of the differential brightness temperature δT_b into a binary field made of fully ionised and fully neutral regions remains a challenge – for an extended discussion of this issue, see Giri et al. (2018a). Note that this is not an issue for the friends-of-friends (Iliev et al. 2006; Friedrich et al. 2011) and watershed methods (Lin et al. 2016) since they segment the data themselves. Additionally, it remains to be seen exactly how to exploit closure phases, and what is the effect of the quality of the data, especially its sparsity, on our results. We would also need to see how foreground re-

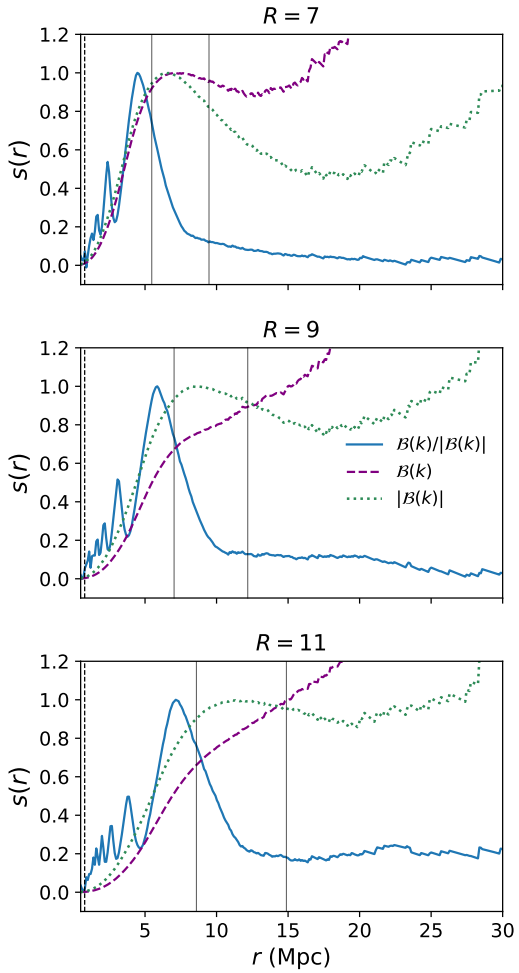

Figure 12. Triangle correlations computed on a box with dimensions $N = 512$ and $L = 400$ Mpc, filled with 50 binary bubbles of radius R. Upper panel corresponds to $R = 7$ px, middle to $R = 9$ px and lower to $R = 11$ px. Each time, the vertical lines correspond to R and $\sqrt{3}R$. The blue solid line is the triangle correlation function as defined before. The purple dashed line corresponds to a triangle correlation function computed for the full bispectrum rather than only its phase factor $\Xi_3^{(1)}(r)$ and the green dotted line to triangle correlations computed from the amplitude of the bispectrum only $\Xi_3^{(2)}(r)$ (see text for details).

moval techniques impact the non-Gaussianity of the signal, and therefore our results. Finally, the practical application of triangle correlations to observational data would require forward-modelling i.e. comparing measurements to the signal obtained for a number of simulations corresponding to various parametrisations of reionisation to infer the reionisation scenario corresponding to the observation. In this perspective, one would need to compute the triangle correlations of many more simulations.

ACKNOWLEDGEMENTS

The authors thank the referee for a useful report which helped improve the results of this paper. They also thank Catherine A. Watkinson, Marian Douspis and Benoît Semelin for useful discussions on various aspects of the analysis; Nithyanandan Thyagarajan for his helpful comments on a draft version of this paper; and Emma Chapman for kindly providing results from OSKAR runs to perform our noise analysis. AG and JRP acknowledge financial support from the European Research Council under ERC grant number 638743-FIRSTDAWN. AG's work is supported by a PhD studentship from the UK Science and Technology Facilities Council (STFC).

This research made use of `astropy`, a community-developed core Python package for astronomy (Astropy Collaboration et al. 2013, 2018); `matplotlib`, a Python library for publication quality graphics (Hunter 2007); `scipy`, a Python-based ecosystem of open-source software for mathematics, science, and engineering (Jones et al. 2001) – including `numpy` (Oliphant 2006), and `emcee`, an implementation of the affine invariant MCMC ensemble sampler (Foreman-Mackey et al. 2013).

REFERENCES

Astropy Collaboration et al., 2013, A&A, 558, A33
Astropy Collaboration et al., 2018, preprint, (arXiv:1801.02634)
Bag S., Mondal R., Sarkar P., Bharadwaj S., Sahni V., 2018, Monthly Notices of the Royal Astronomical Society, 477, 1984
Bharadwaj S., Pandey S. K., 2005, MNRAS, 358, 968
Binnie T., Pritchard J. R., 2019, MNRAS, 487, 1160
Bouwens R. J., Illingworth G. D., Oesch P. A., Caruana J., Holwerda B., Smit R., Wilkins S., 2015, ApJ, 811, 140
Bouwens R. J., Oesch P. A., Illingworth G. D., Ellis R. S., Stefanon M., 2017, ApJ, 843, 129
Carilli C. L., et al., 2018, preprint, (arXiv:1805.00953)
Chapman E., et al., 2015, Advancing Astrophysics with the Square Kilometre Array (AASKA14), p. 5
Chen Z., Xu Y., Wang Y., Chen X., 2018, arXiv e-prints, p. arXiv:1812.10333
Eggemeier A., Smith R. E., 2017, MNRAS, 466, 2496
Eggemeier A., Battefeld T., Smith R. E., Niemeyer J., 2015, MNRAS, 453, 797
Elbers W., van de Weygaert R., 2018, arXiv e-prints, p. arXiv:1812.00462
Foreman-Mackey D., Hogg D. W., Lang D., Goodman J., 2013, PASP, 125, 306
Friedrich M. M., Mellema G., Alvarez M. A., Shapiro P. R., Iliev I. T., 2011, MNRAS, 413, 1353
Furlanetto S. R., Zaldarriaga M., Hernquist L., 2004a, ApJ, 613, 1
Furlanetto S. R., Zaldarriaga M., Hernquist L., 2004b, ApJ, 613, 16
Giri S. K., Mellema G., Dixon K. L., Iliev I. T., 2018a, MNRAS, 473, 2949
Giri S. K., Mellema G., Ghara R., 2018b, MNRAS, 479, 5596
Gleser L., Nusser A., Ciardi B., Desjacques V., 2006, MNRAS, 370, 1329
Gorce A., Douspis M., Aghanim N., Langer M., 2018, A&A, 616, 113
Greig B., Mesinger A., Haiman Z., Simcoe R. A., 2017, MNRAS, 466, 4239
Greig B., Mesinger A., Bañados E., 2018, preprint, p. arXiv:1807.01593 (arXiv:1807.01593)
Hunter J. D., 2007, Computing In Science & Engineering, 9, 90
Iliev I. T., Mellema G., Pen U.-L., Merz H., Shapiro P. R., Alvarez M. A., 2006, MNRAS, 369, 1625

Ishigaki M., Kawamata R., Ouchi M., Oguri M., Shimasaku K., Ono Y., 2015, ApJ, 799, 12
Jennison R. C., 1958, MNRAS, 118, 276
Jones E., Oliphant T., Peterson P., et al., 2001, SciPy: Open source scientific tools for Python, http://www.scipy.org/
Kakiichi K., et al., 2017, MNRAS, 471, 1936
Konno A., et al., 2014, ApJ, 797, 16
Lee K.-G., Cen R., Gott J. Richard I., Trac H., 2008, ApJ, 675, 8
Levrier F., Falgarone E., Viallefond F., 2006, A&A, 456, 205
Lin Y., Oh S. P., Furlanetto S. R., Sutter P. M., 2016, MNRAS, 461, 3361
Majumdar S., Pritchard J. R., Mondal R., Watkinson C. A., Bharadwaj S., Mellema G., 2018, MNRAS, 476, 4007
Mason C. A., Treu T., Dijkstra M., Mesinger A., Trenti M., Pentericci L., de Barros S., Vanzella E., 2018, ApJ, 856, 2
McQuinn M., Lidz A., Zahn O., Dutta S., Hernquist L., Zaldarriaga M., 2007, MNRAS, 377, 1043
Mesinger A., Furlanetto S., 2007, ApJ, 669, 663
Mesinger A., Furlanetto S., Cen R., 2011, MNRAS, 411, 955
Monnier J. D., 2007, New Astron. Rev., 51, 604
Obreschkow D., Power C., Bruderer M., Bonvin C., 2013, ApJ, 762, 115
Oliphant T., 2006, NumPy: A guide to NumPy, USA: Trelgol Publishing, http://www.numpy.org/
OpenMP Architecture Review Board 2013, OpenMP Application Program Interface Version 4.0, https://www.openmp.org/wp-content/uploads/OpenMP-4.0-C.pdf
Planck Collaboration et al., 2016a, A&A, 594, A13
Planck Collaboration et al., 2016b, A&A, 596, A108
Planck Collaboration et al., 2018, preprint, (arXiv:1807.06209)
Pritchard J. R., Loeb A., 2012, Reports on Progress in Physics, 75
Readhead A. C. S., Nakajima T. S., Pearson T. J., Neugebauer G., Oke J. B., Sargent W. L. W., 1988, AJ, 95, 1278
Robertson B. E., Ellis R. S., Furlanetto S. R., Dunlop J. S., 2015, ApJ, 802, L19
Schenker M. A., Ellis R. S., Konidaris N. P., Stark D. P., 2014, The Astrophysical Journal, 795, 20
Seiler J., Hutter A., Sinha M., Croton D., 2019, MNRAS, p. 1578
Thompson A. R., Moran J. M., Swenson George W. J., 2017, Interferometry and Synthesis in Radio Astronomy, 3rd Edition, doi:10.1007/978-3-319-44431-4.
Thyagarajan N., Carilli C. L., Nikolic B., 2018, Phys. Rev. Lett., 120, 251301
Totani T., et al., 2014, Publications of the Astronomical Society of Japan, 66, 63
Trott C. M., et al., 2019, arXiv e-prints, p. arXiv:1905.07161
Visbal E., Loeb A., 2012, Journal of Cosmology and Astro-Particle Physics, 2012, 007
Watkinson C. A., Majumdar S., Pritchard J. R., Mondal R., 2017, MNRAS, 472, 2436
Watkinson C. A., Giri S. K., Ross H. E., Dixon K. L., Iliev I. T., Mellema G., Pritchard J. R., 2019, MNRAS, 482, 2653
Watts P., Coles P., Melott A., 2003, ApJ, 589, L61
Wolstenhulme R., Bonvin C., Obreschkow D., 2015, ApJ, 804, 132
Zahn O., Lidz A., McQuinn M., Dutta S., Hernquist L., Zaldarriaga M., Furlanetto S. R., 2007, ApJ, 654, 12

APPENDIX A: ANALYTICAL DERIVATION FOR A TOY MODEL

Consider a 2D box of volume $V = L^2$ filled with n fully ionised bubbles of radius R, randomly distributed throughout the box so that their centres are located at $\boldsymbol{a}_i$ for $i \in \{1, n\}$. The ionisation field of the box is then

$$x_{\rm H\,II}(\boldsymbol{r}) = \sum_{i=1}^{n} \Theta\left(\frac{|\boldsymbol{r}-\boldsymbol{a}_i|}{R}\right), \tag{A1}$$

where $\Theta(x)$ is the Heaviside step function worth 1 if $x \leq 1$ and 0 otherwise. We need to take the Fourier transform of this field, derived as follows:

$$\begin{aligned}
\hat{x}(\boldsymbol{k}) &= \frac{1}{V}\iint \sum_{i=1}^{n} \Theta\left(\frac{|\boldsymbol{r}-\boldsymbol{a}_i|}{R}\right) \mathrm{e}^{-i\boldsymbol{k}\cdot\boldsymbol{r}}\,\mathrm{d}^2\boldsymbol{r} \\
&= \frac{1}{V}\sum_{i=1}^{n} \mathrm{e}^{-i\boldsymbol{k}\cdot\boldsymbol{a}_i} \int_{r=0}^{R} r\mathrm{d}r \int_{\theta=0}^{2\pi} \mathrm{d}\theta\, \mathrm{e}^{-ikr\cos\theta} \\
&= \frac{1}{V}\sum_{i=1}^{n} \mathrm{e}^{-i\boldsymbol{k}\cdot\boldsymbol{a}_i} \int_{r=0}^{R} r\mathrm{d}r \int_{-\pi}^{\pi} \mathrm{d}\theta\, \mathrm{e}^{ikr\cos\theta} \\
&= \frac{1}{V}\sum_{i=1}^{n} \mathrm{e}^{-i\boldsymbol{k}\cdot\boldsymbol{a}_i} \int_{r=0}^{R} r\mathrm{d}r \times 2\pi J_0(kr) \\
&= \frac{2\pi}{k^2 V}\sum_{i=1}^{n} \mathrm{e}^{-i\boldsymbol{k}\cdot\boldsymbol{a}_i} \int_{0}^{kR} z J_0(z)\,\mathrm{d}z \\
&= \frac{2\pi R}{kV} J_1(kR) \sum_{i=1}^{n} \mathrm{e}^{-i\boldsymbol{k}\cdot\boldsymbol{a}_i}.
\end{aligned} \tag{A2}$$

where to go from the first to the second line, we have used the change of variables $\boldsymbol{r} = \boldsymbol{r} - \boldsymbol{a}_i$. From the fourth to the fifth, we have let $z = kr$ to be able to use:

$$\int_0^v w J_0(w)\,\mathrm{d}w = v J_1(v). \tag{A3}$$

If we define $W(y) = J_1(y)/y$, the Fourier transform of the top-hat window function in 2D, we have the final expression of the Fourier transform of our ionisation field:

$$\hat{x}(\boldsymbol{k}) = \frac{2\pi R^2}{V} W(kR) \sum_{i=1}^{n} \mathrm{e}^{-i\boldsymbol{k}\cdot\boldsymbol{a}_i} \simeq \frac{2\bar{x}_{\rm H\,II}}{n} W(kR) \sum_{i}^{n} \mathrm{e}^{-i\boldsymbol{k}\cdot\boldsymbol{a}_i}. \tag{A4}$$

Indeed, if we let ρ the mean number density of ionised bubbles such that $\rho = n/V$ and ignore overlapping[13], $\bar{x}_{\rm H\,II} = \pi R^2 \rho$. From this we deduce analytic expressions for the power spectrum

$$\begin{aligned}
\mathcal{P}(\boldsymbol{k}) &= |\hat{x}(\boldsymbol{k})|^2 \\
&= 4\pi^2\, W(kR)^2 \left(\frac{R}{L}\right)^4 \sum_{i,j=1}^{n} \mathrm{e}^{-i\boldsymbol{k}\cdot(\boldsymbol{a}_i-\boldsymbol{a}_j)} \\
&= 4\pi^2\, W(kR)^2 \left(\frac{R}{L}\right)^4 \times 2\sum_{i\leq j} \cos\left[\boldsymbol{k}\cdot(\boldsymbol{a}_i-\boldsymbol{a}_j)\right],
\end{aligned} \tag{A5}$$

which is a real number; and the bispectrum of the box

$$\begin{aligned}
\mathcal{B}(\boldsymbol{k},\boldsymbol{q}) &= \hat{x}(\boldsymbol{k})\,\hat{x}(\boldsymbol{q})\,\hat{x}(-\boldsymbol{k}-\boldsymbol{q})\ldots \\
&= 8\pi^3\; W(kR)\,W(qR)\,W\left(|\boldsymbol{k}+\boldsymbol{q}|R\right)\left(\frac{R}{L}\right)^6 \\
&\times \sum_{\alpha,\beta,\gamma=1}^{n} \mathrm{e}^{-i[\boldsymbol{k}\cdot(\boldsymbol{a}_\alpha-\boldsymbol{a}_\gamma)+\boldsymbol{q}\cdot(\boldsymbol{a}_\beta-\boldsymbol{a}_\gamma)]}.
\end{aligned} \tag{A6}$$

[13] This will be a reasonable assumption for the filling fractions considered.

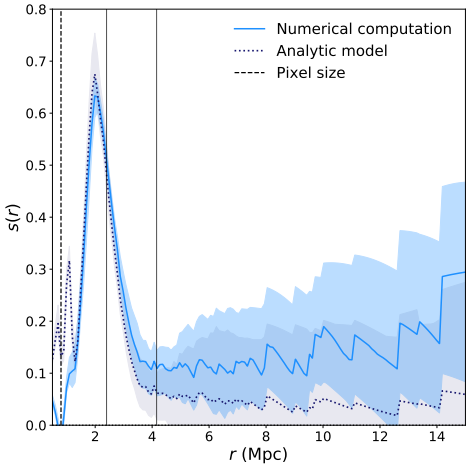

Figure A1. Triangle correlation function computed from the numerical expression of the bispectrum in Eq. 7b (solid line) and from the analytic expression of the bispectrum for a known bubble distribution as in Eq. A6 (dotted line) for 20 realisations a box of 100^2 pixels and side length L = 80 Mpc filled with 20 binary bubbles of radius R = 3 px = 2.4 Mpc. Vertical lines correspond to R and $\sqrt{3}R$.

To find the analytic expression of our triangle correlations function for this toy model, we then plug Eq. A6 into Eq. 15.

In Fig. A1, we compare the result of a numerical integration of the triangle correlation function computed from the bispectrum in Eq. 7b with a version where we compute analytically the triangle correlation function, knowing the locations of the ionised bubbles and the size of the box only, according to Eq. A6 and detailed above. We consider 20 realisations of a box of dimensions L = 80 Mpc for 100^2 pixels, filled with 20 bubbles of radius R = 3 px = 2.4 Mpc[14]. We see that there is a good match between both computational methods: we have the confirmation that our estimator indeed traces the bubble distribution in the ionisation field considered.

This paper has been typeset from a TEX/LATEX file prepared by the author.

[14] The choices of box size and bubble number are limited by the computational cost of the analytic method.

A.3 Improved constraints on reionisation from CMB observations: A parameterisation of the kSZ effect

This article introduces a novel way to parameterise the kSZ power spectrum in terms of reionisation history and morphology, in order to make better use of current and future small-scale CMB observations. It is the product of a collaboration between our group at IAS and Dominique Aubert, from Strasbourg Observatory, who kindly provided the simulations used in this work, and Stéphane Ilic, from IRAP, who wrote the first version of the code used to compute the kSZ power spectrum from `CAMB` and a given P_{ee}. I must also mention Jacob Seiler and Anne Hutter, who produced the `rsage` simulations and kindly let me use them for this work. All the other results are the product of my work – even if, of course, they would have never formed the paper you can read below without the help of my co-authors. This article has been published in Astronomy & Astrophysics in August 2020.

Astronomy & Astrophysics manuscript no. main
June 19, 2020

Improved constraints on reionisation from CMB observations: A parameterisation of the kSZ effect

A. Gorce[1,2], S. Ilić[3,4,5], M. Douspis[1], D. Aubert[6], and M. Langer[1]

[1] Université Paris-Saclay, CNRS, Institut d'Astrophysique Spatiale, 91405, Orsay, France
e-mail: adelie.gorce@ias.u-psud.fr
[2] Department of Physics, Blackett Laboratory, Imperial College, London SW7 2AZ, U.K.
[3] CEICO, Institute of Physics of the Czech Academy of Sciences, Na Slovance 2, Praha 8, Czech Republic
[4] Université PSL, Observatoire de Paris, Sorbonne Université, CNRS, LERMA, F-75014, Paris, France
[5] IRAP, Université de Toulouse, CNRS, CNES, UPS, Toulouse, France
[6] Observatoire Astronomique de Strasbourg, Université de Strasbourg, CNRS UMR 7550, 11 rue de l'Université, 67000 Strasbourg, France

Received *********; accepted *******

ABSTRACT

We show that, in the context of patchy reionisation, an accurate description of the angular power spectrum of the kinetic Sunyaev-Zel'dovich (kSZ) effect is not possible with simple scaling relations between the amplitude of the spectrum and global parameters, such as the reionisation midpoint and its duration. We introduce a new parameterisation of this spectrum, based on a novel description of the power spectrum of the free electrons density contrast $P_{ee}(k, z)$ in terms of the reionisation global history and morphology. We directly relate features of the spectrum to the typical ionised bubble size at different stages in the process and, subsequently, to the angular scale at which the patchy kSZ power spectrum reaches its maximum. We successfully calibrated our results on a custom set of advanced radiative hydrodynamical simulations and later found our parameterisation to be a valid description of a wide range of other simulations and, therefore, reionisation physics. In the end, and as long as the global reionisation history is known, two parameters are sufficient to derive the angular power spectrum. Such an innovative framework applied to cosmic microwave background data and combined with 21cm intensity mapping will allow a first consistent detection of the amplitude and shape of the patchy kSZ signal, giving in turn access to the physics of early light sources.

Key words. Cosmology: dark ages, reionization, first stars – cosmic background radiation – Methods: analytical

1. Introduction

From the launch of the Cosmic Background Explorer (COBE) in 1989 to the publication of the latest results of the Planck satellite in 2018 (Planck Collaboration et al. 2018), the study of the cosmic microwave background (CMB) has triggered a tremendous amount of research. Cosmological parameters have been estimated with exquisite precision and our knowledge of cosmic inflation has been greatly improved. Along the line of sight, the primordial part of the CMB signal is largely modified by the interaction of CMB photons with structures that formed later in the Universe. Notably, their interaction with free electrons in the intergalactic medium (IGM) modify the shape and amplitude of the measured CMB temperature and polarisation power spectra. The presence of these electrons is the result, in particular, of cosmic reionisation, an era potentially extending from a redshift of $z \sim 15$ to $z \sim 5$ when the first galaxies are thought to have ionised the neutral hydrogen and helium in the surrounding IGM.

CMB photons lose energy from scattering off low-energy electrons. In CMB data analysis, this effect is accounted for when computing the Thomson optical depth. To do so, one needs to assume a global history of reionisation, that is, a redshift-evolution for the IGM global ionised fraction $x_e(z)$. In standard Boltzmann solvers which are used to compute theoretical predictions in CMB data analysis such as the CAMB code (Lewis et al. 2000, Howlett et al. 2012)[1], the reionisation scenario used is a step-like transition of $x_e(z)$, where the global ionised fraction jumps from 10% to 75% over a (fixed) redshift interval of $\Delta z = 1.73$ (Planck Collaboration et al. 2016a). However, this parameterisation does not match simulations and observations well since we expect the ionisation fraction to slowly rise when the first sources light up, before taking off as soon as about 20% of the IGM is ionised (Robertson et al. 2015, Greig & Mesinger 2016, Gorce et al. 2018). This minimal model can have a huge impact on reionisation constraints: The value of τ inferred from Planck 2016 data varies from 0.066 ± 0.016 for a step-like process to 0.058 ± 0.012 for a more accurate description (Douspis et al. 2015; Planck Collaboration et al. 2016b). It is therefore essential to take the asymmetric evolution of $x_e(z)$ into account when trying to accurately constrain reionisation, and global parameters such as the reionisation midpoint $z_{\rm re}$ and duration Δz are not sufficient.

CMB photons can also gain energy from scattering off electrons with a non-zero bulk velocity relative to the CMB rest-frame in a process called the kinetic Sunyaev-Zel'dovich effect (hereafter kSZ effect, see Zeldovich & Sunyaev 1969; Sunyaev & Zeldovich 1980). This interaction adds power to the CMB temperature spectrum on small angular scales ($\ell \gtrsim 2000$, that is smaller than about 5 arcminutes), where secondary anisotropies,

[1] Available at https://camb.info.

including kSZ, dominate the signal. The impact of kSZ on the CMB power spectrum is often split between the homogeneous kSZ signal, which come from the Doppler shifting of photons on free electrons that are homogeneously distributed throughout the IGM once reionisation is over, and the patchy kSZ signal, when CMB photons scatter off isolated ionised bubbles along the otherwise neutral line of sight. Therefore, the kSZ power spectrum is sensitive to the duration and morphology of reionisation (McQuinn et al. 2005, Mesinger et al. 2012). For example, the patchy signal is expected to peak around $\ell \sim 2000$, corresponding to the typical bubble size during reionisation (Zahn et al. 2005; Iliev et al. 2007).

Secondary anisotropies only dominate the primordial power spectrum on small scales, where existing all-sky surveys such as Planck perform poorly. The observational efforts of the ground-based Atacama cosmology telescope (ACT)[2] and the South Pole telescope (SPT)[3] have allowed upper constraints to be put on the amplitude of the kSZ power spectrum at $\ell = 3000$. Using ACT observations at 148 GHz, Dunkley et al. (2011) find $\mathcal{D}^{\rm SZ}_{3000} \equiv \ell\,(\ell+1)\,C^{\rm SZ}_{\ell=3000}/2\pi = 6.8 \pm 2.9\ \mu{\rm K}^2$ at the 68% confidence level (C.L.) for the sum of thermal and kinetic SZ. In a first analysis, Reichardt et al. (2012) derive from the three frequency bands used by SPT $\mathcal{D}^{\rm kSZ}_{3000} < 2.8\ \mu{\rm K}^2$ (95% C.L.). This limit is however significantly loosened when anti-correlations between the thermal SZ effect (tSZ) and the cosmic infrared background (CIB) are considered. By combining SPT results with large-scale CMB polarisation measurements, Zahn et al. (2012) are subsequently able to constrain the amplitude of the patchy kSZ by setting an upper limit $\mathcal{D}^{\rm patchy}_{3000} \leq 2.1\ \mu{\rm K}^2$ (95% C.L.) translated into an upper limit on the duration of reionisation $\Delta z \equiv z\,(x_e = 0.20) - z\,(x_e = 0.99) \leq 4.4$ (95% C.L.), again largely loosened when CIB×tSZ correlations are considered. Using Planck's large-scale temperature and polarisation (EE) data, combined with ACT and SPT high-ℓ measurements, and taking the aforementioned correlations into account, Planck Collaboration et al. (2016b) find a more constraining upper limit on the total kSZ signal $\mathcal{D}^{\rm kSZ}_{3000} < 2.6\ \mu{\rm K}^2$ with a 95% confidence level. Finally, adding new data from SPTpol[4] to their previous results (George et al. 2015), Reichardt et al. (2020) claim the first 3σ detection of the kSZ power spectrum with an amplitude $\mathcal{D}^{kSZ}_{3000} = 3.0 \pm 1.0\ \mu{\rm K}^2$, translated into a confidence interval on the patchy amplitude $\mathcal{D}^{pkSZ}_{3000} = 1.1^{+1.0}_{-0.7}\ \mu{\rm K}^2$ using the models of homogeneous signal given in Shaw et al. (2012). These results are further pushed using the scaling relations derived by Battaglia et al. (2013) to obtain an upper limit on the duration of reionisation $\Delta z < 4.1$.

Previous works have focused on relating the amplitude of the kSZ power spectrum at $\ell = 3000$ to common reionisation parameters such as its duration and its midpoint. Battaglia et al. (2013) use large dark matter simulations ($L \gtrsim 2$ Gpc$/h$), post-processed to include reionisation, to construct light-cones of the kSZ signal and estimate its patchy power spectrum. The authors find the scalings $\mathcal{D}^{\rm kSZ}_{3000} \propto \bar{z}$ and $\mathcal{D}^{\rm kSZ}_{3000} \propto \Delta z^{0.51}$ where $\bar{z}$ is approximately the midpoint of reionisation and here $\Delta z \equiv z\,(x_e = 0.25) - z\,(x_e = 0.75)$. Very large box sizes are necessary to capture the large-scale velocity flows contributing to the kSZ power spectrum at high-ℓ and results based on insufficiently large simulations will significantly underestimate the power at these scales. Shaw et al. (2012) find that a simulation box of side length 100 Mpc$/h$ would miss about 60% of the kSZ power at $\ell = 3000$. For their own work, Shaw et al. (2012) therefore choose a completely different approach: they use hydrodynamical simulations to map the gas density to the dark matter power spectrum and later include this bias in a purely analytical derivation of the kSZ angular power spectrum. Because the non-linear dark matter power spectrum can be computed using the HALOFIT procedure (Smith et al. 2003) and because the velocity modes can be estimated fully from linear theory under a few assumptions, they avoid the limitations caused by simulation resolution and size mentioned above. With this method, the authors find a power-law dependence on both the reionisation midpoint $z_{\rm re}$ and the optical depth τ for the homogeneous signal. For their most elaborate simulation, dubbed CSF, the cosmology-dependent scaling relations write $\mathcal{D}^{kSZ}_{3000} \propto \tau^{0.44}$ and $\mathcal{D}^{kSZ}_{3000} \propto {z_{\rm re}}^{0.64}$ but are independent since one parameter is fixed before varying the other. The authors note that the current uncertainties on cosmological parameters such as σ_8 will wash out any potential constraint on $z_{\rm re}$ and τ obtained from the measurement of the kSZ spectrum.

In this work, we choose to follow a similar approach. We build a comprehensive parameterisation allowing the full derivation of the kSZ angular power spectrum from a known reionisation history and morphology. In Sec. 2, we review the theoretical derivation of the kSZ power spectrum and propose a new parameterisation of the power spectrum of free electrons density contrast, based on the shape of the power spectrum of a bubble field. In Sec. 3, we present the simulations we later use to calibrate this parameterisation. In Sec. 4, we use the resulting expression of $P_{ee}(k, z)$ to compute the patchy kSZ angular power spectrum of our simulations and later apply the same procedure to different types of reionisation simulations. Finally, in Sec. 5, we discuss the physical meaning of our parameters and conclude. All distances are in comoving units and the cosmology used is the best-fit cosmology derived from Planck 2015 CMB data (Planck Collaboration et al. 2016a): $h = 0.6774$, $\Omega_{\rm m} = 0.309$, $\Omega_{\rm b}h^2 = 0.02230$, $Y_{\rm p} = 0.2453$, $\sigma_8 = 0.8164$ and $T_{\rm CMB} = 2.7255$ K. Unless stated otherwise, $P_{\delta\delta}$ describes the non-linear total matter power spectrum, $x_e(z)$ is the ratio of H II and He II ions to protons in the IGM, and the reionisation duration is defined by $\Delta z = z\,(x_e = 0.25) - z\,(x_e = 0.75)$. The code used to compute the kSZ power spectrum can be found at https://github.com/adeliegorce/tools4reionisation.

2. Derivation of the kSZ angular power spectrum

2.1. Temperature fluctuations

The CMB temperature anisotropies coming from the scattering of CMB photons off clouds of free electrons with a non-zero bulk velocity $\mathbf{v}$ relative to the CMB rest-frame along the line of sight $\hat{\mathbf{n}}$ write

$$\delta T_{kSZ}(\hat{\mathbf{n}}) = \frac{\sigma_T}{c} \int \frac{{\rm d}\eta}{{\rm d}z} \frac{{\rm d}z}{(1+z)}\, {\rm e}^{-\tau(z)}\, n_e(z)\, \mathbf{v}\cdot\hat{\mathbf{n}}\,, \tag{1}$$

with σ_T being the Thomson cross-section, c the speed of light, η the comoving distance to redshift z and $\mathbf{v}\cdot\hat{\mathbf{n}}$ the component of the peculiar velocity of the electrons along the line of sight. As mentioned before, τ is the Thomson optical depth, $\tau(z) = c\,\sigma_{\rm T} \int_0^z n_e(z')/H(z')\,(1+z')^2\,{\rm d}z'$. n_e is the mean free electrons number density at redshift z from which we derive the density contrast δ_e via $n_e = \bar{n}_e(1+\delta_e)$. We choose the limits of the integral in Eq (1) depending on the type of signal we are interested in: for homogeneous kSZ, we integrate from 0 to $z_{\rm end}$, the

[2] https://act.princeton.edu
[3] http://pole.uchicago.edu
[4] The second camera deployed on SPT, polarisation sensitive.

redshift when reionisation ends; for patchy kSZ, the main focus of this work, we integrate from $z_{\rm end}$ to the highest redshift considered in the simulation (here, $z_{\rm max} = 15$). The contribution from redshifts larger than the onset of reionisation, when the only free electrons in the IGM are leftovers from recombination, is found to be negligible.

We define $\mathbf{q} \equiv \mathbf{v}(1+\delta_e) = \mathbf{v} + \mathbf{v}\delta_e \equiv \mathbf{v} + \mathbf{q}_e$ the density-weighted peculiar velocity of the free electrons. It can be decomposed into a divergence-free $\mathbf{q}_B$ and a curl-free $\mathbf{q}_E$ components. We write their equivalents in the Fourier domain as $\tilde{\mathbf{q}} = \tilde{\mathbf{q}}_E + \tilde{\mathbf{q}}_B$. As pointed out by Jaffe & Kamionkowski (1998), when projected along the line of sight, $\tilde{\mathbf{q}}_E$ will cancel and only the component of $\tilde{\mathbf{q}}$ perpendicular to $\mathbf{k}$, that is $\tilde{\mathbf{q}}_B$, will contribute to the kSZ signal. We want an expression for the kSZ angular power spectrum $C_\ell^{kSZ} \equiv T_{\rm CMB}^2 |\tilde{\delta T}_{\rm kSZ}(k)|^2$ where $k \equiv \ell/\eta$ is the Limber wave-vector and ℓ is the multipole moment, which can be related to an angular scale in the sky. In the small angle limit, the kSZ angular power spectrum can be derived from Eq. (1) using the Limber approximation:

$$C_\ell = \frac{8\pi^2}{(2\ell+1)^3}\frac{\sigma_T^2}{c^2}\int \frac{\bar{n}_e(z)^2}{(1+z)^2}\,\Delta^2_{B,e}(\ell/\eta, z)\,{\rm e}^{-2\tau(z)}\,\eta\,\frac{{\rm d}\eta}{{\rm d}z}\,{\rm d}z, \tag{2}$$

with $\Delta^2_{B,e}(k,z) \equiv k^3 P_{B,e}(k,z)/(2\pi^2)$ and $P_{B,e}$ the power spectrum of the curl component of the momentum field defined by $(2\pi)^3 P_{B,e}\,\delta_D(\mathbf{k}-\mathbf{k}') = \langle \tilde{\mathbf{q}}_{B,e}(\mathbf{k})\,\tilde{\mathbf{q}}^*_{B,e}(\mathbf{k}')\rangle$ where δ_D is the Dirac delta function, the tilde denotes a Fourier transform and the asterisk a complex conjugate.

Expanding $\langle \tilde{\mathbf{q}}_{B,e}\tilde{\mathbf{q}}^*_{B,e}\rangle$, we obtain:

$$\tilde{\mathbf{q}}_{B,e}(\mathbf{k}) = \int \frac{{\rm d}^3\mathbf{k}'}{(2\pi)^3}\,(\hat{\mathbf{k}}' - \mu\hat{\mathbf{k}})\,\tilde{v}(k')\,\tilde{\delta}_e\,(|\mathbf{k}-\mathbf{k}'|)\,, \tag{3}$$

where $\mu = \hat{\mathbf{k}}\cdot\hat{\mathbf{k}}'$, so that

$$\begin{aligned}\frac{\langle \tilde{\mathbf{q}}_{B,e}(\mathbf{k})\,\tilde{\mathbf{q}}^*_{B,e}(\mathbf{k}')\rangle}{(2\pi)^3\delta_D(|\mathbf{k}-\mathbf{k}'|)} &\equiv \frac{2\pi^2}{k^3}\Delta^2_{B,e}(k,z)\\ &= \frac{1}{(2\pi)^3}\int {\rm d}^3k'\,\left[(1-\mu^2)\,P_{ee}(|\mathbf{k}-\mathbf{k}'|)\,P_{vv}(k')\right.\\ &\quad\left. -\frac{(1-\mu^2)\,k'}{|\mathbf{k}-\mathbf{k}'|}P_{ev}(|\mathbf{k}-\mathbf{k}'|)\,P_{ev}(k')\right],\end{aligned} \tag{4}$$

where the z-dependencies have been omitted for simplicity. $P_{ee}(k,z)$ is the power spectrum of the free electrons density fluctuations and P_{ev} is the free electrons density - velocity cross-spectrum. In the linear regime, we can write $\mathbf{v}(\mathbf{k}) = i\mathbf{k}\,(f\dot{a}/k)\,\tilde{\delta}(\mathbf{k})$, where a is the scale factor and f the linear growth rate defined by $f(a) = {\rm d}\ln D/{\rm d}\ln a$ for D the growth function. With this we can compute the velocity power spectrum fully from linear theory and not be limited by the simulation size and resolution:

$$P_{vv}(k,z) = \left(\frac{\dot{a}f(z)}{k}\right)^2 P^{\rm lin}_{\delta\delta}(k,z) \tag{5}$$

where $P^{\rm lin}_{\delta\delta}$ is the linear total matter power spectrum. We also assume for the cross-spectrum:

$$P_{ve}(k,z) \simeq b_{\delta e}(k,z)P_{\delta v}(k,z) = \frac{f\dot{a}(z)}{k}\,b_{\delta e}(k,z)P^{\rm lin}_{\delta\delta}(k,z), \tag{6}$$

where the bias $b_{\delta e}$ is defined by the ratio of the free electrons power spectrum over the non-linear matter power spectrum $b_{\delta e}(k,z)^2 = P_{ee}(k,z)/P_{\delta\delta}(k,z)$. Although coarse, this approximation only has a minor impact on our results: it implies variations of $\sim 0.05\ \mu{\rm K}^2$ in the power spectrum amplitude (see also Alvarez 2016). The final expression of the power spectrum of the curl component of the momentum field then writes

$$\begin{aligned}P_{B,e}(k,z) = \frac{1}{(2\pi)^3}f(z)^2\dot{a}(z)^2\int {\rm d}^3k'(1-\mu^2)\times\\ \left[\frac{1}{k'^2}P_{ee}(|\mathbf{k}-\mathbf{k}'|)\,P^{\rm lin}_{\delta\delta}(k',z)\right.\\ \left.-\frac{b_{\delta e}(k',z)}{|\mathbf{k}-\mathbf{k}'|^2}\,b_{\delta e}(|\mathbf{k}-\mathbf{k}'|,z)\,P^{\rm lin}_{\delta\delta}(|\mathbf{k}-\mathbf{k}'|,z)\,P^{\rm lin}_{\delta\delta}(k',z)\right],\end{aligned} \tag{7}$$

which we can plug into Eq. (2) to find the final expression for the kSZ angular power spectrum.

2.2. The power spectrum of free electrons density contrast

In Shaw et al. (2012), the authors choose to describe the behaviour of the free electrons power spectrum in terms of a biased matter power spectrum: they take $P_{ee}(k,z) \equiv b_{\delta e}(k,z)^2 P_{\delta\delta}(k,z)$ and calibrate $b_{\delta e}(k,z)$ on their simulations, either extrapolating or assuming a reasonable behaviour for the scales and redshifts not covered by the simulations. However, because P_{ee} describes the free electrons density fluctuations, it has a relatively simple structure, close to the power spectrum of a field made of ionised spheres on a neutral background, shown in Fig. 1, and using a bias is not necessary.

Consider a box of volume $V = L^3$ filled with n fully ionised bubbles of radius R, randomly distributed throughout the box so that their centres are located at $\boldsymbol{a}_i$ for $i \in \{1, n\}$. The density of free electrons in the box follows

$$n_e(\boldsymbol{r}) = \frac{\bar{n}_e}{f}\sum_{i=1}^{n}\Theta\left(\frac{|\boldsymbol{r}-\boldsymbol{a}_i|}{R}\right), \tag{8}$$

where $\Theta(x)$ is the Heaviside step function, $\bar{n}_e$ is the mean number density of electrons in the box and f the filling fraction of the box (here, $f = x_e$). $\bar{n}_e/f$ is the number of electrons in one bubble divided by its volume and, ignoring overlaps, $f = 4/3\pi R^3 n/V$. Consider the electron density contrast field δ_e on which $P_{ee}(k,z)$ is built:

$$\delta_e(\boldsymbol{r}) = \frac{n_e(\boldsymbol{r})}{\bar{n}_e} - 1 = \frac{1}{f}\sum_{i=1}^{n}\Theta\left(\frac{|\boldsymbol{r}-\boldsymbol{a}_i|}{R}\right) - 1, \tag{9}$$

represented on Fig. 2 for one of the simulations used in this work. $\delta_e(\boldsymbol{r})$ Fourier–transforms into

$$\tilde{\delta}_e(\boldsymbol{k}) = \frac{L^3}{n}\,W(kR)\sum_{i=1}^{n}{\rm e}^{-i\boldsymbol{k}\cdot\boldsymbol{a}_i}, \tag{10}$$

where W is the spherical top-hat window function $W(y) = (3/y^3)\,[\sin y - y\cos y]$. Using this expression, and following Bharadwaj & Pandey (2005), the power spectrum of the electron density contrast field writes:

$$P_{ee}(\boldsymbol{k}) = \frac{4}{3}\pi R^3\,\frac{1}{f}\,W^2(kR), \tag{11}$$

which has units Mpc^3. Fig. 1 gives an example of such a power spectrum. We have generated an ionisation field made of enough

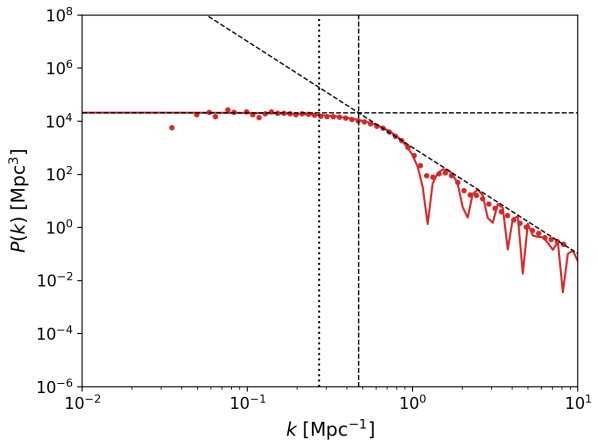

Fig. 1. Free electrons density contrast power spectrum for a box filled with enough bubbles of radius $R = 15$ px $= 5.5$ Mpc to reach a filling fraction $f = 1\%$. Points are results of a numerical computation of the power spectrum, compared to the theoretical model (solid line). The dotted vertical line corresponds to $k = 1/R$, the dashed vertical line to $9^{1/4}/R$, the dashed horizontal line to $4/3\pi R^3/f$ and the tilted dashed line has slope k^{-4}.

bubbles of radius $R = 15$ px $= 5.5$ Mpc[5] to reach a filling fraction $f = 1\%$ in a box of 512^3 pixels and side length $L = 128/h$ Mpc. We compare the expression in Eq. (11) with power spectrum values computed directly from the 3D field and find a good match. On very small or very large scales, the window function behaves as:

$$\begin{aligned} W(y) &\sim \frac{3}{y^3} \times \frac{y^3}{3} = 1 \quad \text{as } y \to 0 \\ W(y) &\sim \frac{3}{y^3} \times y = \frac{3}{y^2} \quad \text{as } y \to \infty \end{aligned} \tag{12}$$

so that $P_{ee}(k) \sim 4/3\pi R^3/f$ is constant (see dashed horizontal line on the figure) on very large scales and has higher amplitude for smaller filling fractions. On small scales, the toy model power spectrum decreases as k^{-4} (see tilted dashed line on the figure). The intersection point of the horizontal and tilted dashed lines on the figure corresponds to $k = 9^{1/4}/R$ (dashed vertical line), hinting at a relation between the cut-off frequency and the bubble size. Interestingly, Xu et al. (2019) find a similar feature, also related to the typical bubble size, in the bias between the H I and matter fields.

This behaviour is close to what we observe in the free electrons density power spectra of the custom set of simulations used in this work in the early stages of reionisation, as can be seen on the right panel of Fig. 2. Therefore, we choose in this work to use a direct parameterisation of the scale and redshift evolution of $P_{ee}(k, z)$ during reionisation and calibrate it on our simulations. The parameters, α_0 and κ, are defined according to:

$$P_{ee}(k, z) = \frac{\alpha_0 \; x_e(z)^{-1/5}}{1 + [k/\kappa]^3 x_e(z)}. \tag{13}$$

In log-space, on large scales, P_{ee} has a constant amplitude which, as mentioned above, depends on the filling fraction and therefore reaches its maximum α_0 at the start of the reionisation process, when the variance in the free electron field is maximal (see Sec. 5.1). It then slowly decreases as $x_e(z)^{-1/5}$. Before the onset of reionisation, despite the few free electrons left over after recombination, the amplitude of P_{ee} is negligible. This constant power decreases above a cut-off frequency that increases with time, following the growth of ionised bubbles, according to $\kappa x_e(z)^{-1/3}$. There is no power above this frequency, that is on smaller scales: there is no smaller ionised region than $r_{\min}(z) = 2\pi x_e^{1/3}/\kappa$ at this time. For empirical reasons, we choose the power to decrease as k^{-3} and not k^{-4} as seen in the theoretical power spectrum on small scales. This difference can be explained by the fact that in our simulations, small ionised regions will keep appearing as new sources light up, maintaining power on scales smaller than the typical bubble size. Additionally, the density resolution will allow correlations between regions within a given bubble, whereas in the toy models ionised bubbles are only filled with ones. The complexity of the electron density contrast field is illustrated for one of the six simulations used in this work on Fig. 2: the underlying matter field is visible within the ionised regions.

Once reionisation is over and all IGM atoms are ionised, the fluctuations in free electrons density follow those of dark matter on large scales ($k < 1$ Mpc^{-1}). On smaller scales, gas thermal pressure induces a drop in $P_{ee}(k, z)$ compared to the dark matter. To describe this evolution at low redshifts, we choose the same parameterisation as Shaw et al. (2012), given in Eq. (14), to describe the gas bias $b_{\delta e}(k, z)^2 = P_{ee}(k, z)/P_{\delta\delta}(k, z)$ but adapt the parameters to our simulations, which however do not cover redshifts lower than 5.5:

$$b_{\delta e}(k, z)^2 = \frac{1}{2}\left[\mathrm{e}^{-k/k_f} + \frac{1}{1 + (gk/k_f)^{7/2}}\right]. \tag{14}$$

We find $k_f = 9.4$ Mpc^{-1} and $g = 0.5$, constant with redshift. Our values for k_f and g are quite different from those obtained by Shaw et al. (2012), as in their work power starts dropping between 0.05 and 0.5 Mpc^{-1} compared to $k \sim 3$ Mpc^{-1} for our simulations. This can be explained by our simulations making use of adaptive mesh refinement, therefore resolving very well the densest regions, so that our spectra are more sensitive to the thermal behaviour of gas. This model, where k_f and g are constant parameters, is a very basic one. It will however be sufficient for this work since we focus on the patchy component of the kSZ effect, at $z \geq 5.5$. Additionally, as shown later, the scales mostly contributing to the patchy kSZ signal correspond to modes $10^{-3} < k/\mathrm{Mpc}^{-1} < 1$ where P_{ee} follows the matter power spectrum, so that a precise knowledge of $b_{\delta e}(k, z)$ is not required. In the future, if we want to apply our results to constrain reionisation with the measured CMB temperature power spectrum, we will need a better model as the observed signal will be the sum of homogeneous and patchy kSZ, with the former dominating on all scales.

To account for the smooth transition of P_{ee} from a power-law to a biased matter power spectrum, illustrated in the right panel of Fig. 2, we write the final form for the free electrons density fluctuations power spectrum as

$$\begin{aligned} P_{ee}(k, z) = [f_{\mathrm{H}} - x_e(z)] \times \frac{\alpha_0 \; x_e(z)^{-1/5}}{1 + [k/\kappa]^3 x_e(z)} \\ + \; x_e(z) \times b_{\delta e}(k, z)^2 P_{\delta\delta}(k, z), \end{aligned} \tag{15}$$

for $f_{\mathrm{H}} = 1 + Y_p/4X_p \simeq 1.08$, with Y_p and X_p the primordial mass fraction of helium and hydrogen respectively. The total matter power spectrum $P_{\delta\delta}$ is computed using the Boltzmann integrator `CAMB` (Lewis et al. 2000; Howlett et al. 2012) for the linear

[5] The bubble radii actually follow a Gaussian distribution centred on 15 px with standard deviation 2 px.

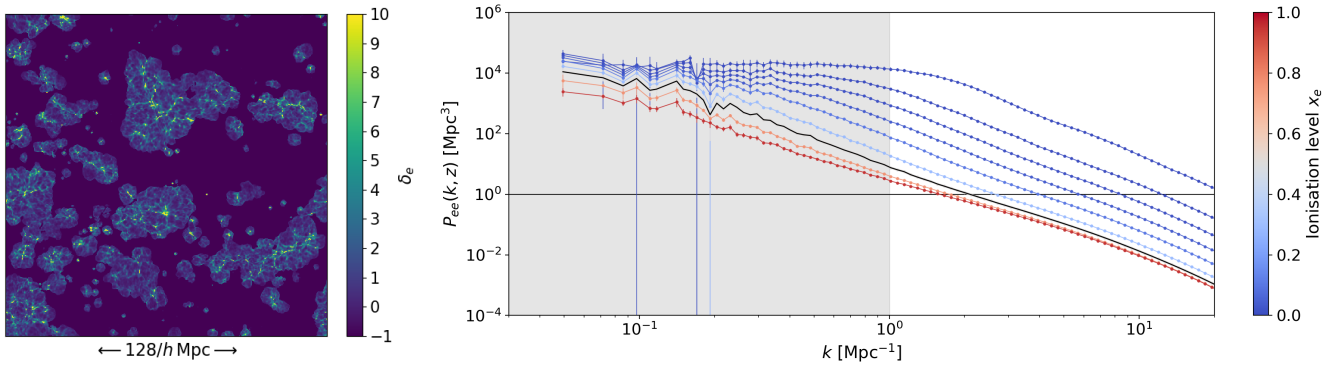

Fig. 2. *Left panel:* Snapshot of the electron density contrast field for the first of the six simulations, at $z = 7.2$ and $x_e = 0.49$. *Right panel:* Free electrons power spectrum of the same simulation at fixed redshifts (fixed ionised levels). The shaded area corresponds to scales contributing $\mathcal{D}_{3000}^{\rm patchy}$ the most (see Sec. 3.2) and the solid black line to the field shown in the left panel.

terms and the HALOFIT procedure for the non-linear contributions (Smith et al. 2003).

3. Calibration on simulations

3.1. Description of the simulations

The simulations we use in this work were produced with the EMMA simulation code (Aubert et al. 2015) and previously used in Chardin et al. (2019). The code tracks the collisionless dynamics of dark matter, the hydrodynamics of baryons, star formation and feedback, and the radiative transfer using a moment-based method (see Aubert et al. 2018; Deparis et al. 2019). This code adheres to an Eulerian description, with fields described on grids, and enables adaptive mesh refinement techniques to increase the resolution in collapsing regions. Six simulations with identical numerical and physical parameters were produced in order to make up for the limited physical size of the box and the associated sample variance. They only differ in the random seeds used to generate the initial displacement phases, resulting in 6 different configurations of structures within the simulated volumes. Each run has a $(128\ {\rm Mpc}/h)^3$ volume sampled with 1024^3 cells at the coarsest level and 1024^3 dark matter particles. Refinement is triggered when the number of dark matter particles exceeds 8, up to 6 refinement levels. Initial conditions were produced using MUSIC (Hahn & Abel 2013) with a starting redshift of $z = 150$, assuming Planck Collaboration et al. (2016a) cosmology. Simulations were stopped at $z \sim 6$, before the full end of reionisation. The dark matter mass resolution is $2.1 \times 10^8 {\rm M}_\odot$ and the stellar mass resolution is $6.1 \times 10^5 {\rm M}_\odot$. Star formation proceeds according to standard recipes described in Rasera & Teyssier (2006), with an overdensity threshold equal to 20 to trigger the gas-to-stellar particle conversion with a 0.1 efficiency: such values allow the first stellar particles to appear at $z \sim 17$. Star particles produce ionising radiation for 3 Myr, with an emissivity provided by the Starburst99 model for a Top-Heavy initial mass function and a $Z = 0.001$ metallicity (Leitherer et al. 1999). Supernova feedback follows the prescription used in Aubert et al. (2018): as they reach an age of 15 million years, stellar particles dump 9.8×10^{11} J per stellar kg in the surrounding gas, 1/3 in the form of thermal energy, 2/3 in the form of kinetic energy. Using these parameters, we obtain a cosmic star formation history consistent with constraints by Bouwens et al. (2015) and end up with 20 millions stellar particles at $z = 6$. The simulations were produced on the Occigen (CINES) and Jean-Zay (IDRIS) supercomputers, using CPU architectures : a reduced speed of light of $0.1c$ has been used to reduce the cost of radiative transfer.

Table 1. Characteristics of the six high resolution simulations used. $z_{\rm re}$ is the midpoint of reionisation $x_e(z_{\rm re}) = 0.5 f_{\rm H}$, $z_{\rm end}$ the redshift at which $x_e(z)$ (extrapolated) reaches $f_{\rm H}$ and τ is the Thompson optical depth. Δz corresponds to $z_{0.25} - z_{0.75}$.

	$z_{\rm re}$	$z_{\rm end}$	τ_{x_e}	Δz
1	7.09	5.96	0.0539	1.17
2	7.16	5.92	0.0545	1.19
3	7.16	5.67	0.0544	1.16
4	7.05	5.60	0.0532	1.16
5	7.03	5.56	0.0531	1.15
6	7.14	5.79	0.0543	1.16
Mean	7.10	5.84	0.0541	1.16

Table 1 gives the midpoint $z_{\rm re}$ and end of reionisation $z_{\rm end}$ for each simulation, as well as the duration of the process, defined as the time elapsed between global ionisation fractions of 25% and of 75%[6]. The upper panel of Fig. 5 shows the interpolated reionisation histories, where data points correspond to the snapshots available for each simulation. Originally, our simulations do not include the first reionisation of helium. We correct for this by multiplying the IGM ionised fraction of hydrogen $x_{\rm H\,II}$ measured in the simulations by $f_{\rm H} = 1 + Y_p/4X_p \simeq 1.08$. Because we limit our study to redshifts $z > 5.5$, the second reionisation of helium is ignored. Fig. 2 shows the electron density contrast field for the first of our six simulations, close to the midpoint of reionisation. The complexity of the structure of this field is summarised in its power spectrum, shown in the right panel. Fig. 3 compares the $P_{ee}(k,z)$ spectra of the six simulations, taken either at fixed redshift (first column) or fixed scale (right column). Despite identical numerical and physical parameters and very similar reionisation histories, the six simulations have different free electrons density power spectra, which translates into different kSZ power spectra.

3.2. Calibration procedure

We simultaneously fit the power spectra of the six simulations to Eq. (15) on a scale range $0.05 < k/{\rm Mpc}^{-1} < 1.00$ (20 bins), corresponding to the scales which contribute the most to the signal at $\ell = 3000$ (see next paragraph), and a redshift

[6] Some of our simulations end before reionisation is achieved, therefore we extrapolate $x_e(z)$ to find the $z_{\rm end}$ value.

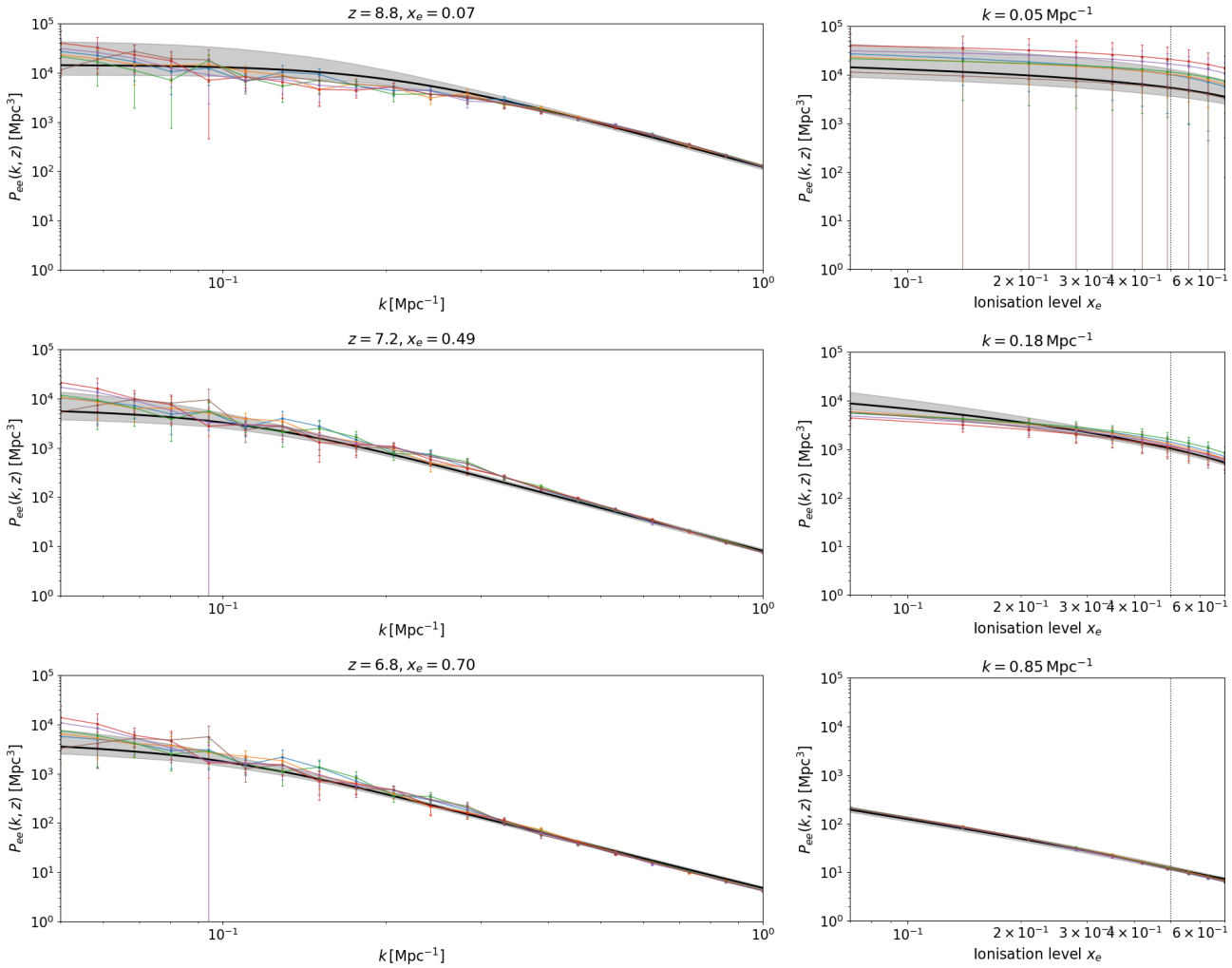

Fig. 3. Result of the fit of Eq. (15) on the free electrons power spectrum of our six simulations, for three redshift bins (left panels) and three scale bins (right panels). The best-fit is shown as the thick black line with the accompanying 68% confidence interval, and the spectra of the six simulations as thin coloured lines. Error bars on data points are computed from the covariance matrix (see text for details).

range of $6.5 \leq z \leq 10.0$ (10 bins), corresponding to the core of the reionisation process ($0.07 < x_e < 0.70$).[7] We sample the parameter space of α_0 and κ on a regular grid (with spacings $\Delta \log \alpha_0 = 0.001$ and $\Delta\kappa = 0.0001$) for which we compute the following likelihood:

$$\chi^2 = \sum_{\mathrm{n}=1}^{6} \sum_{z_i} \sum_{k_j} \frac{1}{\sigma_e^2} \left[P_{ee}^{\mathrm{data}}(k_j, z_i) - P_{ee}^{\mathrm{model}}(k_j, z_i) \right]^2, \tag{16}$$

where $\{z_i\}$ and $\{k_j\}$ are the redshift and scale bins and the first sum is over the six simulations. Because our sample of six simulations is not sufficient to derive a meaningful covariance matrix, we choose to ignore correlations between scales across redshifts and use the diagonal of the covariance matrix to derive error bars σ_e for each data point. We refer the interested reader to a discussion of this choice in Appendix A. We choose the best-fit as the duplet (α_0, κ) for which the reduced χ^2 reaches its minimum value of 1.05[8]. The best-fit values, with their 68% confidence intervals are

$$\begin{aligned} \log \alpha_0 / \mathrm{Mpc}^3 &= 3.93^{+0.05}_{-0.06} \\ \kappa &= 0.084^{+0.003}_{-0.004}\ \mathrm{Mpc}^{-1}. \end{aligned} \tag{17}$$

We note a strong correlation between the two parameters due to both physical – see Sec. 5.1 – and analytical reasons. Indeed, the value of κ impacts the low-frequency amplitude of the $P_{ee}(k, z)$ model. The best-fit model, compared to the $P_{ee}(k, z)$ spectra of the six simulations Eq. (15) is fitted on, can be seen in Fig. 3 for three different redshift bins (left-hand column) and three different scale bins (right-hand column). Overall, we see a good agreement between the fit and the data points on the scales of interest, despite the simplicity of our model.

Given the large number of $P_{ee}(k, z)$ data points originally ($\sim$ 3500) and the complexity of the evolution of P_{ee} with k and z, we must limit our fits to given ranges. In order to assess what scales and redshifts contribute the most to the final kSZ signal, we look at the evolution of the integrand on z in Eq. (2) with time and at the evolution of the integral on k in Eq. (7) with scales. The results are shown in Fig. 4. The left (resp. right) upper panel presents the evolution of $P_{ee}(k, z)$ with scales (resp.

[7] Because the snapshots of each simulation are not taken at the same redshifts or ionisation levels, we interpolate $P_{ee}(k, z)$ for each simulation and then compute the interpolated spectra for a common set of ionisation levels, with less elements than the original number of snapshots. Note that the original binning in scales for $P_{ee}(k, z)$ is the same for the six simulations but reduced from 38 to 20 bins.

[8] The raw value is $\chi^2 \sim 2500$.

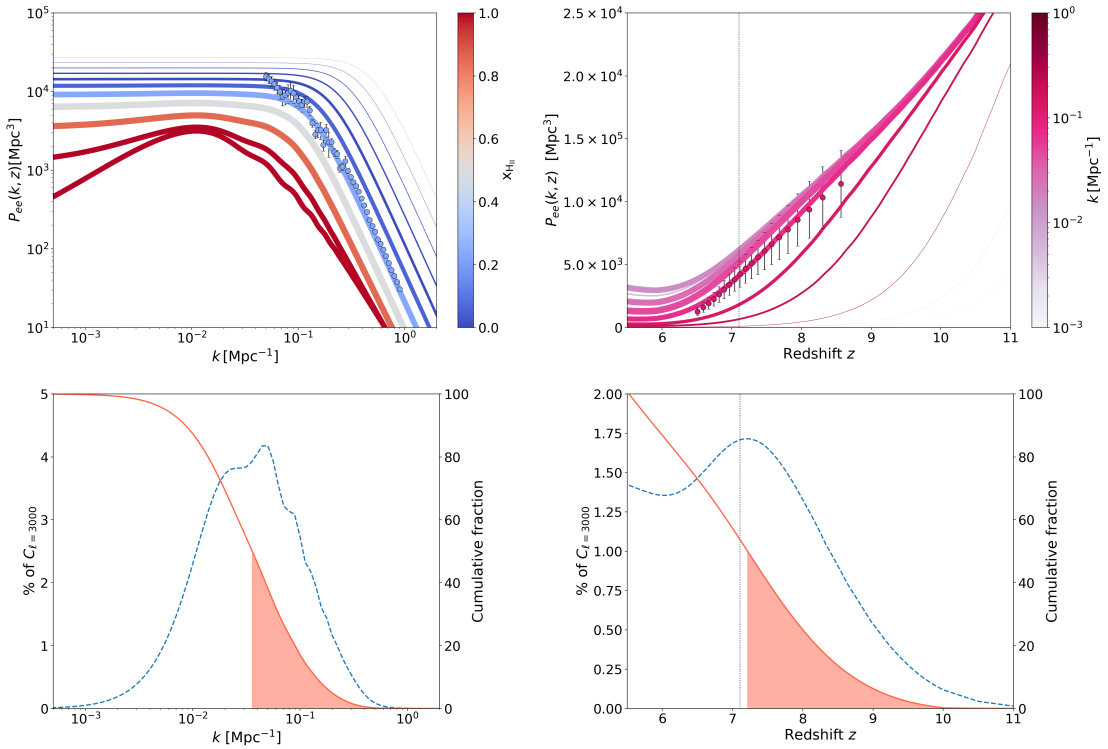

Fig. 4. *Upper panels:* $P_{ee}(k, z)$ as fitted on spectra from the fourth simulation, as a function of scales (left panel) and of redshift (right panel). For reference, the fit is compared to data points for $z = 7.8$ ($x_e = 0.26$) and $k = 0.14$ Mpc^{-1} respectively, with corresponding colour. The width of each line represents the contribution of the redshift (resp. scale) of the corresponding scale (resp. redshift) to the final patchy kSZ amplitude at $\ell = 3000$. *Lower panels:* Corresponding probability densities (dashed lines) and cumulative distributions (solid lines). Shaded areas correspond to the first 50% of the signal. The dotted vertical line on the lower right panel marks the midpoint of reionisation.

redshift) after applying the fitting procedure described above. The width of each line represents the contribution of the redshift (resp. scale) of the corresponding colour to the final patchy kSZ amplitude at $\ell = 3000$. The lower panels present the corresponding probability density and cumulative distribution functions. We find that redshifts throughout reionisation contribute homogeneously to the signal, since 50% stems from redshifts $z \leq 7.2$, slightly before the midpoint $z_{\rm re} = 7.0$. Redshifts on the range $6.5 < z < 8.5$ contribute the most as they represent about 75% of the final kSZ power. Conversely, redshifts $z > 10$ contribute to only 0.4% of the total signal. On the lower panel, we see that scales outside the range 10^{-3} Mpc$^{-1} < k < 1$ Mpc^{-1} contribute very marginally to the final signal (about 0.2%), whereas the range $10^{-2} < k/\mathrm{Mpc}^{-1} < 10^{-1}$ makes up about 70% of $\mathcal{D}_{3000}$. Therefore, we choose to only keep data within the redshift range $6.5 < z < 10.0$ (i.e. $7\% < x_e < 70\%$) and the scale range $10^{-3} < k/\mathrm{Mpc}^{-1} < 1$ to constrain our fits. For reference, on Fig. 4, we compare the fit to data points at $z = 7.8$ ($x_e = 0.26$) and $k = 0.14$ Mpc^{-1} for the first simulation, and find an overall good match.

4. Propagation to the kSZ power spectrum

4.1. Results on our six simulations

Now that we have a fitted $P_{ee}(k, z)$, we can compute the kSZ angular power spectrum using Eq. (2). We find:

$$\mathcal{D}^{\rm p}_{3000} = 0.80 \pm 0.06\ \mu\mathrm{K}^2 \tag{18}$$

and the angular scale at which the patchy angular spectrum reaches its maximum is $\ell^{\rm max} = 1800^{+300}_{-100}$. The angular patchy power spectrum is shown on the lower panel of Fig. 5. The error bars correspond to the propagated 68% confidence interval on the fit parameters. The amplitude of the homogeneous signal largely dominates that of the patchy signal, being about 4 times larger. The total kSZ amplitude reaches $\mathcal{D}_{3000} = 4.2\ \mu\mathrm{K}^2$ and so slightly exceeds the upper limits on the total kSZ amplitude given by SPT and Planck when SZxCIB correlations are allowed (resp. Reichardt et al. 2020; Planck Collaboration et al. 2016b) but is however within the error bars of the ACT results (Sievers et al. 2013). With respect to the patchy signal, the amplitude is in perfect agreement with the claimed detection by the SPT at $\mathcal{D}^{\rm patchy}_{3000} = 1.1^{+1.0}_{-0.7}\ \mu\mathrm{K}^2$ (Reichardt et al. 2020), noting that our simulations reionise in a time very close to their constraint $\Delta z = 1.1^{+1.6}_{-0.7}$. The spectrum exhibits the expected bump in amplitude, here around $\ell \sim 1800$, corresponding to larger scales than those found in other works (Iliev et al. 2007; Mesinger et al. 2012), hinting at larger ionised bubbles on average. Fig. 5 gives an idea of the variance in the kSZ angular power spectrum for given physics – in particular a given matter distribution, and very similar reionisation histories: the distribution among simulations gives a reionisation midpoint defined at $z_{\rm re} = 7.10 \pm 0.06$, corresponding to a range of kSZ power spectrum amplitude $\mathcal{D}_{3000} = 0.80 \pm 0.06\ \mu\mathrm{K}^2$ (at 68% confidence level). Part of this variance can be related to sample variance, since our simulations have a too small side length ($L = 128$ Mpc$/h$) to avoid it (Iliev et al. 2007). We compare in Fig. 5 the kSZ power spectrum resulting from fitting Eq. (15) on our six simulations simultaneously to the six spectra obtained when interpolating the $P_{ee}(k, z)$ data points available for each simulation: the six interpolated spectra lie withing the confidence limits of our best-fit.

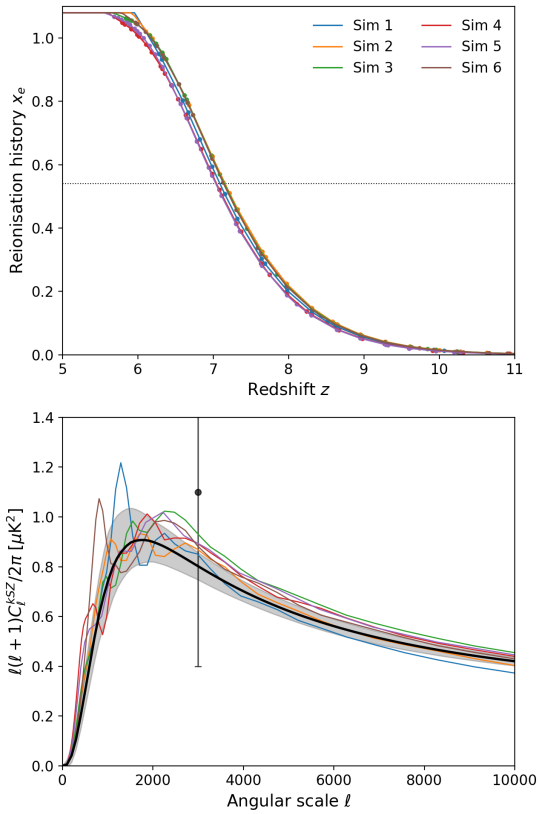

Fig. 5. Results for our six simulations. *Upper panel:* Global reionisation histories, for H II and He II. The dotted horizontal line marks the reionisation midpoint $z_{\rm re}$. *Lower panel:* Angular kSZ power spectrum after fitting Eq. (15) to the $P_{ee}(k, z)$ data points from our six simulations (thick solid line) compared to the spectra obtained when interpolating the data points for each simulation (thin solid lines). Error bars correspond to the propagation of the 68% confidence interval on the fit parameters. The data point corresponds to constraints from Reichardt et al. (2020) at $\ell = 3000$.

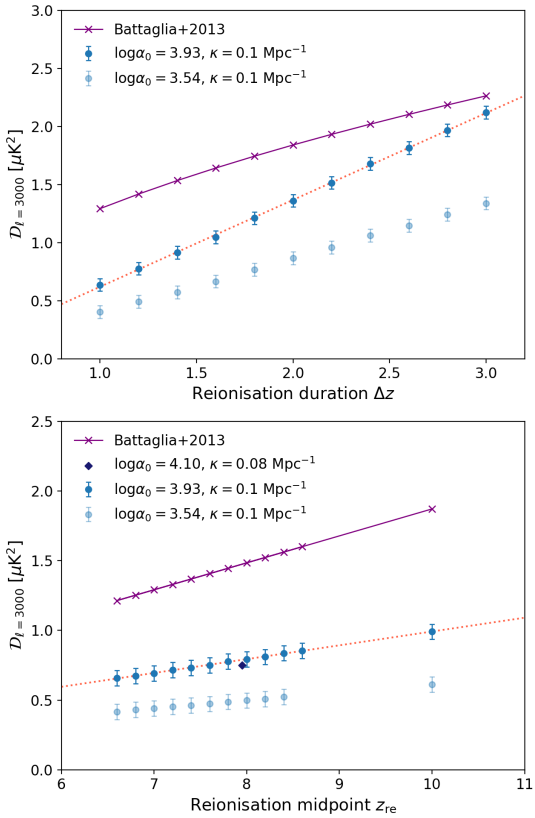

Fig. 6. Evolution of the amplitude of the patchy power spectrum at $\ell = 3000$, $\mathcal{D}_{3000}$ with the reionisation duration (upper panel) and the reionisation midpoint $z_{\rm re}$ (lower panel), for different values of our parameters. Error bars correspond to the dispersion of kSZ amplitude at $\ell = 3000$ (68% confidence level) propagated from errors on the fit parameters. The diamond data point corresponds to a seventh simulation, with reionisation happening earlier. In both panels, results are compared to those of Battaglia et al. (2013), rescaled to our cosmology.

Fixing the fit parameters to their most likely value for the fourth simulation, we artificially vary the reionisation history and compute the corresponding power spectrum. We successively fix the reionisation redshift but increase its duration Δz or fix the duration but shift the midpoint $z_{\rm re}$. This corresponds to a scenario where the reionisation morphology is exactly the same, but happens later or earlier in time. We find clear scaling relations between the amplitude of the signal at $\ell = 3000$, $\mathcal{D}_{3000}$, and both the reionisation duration Δz and its midpoint $z_{\rm re}$. However, they are sensibly different from the results of Battaglia et al. (2013) as can be seen in Fig. 6. Even after rescaling to their $z_{\rm re} = 8$ and cosmology, we get a much lower amplitude. Note also that their patchy spectra bump around $\ell = 3000$, whereas in our simulations the power has already dropped by $\ell = 3000$ (Fig. 5), hinting at a very different reionisation morphology from ours. When we vary κ and α_0 artificially, by fixing $\log\alpha_0 = 3.54$ instead of 3.70 as before, there is still a scaling relation, but both the slope and the intercept change. All of this demonstrates that the amplitude of the patchy signal largely depends on the physics of reionisation (here via the κ and α_0 parameters) and Δz and $z_{\rm re}$ are not sufficient to derive $\mathcal{D}_{3000}$. Simulations closer to those used in Battaglia et al. (2013) would likely give larger values for κ and α_0, therefore increasing the amplitude to values closer to the authors' results. To confirm this, we generate a new simulation, with same resolution and box size but with twice as much star formation as in the six initial simulations, therefore reionising earlier ($z_{\rm re} = 7.94$) but on a similar redshift interval ($\Delta z = 1.20$). Applying the fitting procedure described above, we find $\log\alpha_0 = 4.10$ and $\kappa = 0.08$ Mpc^{-1}. The resulting patchy kSZ power spectrum can be seen in Fig. 7, along with the reionisation histories and the evolution of the typical bubble size $r_{\rm min} = 2\pi/\kappa x_e(z)^{1/3}$. Results for this simulation are compared with what was obtained for our six simulations. The kSZ spectrum corresponding to an early reionisation scenario bumps at larger scales ($\ell^{\rm max} = 1400$) with a much larger maximum amplitude ($\mathcal{D}_{\rm max} = 0.98\ \mu$K^2) but interestingly the amplitudes at $\ell = 3000$ are similar. This suggests that focusing on $\mathcal{D}_{3000}$ is not sufficient to characterise the kSZ signal.

These results corroborate the work of Park et al. (2013), who found that the scalings derived in Battaglia et al. (2013) are largely dependent on the simulations they were calibrated on, and therefore cannot be used as a universal formula to constrain reionisation. Notably, an asymmetric reionisation history $x_e(z)$ naturally deviates from this relation. Global parameters such as Δz and $z_{\rm re}$ are not sufficient to accurately describe the patchy kSZ signal, and one needs to take the physics of reionisation into account to get an accurate estimation of not only the shape, but also the amplitude of the power spectrum. Additionally, limiting ourselves to the amplitude at $\ell = 3000$ to constrain reionisation can be misleading.

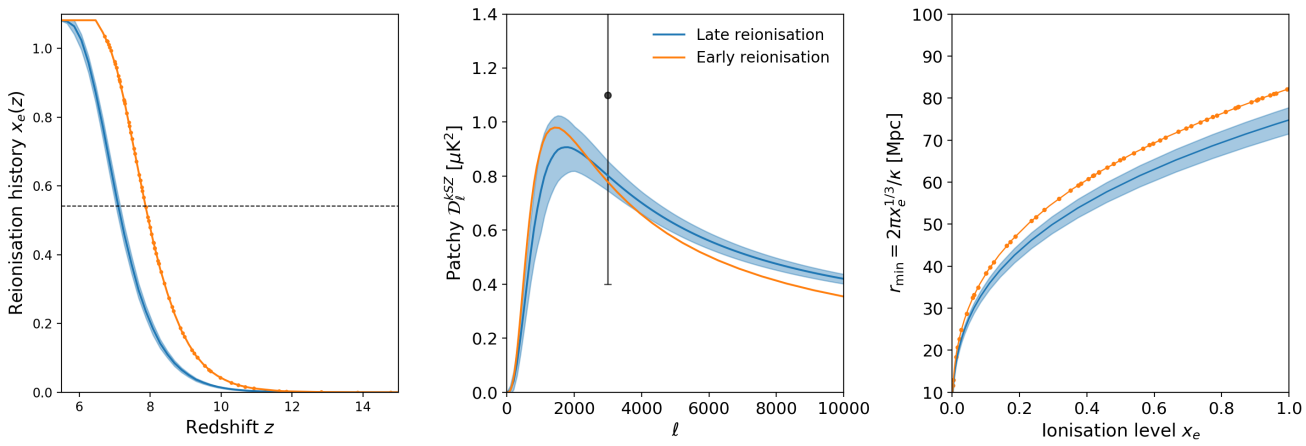

Fig. 7. Comparison of results for our six initial simulations, corresponding to a late reionisation scenario, and for an additional seventh simulation, corresponding to an early reionisation scenario. *Left panel:* Reionisation histories. *Middle panel:* Patchy kSZ angular power spectra. The data point corresponds to constraints from Reichardt et al. (2020). *Right panel:* Minimal size of ionised regions as a function of global ionised level. Shaded areas correspond to the 68% confidence level on kSZ amplitude propagated from the probability distributions of the fit parameters.

4.2. Tests on other simulations

We now look at the `rsage` simulation, described in Seiler et al. (2019), to test the robustness of our parameterisation. This simulation starts off as an N-body simulation (Seiler et al. 2018), containing 2400^3 dark matter particles within a 160 Mpc side box, resolving halos of mass $\sim 4 \times 10^8$ M$_\odot$ with 32 particles. Galaxies are evolved over cosmic time following the Semi-Analytic Galaxy Evolution (SAGE) model of Croton et al. (2016), modified to include an improved modelling of galaxy evolution during the Epoch of Reionisation, including the feedback of ionisation on galaxy evolution. The semi-numerical code `cifog` (Hutter 2018a,b) is used to generate an inhomogeneous ultraviolet background (UVB) and follow the evolution of ionised hydrogen during the EoR. Three versions of the `rsage` simulation are used, each corresponding to a different way of modelling the escape fraction $f_{\rm esc}$ of ionising photons from their host galaxy into the IGM. The first, dubbed `rsage const`, takes $f_{\rm esc}$ constant and equal to 20%. The second, `rsage fej`, considers a positive scaling of $f_{\rm esc}$ with $f_{\rm ej}$, the fraction of baryons that have been ejected from the galaxy compared to the number remaining as hot and cold gas. In the last one, `rsage SFR`, $f_{\rm esc}$ scales with the star formation rate and thus roughly with the halo mass. Because they are based on the same dark matter distribution, the three simulations start reionising at similar times ($z \sim 13$), but different source properties lead to different reionisation histories, shown in the left upper panel of Fig. 8. In `rsage SFR`, the ionised bubbles are statistically larger than the other two simulations at a given redshift: this results into `rsage SFR` reaching 50% of ionisation at $z_{\rm re} = 7.56$ vs. $z_{\rm re} = 7.45$ and $z_{\rm re} = 7.37$ for `rsage const` and `rsage fej` respectively, and the full ionisation being achieved in a shorter time. For more details, we refer the interested reader to Seiler et al. (2019). Applying the fitting procedure to the three simulations, we find that the parameterisation of Eq. (15) is an accurate description of the evolution of their $P_{ee}(k, z)$ spectra (detailed fit results are given in App. B.2). Resulting patchy kSZ angular power spectra are shown in the upper middle panel of Fig. 8. First, we find that `rsage fej` has the smallest α_0 value, with $\log \alpha_0 = 2.87 \pm 0.04$. Because α_0 is the maximum amplitude of the $P_{ee}(k, z)$ spectrum, built upon the free electrons density contrast field $\delta_e(r) = n_e(r)/\bar{n}_e - 1$, it will scale with the variance of the $n_e(r)$ field. Therefore a smaller α_0 value is equivalent to a smaller field variance at all times. This is consistent with the picture of the different `rsage` simulations we have: as presented in Seiler et al. (2019), `rsage fej` exhibits the smallest ionised bubbles on average. For a given filling fraction, a field made of many small bubbles covering the neutral background rather homogeneously will have smaller variance than one made of a few large bubbles. This in turn explains why `rsage SFR` gives the largest α_0 value ($\log \alpha_0 = 3.47 \pm 0.04$), and, later, the largest kSZ amplitude (Fig. 8). Second, the `rsage SFR` simulation has the smallest value of κ ($\kappa = 0.123 \pm 0.004$ Mpc^{-1}): the upper right panel of Fig. 8 shows the evolution of $r_{\rm min} = 2\pi/\kappa x_e^{1/3}$ with ionisation level for the three models. Because `rsage SFR` has the largest ionised bubbles on average (Seiler et al. 2019), this result confirms the interpretation of $1/\kappa$ as an estimate of the typical bubble size during reionisation. Additionally, the patchy power spectrum derived from `rsage SFR` peaks at larger angular scales ($\ell^{\rm max} \sim 2400$) than for the other simulations, as can be seen in the upper middle panel of the figure. Interestingly, the largest α_0 value leads to the strongest kSZ signal and the smallest κ value to the spectrum whose bump is observed on the largest scales (the smallest $\ell^{\rm max}$). We investigate these potential links in the next section.

We now turn to three 21CMFAST (Mesinger & Furlanetto 2007; Mesinger et al. 2011) simulations with dimensions $L = 160$ Mpc for 256^3 cells (same box size and resolution as `rsage`). Between the three runs, we vary the parameter $M_{\rm turn}$, the turnover mass, which corresponds to the minimum halo mass before exponential suppression of star formation. For $M_{\rm turn} = 10^8 M_\odot$, the box is fully ionised by $z_{\rm end} = 6.25$ and the midpoint of reionisation is reached at $z_{\rm re} = 8.92$ for a process lasting $\Delta z = 1.91$. For $M_{\rm turn} = 10^9 M_\odot$, we find $z_{\rm end} = 4.69$, $z_{\rm re} = 7.11$ and $\Delta z = 1.66$, which is closest to `rsage` and our initial six simulations. Finally, $M_{\rm turn} = 10^{10} M_\odot$ yields $z_{\rm end} = 3.37$, $z_{\rm re} = 5.41$ and $\Delta z = 1.47$. Indeed, the point of these simulations is not only to test the sensitivity of our approach to astrophysical parameters, but also to see the impact of very different reionisation histories on the patchy kSZ power. We find that Eq. (15) again nicely fits the evolution of the $P_{ee}(k, z)$ spectra of these simulations, as shown in App. B.1. The resulting reionisation histories, patchy kSZ spectra and $r_{\rm min}(x_e)$ are shown in the lower panels of Fig. 8. For $M_{\rm turn} = 10^8 M_\odot$, many small-mass halos

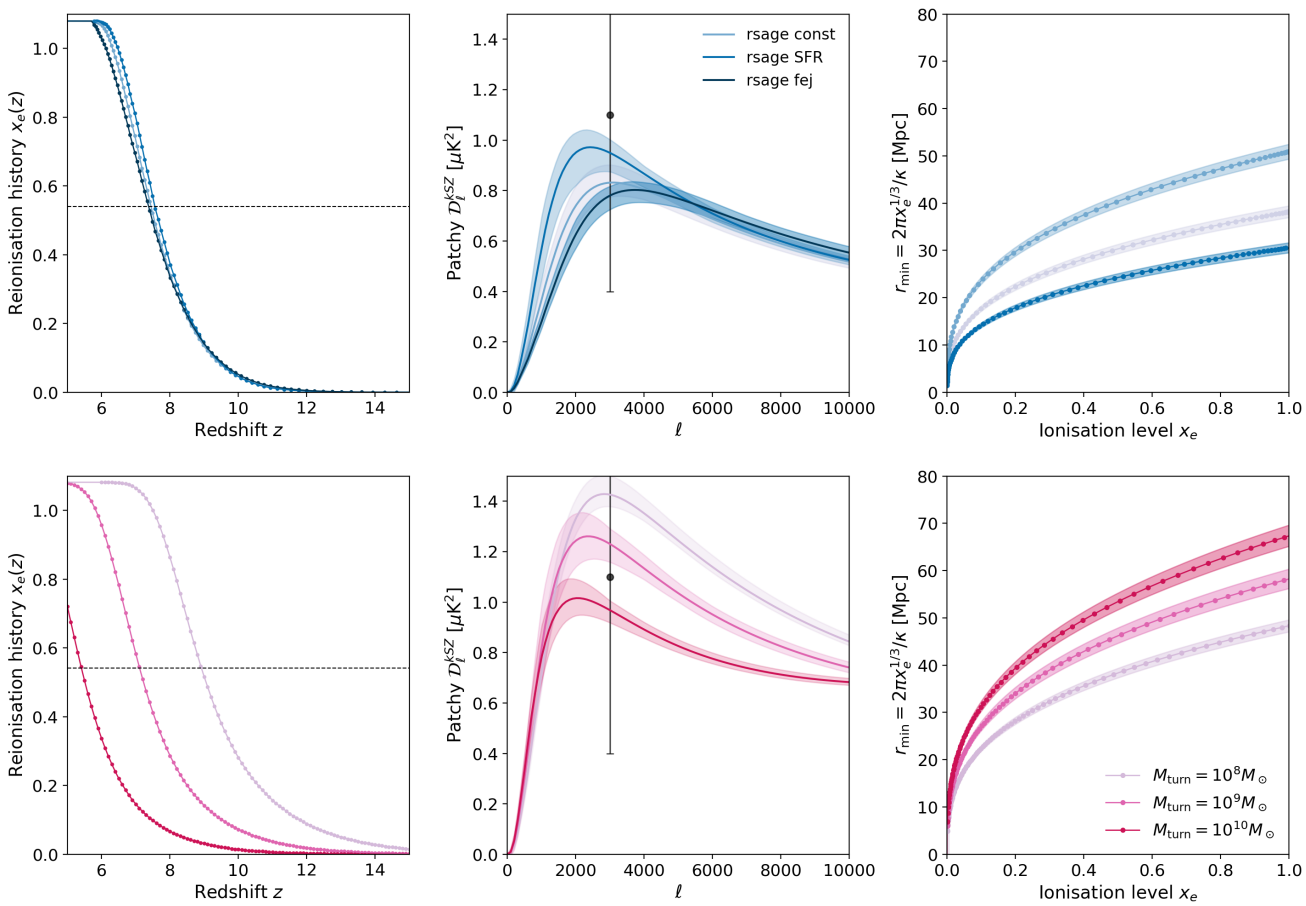

Fig. 8. Comparison of results for the three `rsage` simulations (upper panels) and the three 21CMFAST runs (lower panels) considered. *Left panels:* Reionisation histories. *Middle panels:* Patchy kSZ angular power spectra. The data point corresponds to constraints from Reichardt et al. (2020). *Right panels:* Minimal size of ionised regions as a function of global ionised level. The shaded areas correspond to the 68% confidence interval propagated from the 68% confidence intervals on the fit parameters.

are active ionising sources, resulting in an ionising field made of many small bubbles at the start of the process. This translates into this simulation having the largest best-fit κ value of the three ($\kappa = 0.130 \pm 0.003$ Mpc^{-1}) and so the smallest $r_{\rm min}(x_e)$. Naturally, the resulting kSZ spectrum peaks at smaller angular scales. For the other extreme case $M_{\rm turn} = 10^{10} M_\odot$, because the minimal mass required to start ionising is larger, the ionising sources are more efficient and the ionised bubbles larger. Indeed, we find a smaller value of $\kappa = 0.093 \pm 0.003$ Mpc^{-1}. With larger bubbles, we also expect the variance in the ionisation field at the start of the process to be higher than if many small ionised regions cover the neutral background. This corresponds to the larger value of $\log \alpha_0 = 3.79 \pm 0.04$ found for this simulation, compared to 3.30 ± 0.03 for the first one. However, this larger value of α_0 this time does not result into the strongest kSZ signal because of the very different reionisation histories of the three simulations. As we have seen in the previous section, the amplitude of the signal is strongly correlated with the duration and midpoint of reionisation, resulting in the first simulation ($M_{\rm turn} = 10^8 M_\odot$), corresponding to the earliest reionisation, having the strongest signal. This again emphasises how essential it is to consider both reionisation morphology and global history to derive the final kSZ spectrum.

These results show that our proposed simple two-parameter expression for $P_{ee}(k, z)$ can accurately describe different types of simulations, that is different types of physics, further validating the physical interpretation of the parameters α_0 and κ detailed in the next Section.

5. Discussion and conclusions

5.1. Physical interpretation of the parameters

Many previous works have empirically related the angular scale at which the patchy kSZ power spectrum reaches its maximum $\ell^{\rm max}$ to the typical size of bubbles during reionisation (McQuinn et al. 2005; Iliev et al. 2007; Mesinger et al. 2012). To test for this relation, we compute the patchy kSZ power spectrum for a given reionisation history $x_e(z)$ and α_0 but let κ values vary. We find a clear linear relation between κ and $\ell^{\rm max}$ as shown in Fig. 9. Despite very different reionisation histories and physics at stake, previous results on the six high-resolution simulations, on 21CMFAST, and on `rsage`, roughly lie along this line. This means that a detection of the patchy power spectrum in CMB observations would make it possible to directly estimate $\ell^{\rm max}$, giving access to κ without bias from reionisation history, and to the evolution of the typical bubble size. As the growth of ionised regions depends on the physical properties of early galaxies, such as their ionising efficiency or their star formation rate and on the density of the IGM, constraints on κ could, in turn, give constraints on the nature of early light sources and of the early IGM.

Additionally, we can link the theoretical expression of the large-scale amplitude of the bubble power spectrum in Eq. (11)

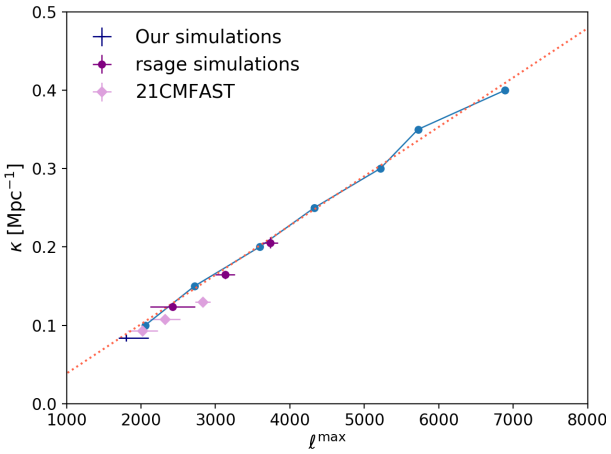

Fig. 9. Evolution of the peaking angular scale of the patchy kSZ power spectrum for one given reionisation history but different values of the κ parameter. The red dotted line is the result of a linear regression. Inferences are compared to results for different simulations.

with our parameterisation of $P_{ee}(k, z)$ in Eq. (13): $\alpha_0 x_e^{-1/5} \leftrightarrow 4/3\pi R^3/x_e(z)$. Because of the simplicity of the toy model, this relation is not an equivalence. For example, contrary to the toy model, in our simulations, the locations of the different ionised bubbles are correlated, following the underlying dark matter distribution and this correlation will add power to the spectrum on large scales. This analogy can however explain the correlation observed between α_0 and κ when fitting Eq. (15) to data (recall that $R \propto 1/\kappa$). Finally, since α_0 is independent of redshift, it will be a pre-factor for the left-hand side of Eq. (7), therefore we expect a strong correlation between this parameter and the amplitude of the spectrum at $\ell = 3000$ and with the maximum amplitude reached by the spectrum. We confirm this intuition by fixing the reionisation history and κ but varying α_0 on the range $3.0 < \log \alpha_0 < 4.4$ and comparing the resulting spectra: there is a clear linear relation between these two parameters and α_0, but in this case results for `rsage` and 21CMFAST do not follow the correlation. Interestingly, the shape of the different resulting kSZ power spectra is strictly identical (namely, $\ell^{\rm max}$ does not change when varying α_0), hinting at the fact that $\ell^{\rm max}$ depends only on κ and not α_0 or reionisation history. Therefore it will be possible to make an unbiased estimate of κ from the shape of the measured spectrum. The `rsage` simulations show that, for a similar reionisation history, a larger value of α_0 will lead to a stronger kSZ signal; but looking at 21CMFAST, we found that an early reionisation scenario can counterbalance this effect and lead to high amplitude despite low α_0 values. This corroborates the results of Mesinger et al. (2012), which find that the amplitude of the spectrum is determined by both the morphology (and so the α_0 value) and the reionisation history. Therefore, fitting CMB data to our parameterisation will likely lead to strongly correlated values of α_0 and parameters such as Δz or $z_{\rm re}$. Other methods should be used to constrain the reionisation history and break this degeneracy, such as constraints from the value of the Thomson optical depth, or astrophysical constraints on the IGM ionised level. Conversely, 21cm intensity mapping should be able to give independent constraints on α_0.

5.2. Conclusions & prospects

In this work, we have used state-of-the-art reionisation simulations (Aubert et al. 2015) to calibrate an analytical expression of the angular power spectrum of the kSZ effect stemming from patchy reionisation. We have shown that describing the shape, but also amplitude of the signal only in terms of global parameters such as the reionisation duration Δz and its midpoint $z_{\rm re}$ is not sufficient: it is essential to take the physics of the process into account. In our new proposed expression, the parameters can be directly related to both the global reionisation history $x_e(z)$ and to the morphology of the process. With as few as these three parameters, we can fully recover the patchy kSZ angular power spectrum, in a way that is quick and easy to forward-model. Our formalism contrasts with current works, which use an arbitrary patchy kSZ power spectrum template enclosing an outdated model of reionisation. Applying it to CMB data will result in obtaining for the first time the actual shape of the patchy kSZ power spectrum, taking consistently into account reionisation history and morphology. In future works, we will apply this framework to CMB observations from SPT and, later, CMB-S4 experiments. Then, the inferred values of α_0 and κ will provide us with detailed information about the physics of reionisation: κ will constrain the growth of ionised bubbles with time and α_0 the evolution of the variance of the ionisation field during EoR, both being related to the ionising properties of early galaxies. The complex derivation of the kSZ signal, based on a series of integrals, leads to correlations between our parameters. For example, a high amplitude of the spectrum can be explained either by a large value of α_0 due to a high ionising efficiency of galaxies, or by an early reionisation. Such degeneracies, however, could be broken by combining CMB data with other observations: astrophysical observations of early galaxies and quasars will help grasp the global history of reionisation and constrain parameters such as Δz and $z_{\rm re}$, while 21cm intensity mapping will help understand reionisation morphology, putting independent constraints on α_0 and κ. The main challenge remains to separate first the kSZ signal from other foregrounds, and then the patchy kSZ signal from the homogeneous one. To solve the first part of this problem, Calabrese et al. (2014) suggest to subtract the theoretical primary power spectrum (derived from independent cosmological parameter constraints obtained from polarisation measurements) from the observed one so that the signal left is the kSZ power spectrum alone. Secondly, one would need a good description of the homogeneous spectrum, similar to the results of Shaw et al. (2012) but updated with more recent simulations, in order to estimate how accurately one can recover the patchy signal. Additionally, this result sheds light on the scaling relations observed in previous works by giving them a physical ground. For example, features in the free electron contrast density power spectrum explain the relation between the amplitude at which the patchy kSZ spectrum bumps $\ell^{\rm max}$ and the typical bubble size, which was observed empirically in many previous works (McQuinn et al. 2005; Iliev et al. 2007; Mesinger et al. 2012).

On average, our results are in good agreement with previous works, despite a low amplitude of the patchy kSZ angular power spectrum at $\ell = 3000$ ($\sim 0.80\,\mu$K^2) for our fiducial simulations. There is undoubtedly a bump around scales $\ell \sim 2000$ that can be related to the typical bubble size and the amplitude of the total (patchy) kinetic SZ spectrum ranges from 4 to 5 μK^2 (0.5 to 1.5 μK^2, respectively) for plausible reionisation scenarios, therefore lying within the error bars of the latest observational results of ACT (Sievers et al. 2013) and SPT (Reichardt et al. 2020). We have found that the majority of the patchy kSZ signal stems from scales $10^{-3} < k/{\rm Mpc}^{-1} < 1$ and from the core of the reionisation process ($10\% < x_e < 80\%$), ranges on which we must focus our efforts to obtain an accurate description. This analysis does not

consider third- and fourth-order components of the kSZ signal, which can represent as much as 10% of the total signal (Alvarez 2016), and uses a coarse approximation for the electrons density - velocity cross spectra. In contrast to previous works, these results are not simulation-dependent as we have tested the robustness of our model by confronting it to different types of simulations, capturing different aspects of the process. However, the analytic formulation of our derivations was calibrated on a relatively small simulation, of side length 128 Mpc/h, which could bias our results. To further support our approach, using a larger radiative hydrodynamical simulation would be useful. Additionally, one could derive the kSZ power from lightcones constructed with our simulation, but the limited size of the simulation might lead to a significant underestimate of the kSZ power (Shaw et al. 2012; Alvarez 2016).

Acknowledgements. The authors thank Anne Hutter and Jacob Seiler for kindly providing runs of their simulations, as well as Jonathan Pritchard and Ian Hothi for fruitful discussions at various stages of this analysis. They also thank the referee for useful comments which helped imoprove the quality of these results. AG acknowledges financial support from the European Research Council under ERC grant number 638743-FIRSTDAWN and her work is supported by a PhD studentship from the UK Science and Technology Facilities Council (STFC). This work was initiated during LSS2LSS, a Ψ^2 thematic programme organised by the Institut d'Astrophysique Spatiale and funded by the Université Paris-Saclay in July 2018 (see https://www.ias.u-psud.fr/LSS2LSS). The authors were granted access to the HPC resources of CINES and IDRIS under the allocation A0070411049 attributed by GENCI (Grand Equipement National de Calcul Intensif) and the Jean-Zay Grand Challenge (CT4) "Émulation de simulations de Réionisation par apprentissage profond". This work was additionally supported by the Programme National Cosmology et Galaxies (PNCG) of CNRS/INSU with INP and IN2P3, co-funded by CEA and CNES. SI was supported by the European Structural and Investment Fund and the Czech Ministry of Education, Youth and Sports (Project CoGraDS - CZ.02.1.01/0.0/0.0/15_003/0000437).
This research made use of `astropy`, a community-developed core Python package for astronomy (Astropy Collaboration et al. 2013, 2018); `matplotlib`, a Python library for publication quality graphics (Hunter 2007); `scipy`, a Python-based ecosystem of open-source software for mathematics, science, and engineering (Jones et al. 2001) – including `numpy` (Oliphant 2006), and `emcee`, an implementation of the affine invariant MCMC ensemble sampler (Foreman-Mackey et al. 2013).

References

Alvarez, M. A. 2016, ApJ, 824, 118
Astropy Collaboration, Price-Whelan, A. M., Sipőcz, B. M., et al. 2018, ArXiv e-prints [arXiv:1801.02634]
Astropy Collaboration, Robitaille, T. P., Tollerud, E. J., et al. 2013, A&A, 558, A33
Aubert, D., Deparis, N., & Ocvirk, P. 2015, Monthly Notices of the Royal Astronomical Society, 454, 1012
Aubert, D., Deparis, N., Ocvirk, P., et al. 2018, ApJ, 856, L22
Battaglia, N., Natarajan, A., Trac, H., Cen, R., & Loeb, A. 2013, ApJ, 776, 83
Bharadwaj, S. & Pandey, S. K. 2005, MNRAS, 358, 968
Bouwens, R. J., Illingworth, G. D., Oesch, P. A., et al. 2015, ApJ, 803, 34
Calabrese, E., Hložek, R., Battaglia, N., et al. 2014, Journal of Cosmology and Astroparticle Physics, 2014, 010
Chardin, J., Uhlrich, G., Aubert, D., et al. 2019, MNRAS, 490, 1055
Croton, D. J., Stevens, A. R. H., Tonini, C., et al. 2016, ApJS, 222, 22
Deparis, N., Aubert, D., Ocvirk, P., Chardin, J., & Lewis, J. 2019, A&A, 622, A142
Douspis, M., Aghanim, N., Ilić, S., & Langer, M. 2015, A&A, 580, L4
Dunkley, J., Hlozek, R., Sievers, J., et al. 2011, ApJ, 739, 52
Foreman-Mackey, D., Hogg, D. W., Lang, D., & Goodman, J. 2013, PASP, 125, 306
George, E. M., Reichardt, C. L., Aird, K. A., et al. 2015, ApJ, 799, 177
Gorce, A., Douspis, M., Aghanim, N., & Langer, M. 2018, A&A, 616, 113
Greig, B. & Mesinger, A. 2016, Monthly Notices of the Royal Astronomical Society, 465, 4838
Hahn, O. & Abel, T. 2013, MUSIC: MUlti-Scale Initial Conditions
Howlett, C., Lewis, A., Hall, A., & Challinor, A. 2012, J. Cosmology Astropart. Phys., 1204, 027
Hunter, J. D. 2007, Computing In Science & Engineering, 9, 90
Hutter, A. 2018a, CIFOG: Cosmological Ionization Fields frOm Galaxies
Hutter, A. 2018b, MNRAS, 477, 1549
Iliev, I. T., Pen, U.-L., Bond, J. R., Mellema, G., & Shapiro, P. R. 2007, ApJ, 660, 933
Jaffe, A. H. & Kamionkowski, M. 1998, Phys. Rev. D, 58, 043001
Jones, E., Oliphant, T., Peterson, P., et al. 2001, SciPy: Open source scientific tools for Python
Kaur, H. D., Gillet, N., & Mesinger, A. 2020, MNRAS
Leitherer, C., Schaerer, D., Goldader, J. D., et al. 1999, ApJS, 123, 3
Lewis, A., Challinor, A., & Lasenby, A. 2000, ApJ, 538, 473
McQuinn, M., Furlanetto, S. R., Hernquist, L., Zahn, O., & Zaldarriaga, M. 2005, ApJ, 630, 643
Mesinger, A. & Furlanetto, S. 2007, ApJ, 669, 663
Mesinger, A., Furlanetto, S., & Cen, R. 2011, MNRAS, 411, 955
Mesinger, A., McQuinn, M., & Spergel, D. N. 2012, Monthly Notices of the Royal Astronomical Society, 422, 1403
Oliphant, T. 2006, NumPy: A guide to NumPy, USA: Trelgol Publishing, [Online; accessed <today>]
Park, H., Shapiro, P. R., Komatsu, E., et al. 2013, ApJ, 769, 93
Planck Collaboration, Adam, R., Ade, P. A. R., et al. 2016a, A&A, 594, A1
Planck Collaboration, Akrami, Y., Arroja, F., et al. 2018, arXiv e-prints, arXiv:1807.06205
Planck Collaboration et al. 2016b, A & A, 596, A108
Rasera, Y. & Teyssier, R. 2006, A&A, 445, 1
Reichardt, C. L., Patil, S., Ade, P. A. R., et al. 2020, arXiv e-prints, arXiv:2002.06197
Reichardt, C. L., Shaw, L., Zahn, O., et al. 2012, ApJ, 755, 70
Robertson, B. E., Ellis, R. S., Furlanetto, S. R., & Dunlop, J. S. 2015, The Astrophysical Journal, 802, L19
Seiler, J., Hutter, A., Sinha, M., & Croton, D. 2018, MNRAS, 480, L33
Seiler, J., Hutter, A., Sinha, M., & Croton, D. 2019, MNRAS, 1578
Shaw, L. D., Rudd, D. H., & Nagai, D. 2012, ApJ, 756, 15
Sievers, J. L., Hlozek, R. A., Nolta, M. R., et al. 2013, J. Cosmology Astropart. Phys., 2013, 060
Smith, R. E., Peacock, J. A., Jenkins, A., et al. 2003, MNRAS, 341, 1311
Sunyaev, R. A. & Zeldovich, I. B. 1980, ARA&A, 18, 537
Xu, W., Xu, Y., Yue, B., et al. 2019, MNRAS, 490, 5739
Zahn, O., Reichardt, C. L., Shaw, L., et al. 2012, ApJ, 756, 65
Zahn, O., Zaldarriaga, M., Hernquist, L., & McQuinn, M. 2005, ApJ, 630, 657
Zeldovich, Y. B. & Sunyaev, R. A. 1969, Astrophysics and Space Science, 4, 301

Table A.1. Results obtained when fitting Eq. 15 to the six simulations separately. Maximum likelihood parameters are given with 68% confidence intervals.

Sim	$\log \alpha_0$ [Mpc^3]	κ [Mpc^{-1}]	$\mathcal{D}^p_{3000}$ [μK^2]	$\ell^{\max}$
1	3.86 ± 0.08	0.093 ± 0.006	0.75 μK^2	1900
2	3.85 ± 0.08	0.094 ± 0.006	0.81 μK^2	1900
3	3.80 ± 0.08	0.098 ± 0.007	0.86 μK^2	1900
4	3.78 ± 0.08	0.100 ± 0.007	0.82 μK^2	1900
5	3.91 ± 0.08	0.089 ± 0.007	0.82 μK^2	1800
6	3.87 ± 0.08	0.093 ± 0.006	0.83 μK^2	1900

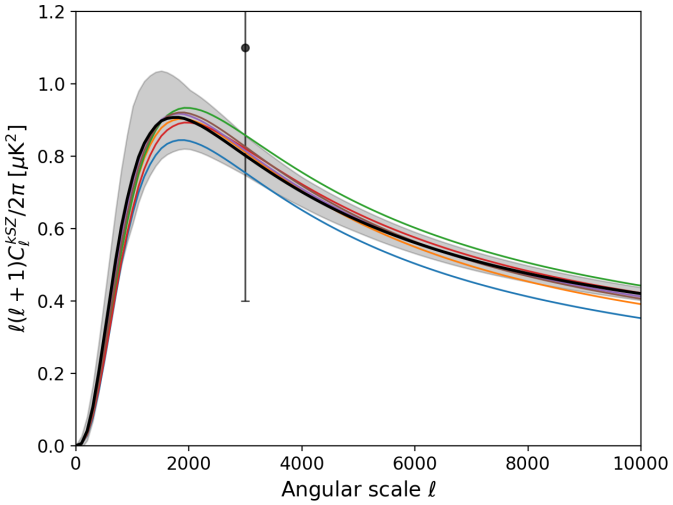

Fig. A.1. Comparison of the patchy kSZ power spectra resulting from one fit on the six simulations (black solid line, with 68% confidence interval as the shaded area) or from six fits (coloured solid lines). The data point corresponds to constraints from Reichardt et al. (2020).

Appendix A: Variations on the fit

Appendix A.1: Six fits for six simulations

Instead of fitting the six simulations simultaneously, we choose to fit each simulation individually to Eq. 15 with the same error bars as the fitting procedure described in Sec. 4. This allows to use the original $P_{ee}(k, z)$ data points from each simulation, without interpolating them, and the original reionisation history rather than an averaged one. The results are shown in Table A.1, where the maximum likelihood parameters, along with their 68% confidence intervals, and the corresponding values of $\mathcal{D}_{3000}$ and $\ell^{\max}$ are given. The six maximum likelihood values of α_0 and κ lie within the 95% confidence interval of the parameter distributions obtained in Sec. 4 and so do the resulting patchy kSZ spectra, as shown in Fig. A.1.

Appendix A.2: Attempt at deriving a covariance matrix from a sample of six

Because of the very insufficient number of simulations available to derive a covariance matrix, even when bootstrapping, we choose to average covariance matrices over bins.

Average over z-bins First, we choose to ignore correlations between scales over redshifts and use a covariance matrix $\boldsymbol{C}$, average of the 6×10 covariance matrices obtained for each simulation and each redshift bin. $\boldsymbol{C}$ has therefore dimensions $(20, 20)$[9]. We fit Eq. 15 to the six simulations, trying to minimise:

$$\chi^2 = \sum_{z_i} X_i^{\mathrm{T}} \boldsymbol{C}^{-1} X_i, \tag{A.1}$$

where $X_i = P_{ee}^{\mathrm{data}}(\{k_j\}, x_i) - P_{ee}^{\mathrm{model}}(\{k_j\}, x_i)$. We find a minimal reduced χ^2 of 125, reached for $\log \alpha_0 = 4.12$ and $\kappa = 0.078$ Mpc^{-1} and giving $\mathcal{D}^{\mathrm{p}}_{3000} = 0.97\ \mu\mathrm{K}^2$ and $\ell^{\max} = 1500$. This difference comes from a poor match between the maximum likelihood $P_{ee}(k, z)$ and the data points on scales $0.1 < k/\mathrm{Mpc}^{-1} < 0.3$. These scales correspond to the power cut-off, so that the value of κ is poorly constrained and, later, the kSZ power spectrum is distorted.

Average over k-bins Secondly, we choose to ignore correlations between redshifts over scales and use a covariance matrix $\boldsymbol{C}$, average of the 6×20 covariance matrices obtained for each simulation and each scale bin. $\boldsymbol{C}$ has therefore dimensions $(10, 10)$. Comparing the correlation coefficients obtained for the two approaches, we note that the correlations are higher for this approach. We fit Eq. 15 to the six simulations, trying to minimise:

$$\chi^2 = \sum_{k_i} X_i^{\mathrm{T}} \boldsymbol{C}^{-1} X_i, \tag{A.2}$$

where $X_i = P_{ee}^{\mathrm{data}}(k_i, \{x_j\}) - P_{ee}^{\mathrm{model}}(k_i, \{x_j\})$. We find a minimal reduced χ^2 of 4.46, reached for $\log \alpha_0 = 3.65$ and $\kappa = 0.135$ Mpc^{-1} and giving $\mathcal{D}^{\mathrm{p}}_{3000} = 1.46\ \mu\mathrm{K}^2$ and $\ell^{\max} = 2700$. The excess power comes from the fact that the fit systematically overestimate the P_{ee} power on small scales ($k > 0.3$ Mpc^{-1}).

Appendix B: Detailed results on `rsage` and 21CMFAST

Appendix B.1: Fits on 21CMFAST

We now fit Eq. (15) to the power spectra of our three 21CMFAST runs. To account for sample variance, we perform 20 realisations of each simulation – the choice of 20 being motivated by Kaur et al. (2020) and computational limitations. From these 20 realisations we derive relative error bars on $P_{ee}(k, z)$ values, corresponding to the 68% confidence level on the distribution of values for each bin. The results obtained for 21CMFAST and their interpretation are consistent with what is obtained for the other simulations. The upper panel of Fig. B.1 shows the best-fit model for $P_{ee}(k, z)$, along with snapshot values, for the second simulation.

Appendix B.2: Fits on `rsage`

Because we only have one realisation of each `rsage` simulation, we apply the relative error bars derived from 21CMFAST to the `rsage` $P_{ee}(k, z)$ data points. On the scales and redshifts range covered by the fit, the error bars $\sigma(k, z)$ derived from the 20 realisations of each of the three 21CMFAST simulations follow $\sigma(k, z) = 10^b Pee(k, z) k^a$, where $a = -1.12 \pm 0.79$ and $b = -1.74 \pm 0.70$ have been found by fitting the $\sigma(k, z)$ values of the 60 simulations simultaneously. We then apply this expression to the spectra of the `rsage` simulations, a reasonable first

[9] Recall we have 10 redshift bins and 20 scale bins after interpolating the spectra.

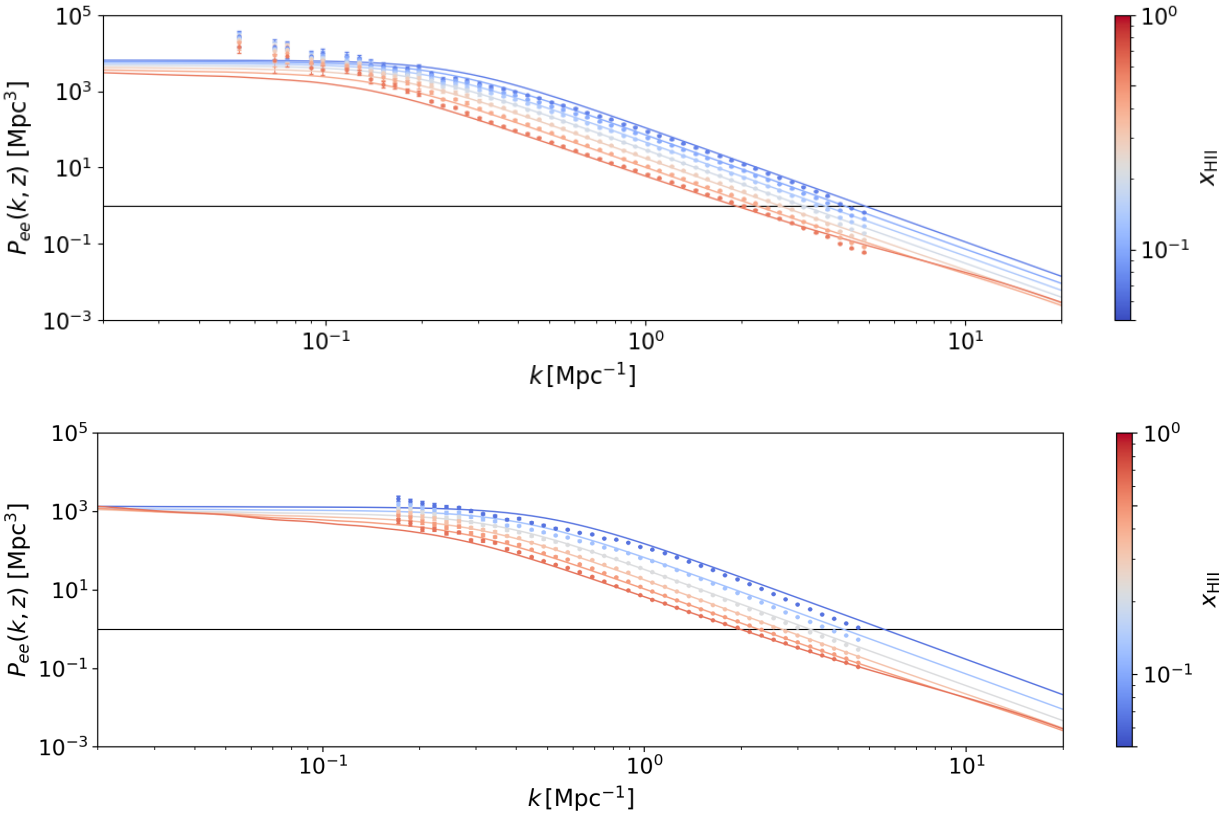

Fig. B.1. Result of fitting Eq, (13) to the spectra of the 21CMFAST run for $M_{\rm turn} = 10^9 M_\odot$ (upper panel) and of `rsage fej` (lower panel). The error bars correspond to the 68% confidence level on the spectra of 20 realisations of the same 21CMFAST run.

approximation of cosmic variance. We fit Eq. (15) to the spectra of the three simulations. The lower panel of Fig. B.1 shows the best-fit model for $P_{ee}(k, z)$, along with snapshot values, for `rsage fej`. Note that here, we only show the spectra on the redshift range used for the fit, where the power-law structure is not as striking as for higher redshifts.

Appendix B

Simulations

Many simulations of the 21cm signal have been developed in the recent years in order to efficiently prepare for forthcoming observations from, for instance, the SKA. However, reionisation simulations are difficult to write, for many different reasons. The main issue is that a large variety of scales is relevant to the study of reionisation, as well as a large variety of physical processes need to be considered: small-scale physics, via radiative transfers, governs the propagation of the ionising front – but we also need to have an image of the IGM on large scales to statistically sample the distribution of ionised regions during reionisation. Here, we present the different simulations used in this work.

B.1 EMMA

The EMMA simulation code Aubert et al. (2015) tracks the collisionless dynamics of dark matter, the hydrodynamics of baryons, star formation and feedback, and the radiative transfer using a moment-based method (see Aubert et al. 2018; Deparis et al. 2019). This code adheres to an Eulerian description, with fields described on grids, and enables adaptive mesh refinement techniques to increase the resolution in collapsing regions. Six simulations with identical numerical and physical parameters were produced in order to make up for the limited physical size of the box and the associated sample variance. They only differ in the random seeds used to generate the initial displacement phases, resulting in 6 different configurations of structures within the simulated volumes. Each run has a $(128\ \mathrm{Mpc}/h)^3$ volume sampled with 1024^3 cells at the coarsest level and 1024^3 dark matter particles. Refinement is triggered when the number of dark matter particles exceeds 8, up to 6 refinement levels. Initial conditions were produced using MUSIC (Hahn & Abel 2013) with a starting redshift of $z = 150$, assuming Planck Collaboration et al. (2016b) cosmology. Simulations were stopped at $z \sim 6$, before the full end of reionisation. The dark matter mass resolution is $2.1 \times 10^8 \mathrm{M}_\odot$ and the stellar mass resolution is $6.1 \times 10^5 \mathrm{M}_\odot$. Star formation proceeds according to standard recipes described in Rasera & Teyssier (2006), with an overdensity threshold equals to 20 to trigger the gas-to-stellar particle conversion with a 0.1 efficiency: such values allow the first stellar particles to appear at $z \sim 17$.

Table B.1: Characteristics of the six EMMA simulations. $z_{\rm re}$ is the midpoint of reionisation $x_e(z_{\rm re}) = 0.5 f_{\rm H}$, $z_{\rm end}$ the redshift at which $x_e(z)$ (extrapolated) reaches $f_{\rm H}$ and τ is the Thompson optical depth. Δz corresponds to $z_{0.25} - z_{0.75}$.

	$z_{\rm re}$	$z_{\rm end}$	τ_{x_e}	Δz
1	7.09	5.96	0.0539	1.17
2	7.16	5.92	0.0545	1.19
3	7.16	5.67	0.0544	1.16
4	7.05	5.60	0.0532	1.16
5	7.03	5.56	0.0531	1.15
6	7.14	5.79	0.0543	1.16

Star particles produce ionising radiation for 3 Myr, with an emissivity provided by the Starburst99 model for a Top-Heavy initial mass function and a $Z = 0.001$ metallicity (Leitherer et al. 1999). Supernovae feedback follows the prescription used in Aubert et al. (2018): as they reach an age of 15 million years, stellar particles dump 9.8×10^{11} J per stellar kg in the surrounding gas, 1/3 in the form of thermal energy, 2/3 in the form of kinetic energy. Using these parameters, we obtain a cosmic star formation history consistent with constraints by Bouwens et al. (2015b) and end up with 20 millions stellar particles at $z = 6$. The simulations were produced on the Occigen (CINES) and Jean-Zay (IDRIS) supercomputers, using CPU architectures : a reduced speed of light of $0.1c$ has been used to reduce the cost of radiative transfer.

Table B.1 gives the midpoint $z_{\rm re}$ and end of reionisation $z_{\rm end}$ for each simulation, as well as the duration of the process, defined as the time elapsed between a global ionisation fraction of 25% and of 75%. The mean values are $z_{\rm re} = 7.10$, $\Delta z = 1.16$ and $z_{\rm end} = 5.75$ giving a mean Thomson optical depth for H II and He II $\tau = 0.0539$. Fig. B.1 shows the interpolated reionisation histories, where data points correspond to the snapshots available for each simulation. Note that the simulations stop before the reionisation process is fully over, therefore we need to extrapolate $x_e(z)$ to find the $z_{\rm end}$ value given in Table B.1. Additionally, the simulations originally do not include the first reionisation of helium. We correct for this by multiplying the IGM ionised fraction of hydrogen $x_{\rm H\,II}$ measured in the simulations by $f_{\rm H} = 1 + Y_p/4X_p \simeq 1.08$ where Y_p and X_p are the primordial mass fraction of helium and hydrogen respectively. Because we limit our study to redshifts $z > 5.5$, the second reionisation of helium is ignored.

B.2 RSAGE

The `rsage` simulations were introduced in Seiler et al. (2019). They start off as a N-body simulation (Seiler et al. 2018), containing 2400^3 dark matter particles within a 160 Mpc side box, resolving halos of mass $\sim 4 \times 10^8$ $M_\odot$ with 32 particles. The galaxies are evolved over cosmic time following the Semi-Analytic Galaxy Evolution (SAGE) model of Croton et al. (2016), modified to include an improved modelling of galaxy evolution during the Epoch of Reionisation, including the feedback of ionisation on galaxy evolution.

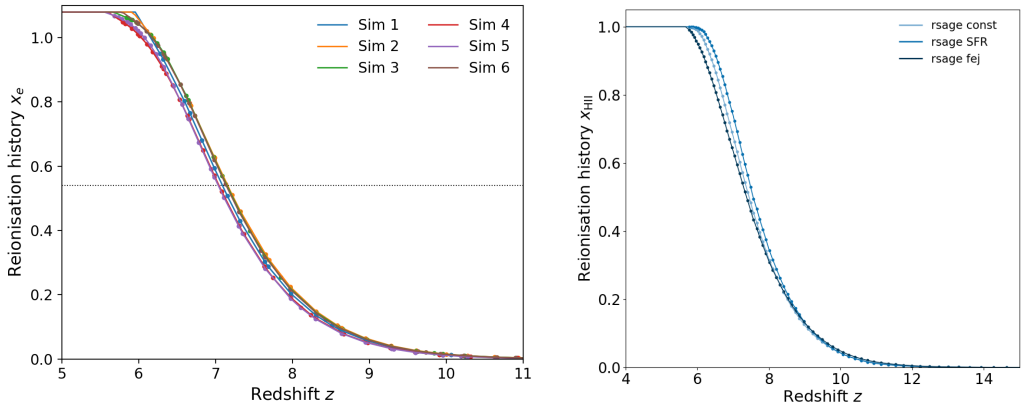

Figure B.1: Global reionisation histories of the six EMMA (left panel) and three `rsage` (right panel) simulations used throughout this work. The solid line is the result of interpolating between the available snapshots, shown as filled circles.

The semi-numerical code `cifog` (Hutter 2018a,b) is used to generate an inhomogeneous ultraviolet background (UVB) and follow the evolution of ionised hydrogen during the EoR. Three versions of the `rsage` simulation exist, each corresponding to a different way of modelling the escape fraction $f_{\rm esc}$ of ionising photons from their host galaxy into the IGM. The first, dubbed `rsage const`, takes $f_{\rm esc}$ constant and equal to 20%. The second, `rsage fej`, considers a positive scaling of $f_{\rm esc}$ with $f_{\rm ej}$, the fraction of baryons that have been ejected from the galaxy compared to the number remaining as hot and cold gas. In the last one, `rsage SFR`, $f_{\rm esc}$ scales with the star formation rate and thus roughly with the halo mass. Because they are based on the same dark matter distribution, the three simulations start reionising at similar times ($z \sim 13$), but different source properties lead to different reionisation histories, shown on Fig. B.1. In `rsage SFR`, the ionised bubbles are statistically larger than the other two simulations at a given redshift: this results into `rsage SFR` reaching 50% of ionisation at $z_{\rm re} = 7.56$ vs. $z_{\rm re} = 7.45$ and $z_{\rm re} = 7.37$ for `rsage const` and `rsage fej` respectively, and the full ionisation being achieved in a shorter time. For more details, we refer the interested reader to Seiler et al. (2019).

B.3 21CMFAST

21CMFAST is a publicly available simulation (Mesinger & Furlanetto 2007; Mesinger et al. 2011) based on a semi-numerical code using excursion-set formalism (Furlanetto et al. 2004a): starting off a matter overdensity field, it assumes a cell ionised if there are at least enough photons to ionise all the baryons in it. Different parameters of the simulation can be varied to vary the physics at stake and result in different reionisation histories and morphologies. Here, we choose to vary the parameter $M_{\rm turn}$, the turnover mass, which corresponds to the minimum halo mass before exponential suppression of star formation. For example, $M_{\rm turn} = 10^8 M_\odot$ corresponds to a virial temperature of 10^4 K, allowing Lyα cooling. We generate three simulations, of same dimensions and resolution as `rsage`, for

$M_{\rm turn} = 10^8 M_\odot$, $10^9 M_\odot$ and $10^{10} M_\odot$, dubbed respectively M8, M9 and M10. Snapshots of the ionisation fields of the three simulations for a global ionisation level of $x_e = 30\%$ can be seen in the lower panels of Fig. 3.1. We see that despite having the same underlying matter field, the three runs exhibit different sizes of ionised regions. Contrary to `rsage`, the ionised regions are not spherical, but we can notice that M8 shows many small ionised regions distributed throughout the neutral background, whereas the ionised regions are concentrated in large clumps in M10. The corresponding global reionisation histories are shown in Fig. B.2. The high number of sources in M8 leads to an earlier reionisation than for the other two runs. Despite starting at different times, the duration of the process is similar for the three simulations.

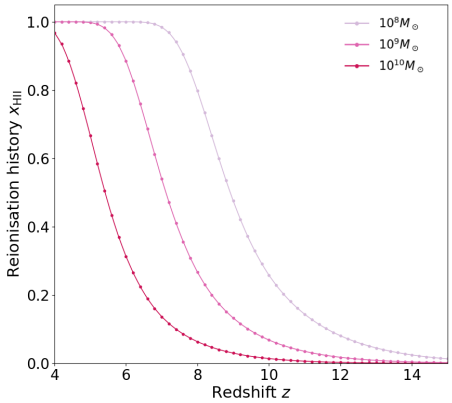

Figure B.2: Global reionisation histories of the three 21CMFAST simulations used throughout this work. The solid line is the result of interpolating between the available snapshots, shown as filled circles.

Bibliography

Abazajian, K. N., Adshead, P., Ahmed, Z., et al. 2016, arXiv e-prints, arXiv:1610.02743

Ade, P., Aguirre, J., Ahmed, Z., et al. 2019, J. Cosmology Astropart. Phys., 2019, 056

Aghanim, N., Desert, F. X., Puget, J. L., & Gispert, R. 1996, A&A, 311, 1

Aghanim, N., Majumdar, S., & Silk, J. 2008, Reports on Progress in Physics, 71, 066902

Alfvén, H. & Herlofson, N. 1950, Phys. Rev., 78, 616

Alvarez, M. A. 2016, ApJ, 824, 118

Aubert, D., Deparis, N., & Ocvirk, P. 2015, MNRAS, 454, 1012

Aubert, D., Deparis, N., Ocvirk, P., et al. 2018, ApJL, 856, L22

Bañados, E., Venemans, B. P., Mazzucchelli, C., et al. 2018, Nature, 553, 473

Bag, S., Mondal, R., Sarkar, P., Bharadwaj, S., & Sahni, V. 2018, MNRAS, 477, 1984

Barkana, R. 2018, Nature, 555, 71

Barreira, A., Krause, E., & Schmidt, F. 2018, J. Cosmology Astropart. Phys., 2018, 053

Battaglia, N., Natarajan, A., Trac, H., Cen, R., & Loeb, A. 2013, ApJ, 776, 83

Becker, G. D. & Bolton, J. S. 2013, MNRAS, 436, 1023

Becker, G. D., Bolton, J. S., Haehnelt, M. G., & Sargent, W. L. W. 2011, MNRAS, 410, 1096

Becker, G. D., Bolton, J. S., Madau, P., et al. 2015, MNRAS, 447, 3402

Becker, R. H., Fan, X., White, R. L., et al. 2001, AJ, 122, 2850

Bennett, C. L., Smoot, G. F., Hinshaw, G., et al. 1992, ApJ Letters, 396, L7

Bharadwaj, S. & Pandey, S. K. 2005, MNRAS, 358, 968

Binnie, T. & Pritchard, J. R. 2019, MNRAS, 487, 1160

Boera, E., Becker, G. D., Bolton, J. S., & Nasir, F. 2019, ApJ, 872, 101

Bolton, J. S., Becker, G. D., Raskutti, S., et al. 2012, MNRAS, 419, 2880

Bolton, J. S. & Haehnelt, M. G. 2007, MNRAS, 382, 325

Bouwens, R. J., Illingworth, G. D., Oesch, P. A., et al. 2015a, ApJ, 811, 140

Bouwens, R. J., Illingworth, G. D., Oesch, P. A., et al. 2015b, ApJ, 803, 34

Bowler, R. A. A., Jarvis, M. J., Dunlop, J. S., et al. 2020, MNRAS, 493, 2059

Bowman, J. D., Rogers, A. E. E., & Hewitt, J. N. 2008, ApJ, 676, 1

Bowman, J. D., Rogers, A. E. E., Monsalve, R. A., Mozdzen, T. J., & Mahesh, N. 2018, Nature, 555, 67 EP

Carilli, C. L., Nikolic, B., Thyagarajan, N., et al. 2018, Radio Sci., 53, 845

Carucci, I. P., Villaescusa-Navarro, F., & Viel, M. 2017, J. Cosmology Astropart. Phys.,

2017, 001
Chapman, E., Abdalla, F. B., Bobin, J., et al. 2013, MNRAS, 429, 165
Chapman, E., Abdalla, F. B., Harker, G., et al. 2012, MNRAS, 423, 2518
Chapman, E. & Jelić, V. 2019, arXiv e-prints, arXiv:1909.12369
Chen, N., Doussot, A., Trac, H., & Cen, R. 2020, arXiv e-prints, arXiv:2004.07854
Chen, Z., Xu, Y., Wang, Y., & Chen, X. 2018, arXiv e-prints, arXiv:1812.10333
Ciardi, B., Bolton, J. S., Maselli, A., & Graziani, L. 2012, MNRAS, 423, 558
Ciardi, B., Ferrara, A., Marri, S., & Raimondo, G. 2001, MNRAS, 324, 381
Ciardi, B. & Loeb, A. 2000, ApJ, 540, 687
Cordes, J. M. & Chatterjee, S. 2019, ARA&A, 57, 417
Crain, R. A., Schaye, J., Bower, R. G., et al. 2015, MNRAS, 450, 1937
Croton, D. J., Stevens, A. R. H., Tonini, C., et al. 2016, Astrophys. J. Suppl. Ser., 222, 22
Das, S., Louis, T., Nolta, M. R., et al. 2014, J. Cosmology Astropart. Phys., 2014, 014
Datta, A., Bowman, J. D., & Carilli, C. L. 2010, ApJ, 724, 526
DeBoer, D. R., Parsons, A. R., Aguirre, J. E., et al. 2017, Publications of the Astronomical Society of the Pacific, 129, 045001
Deparis, N., Aubert, D., Ocvirk, P., Chardin, J., & Lewis, J. 2019, A&A, 622, A142
Douspis, M., Aghanim, N., Ilić, S., & Langer, M. 2015, A&A, 580, L4
Dunkley, J., Hlozek, R., Sievers, J., & others. 2011, ApJ, 739, 52
Dunlop, J. S., Rogers, A. B., McLure, R. J., et al. 2013, MNRAS, 432, 3520
Dvorkin, C. & Smith, K. M. 2009, Phys. Rev. D, 79, 043003
Eggemeier, A., Battefeld, T., Smith, R. E., & Niemeyer, J. 2015, MNRAS, 453, 797
Ewen, H. I. & Purcell, E. M. 1951, Nature, 168, 356
Fan, X., Carilli, C. L., & Keating, B. 2006a, ARA&A, 44, 415
Fan, X., Narayanan, V. K., Lupton, R. H., et al. 2001, AJ, 122, 2833
Fan, X., Strauss, M. A., Becker, R. H., et al. 2006b, ApJ, 132, 117
Fanaroff, B. L. & Riley, J. M. 1974, MNRAS, 167, 31P
Faucher-Giguère, C.-A., Kereš, D., & Ma, C.-P. 2011, MNRAS, 417, 2982
Feretti, L. 2005, Advances in Space Research, 36, 729 , clusters of Galaxies: New Insights from XMM-Newton, Chandra and INTEGRAL
Feretti, L., Giovannini, G., Govoni, F., & Murgia, M. 2012, The Astronomy and Astrophysics Review, 20, 54
Fialkov, A. & Barkana, R. 2014, MNRAS, 445, 213
Field, G. B. 1958, Proceedings of the IRE, 46, 240
Finkelstein, S. L., Ryan, Jr., R. E., Papovich, C., et al. 2015, ApJ, 810, 71
Finlator, K., Oh, S. P., Özel, F., & Davé, R. 2012, MNRAS, 427, 2464
Fixsen, D. J. 2009, ApJ, 707, 916
Furlanetto, S. R., Hernquist, L., & Zaldarriaga, M. 2004a, MNRAS, 354, 695
Furlanetto, S. R. & Lidz, A. 2007, ApJ, 660, 1030
Furlanetto, S. R. & Oh, S. P. 2005, MNRAS, 363, 1031

Furlanetto, S. R., Zaldarriaga, M., & Hernquist, L. 2004b, ApJ, 613, 1
Gardner, J. P., Mather, J. C., Clampin, M., et al. 2006, Space Sci. Rev., 123, 485
Gaskin, J. A., Swartz, D. A., Vikhlinin, A., et al. 2019, Journal of Astronomical Telescopes, Instruments, and Systems, 5, 021001
Gelman, A. & Rubin, D. B. 1992, Statistical Science, 7, 457
George, E. M., Reichardt, C. L., Aird, K. A., et al. 2015, ApJ, 799, 177
Ghara, R., Choudhury, T. R., & Datta, K. K. 2015, MNRAS, 447, 1806
Gleser, L., Nusser, A., Ciardi, B., & Desjacques, V. 2006, MNRAS, 370, 1329
Gnedin, N. Y. 2014, ApJ, 793, 29
Gnedin, N. Y., Kravtsov, A. V., & Chen, H.-W. 2008, ApJ, 672, 765
Gorce, A., Douspis, M., Aghanim, N., & Langer, M. 2018, A&A
Gorce, A., Ilić, S., Douspis, M., Aubert, D., & Langer, M. 2020, A&A, 640, A90
Gorce, A. & Pritchard, J. R. 2019, MNRAS, 489, 1321
Gorce, A. et al. in prep
Grazian, A., Giallongo, E., Boutsia, K., et al. 2018, ArXiv e-prints 1802.01953
Green, J., Schechter, P., Baltay, C., et al. 2012, arXiv e-prints, arXiv:1208.4012
Greig, B. & Mesinger, A. 2017, MNRAS, 465, 4838
Gunn, J. E. & Peterson, B. A. 1965, ApJ, 142, 1633
Haardt, F. & Madau, P. 2012, ApJ, 746, 125
Hahn, O. & Abel, T. 2013, MUSIC: MUlti-Scale Initial Conditions
Hazra, D. K., Paoletti, D., Finelli, F., & Smoot, G. F. 2019, arXiv e-prints, arXiv:1904.01547
Hazumi, M., Borrill, J., Chinone, Y., et al. 2012, in SPIE Conference Series, Vol. 8442, Space Telescopes and Instrumentation 2012: Optical, Infrared, and Millimeter Wave, 844219
Heinrich, C. & Hu, W. 2018, Phys. Rev. D, 98, 063514
Henry, P. S. 1971, Nature, 231, 516
Hinshaw, G., Larson, D., Komatsu, E., Spergel, D. N., et al. 2013, ApJ Supplements, 208, 19
Hiss, H., Walther, M., Hennawi, J. F., et al. 2018, ApJ, 865, 42
Howlett, C., Lewis, A., Hall, A., & Challinor, A. 2012, J. Cosmology Astropart. Phys., 1204, 027
Hu, W. & Kravtsov, A. V. 2003, ApJ, 584, 702
Hui, L. & Haiman, Z. 2003, ApJ, 596, 9
Hutter, A. 2018a, CIFOG: Cosmological Ionization Fields frOm Galaxies
Hutter, A. 2018b, MNRAS, 477, 1549
Hutter, A., Dayal, P., Müller, V., & Trott, C. M. 2017, ApJ, 836, 176
Hutter, A., Dayal, P., Partl, A. M., & Müller, V. 2014, MNRAS, 441, 2861
Hutter, A., Watkinson, C. A., Seiler, J., et al. 2020, MNRAS, 492, 653
Iliev, I. T., Mellema, G., Ahn, K., et al. 2014, MNRAS, 439, 725

Iliev, I. T., Mellema, G., Pen, U.-L., et al. 2006, MNRAS, 369, 1625
Iliev, I. T., Mellema, G., Shapiro, P. R., & Pen, U.-L. 2007a, MNRAS, 376, 534
Iliev, I. T., Pen, U.-L., Bond, J. R., Mellema, G., & Shapiro, P. R. 2007b, ApJ, 660, 933
Ishigaki, M., Kawamata, R., Ouchi, M., et al. 2015, ApJ, 799, 12
Ishigaki, M., Kawamata, R., Ouchi, M., et al. 2018, ApJ, 854, 73
Ivezić, Ž. 2018, in IAU Symposium, Vol. 333, Peering towards Cosmic Dawn, ed. V. Jelić & T. van der Hulst, 222–227
Iwata, I., Inoue, A. K., Matsuda, Y., et al. 2009, ApJ, 692, 1287
Jaffe, A. H. & Kamionkowski, M. 1998, Phys. Rev. D, 58, 043001
Jelić, V., Zaroubi, S., Aghanim, N., et al. 2010, MNRAS, 402, 2279
Jelić, V., Zaroubi, S., Labropoulos, P., et al. 2008, MNRAS, 389, 1319
Kakiichi, K., Majumdar, S., Mellema, G., et al. ????, MNRAS
Kaplan, J., Delabrouille, J., Fosalba, P., & Rosset, P. 2003, Comptes Rendus Physique, 4, 917
Kashikawa, N., Shimasaku, K., Malkan, M. A., et al. 2006, ApJ, 648, 7
Kaur, H. D., Gillet, N., & Mesinger, A. 2020, MNRAS
Keating, B. G., Ade, P. A. R., Bock, J. J., et al. 2003, in SPIE Conference Series, Vol. 4843, Polarimetry in Astronomy, ed. S. Fineschi, 284–295
Kennicutt, Robert C., J. 1998, ARA&A, 36, 189
Kermish, Z. D., Ade, P., Anthony, A., et al. 2012, in SPIE Conference Series, Vol. 8452, Millimeter, Submillimeter, and Far-Infrared Detectors and Instrumentation for Astronomy VI, 84521C
Koopmans, L., Pritchard, J., Mellema, G., et al. 2015, Advancing Astrophysics with the Square Kilometre Array (AASKA14), 1
Kosowsky, A. 2003, New Astron. Rev., 47, 939
Kuhlen, M. & Faucher-Giguère, C.-A. 2012, MNRAS, 423, 862
La Plante, P., Lidz, A., Aguirre, J., & Kohn, S. 2020, arXiv e-prints, arXiv:2005.07206
Lacasa, F. & Grain, J. 2019a, A & A, 624, A61
Lacasa, F. & Grain, J. 2019b, VizieR Online Data Catalog, J/A+A/624/A61
Lacasa, F., Lima, M., & Aguena, M. 2018, A & A, 611, A83
Lacasa, F. & Rosenfeld, R. 2016, J. Cosmology Astropart. Phys., 2016, 005
Laureijs, R., Amiaux, J., Arduini, S., et al. 2011, arXiv e-prints, arXiv:1110.3193
Leitherer, C., Schaerer, D., Goldader, J. D., et al. 1999, Astrophys. J. Suppl. Ser., 123, 3
Levrier, F., Falgarone, E., & Viallefond, F. 2006, A&A, 456, 205
Lewis, A. 2011, J. Cosmology Astropart. Phys., 2011, 026
Lewis, A. & Bridle, S. 2002, Phys. Rev., D66, 103511
Lewis, A., Challinor, A., & Lasenby, A. 2000, ApJ, 538, 473
Lidz, A., Faucher-Giguère, C.-A., Dall'Aglio, A., et al. 2010, ApJ, 718, 199
Linder, E. V. 2020, Phys. Rev. D, 101, 103019
Liu, A., Parsons, A. R., & Trott, C. M. 2014, Phys. Rev. D, 90, 023018

Liu, A., Pritchard, J. R., Allison, R., et al. 2016, Physical Review D, 93, 043013

Livermore, R. C., Finkelstein, S. L., & Lotz, J. M. 2017, ApJ, 835, 113

Loeb, A. & Furlanetto, S. 2013, The First Galaxies in the Universe (Princeton University Press)

LSST Science Collaboration, Abell, P. A., Allison, J., et al. 2009, arXiv e-prints, arXiv:0912.0201

Ma, X., Kasen, D., Hopkins, P. F., et al. 2015, MNRAS, 453, 960

Madau, P. & Dickinson, M. 2014, Annual Review of A&A, 52, 415

Madau, P. & Haardt, F. 2015, ApJ Letters, 813, L8

Madau, P., Meiksin, A., & Rees, M. J. 1997, ApJ, 475, 429

Majumdar, S., Pritchard, J. R., Mondal, R., et al. 2018, MNRAS, 476, 4007

Mao, Y., Koda, J., Shapiro, P. R., et al. 2020, MNRAS, 491, 1600

McGreer, I. D., Mesinger, A., & D'Odorico, V. 2015, MNRAS, 447, 499

McLure, R. J., Dunlop, J. S., Bowler, R. A. A., et al. 2013, MNRAS, 432, 2696

McQuinn, M., Furlanetto, S. R., Hernquist, L., Zahn, O., & Zaldarriaga, M. 2005, ApJ, 630, 643

Meerburg, P. D., Dvorkin, C., & Spergel, D. N. 2013, ApJ, 779, 124

Mellema, G., Iliev, I. T., Pen, U.-L., & Shapiro, P. R. 2006, MNRAS, 372, 679

Mertens, F. G., Mevius, M., Koopmans, L. V. E., et al. 2020, MNRAS, 493, 1662

Mesinger, A. 2010, MNRAS, 407, 1328

Mesinger, A., ed. 2016, Astrophysics and Space Science Library, Vol. 423, Understanding the Epoch of Cosmic Reionization

Mesinger, A. & Furlanetto, S. 2007, ApJ, 669, 663

Mesinger, A., Furlanetto, S., & Cen, R. 2011, MNRAS, 411, 955

Mesinger, A., McQuinn, M., & Spergel, D. N. 2012, MNRAS, 422, 1403

Minkowski, R. 1960, ApJ, 132, 908

Miralda-Escudé, J. & Rees, M. J. 1994, MNRAS, 266, 343

Miranda, V., Lidz, A., Heinrich, C. H., & Hu, W. 2017, MNRAS, 467, 4050

Mitra, S., Ferrara, A., & Choudhury, T. R. 2012, MNRAS: Letters, 428, L1

Monnier, J. D. 2007, New Astron. Rev., 51, 604

Mortlock, D. 2014, arXiv e-prints, arXiv:1405.4701

Muñoz, J. B. & Cyr-Racine, F.-Y. 2020, arXiv e-prints, arXiv:2005.03664

Mukherjee, S., Paul, S., & Choudhury, T. R. 2019, MNRAS, 486, 2042

Muller, C. A. & Oort, J. H. 1951, Nature, 168, 357

Obreschkow, D., Power, C., Bruderer, M., & Bonvin, C. 2013, ApJ, 762, 115

Ocvirk, P., Gillet, N., Shapiro, P. R., et al. 2016, MNRAS, 463, 1462

Oesch, P. A., Bouwens, R. J., Illingworth, G. D., et al. 2015, ApJ, 808, 104

Oesch, P. A., Brammer, G., van Dokkum, P. G., et al. 2016, ApJ, 819, 129

Osterbrock, D. E. 1989, Astrophysics of gaseous nebulae and active galactic nuclei (University Science Books)

Paciga, G., Chang, T.-C., Gupta, Y., et al. 2011, MNRAS, 413, 1174
Park, H., Shapiro, P. R., Komatsu, E., et al. 2013, ApJ, 769, 93
Park, J., Mesinger, A., Greig, B., & Gillet, N. 2019, MNRAS, 484, 933
Parsons, A. R., Backer, D. C., Foster, G. S., et al. 2010, ApJ, 139, 1468
Partridge, R. B. & Peebles, P. J. E. 1967, ApJ, 147, 868
Patel, M., Warren, S. J., Mortlock, D. J., & Fynbo, J. P. U. 2010, A&A, 512, L3
Patil, A. H., Yatawatta, S., Koopmans, L. V. E., et al. 2017, ApJ, 838, 65
Pawlik, A. H., Rahmati, A., Schaye, J., Jeon, M., & Dalla Vecchia, C. 2017, MNRAS, 466, 960
Pawlik, A. H., Schaye, J., & van Scherpenzeel, E. 2009, MNRAS, 394, 1812
Peebles, P. J. E. 1968, ApJ, 153, 1
Peebles, P. J. E. & Yu, J. T. 1970, ApJ, 162, 815
Planck Collaboration, Ade, P. A. R., Aghanim, N., et al. 2014, A&A, 571, A16
Planck Collaboration, Ade, P. A. R., Aghanim, N., et al. 2016a, A&A, 594, A13
Planck Collaboration et al. 2016b, A&A, 594, A1
Planck Collaboration et al. 2016c, A & A, 594, A11
Planck Collaboration et al. 2016d, A&A, 596, A108
Planck Collaboration et al. 2018, arXiv e-prints, arXiv:1807.06205
Price, L. C., Trac, H., & Cen, R. 2016, arXiv e-prints, arXiv:1605.03970
Pritchard, J. R. & Loeb, A. 2012, Reports on Progress in Physics, 75
Qin, Y., Mesinger, A., Park, J., Greig, B., & Muñoz, J. B. 2020a, MNRAS, 495, 123
Qin, Y., Poulin, V., Mesinger, A., et al. 2020b, arXiv e-prints, arXiv:2006.16828
Raičević, M. & Theuns, T. 2011, MNRAS, 412, L16
Rasera, Y. & Teyssier, R. 2006, A&A, 445, 1
Rauch, M. 1998, ARA&A, 36, 267
Readhead, A. C. S., Nakajima, T. S., Pearson, T. J., et al. 1988, AJ, 95, 1278
Reichardt, C. L., Patil, S., Ade, P. A. R., Anderson, A. J., et al. 2020, arXiv e-prints, arXiv:2002.06197
Reichardt, C. L., Shaw, L., Zahn, O., Aird, K. A., et al. 2012, ApJ, 755, 70
Richards, G. T., Myers, A. D., Peters, C. M., et al. 2015, Astrophys. J. Suppl. Ser., 219, 39
Robertson, B. E., Ellis, R. S., Furlanetto, S. R., & Dunlop, J. S. 2015, ApJ Letters, 802, L19
Robertson, B. E., Furlanetto, S. R., Schneider, E., et al. 2013, ApJ, 768, 71
Roy, A., Kulkarni, G., Meerburg, P. D., et al. 2020a, arXiv e-prints, arXiv:2004.02927
Roy, A., Lapi, A., Spergel, D., & Baccigalupi, C. 2018, J. Cosmology Astropart. Phys., 2018, 014
Roy, A., Lapi, A., Spergel, D., Basak, S., & Baccigalupi, C. 2020b, J. Cosmology Astropart. Phys., 2020, 062
Ruhl, J., Ade, P. A. R., Carlstrom, J. E., et al. 2004, in SPIE Conference Series, Vol. 5498,

Z-Spec: a broadband millimeter-wave grating spectrometer, ed. C. M. Bradford et al., 11–29
Rybicki, G. B. & Lightman, A. P. 1986, Radiative Processes in Astrophysics
Sachs, R. K. & Wolfe, A. M. 1967, ApJ, 147, 73
Sakharov, A. D. 1966, Journal of Experimental and Theoretical Physics, 22, 241
Salvaterra, R., Della Valle, M., Campana, S., et al. 2009, Nature, 461, 1258
Santos, M. R. 2004, MNRAS, 349, 1137
Schaye, J., Crain, R. A., Bower, R. G., et al. 2014, MNRAS, 446, 521
Schenker, M. A., Robertson, B. E., Ellis, R. S., et al. 2013, ApJ, 768, 196
Schmidt, M. 1963, Nature, 197, 1040
Seager, S., Sasselov, D. D., & Scott, D. 2000, ApJ Supplements, 128, 407
Seiler, J., Hutter, A., Sinha, M., & Croton, D. 2018, MNRAS, 480, L33
Seiler, J., Hutter, A., Sinha, M., & Croton, D. 2019, MNRAS, 1578
Shapiro, P. R. & Giroux, M. L. 1987, ApJ, 321, L107
Shaw, L. D., Rudd, D. H., & Nagai, D. 2012, ApJ, 756, 15
Shimabukuro, H., Yoshiura, S., Takahashi, K., Yokoyama, S., & Ichiki, K. 2016, MNRAS, 458, 3003
Shimabukuro, H., Yoshiura, S., Takahashi, K., Yokoyama, S., & Ichiki, K. 2017, MNRAS, 468, 1542
Shull, J. M., Harness, A., Trenti, M., & Smith, B. D. 2012, ApJ, 747, 100
Silk, J. 1968, ApJ, 151, 459
Singh, S., Subrahmanyan, R., Udaya Shankar, N., et al. 2018, ApJ, 858, 54
Smith, R. E., Peacock, J. A., Jenkins, A., et al. 2003, MNRAS, 341, 1311
Smoot, G. F., Gorenstein, M. V., & Muller, R. A. 1977, PRL, 39, 898
Sobacchi, E. & Mesinger, A. 2014, MNRAS, 440, 1662
Sobacchi, E., Mesinger, A., & Greig, B. 2016, MNRAS, 459, 2741
Sokasian, A., Abel, T., Hernquist, L., & Springel, V. 2003, MNRAS, 344, 607
Steidel, C. C., Pettini, M., & Adelberger, K. L. 2001, ApJ, 546, 665
Strömgren, B. 1939, ApJ, 89, 526
Sunyaev, R. A. & Zeldovich, Y. B. 1970, Astrophysics and Space Science, 7, 3
Tanvir, N. R., Fox, D. B., Levan, A. J., et al. 2009, Nature, 461, 1254
Tashiro, H., Aghanim, N., Langer, M., et al. 2011, MNRAS, 414, 3424
The Dark Energy Survey Collaboration. 2005, arXiv e-prints, astro
Thomas, R. M., Zaroubi, S., Ciardi, B., et al. 2009, MNRAS, 393, 32
Thompson, A. R., Moran, J. M., & Swenson, George W., J. 2017, Interferometry and Synthesis in Radio Astronomy, 3rd Edition
Thyagarajan, N., Carilli, C. L., & Nikolic, B. 2018, Phys. Rev. Lett., 120, 251301
Tingay, S. J., Goeke, R., Bowman, J. D., et al. 2013, Publications of the Astronomical Society of Australia, 30, e007
Tingay, S. J., Goeke, R., Bowman, J. D., et al. 2013, PASA, 30, e007

Trac, H. & Cen, R. 2007, ApJ, 671, 1
Trac, H. Y. & Gnedin, N. Y. 2011, Advanced Science Letters, 4, 228
Trott, C. M., Jordan, C. H., Midgley, S., et al. 2020, MNRAS, 493, 4711
Trott, C. M., Pindor, B., Procopio, P., et al. 2016, ApJ, 818, 139
Trott, C. M., Watkinson, C. A., Jordan, C. H., et al. 2019, arXiv e-prints, arXiv:1905.07161
van Haarlem, M. P., Wise, M. W., Gunst, A. W., et al. 2013a, A&A, 556, A2
van Haarlem, M. P., Wise, M. W., Gunst, A. W., et al. 2013b, A & A, 556, A2
Vrbanec, D., Ciardi, B., Jelić, V., et al. 2016, MNRAS, 457, 666
Watkinson, C. A., Giri, S. K., Ross, H. E., et al. 2019, MNRAS, 482, 2653
Watkinson, C. A., Majumdar, S., Pritchard, J. R., & Mondal, R. 2017, MNRAS, 472, 2436
Watkinson, C. A. & Pritchard, J. R. 2014, MNRAS, 443, 3090
Watkinson, C. A., Trott, C. M., & Hothi, I. 2020, arXiv e-prints, arXiv:2002.05992
Westerhout, G. 1958, Bulletin of the Astronomical Institutes of the Netherlands, 14, 215
White, R. L., Becker, R. H., Fan, X., & Strauss, M. A. 2003, AJ, 126, 1
Wise, J. H. 2019, arXiv e-prints, arXiv:1907.06653
Wise, J. H. & Cen, R. 2009, ApJ, 693, 984
Wise, J. H., Turk, M. J., Norman, M. L., & Abel, T. 2012, ApJ, 745, 50
Wolstenhulme, R., Bonvin, C., & Obreschkow, D. 2015, ApJ, 804, 132
Xu, H., Wise, J. H., Norman, M. L., Ahn, K., & O'Shea, B. W. 2016, ApJ, 833, 84
Xu, W., Xu, Y., Yue, B., et al. 2019, MNRAS, 490, 5739
Yajima, H., Li, Y., Zhu, Q., et al. 2014, MNRAS, 440, 776
York, D. G., Adelman, J., Anderson, John E., J., et al. 2000, AJ, 120, 1579
Zackrisson, E. 2020, talk at 'The First Billion Years of the Universe', Indore, India
Zahn, O., Lidz, A., McQuinn, M., et al. 2007, ApJ, 654, 12
Zahn, O., Reichardt, C. L., Shaw, L., Lidz, A., et al. 2012, ApJ, 756, 65
Zaroubi, S. 2013, in Astrophysics and Space Science Library, Vol. 396, The First Galaxies, ed. T. Wiklind, B. Mobasher, & V. Bromm, 45
Zel'dovich, Y. B., Kurt, V. G., & Syunyaev, R. A. 1969, Soviet Journal of Experimental and Theoretical Physics, 28, 146
Zeldovich, Y. B. & Sunyaev, R. A. 1969, Astrophysics and Space Science, 4, 301

université PARIS-SACLAY

ÉCOLE DOCTORALE
Astronomie et Astrophysique d'île-de-France

Titre: Signatures cosmologiques de l'époque de la réionisation

Mots clés: cosmologie – réionisation, premières étoiles – fond diffus cosmologique – signal à 21cm

Résumé: La réionisation cosmique, pendant laquelle les premières étoiles ionisent les atomes du milieu intergalactique, est encore méconnue. Dans ce travail, je développe des outils permettant d'améliorer l'analyse et l'interprétation des données pour mieux comprendre cette époque. M'intéressant au processus global dans un premier temps, je donne un scénario de référence pour la réionisation, fondé sur quelques hypothèses simples à propos de l'Univers jeune, mené par les galaxies, et qui pour la première fois est en accord avec toutes les données disponibles. Cependant, la réionisation intervient également à de plus petites échelles, et s'intéresser à la façon dont les galaxies ionisent leur environnement immédiat peut nous renseigner sur leurs propriétés physiques. C'est pourquoi dans un second chapitre, j'introduis des outils statistiques innovants qui pourront être appliqués à des cartes d'intensité du signal à 21cm et aux observations à petites échelles du fond diffus cosmologique. Ces méthodes sont conçues spécialement pour l'étude de la réionisation, et plus particulièrement pour être robustes aux contraintes liées à l'observation du signal 21cm. Elles sont disponibles publiquement. Enfin, je présente les limites de mes différents outils, liées à la fois aux méthodes d'observation elles-mêmes, ainsi qu'à des erreurs de modélisation. Avec ce travail, j'ouvre la voie à une analyse cosmologique cohérente des données qui permettra d'obtenir, une fois que la nouvelle génération de télescopes aura donné ses premiers résultats, une compréhension à la fois globale et locale de la réionisation, c'est-à-dire nous renseignant sur l'Univers dans son intégralité, mais également sur la nature de ses premières sources de lumière.

Title: Cosmological signatures of the Epoch of Reionisation

Keywords: cosmology – dark ages, reionization, first stars – cosmic background radiation – 21cm signal

Abstract: The Epoch of Reionisation, when the first galaxies slowly ionise the atoms of their surrounding intergalactic medium is still poorly known. During my PhD, I have developed new ways to constrain reionisation, in order to improve the analysis and interpretation of current and future observations. Choosing an outside-in approach, I first give a simple, comprehensive history of reionisation, finally able to fit all the available data, where few galaxies perform the full IGM reionisation and based on reasonable assumptions on the nature of the high-redshift Universe. However, reionisation is not only a large-scale process, and we can learn about the properties of the first stars and galaxies when looking at how they ionise their immediate surroundings, on scales of a few hundreds of megaparsecs. In this perspective, in a second chapter, I introduce new statistical tools to be applied to small-scale data, from intensity mapping of the 21cm signal of neutral hydrogen to high-multipole CMB observations. These methods are designed to study reionisation, and in particular to be robust to instrumental effects, a central issue of 21cm observations. In the last chapter, I discuss the observations- and model-related limitations of current results, by looking at the way poorly known parameters impact our current scenarios of reionisation and by proposing unbiased and efficient observational strategies. In these three years of work, I have developed new tools, designed for the study of the EoR, namely to overcome specific model- and observations-related limitations, and made them available for the community. Doing so, I have paved the way for a clean cosmological analysis of reionisation data. Once next-generation data is available, these methods will give reliable constraints on the global and local history of cosmic reionisation, telling us about the Universe as a whole and about the nature of its early light sources.

Université Paris-Saclay
Espace Technologique / Immeuble Discovery
Route de l’Orme aux Merisiers RD 128 / 91190 Saint-Aubin, France